The Structure, Stellar Content and Dynamics of Dwarf Galaxies in the Local Volume

Bonita E. De Swardt

Department of Astronomy
University of Cape Town
South Africa

A dissertation submitted in fulfillment for the degree of Doctor of Philosophy in the Department of Astronomy
UNIVERSITY OF CAPE TOWN

February 2009

Supervisors: *Prof. R. C. Kraan-Korteweg, Dr. H. Jerjen*

Abstract

In the first part of the thesis, we present a detailed near-infrared (NIR) J-, H- and K_s-band photometric study of six Local Volume ($D \lesssim 10$Mpc) dwarf galaxies using the 1.4m Infrared Survey Facility (IRSF). Three galaxies in the sample having absolute B-band magnitudes $M_B \gtrsim -15\overset{\mathrm{m}}{.}0$ are detected for the first time. We find that the magnitudes of those dwarfs previously detected by 2MASS were underestimated by up to $0\overset{\mathrm{m}}{.}5$. The deep NIR observations allow for the surface brightness profiles of the galaxies to be extracted to low surface brightnesses of 25mag arcsec^{-2} in the J- and H-bands, and 23.5mag arcsec^{-2} in the K_s-band. The central structure of the galaxies was revealed by carrying out a two-component decomposition of the light profiles. The $J - K_s$ colour of the galaxies was used to explore the luminosity-metallicity relation. The six dwarfs are found to closely follow the B- versus H-band luminosity relation defined for brighter galaxies in the Virgo Cluster. Finally, using the H-band photometry, the stellar masses of the galaxies were determined.

In the second part of the thesis, a pilot study of the search for an intermediate-mass black hole (IMBH) in the center of the Sculptor group dwarf galaxy NGC 59 is presented. Longslit optical spectra were obtained during the commissioning phase of the 10m Southern African Large Telescope (SALT). These spectra were used to derive the kinematics as well as the chemical content of the galaxy. We determine a central velocity dispersion of $\sigma_0 = 83.5 \pm 8.2$km s^{-1} which allows us to infer an estimate of $M_{\mathrm{BH}} \sim 4 \times 10^6\,\mathrm{M}_\odot$ for a possible central IMBH by extrapolating the $M_{\mathrm{BH}} - \sigma_0$ relation to the lower BH mass regime.

Acknowledgements

I would like to thank my supervisors Prof Renée Kraan-Korteweg and Dr Helmut Jerjen for their support throughout my PhD degree. I am indebted to them for their words of wisdom and for all I have learnt from them.

I am extremely grateful to the SALT astronomers Petri Vaisanen and Alexei Kniazev for all the time they devoted to answering my questions and for their patience during our numerous discussions. I would also like to thank the faculty and staff of the Department of Astronomy for creating a stimulating environment in which to conduct my research. Not forgetting my fellow students for their friendship and encouragement, I would like to thank, in particular, my dear officemates Paul Kotze, Michelle Cluver and Ihab Riad for many fruitful discussions.

I would like to express my gratitude to the National Research Foundation of South Africa without whom this PhD degree would never be possible.

Contents

List of Figures

List of Tables

Chapter 1

Introduction

1.1 Overview of Dwarf Galaxies

The significance of dwarf galaxies in the Universe has largely been underestimated because of the modest luminosities and sizes of these systems compared to their larger counterparts. It is now known that dwarf galaxies are the most numerous type of galaxy in the nearby Universe (Ferguson & Binggeli 1994). Still dwarf galaxies remain the most poorly studied stellar systems due to their low surface brightness ($\mu_{V,\mathrm{eff}} \gtrsim 22\mathrm{mag\ arcsec}^{-2}$). These galaxies can provide more insight into the physical processes governing galaxy formation and evolution. In hierarchical structure formation theories (e.g., Toomre & Toomre 1972; Kauffmann et al. 1993; Moore et al. 1999; Cole et al. 2000), dwarf galaxies constitute the building blocks of larger stellar systems. This illustrates the fundamental role that dwarfs can play in the formation of large-scale structure within the Universe, and cosmology in general. Moreover, the abundance of dwarf galaxies in the local Universe allows for a detailed study of their physical and chemical evolution in various environments.

Dwarf galaxies show a wide range of masses, luminosities, morphologies, gas content, and star formation histories (e.g., Mateo 1998). The distinction between dwarfs and giant galaxies is primarily based on their luminosity, where dwarf galaxies are defined as having absolute magnitudes $M_V \geq -18\overset{\mathrm{m}}{.}0$ (Grebel 2001). Following Hubble's classification scheme for giant galaxies (Hubble 1926), dwarf galaxies are generally subdivided into two classes based on their optical appearance: early-type and late-type dwarfs. The early-type dwarfs include dwarf elliptical (dE) and dwarf spheroidal (dSph) galaxies which show a smooth light distribution. The dE galaxies are more massive, centrally concentrated (sometimes nucleated) and have higher surface brightness than the dSph's, which are faint and diffuse stellar systems. The late-type dwarfs consist of dwarf irregular (dIrr) galaxies and blue compact dwarfs. These galaxies are blue, exhibit a non-uniform light distribution in the optical and do not show nucleation. As an example, the morphology difference between an early- and late-type dwarf is illustrated for the galaxies NGC 185 and Ho IV in Fig. 1.1. The B-band image of the dIrr galaxy Ho IV shows the clumpy substructure in the light distribution which corresponds to young star clusters. On the other hand, a smooth light distribution is observed for the dE galaxy NGC 185.

Apart from the optical morphology, there are other properties distinguishing early- and late-type dwarfs. Early-type dwarfs are gas-poor, and they host an old and/or intermediate-age stellar population (Held 2005). These galaxies have low star formation rates (SFR) owing to their lack of neutral hydrogen (H I) gas (Bouchard et al. 2005). In contrast, the late-type dwarfs host a younger stellar population and have a higher SFR (Skillman et al. 2003). These

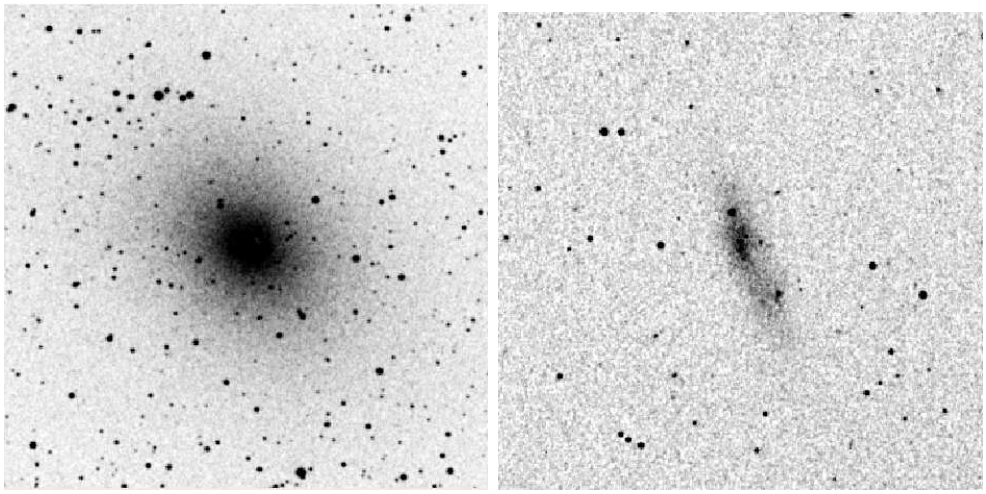

Figure 1.1 Comparison of the optical morphology of dE and dIrr galaxies. The B-band Digitized Sky Survey image of dE galaxy NGC 185 and dIrr galaxy Ho IV is shown on the left and right, respectively. The size of both galaxy images is $10' \times 10'$.

dwarfs contain a significant amount of H I gas which fuels the star formation activity in the galaxy. The evolutionary link between early- and late-type dwarfs is not clear. It has been suggested that gas-deficient dSph's are simply dIrr galaxies which have been stripped of their interstellar medium (ISM) (Grebel 2005). In the Local Group (LG), the proximity of dSph's to massive galaxies supports this idea. Interactions with a massive galaxy may be an effective agent in removing the ISM from the dwarfs (e.g., Mayer et al. 2001). A different picture is given by the metallicity-luminosity relation for these galaxies. Both dSph's and dIrr's follow the trend of increasing metallicity with increasing galaxy luminosity (e.g., Caldwell et al. 1992; van Zee et al. 1997). The metallicity-luminosity relation for the two galaxy types are, however, offset from each other with the dSph's showing higher mean stellar metallicities at a given optical luminosity (Skillman & Bender 1995). This may indicate that the dSph's have experienced more rapid star formation and enrichment at early times compared to the dIrr's (Grebel et al. 2003).

Generally, it is difficult to distinguish between early- and late-type dwarfs based on their kinematical properties alone. The late-type dwarfs are supported by rotation (see e.g., Mateo 1998). Less consistency in the kinematics is seen for early-type dwarfs with various degrees of rotational support detected for dE galaxies (De Rijcke et al. 2001, 2003; Pedraz et al. 2002; Geha et al. 2002, 2003, 2006). This is contrary to earlier claims which state that dE's are purely flattened by velocity anisotropy (e.g., Bender & Nieto 1990; Bender et al. 1991). The dSph galaxies are not, however, supported by rotation and appear to be strongly dark matter (DM) dominated (see the review by Mateo 1998). This last point was recently emphasized by Strigari et al. (2008), who obtained high mass-to-light (M/L) estimates – approaching $1000(M/L)_{\odot}$ – for dSph satellites of the Milky Way. The large DM content of dSph's is inferred from their velocity dispersion which gives high mass-to-light ratios under

the assumption of virial equilibrium (e.g., Kleyna et al. 2002). Embedded morphological structures have been detected in early-type dwarf galaxies (De Rijcke et al. 2003). These include stellar disks sometimes harbouring spiral arms or bars (Jerjen et al. 2000c; Barazza et al. 2002; Corsini et al. 2007; Lisker et al. 2006). The embedded features together with the galaxy rotation strengthen the evolutionary connection between early-type dwarfs and late-type galaxies. It is possible that early-type dwarfs may have inherited other kinematical features from its progenitor galaxy such as the hosting of a black hole (BH) in its center. A detailed study of the internal kinematics and dynamics of dwarf galaxies is needed to help constrain the evolutionary scenarios of these complex stellar systems.

The past decade has seen an explosion in the detection of dwarf galaxies in the Local Volume (LV, $D \lesssim 10$Mpc) (Côté et al. 1997; Karachentseva & Karachentsev 1998; Jerjen et al. 1998; Karachentseva et al. 1999; Karachentseva & Karachentsev 2000; Karachentsev et al. 2000a; Jerjen et al. 2000a; Karachentsev et al. 2001). This is attributed to the construction of large aperture telescopes and the availability of larger, more sensitive detectors. Dwarfs in the LG are spatially well-resolved but their low surface brightnesses ($\mu_V \gtrsim 22$mag arcsec^{-2}) has limited a detailed study of these galaxies. Some dSph galaxies in the LG have only been recently discovered, and more faint candidates are continuously being found (e.g., Zucker et al. 2004a,b; Willman et al. 2005; Martin et al. 2006). These dwarfs contribute significantly to the faint end of the galaxy luminosity function (see e.g., Chiboucas et al. 2009). A larger sample of dwarf galaxies than that seen in the LG is, however, needed to investigate the physical mechanisms driving the formation and evolution of these pristine galaxies. Dwarf galaxies within the LV are seen as ideal laboratories in which to study the nature of dwarfs in different environments. Even though dwarf galaxies in the LV are fainter than those in cluster environments, the higher spatial resolution for these nearby systems will allow for a more accurate determination of their physical and internal properties.

The local observing facilities in Sutherland, South Africa, can help contribute to the current knowledge of dwarf galaxies. An excellent opportunity to study nearby dwarfs was given during the commissioning of the 10m Southern African Large Telescope (SALT) from May–August 2006. The Robert Stobie Spectrograph (RSS) of SALT can be used to obtain longslit optical spectra of dwarf galaxies and therewith determine their internal kinematics. For this reason, a large sample of ~ 40 LV dwarf galaxies was identified (see Appendix A). The dwarf galaxies generally have an effective surface brightness of $\mu_{B,\mathrm{eff}} > 21$mag arcsec^{-2} in the B-band. The sample dwarf galaxies also vary in angular size from $D_{\mathrm{ext}} \sim 40'$ for the extended Sculptor dE to those having $D_{\mathrm{ext}} < 1'$. Their spectra will allow for a detailed kinematic study of dwarfs which can give more clarity to two important issues: the kinematic support structure of early-type dwarfs and the possibility of these systems hosting a central massive BH. In addition, the 1.4m Infrared Survey Facility (IRSF) telescope in Sutherland can be used to obtain deep simultaneous J-, H- and K_s-band imaging of the galaxies. The deep near-infrared (NIR) imaging can be used to study the NIR structure and stellar content of the dwarf galaxies. The NIR observations in conjunction with the optical spectra will be used in modeling the dynamics of the dwarfs to ascertain the possibility of them hosting a BH, and to determine their DM content. These are crucial pieces of information needed to

place further constraints on current galaxy formation and evolution theories.

1.2 The Internal Kinematics and Dynamics of Dwarf Galaxies

The kinematic studies of dwarf galaxies are observationally challenging due to their low surface brightness ($\mu_{V,\mathrm{eff}} \gtrsim 22\mathrm{mag\ arcsec}^{-2}$). Their kinematic profiles (i.e., the radial velocity and velocity dispersion profiles) are usually derived from the integrated light spectrum of the galaxy. The spectra of most early-type dwarfs are devoid of emission lines as these galaxies lack an ISM. The internal kinematics of these dwarfs are measured from the absorption line features in the spectrum which require a high signal-to-noise (S/N) ratio. The kinematic studies of dwarf galaxies are therefore constrained by long exposure times in order to achieve sufficiently high S/N levels for these faint stellar systems. Because of this constraint, the first kinematical measurements of dE galaxies (Bender & Nieto 1990) were conducted more than a decade after the absorption line kinematic studies of giant elliptical galaxies (e.g., Bertola & Capaccioli 1975). The first kinematic profiles for dwarf galaxies were derived for dE's in the LG and two of the brightest dE galaxies in the Virgo cluster (Bender & Nieto 1990; Bender et al. 1991; Held et al. 1990). These initial observations only allowed for the derivation of global velocity dispersions of dE's outside of the LG (Peterson & Caldwell 1993).

The availability of large telescopes with more sensitive detectors has facilitated the kinematic studies of dwarf galaxies. It is now possible to obtain spatially-resolved kinematics of dwarf galaxies beyond the LG. Recent studies have focused on determining the internal kinematics of dE galaxies in the Fornax and Virgo Clusters (e.g., Chilingarian 2008). The galaxy luminosity function of nearby clusters is dominated by early-type dwarfs (Trentham & Tully 2002). Dwarf elliptical galaxies are known to thrive in dense cluster environments, more so than any other galaxy type (Ferguson & Binggeli 1994). Contrary to hierarchical models, the gregarious nature of dE galaxies favour their formation from a progenitor galaxy population. Spiral and irregular galaxies have been proposed as progenitors of dE's that are morphologically transformed through the process of galaxy harassment and interaction (e.g., Moore et al. 1998). Nearby clusters are seen as ideal environments in which to test these scenarios by carrying out detailed kinematic studies of dE galaxies.

The kinematical profiles of dE and dS0 galaxies in the Fornax and Virgo Clusters show various degrees of rotational support for these dwarfs (De Rijcke et al. 2001, 2003; Geha et al. 2002, 2003; Pedraz et al. 2002; Simien & Prugniel 2002; van Zee et al. 2004; Chilingarian 2008). Kinematically decoupled components are detected in some dwarf galaxies (De Rijcke et al. 2004; Geha et al. 2005; Prugniel et al. 2005). These kinematic features together with the presence of stellar disks (e.g., Jerjen et al. 2000c; Barazza et al. 2002) support an evolutionary connection between early-type dwarfs and late-type galaxies. In particular, the models of Moore et al. (1998) demonstrate that in cluster environments, a spiral galaxy can be morphologically transformed into a dE through the process of galaxy harassment. This process has been found to increase the velocity dispersion in the resulting galaxy while maintaining a significant fraction of the progenitor's rotation. By measuring the internal kinematics of early-type dwarfs, constraints can be placed on the progenitor type galaxy and

possibly the amount of disruption required for the transformation.

The kinematic studies of dwarf galaxies in the LV are hampered by the low surface brightness ($\mu_B \gtrsim 23$mag arcsec^{-2}) of these systems. However, the proximity of the LV dwarfs results in a higher spatial resolution for these galaxies compared to that obtained for dwarfs in the more distant clusters. Detailed kinematic profiles have only been constructed for one early-type dwarf, NGC 205, a dE companion of the Andromeda galaxy (Geha et al. 2006). This dwarf is supported by a combination of rotation and anisotropic pressure similarly to that seen for dE galaxies in cluster environments. The resolved stellar kinematics were also used to explore the possibility of NGC 205 hosting a BH in its center (Valluri et al. 2005). Dynamical models of the galaxy were used to place an upper limit on the mass of a central BH. Their results illustrate that the kinematic profiles of dwarf galaxies can also give more insight to the possibility of these systems hosting a central massive BH. The LV provides a diverse environment in which to study the formation of BHs in dwarf galaxies which will give further clues to the evolutionary link between dwarfs and their giant counterparts.

1.2.1 Evidence for Black Holes

Dynamical models of galaxies strongly favour the presence of a supermassive BH (SMBH) in the centers of all massive galaxies with a spheroidal component such as ellipticals, lenticulars and early-type spirals with bulges (Richstone et al. 1998). Direct measurements of the BH mass have been carried out for a few dozen of these galaxies yielding masses in the range of $10^6 - 10^9\,\mathrm{M}_\odot$ (see the review by Ferrarese & Ford 2005). The BH mass of the galaxies is measured from either spatially-resolved stellar or gas kinematics for quiescent nuclei, or from reverberation mapping of broad-line regions for active nuclei (Gebhardt et al. 2003; Ferrarese et al. 2001; Onken et al. 2004; Peterson et al. 2004). The masses of the SMBHs are found to correlate well with the fundamental properties of the host galaxies: this includes the bulge mass (Kormendy & Richstone 1995; Magorrian et al. 1998), central velocity dispersion (Ferrarese & Merritt 2000; Gebhardt et al. 2000a), central light concentration (Graham et al. 2001; Erwin et al. 2004) and mass of the dark matter halo (Ferrarese 2002).

The tight correlation between BH mass (M_{BH}) and stellar velocity dispersion (σ_0) of the host spheroid is the basis upon which the SMBH demographics is built (Ferrarese & Merritt 2000; Gebhardt et al. 2000a; Tremaine et al. 2002). This relation is, however, largely limited to galaxies with massive bulges having central velocity dispersion $\sigma_0 \gtrsim 80$ km s^{-1}, which corresponds to $M_{\mathrm{BH}} > 2 \times 10^6\,\mathrm{M}_\odot$. The extension of the $M_{\mathrm{BH}} - \sigma_0$ relation to the intermediate-mass BH (IMBH) regime of $M_{\mathrm{BH}} \lesssim 10^6\,\mathrm{M}_\odot$ is crucial for constraining models of BH formation (e.g., Cattaneo et al. 1999). For example, what are the minimal values of the galaxy mass or velocity dispersion below which BHs are unable to form or grow (Bromley et al. 2004)? From a cosmological perspective, IMBHs can contribute a significant fraction to the missing baryonic DM in the Universe (Lacey & Ostriker 1985; van der Marel 2004).

By assuming that the $M_{\mathrm{BH}} - \sigma_0$ relation can be extrapolated to the low BH mass regime, it can then be inferred that IMBHs should exist in galaxies (or dense stellar clusters) having central velocity dispersion in the range of $20 \lesssim \sigma_0 \lesssim 80$ km s^{-1} (see Fig 1.2). Dwarf galaxies are known to have central velocity dispersions in this range (e.g., Mateo 1998), making them

likely candidates for hosting an IMBH in their centers. At the same time, it is expected that late-type galaxies can host an IMBH owing to their less massive spheroids and correspondingly smaller velocity dispersions. Currently there exists no firm detection of an IMBH in either a late-type galaxy or dwarf galaxy.

The presence of a BH is revealed by the influence it has on its immediate environment. The observational signature of a BH can be in the form of accretion or seen as a gravitational effect on the surrounding stars. Indirect evidence for an IMBH exists in the centers of some Seyfert galaxies hosting an active galactic nucleus (AGN) (Kraemer et al. 1999; Filippenko & Ho 2003; Barth et al. 2004; Greene & Ho 2004; Barth et al. 2005). Figure 1.2 shows the location of the Seyfert galaxies in the $M_{\rm BH} - \sigma_0$ plane. Seyfert galaxies are generally found to have BH masses just above the IMBH range ($M_{\rm BH} \gtrsim 10^6\,{\rm M}_\odot$). They seem to follow the $M_{\rm BH} - \sigma_0$ relation of Tremaine et al. (2002) which is consistent with a simple extrapolation of this relation to low BH masses. A dynamical detection of an IMBH in Seyfert galaxies is, however, still lacking.

A dynamical detection of a BH becomes even more challenging in late-type and dwarf galaxies showing no signs of accretion. These galaxies can host nuclear star clusters of mass $10^6 - 10^7\,{\rm M}_\odot$ in their centers (Böker et al. 2002), which is often barely resolved even with the resolution of HST. The gravitational influence of the nuclear star cluster on the surrounding stars is therefore indistinguishable from that of a BH. The ambiguity between these two objects can only be resolved through detailed dynamical modeling of the galaxy. In the Local Group, the search for an IMBH was carried out for two galaxies: the late-type spiral M33 (Gebhardt et al. 2001; Merritt et al. 2001) and the nucleated dwarf elliptical galaxy NGC 205 (Valluri et al. 2005). A firm detection of an IMBH could not be made for either galaxy. However, the dynamical modeling of the stellar kinematics yields an upper BH mass limit for the galaxies (see Fig. 1.2). An upper BH mass limit of $3.5 \times 10^4\,{\rm M}_\odot$ was determined for NGC 205 while a BH mass limit in the range of $1500\,{\rm M}_\odot$ (Gebhardt et al. 2001) and $3000\,{\rm M}_\odot$ (Merritt et al. 2001) was obtained for M33. These values are found to lie below the $M_{\rm BH} - \sigma_0$ relation for early-type galaxies. Beyond the LG, Geha et al. (2002) inferred upper limits in the BH mass range of $10^6 - 10^7\,{\rm M}_\odot$ for six dE galaxies in the Virgo Cluster.

It has been suggested that massive globular clusters (GCs) may be the remnant nuclei of tidally stripped dwarf galaxies (see e.g., Goerdt et al. 2008). This makes GCs exhibiting dense and massive cores possible sites for hosting of an IMBH (Baumgardt et al. 2005). One such study was recently conducted by Noyola et al. (2008) who determined the central kinematics of the largest and most massive member ($5.1 \times 10^6\,{\rm M}_\odot$, Harris 1996) of the Galactic GC system, ω Centauri (NGC 5139). The flattening of ω Cen together with its complex stellar population makes this GC a good candidate for being a stripped core of an accreted dwarf galaxy for the realization of this scenario. The dynamics of ω Cen can be explained by invoking an isotropic, spherical model with a BH mass of $4 \times 10^4\,{\rm M}_\odot$. However, the degeneracy in the dynamical models does not require this GC to host an IMBH in its center. Apart from ω Cen, two other GCs have been suggested for harbouring an IMBH in their nucleus: the Galactic GC M15 (Gebhardt et al. 2000b; Gerssen et al. 2002, 2003), and G1, a giant GC around M31 (Gebhardt et al. 2002, 2005). The IMBH detections in the centers of these GCs remain

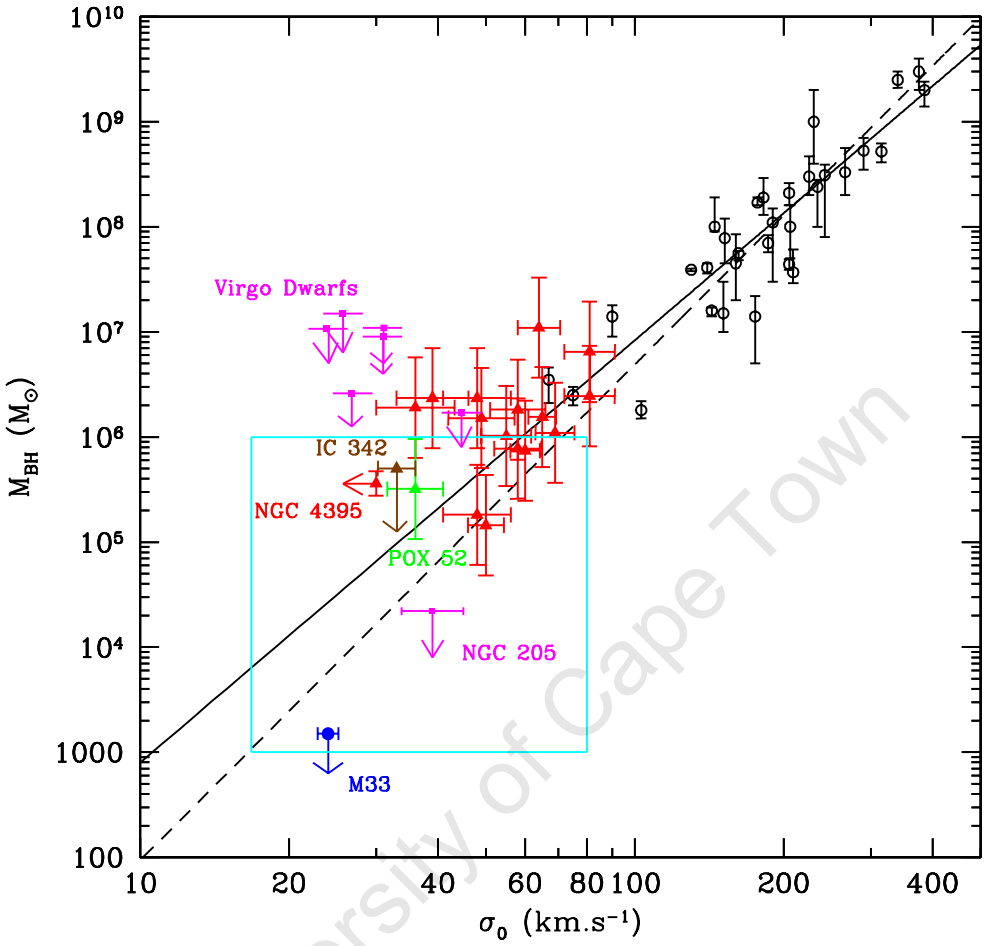

Figure 1.2 BH mass versus bulge velocity dispersion (σ_0) relation. Early-type galaxies from Ferrarese & Merritt (2000), Gebhardt et al. (2000a) and Tremaine et al. (2002) are shown in black. Seyfert1 galaxies (including Pox 52 and IC 342) are taken from Barth et al. (2005) and are plotted in red. The upper BH mass limits for six Virgo dE's (Geha et al. 2002) and the nucleated dE NGC 205 (Valluri et al. 2005) are shown. Additionally, the upper BH mass limit for the late-type spiral M33 is shown in blue (Merritt et al. 2001). The solid and dashed lines indicate the $M_{\rm BH} - \sigma_0$ relations derived from Tremaine et al. (2002) and Merritt et al. (2001), respectively. The boxed region indicates the expected range in BH mass and velocity dispersion for an IMBH detection in dwarf galaxies.

questionable (Baumgardt et al. 2003a,b; McNamara et al. 2003).

The newly constructed 10m SALT telescope provides an excellent opportunity to investigate the possible existence of IMBHs in dwarf galaxies as well as in GC systems. By restricting the IMBH search to LV dwarf galaxies and Galactic GCs, high enough spatial resolution can be achieved for a BH detection. Part of this thesis is dedicated to the search for an IMBH in these two distinct stellar systems using the SALT telescope. It will make use of data acquired during the commissioning phase of the telescope. The results are therefore seen as a pilot study for the search of the elusive IMBH in dwarf galaxies and Galactic GCs.

1.3 Thesis Outline

The thesis consists of two main chapters. In the first chapter, we present a detailed photometric study of six LV dwarf galaxies in the NIR. This study makes use of deep J-, H- and K_s-band imaging obtained with the 1.4m IRSF telescope. The chapter begins with a description of the criteria used for selecting the six dwarfs (section 2.2.1). A review of the known properties of the galaxies is given in section 2.2.2. This is followed by a detailed description of the reduction and calibration procedures for the NIR data (sections 2.4–2.6). The surface photometry of the dwarfs is performed in section 2.7 where the surface brightness and colour profiles of the galaxies are derived. The total magnitude is measured for each galaxy and then compared to the values obtained by the Two Micron All Sky Survey (2MASS). The NIR structure of the galaxies is explored in section 2.8. Two different fitting techniques are employed for this purpose. The first method involves fitting an analytic function to the one-dimensional surface brightness profile from which the structural parameters of the galaxy are determined. In the second, the structural parameters are derived by performing a photometric decomposition of the two-dimensional galaxy image using the GALFIT software. The effectiveness of both techniques for our NIR study is illustrated. Given the NIR colours, we are able to investigate the metallicity-luminosity relation for the dwarf galaxies (section 2.9.1). By combining the NIR magnitudes with existing B-band magnitudes, the evolutionary sequence and morphology of the galaxies are explored in section 2.9.2. The total stellar masses of the dwarfs are derived from their H-band observations in section 2.9.3.

In the second part of the thesis (Chapter 3), a pilot study for the search of an IMBH is presented for the Sculptor group dwarf NGC 59. Longslit optical spectra of NGC 59 were obtained during the commissioning phase of the 10m SALT telescope (May–August 2006). The observations carried out for this galaxy are described in section 3.3. The reduction procedure for the SALT spectra is found in section 3.4. A detailed kinematical analysis of the galaxy is carried out in section 3.5. The SALT spectra together with the NIR imaging for NGC 59 are used to investigate the kinematic profiles obtained for the galaxy. The kinematic profiles provide the first clues to whether this galaxy might possibly contain a BH in its center. The chemical content of NGC 59 is derived from the SALT spectra in section 3.6. These results allow us to explore the NIR luminosity-metallicity relation for this dwarf galaxy.

In continuing our BH search, a pilot study for the search of IMBHs is presented for six Galactic GCs in Appendix E. The longslit optical spectra of the GCs were also obtained

during the commissioning phase of SALT. The stellar kinematic profiles are derived for each GC. At the same time, the feasibility of conducting the IMBH search with the SALT/RSS spectrograph is assessed.

The main results of the thesis and some future prospects are given in Chapter 4.

Chapter 2

Photometric Properties of Six Local Volume Dwarf Galaxies from Deep Near-infrared Observations

2.1 Introduction

Dwarf galaxies are, apart from stellar clusters, the most fundamental stellar systems. They are believed to be the building blocks of larger galaxies in hierarchical galaxy formation theories (e.g., Bullock et al. 2001) and can provide insight into galaxy formation and evolution on the smallest scales (Taylor & Babul 2003). The Local Volume (LV, $D \lesssim 10$Mpc) provides a diverse environment in which these systems can be studied. The observations of nearby dwarf galaxies, however, remain challenging due to their characteristic low surface brightness ($\mu_{V,\mathrm{eff}} \gtrsim 22$mag arcsec^{-2}). The availability of more sensitive detectors has not only led to the discovery of even fainter dwarfs, but allows for the measurement of their physical properties (e.g., stellar, gas and dark matter content). An understanding of the physical mechanisms driving the observational properties of dwarf galaxies can significantly impact our current views of galaxy formation and evolution, as well as the nature of dark matter.

Extensive optical galaxy surveys of the local neighbourhood ($D \lesssim 10$Mpc) of the Milky Way (Kraan-Korteweg & Tammann 1979; Schmidt & Boller 1992; Karachentsev et al. 2004) have been carried out for well over two decades. Increasingly fainter and lower SB galaxies have been detected with the development of more sensitive instruments within this time frame. These include the discovery of numerous dwarf galaxies in the LV (Côté et al. 1997; Karachentseva & Karachentsev 1998; Jerjen et al. 1998; Karachentseva et al. 1999; Karachentseva & Karachentsev 2000; Karachentsev et al. 2000a; Jerjen et al. 2000a; Karachentsev et al. 2001). The dwarf galaxies constitute ∼85% of the nearby galaxy population. Dwarf galaxies in the LV are therefore a representative sample for which a detailed study of their physical properties can be explored.

Follow-up observations of the newly discovered dwarfs have primarily focused on obtaining distance estimates and stellar population studies for these galaxies (see Karachentsev et al. 1999, 2007; Seitzer et al. 2001, and references therein). Deep B- and R-band imaging of the new dwarf members in the Centaurus A and Sculptor groups was performed by Jerjen et al. (1998, 2000a,b). They derive a distance estimate for each galaxy using the surface brightness fluctuation method. The photometric and structural parameters of the galaxies were also measured. A detailed BR photometric analysis of a larger sample of LV dwarf galaxies (from the Karachentseva & Karachentsev (1998) sample) was later carried out by Parodi et al. (2002). Their goal was to establish a surface photometry database for a large, homogeneous sample of nearby dwarf galaxies. The photometric database provides a systematic

means of studying structural differences in the dwarf galaxies. Multi-wavelength observations ranging from the optical to the infrared wavelengths are, however, needed to gain a complete understanding of the morphology and evolutionary state of these galaxies.

The main contribution to the stellar mass of galaxies arises from the underlying old stellar component. The morphology of the individual galaxies is established by this underlying component which is thought to be the "backbone" of the galaxy. The distribution of the old stellar component is effectively probed at near-infrared (NIR) wavelengths. The NIR wavelengths are minimally influenced by dust attenuation revealing the internal galaxy structure. The largest NIR database containing the photometric and structural parameters of nearby dwarf galaxies has been constructed using observations from the Two Micron All Sky Survey (2MASS, Jarrett 2000; Jarrett et al. 2003). The inadequacy of the 2MASS photometry for deriving these parameters is, however, continuously being highlighted as deeper observations of the dwarf galaxies are obtained. These effects are more evident for the low SB galaxies where the short exposures of 2MASS result in either the galaxy being undetected or its total flux being underestimated by up to 70% (Andreon 2002; Kirby et al. 2008). Deep NIR observations of the LV dwarf galaxies are thus needed to avoid the selection effects of 2MASS photometry at low luminosities and low star densities.

Deep NIR observations are hardly available for nearby dwarf galaxies because of the large integration times required for imaging these faint stellar systems. The deep NIR imaging of nearby dwarfs have subsequently focused on those galaxies showing star formation activity such as the dwarf irregular galaxies (Vaduvescu et al. 2005) and blue compact dwarfs (e.g., Cairós et al. 2003). Recently, Kirby et al. (2008) have obtained deep H-band (1.65μm) observations of a large sample of 57 LV galaxies consisting mostly of irregular galaxies. Their deep observations allow for the galaxies to be detected 4mag arcsec^{-2} or 40 times fainter than 2MASS. Given the high spatial resolution of the images, they were able to derive photometric and structural parameters for the galaxies, eight of which are dwarf members of the LV.

The observations by Kirby et al. (2008) and Vaduvescu et al. (2005) are seen as the first contributions to an extensive NIR photometric database of LV dwarf galaxies. To add to this effort, we have obtained simultaneous, deep J- (1.25μm), H- (1.65μm) and K_s-band (2.15μm) observations of a sample of six LV dwarf galaxies. The galaxies are members of a large sample of $\sim$ 40 LV dwarf galaxies, selected as possible candidates for hosting an intermediate-mass black hole in its center (see Chapter 1, section 1.2.1). The photometric analysis includes the derivation of the surface brightness and colour profiles of the galaxies. The structural and photometric parameters are obtained by fitting various functional forms to the light distribution of the galaxy. In addition, the deep JHK_s observations allow for a more accurate measure of the galaxy magnitudes compared to 2MASS. The NIR photometric parameters of the three faintest dwarfs in the sample are measured for the first time. We have also derived the luminosities and stellar masses of the galaxies. The photometric results presented in this chapter will complement the BV surface photometry database already established for these galaxies. The deep NIR observations will eventually be extended to include all LV dwarfs in the large galaxy sample.

2.2 Sample Selection

2.2.1 Selection Criteria

Deep near-infrared (NIR) J-, H- and K_s-band imaging was obtained for six dwarf galaxies with the 1.4m Infrared Survey Facility (IRSF) telescope located at Sutherland, South Africa (see section 2.3 for details). The target galaxies were selected from the large sample of LV dwarf galaxies listed in Appendix A. The following criteria led to the selection of the six target galaxies for NIR observations:

1. The dwarf galaxies are required to have an angular size smaller than $\sim 4'$ in the B-band. The galaxy then falls completely in the $7\farcm8 \times 7\farcm8$ field-of-view (FoV) of the IRSF telescope. This criterion will allow a reliable measure of the sky background within the FoV of the galaxy images.

2. Given the wide range in right ascension of all the target galaxies, the galaxies within the February–June visibility window of the SAAO site were selected. This was the period corresponding to the allocated semester for observing the dwarf galaxies.

3. Extremely low surface brightness (SB) galaxies ($\mu_{B,\mathrm{eff}} \gtrsim 24.5$mag arcsec^{-2}) were as yet excluded. The NIR photometric results for the sample of six dwarf galaxies will later be used to estimate optimal exposure times for these fainter galaxies.

The main known optical properties of the six target galaxies are listed in Tables 2.1 and 2.2. The sample mainly consists of early-type dwarf galaxies. The morphological types range from dwarf elliptical galaxies showing a nuclear component (dE,N) to dwarf lenticulars (dSO) exhibiting a disk component. Those dwarf galaxies having a nuclear component are the more likely candidates for hosting a central IMBH (see Chapter 1 for a detailed discussion).

The galaxies span a range of distances within the LV, from 3.5–10Mpc. The membership of dwarf galaxies to the Centaurus A (Cen A) and Sculptor (Scl) groups was determined from surface brightness fluctuation (SBF) distance measurements (Jerjen et al. 1998). The galaxies ESO 384-016 and NGC 5206 were identified as part of the Cen A group (Côté et al. 1997; Jerjen et al. 2000a), while NGC 59 was found to be a member of the Scl group (Jerjen et al. 1998). Complementary longslit observations of NGC 59 have been obtained with the SALT spectrograph. A detailed study of this dwarf galaxy based on the deep NIR observations described here, and the longslit spectroscopic observations are presented in Chapter 3. The remaining galaxies in the sample are more distant dwellers and lie on the outskirts of the LV (Karachentsev et al. 2004, and references therein).

Deep B- and R-band imaging of five of the target galaxies are available[1] from Jerjen et al. (2000b) and Parodi et al. (2002). The B- or R-band optical image of the individual galaxies are shown in Fig. 2.1. Deep optical imaging has not been carried out for the dwarf galaxy NGC 5206. The Space Telescope Science Institute (STScI) Digitized Sky Survey (DSS) image of this galaxy is shown in Fig. 2.1. The galaxies NGC 59, NGC 3115 DW01 and NGC 5206 are

[1]Unfortunately, the optical data sets for the five dwarf galaxies cannot be recovered from the archives or PI's of these observations. The optical imaging of the galaxies NGC 3115 DW01, LEDA 166099 and UGCA 200 has been deleted by the PI while the optical data for ESO 384-016 and NGC 59 were destroyed in the 2003 bushfire's at Mount Stromlo Observatory, Canberra (Australia).

Table 2.1. Basic properties of sample dwarf galaxies.

Galaxy (1)	Type (2)	D (Mpc) (3)	Method (4)	$v_\odot$ (km s^{-1}) (5)	$v_{\rm LG}$ (km s^{-1}) (6)	M_B (mag) (7)	$\log_{10}(L_B)$ (8)	H I Observations H I Observed (9)	H I Observations Limit ($M_\odot$) (10)	H I Observations Mass ($M_\odot$) (11)
ESO 384-016	dS0/Im	4.2	SBF	561 ± 32 [a]	350	-13.06	7.4	yes	1.0×10^6	$(5.6 \pm 0.3) \times 10^6$
LEDA 166099	dE,N	9.8	MEM	–	–	-14.46	8.0	no	–	–
NGC 59	dS0	4.4	SBF	362 ± 10 [b]	431	-15.74	8.5	yes	5.3×10^5	$(1.5 \pm 0.3) \times 10^7$
NGC 5206	SB?(r?)	3.6	MEM	571 ± 10 [c]	322	-16.66	8.9	yes	7.8×10^6	$< 5.5 \times 10^5$ [f]
NGC 3115 DW01	dE,N	9.7	MEM	698 ± 42 [d]	456	-16.55	8.8	no	–	–
UGCA 200	dE,N	9.7	MEM	721 ± 30 [e]	479	-13.78	7.7	no	–	–

Note. — Columns: (1) Galaxy designation; (2) Morphological classification taken from Jerjen et al. (2000b) and Parodi et al. (2002), with the exception of NGC 5206 which is given by the NASA/IPAC Extragalactic Database (NED); (3) and (4) Distance to the galaxy in Megaparsecs with an indication of the method used (Jerjen et al. 2000a,b; Karachentsev et al. 2004): SBF – via fluctuation of surface brightness; MEM – from membership in the known groups; (5) Heliocentric radial velocity of galaxy from optical emission lines: [a]Jerjen et al. (2000a), [b]Beaulieu et al. (2006), [c]Côté et al. (1997), [d]da Costa et al. (1998). [e]The heliocentric velocity of UGCA 200 was computed by averaging the radial velocities of six globular clusters measured by Puzia & Sharina (2008). Note that the globular cluster having an elevated radial velocity of $v_\odot = 1210 \pm 27$km s^{-1} was excluded as it might be associated with the disk component of NGC 3115 rather than UGCA 200; (6) Local Group velocity from NED; (7) Absolute B-band magnitude (corrected for Galactic extinction); (8) B-band luminosity. The H I parameters: (9) Observed in H I? (10) H I detection limit of 21cm line observations – ESO 384-016 and NGC 59 from Beaulieu et al. (2006); NGC 5206 from Côté et al. (1997); (11) H I mass of galaxies: [f]The upper H I mass limit of NGC 5206 is quoted.

Table 2.2. Parameters of sample dwarf galaxies.

Galaxy (1)	Type (2)	PA (degrees) (3)	Major Axis (arcsec) (4)	B (mag) (5)	$B-R$ (mag) (6)	$\mu_{B,0}$ (mag arcsec^{-2}) (7)	$\mu_{B,\mathrm{eff}}$ (mag arcsec^{-2}) (8)	$R_{B,\mathrm{eff}}$ (arcsec) (9)	Θ (10)	MD (11)
ESO 384-016	dS0/Im	67	78	15.11	1.09	21.51	23.22	16.70	0.3	NGC 5128
LEDA 166099	dE,N	-60	54	15.50	1.16	23.09	23.95	19.52	4.1	NGC 2784
NGC 59	dS0	120	156	12.97	1.07	19.59	21.27	21.30	-0.6	NGC 253
NGC 5206	SB?(r?)	23	222	11.64	1.22	20.24	23.88	172.00	1.1	NGC 4945
NGC 3115 DW01	dE,N	2	102	13.38	1.38	22.26	22.76	29.98	3.6	NGC 3115
UGCA 200	dE,N	-31	66	16.16	1.38	23.19	24.43	17.99	4.5	NGC 3115

Note. — Columns: (1) Galaxy designation; (2) Morphological classification; (3) B-band position angle of galaxy (Lauberts & Valentijn 1989; Parodi et al. 2002); (4) Length of the semi major-axis given by NED. The photometric and structural parameters: (5) total apparent B-band magnitude; (6) $B-R$ colour; (7) central surface brightness; (8) and (9) effective surface brightness and radius of the galaxy. Photometric parameters from Parodi et al. (2002) and Jerjen et al. (2000b), with the exception of NGC 5206 which is taken from Lauberts & Valentijn (1989). (10) Tidal index Θ given by Karachentsev et al. (2004) with negative values corresponding to isolated galaxies and positive values are typical of group members. (11) Name of a neighboring galaxy, classified as the main disturber (MD), producing the maximum tidal action on the given galaxy (Karachentsev et al. 2004).

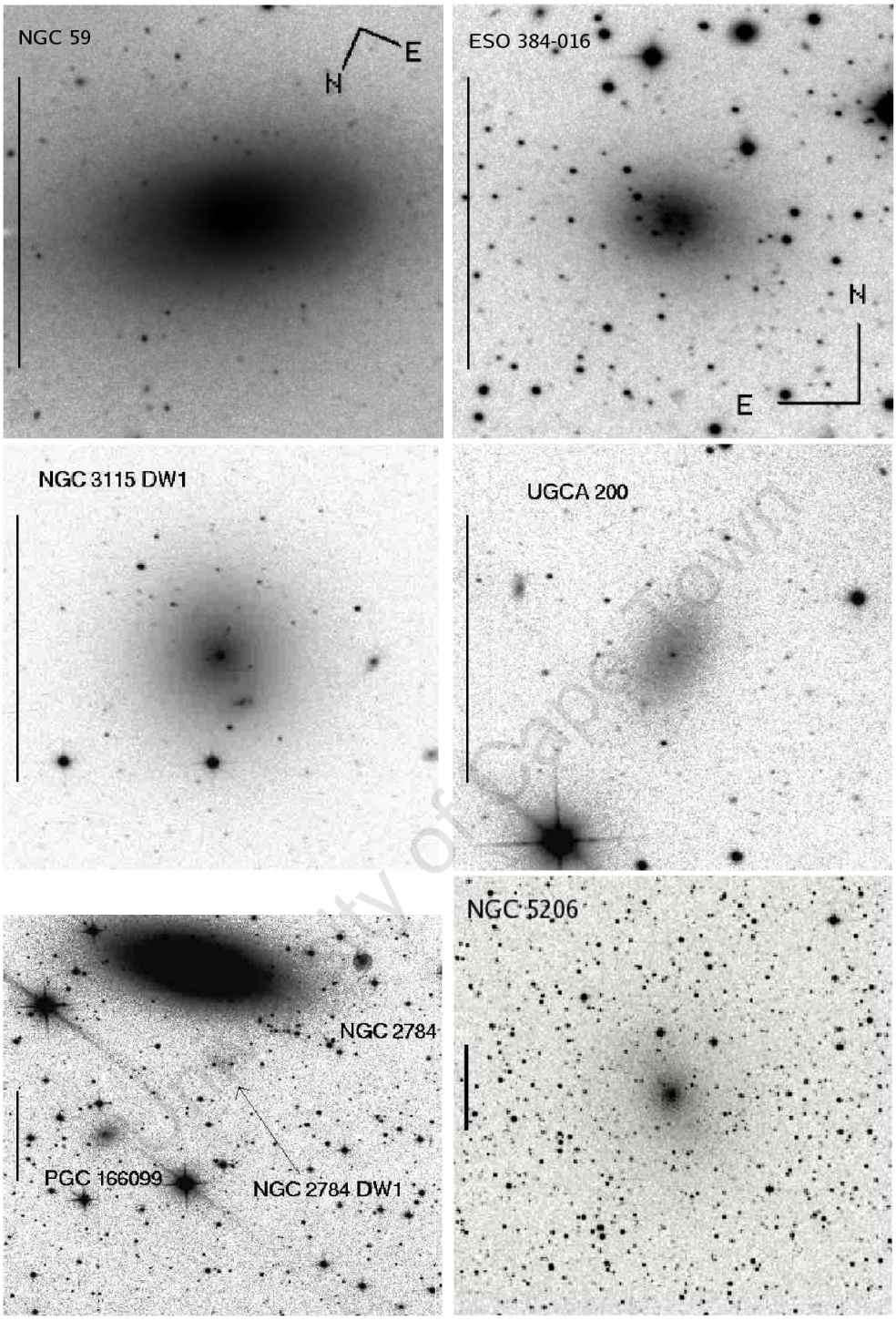

Figure 2.1 Optical imaging of the six dwarf galaxies. The R-band images of NGC 59 (*top left*) and ESO 384-016 (*top right*) are taken from Jerjen et al. (2000b) and Jerjen et al. (2000a), respectively. The image size is $3'$. The B-band images of NGC 3115 DW01 (*middle left*), UGCA 200 (*middle right*) and LEDA (or PGC) 166099 (*bottom left*) are taken from Parodi et al. (2002). The images of NGC 3115 DW01 and UGCA 200 have a FoV of $3\farcm3\times3\farcm3$ while a larger FoV of $9\farcm9\times9\farcm9$ is shown for LEDA 166099. The DSS B-band image of NGC 5206 (*bottom right*) has FoV $10\farcm8\times10\farcm8$. The relative scale of the images is given by the vertical bar which has a length of $2'$. The convention of North–up and East–left is used in those images not showing the orientation.

the brightest in the sample with total apparent magnitude of $B \lesssim 13\overset{\mathrm{m}}{.}4$. The fainter dwarf galaxies in the sample ($B > 15\overset{\mathrm{m}}{.}0$) are less spatially extended on the sky with LEDA 166099 having an angular size of $D_{\mathrm{ext}} < 1$ arcminute (see Table 2.2).

2.2.2 Review of the Properties of Sample Galaxies

In this section, a review of the known properties of the six dwarf galaxies is provided. The main properties of the dwarfs are listed in Tables 2.1 and 2.2 which serve as a quick reference. To help assess the current evolutionary state of the individual galaxies, the findings of various studies for these galaxies from the literature, are described here. The evolutionary portrait of each galaxy will later contribute to the photometric analysis and interpretation of our deep NIR observations.

ESO 384-016

The dwarf galaxy ESO 384-016 is classified as a mixed-type dS0/Im with total apparent magnitude of $B = 15\overset{\mathrm{m}}{.}1$. It is a member of the nearby Cen A group. The membership of ESO 384-016 to the Cen A group was established through the radial velocity measurements of Jerjen et al. (2000a). They measure a heliocentric velocity of $v_{\odot} = 561 \pm 32\mathrm{km\ s^{-1}}$ for ESO 384-016 which is in good agreement with the velocities for well-known Cen A group galaxies such as NGC 5128 ($v_{\odot} = 562\mathrm{km\ s^{-1}}$) and NGC 5236 ($v_{\odot} = 516\mathrm{km\ s^{-1}}$). Jerjen et al. (2000a) have obtained deep B- and R-band imaging of this galaxy. They measure a distance of 4.2Mpc or $v_{\mathrm{LG}} = 350\mathrm{km\ s^{-1}}$ ($H_0 = 73\mathrm{km\ sec^{-1}\ Mpc^{-1}}$; Karachentsev & Makarov 1996) for the galaxy using the SBF method. The location of ESO 384-016 in the Cen A group is shown in Fig. 2.2. The galaxy does not show any association with the major members of the group and appears to be rather isolated.

Jerjen et al. (2000a) obtained longslit spectra of ESO 384-016 in the blue. The blue spectrum of the galaxy covers the wavelength range of 3500–5500Å and can be seen in Fig. 2.3. The spectrum of ESO 384-016 shows strong Balmer lines (Hβ λ4861, Hγ λ4340, Hδ λ4101) and Ca II K (λ3933) and H (λ3968) absorption features. The age and metallicity of the galaxy were estimated by comparing the observed index strengths of the lines C_2 (λ4668) (Worthey 1994) and Hδ (Jones & Worthey 1995) with the index strengths computed from single-burst population models. The C_2 (λ4668) line is a blend from C_2, Mg, Fe and other elements and is therefore considered to be a good indicator of the metallicity. The age-metallicity analysis of Jerjen et al. (2000a) shows that ESO 384-016 is composed of an old and metal-poor stellar population. This finding is supported by Karachentsev et al. (2007) who determined a metallicity of $[\mathrm{Fe/H}]_{V-I} = -1.6$ from spatially resolved HST/ACS stellar photometry of the galaxy.

The B- and R-band surface photometry of ESO 384-016 was presented by Jerjen et al. (2000b). The SB profiles of the galaxy is shown in Fig. 2.4. The SB profiles were measured out to a radius of $r \sim 70''$ in the B-band. The corresponding $B-R$ colour profile of ESO 384-016 can be seen in Fig. 2.4. A large colour gradient of $\Delta(B-R) \sim 0\overset{\mathrm{m}}{.}7$ is detected in this galaxy. The colour varies from $B-R \sim 0\overset{\mathrm{m}}{.}8$ in the center to $B-R \sim 1\overset{\mathrm{m}}{.}5$ in the outer parts of the galaxy. The colour in the outer parts of the galaxy is typical for early-type systems (E-S0), while the colour in the center is similar to late-type spiral and irregular galaxies. The bluer

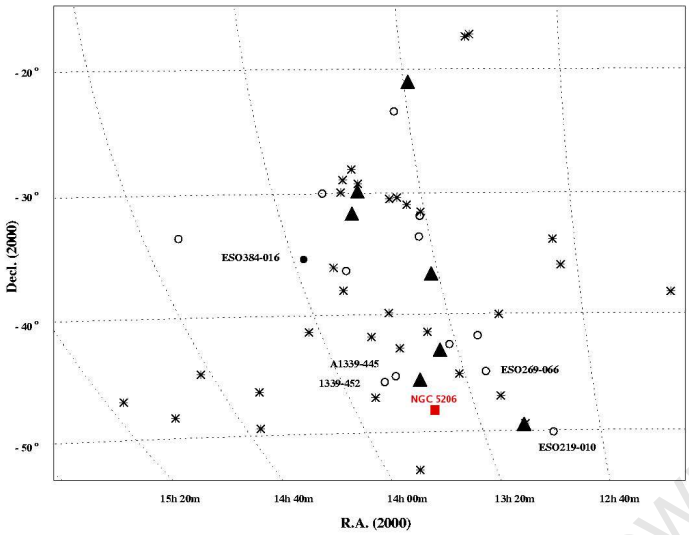

Figure 2.2 Sky distribution of galaxies in the Cen A group taken from Beaulieu et al. (2006): *triangles* – major group members; *asterisks* – late-type dwarf galaxies (Côté et al. 1997; Jerjen et al. 2000a); *circles* – early-type dwarf galaxies which includes ESO 384-016 represented by a filled circle. The location of the late-type dwarf galaxy, NGC 5206, is shown in red.

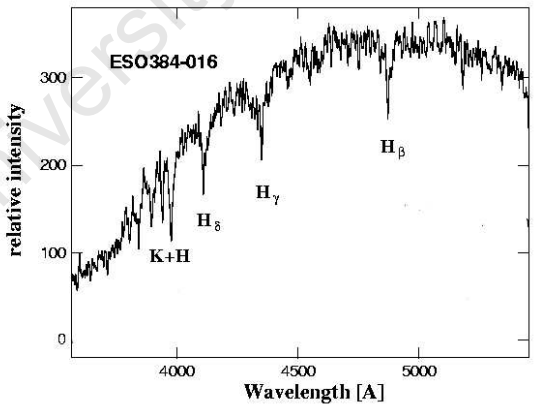

Figure 2.3 Blue spectrum (3500–5500Å) of ESO 384-016 obtained by Jerjen et al. (2000a). The prominent absorption features in the galaxy spectrum are labeled.

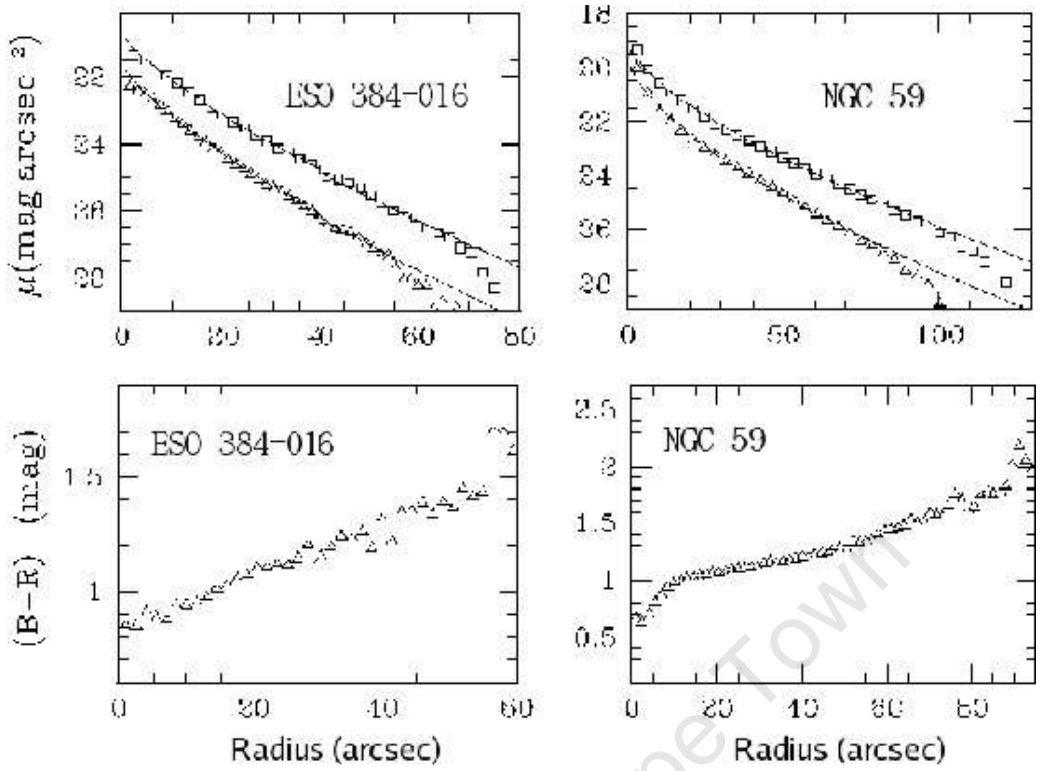

Figure 2.4 Surface photometry results for the dwarf galaxies ES0 384-016 (*left*) and NGC 59 (*right*) obtained by Jerjen et al. (2000b). *Top*: Radial surface brightness profiles in the *B*- (*bottom curve*) and *R*- (*top curve*) bands. The best-fitting Sérsic profiles are shown by the solid lines. *Bottom*: Radial $B - R$ colour profiles out to the isophotal radius of $\mu_B = 28$mag arcsec^{-2}.

colours may be an indication of star-formation activity in the central regions of ESO 384-016. More recently, Bouchard et al. (2009) have detected faint and diffuse Hα emission near the galaxy center giving a star formation rate of $(23 \pm 6) \times 10^{-5}\,\mathrm{M_\odot yr^{-1}}$ for ESO 384-016.

ESO 384-016 was mapped in H I by Beaulieu et al. (2006) using the Australian Compact Array (ATCA) Telescope. These observations were carried out with an H I detection limit of $\sim 1 \times 10^6\,\mathrm{M_\odot}$. They measure an H I mass of $M_{\mathrm{H\,I}} \sim (5.6 \pm 0.3) \times 10^6\,\mathrm{M_\odot}$ for this galaxy. The H I mass to B-band luminosity for the galaxy is $M_{\mathrm{H\,I}}/L_B = 0.21$, which lies close to the values measured for dSph/dIrr galaxies (e.g., $M_{\mathrm{H\,I}}/L_B \sim 0.21$ for Phoenix; St-Germain et al. 1999). More recently, Bouchard et al. (2007) obtained H I observations of low-mass dwarf galaxies in the Cen A group from ATCA. They point out that ESO 384-016 represents one of two mixed-morphology dwarfs in this group which is detected in H I. The H I contour map for ESO 384-016 is shown in Fig. 2.5. The contours are compressed on the west side of the galaxy. The east side shows however less compression and elongated contours. Beaulieu et al. (2006) argue that this distribution in the H I gas is expected if the galaxy was falling toward the center of the Cen A group while interacting with the intergalactic medium (IGM). In

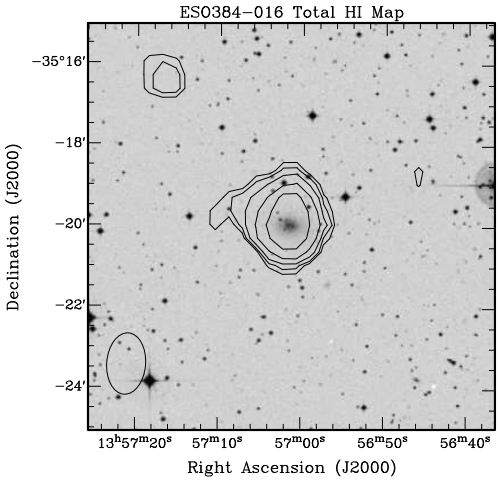

Figure 2.5 Total H I map of ESO 384-016 from Beaulieu et al. (2006) superimposed on the DSS optical image. The beam size of ATCA is shown in the lower left corner.

addition, a gap in the H I properties of low-mass dwarf galaxies in the Cen A was observed by Bouchard et al. (2007): dwarfs either have H I mass of $M_{\rm H\,I} > 10^7\,{\rm M}_\odot$ or are not detected (i.e. dwarfs having an H I mass below the detection limit of $M_{\rm H\,I} \lesssim 10^6\,{\rm M}_\odot$). Bouchard et al. (2007) have shown that this gap in the H I mass can be a result of the ram pressure exerted by an IGM of density $\rho_{\rm IGM} \sim 10^{-3}{\rm cm}^{-3}$.

Beaulieu et al. (2006) compare the H I content of ESO 384-016 to the values obtained for dE galaxies in the Virgo Cluster (Conselice et al. 2003). The sample of Conselice et al. (2003) consists of 22 dE galaxies of which two dwarfs were detected in H I. The measured $M_{\rm H\,I}/L_B$ for ESO 384-016 is slightly lower than the mean value of 0.36 ± 0.16 for the two Virgo dEs. The H I mass of the Virgo dEs are a factor of ~ 10 times larger than that measured for ESO 384-016. Beaulieu et al. (2006) note that as with the Virgo Cluster, the H I detected systems of the Cen A group are also located on the outskirts of the group.

LEDA 166099

LEDA 166099 is one of the faintest dwarf galaxies in our sample having an apparent magnitude of $B = 15\overset{\rm m}{.}5$. This galaxy shows a distinct nuclear component in the optical (see Fig. 2.1) and is classified as a dE,N galaxy (Parodi et al. 2002). The distance estimate of 9.8Mpc for this galaxy (Karachentsev et al. 2004) assumes that LEDA 166099 is a dwarf companion of the spiral (Sa) galaxy NGC 2784. The relative position of NGC 2784 and its two dwarf companions (LEDA 166099 and NGC 2784 DW01) are shown in Fig. 2.1. The satellite galaxy LEDA 166099 lies at a projected distance of ~ 5.3kpc from its parent galaxy. The optical observations of Parodi et al. (2002) led to the detection of the second companion galaxy, NGC 2784 DW01. Given its size and proximity to the larger galaxy, this extremely

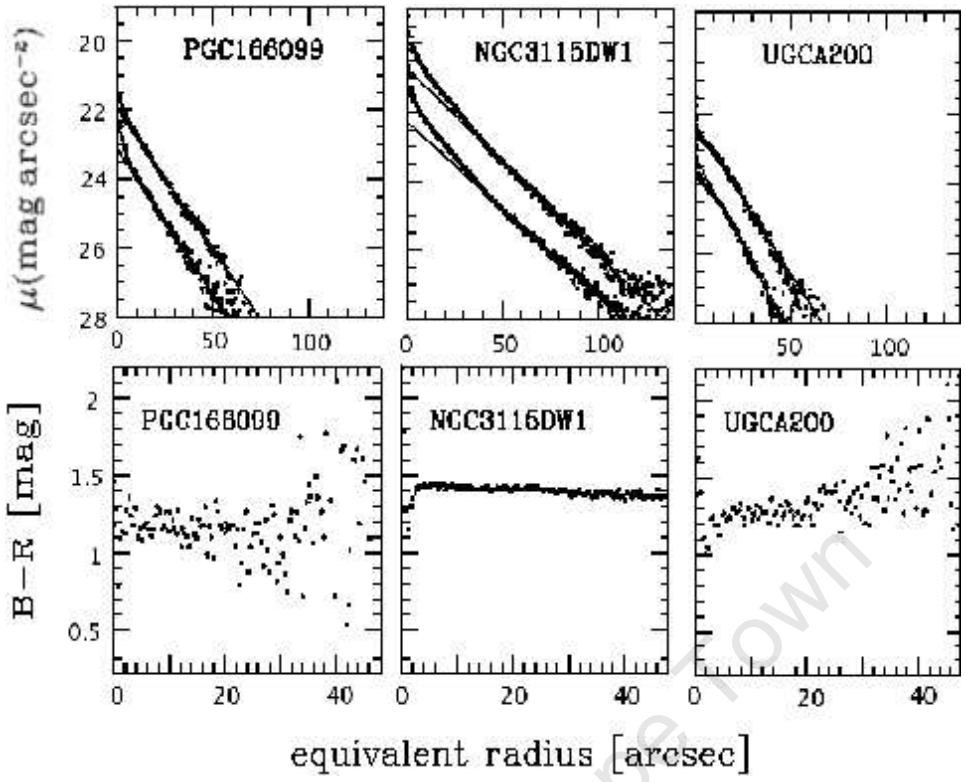

Figure 2.6 Surface photometry results for the dwarf galaxies LEDA 166099 (*left*), NGC 3115 DW01 (*middle*) and UGCA 200 (*right*) obtained by Parodi et al. (2002). *Top*: Radial surface brightness profiles in the B- (*bottom curve*) and R- (*top curve*) bands. The best-fitting exponential profiles are shown by the solid lines. *Bottom*: Radial $B-R$ colour profiles.

low SB galaxy ($B = 17\overset{\mathrm{m}}{.}3$) is also thought to be a bound companion of NGC 2784.

Parodi et al. (2002) have obtained deep B- and R-band imaging of LEDA 166099. The SB profiles of the galaxy are shown in Fig. 2.6. The galaxy is detected down to the $\mu \sim$ 28mag arsec^{-2} isophote in both bands. This SB level corresponds to a radius of $r \sim 60''$ in the B-band. The $B-R$ colour profile of LEDA 166099 is displayed in Fig. 2.6. The low SB of the galaxy results in the large scatter (up to $\Delta(B-R) \sim 0\overset{\mathrm{m}}{.}4$ within the radial range of $0'' \lesssim r \lesssim 30''$) of the data points. Parodi et al. (2002) measure a mean $B-R$ colour of $1\overset{\mathrm{m}}{.}16$ for this dwarf making it one of the bluer dE galaxies in our sample. The $B-R$ profile shows no obvious indication of a colour gradient given the large scatter of the data points.

NGC 59

A detailed description of the properties of NGC 59 and its environment is given in Chapter 3. In this section, we only provide a summary of those properties that will give immediate insight to the current evolutionary state of this galaxy.

The galaxy NGC 59 is classified as a dwarf lenticular (dS0). The optical morphology of this dwarf reveals the prominent disc and bulge component of the galaxy. NGC 59 is located

on the outskirts of the Sculptor (Scl) group at a distance of 4.4Mpc (Jerjen et al. 1998). The galaxy is situated in a relatively isolated environment in which it experiences minimum interaction with neighbouring galaxies in the group. NGC 59 is known to be one of the brightest dwarfs in the Scl group having an absolute magnitude of $M_B = -15\overset{\mathrm{m}}{.}3$.

Deep B- and R-band imaging of NGC 59 was obtained by Jerjen et al. (1998). The surface photometry measurements allow for the extraction of the SB profiles in the respective bands. The B- and R-band SB profiles of the galaxy are shown in Fig. 2.4. These profiles were measured out to a radius of $r{\sim}100''$ in the B-band. The $B-R$ colour profile was determined directly from the SB profiles and is shown in Fig. 2.4. The galaxy shows a strong colour gradient over the radial range of $0'' \lesssim r \lesssim 100''$. Similar to ESO 384-016, a decrease in the colour of $B-R \sim 1\overset{\mathrm{m}}{.}5$ is observed towards the galaxy center. The bluer colours in the center are more likely a result of a younger stellar population in the central regions of NGC 59.

The detection of the Hα line in the spectrum of NGC 59 provided the first indication of star-forming activity in the galaxy (Côté et al. 1997). The narrow-band Hα imaging of Skillman et al. (2003) maps the distribution of the ionized gas in the galaxy. These observations reveal ionized gas in the central $15''$ of the galaxy. The location of the H II region provides further evidence for recent star-formation in the center of NGC 59. However, the mechanism triggering star-formation in this relatively isolated galaxy remains poorly understood.

A measurement of the H I content of NGC 59 was recently obtained by Beaulieu et al. (2006). They measure an H I mass of $M_{\mathrm{H\,I}} \sim (1.5 \pm 0.3) \times 10^7\,\mathrm{M}_\odot$ for this galaxy. The H I mass of NGC 59 is one of the largest detections of neutral hydrogen gas for an early-type dwarf in the Scl group (Bouchard et al. 2005). Beaulieu et al. (2006) obtained a mass-to-light ratio of $M_{\mathrm{H\,I}}/L_B \sim 0.07$ for NGC 59. Effective tracing of the neutral hydrogen gas distribution in the galaxy cannot be achieved given the low-resolution of the H I mapping.

NGC 5206

The dwarf galaxy NGC 5206 is the brightest galaxy in our sample having an apparent B-band magnitude of $B \sim 11\overset{\mathrm{m}}{.}6$. NGC 5206 is a member of the Cen A group. Its location in the Cen A group is shown in Fig. 2.2. NGC 5206 is one of the most poorly studied dwarfs in the sample regardless of its vicinity and high SB. The photographic plate observations of Caldwell & Bothun (1987) and Prugniel et al. (1993) were used to measure the $B-V$ colour of the galaxy. They measure $B-V \sim 0\overset{\mathrm{m}}{.}9$ for NGC 5206 which indicates the presence of an old stellar population. Additional $B-R$ colour information for NGC 5206 is given by Lauberts & Valentijn (1989). They measure $B-R \sim 1\overset{\mathrm{m}}{.}2$ for this galaxy which provides further confirmation that NGC 5206 is a late-type dwarf. Deep photometric studies are currently not available for this galaxy.

H I observations of dwarf galaxies in the Cen A group were carried out by Côté et al. (1997). The gas content of NGC 5206 was not detected using an H I limit of $7.8 \times 10^6\,\mathrm{M}_\odot$ for Cen A members. Côté et al. (1997) place an upper mass estimate of $M_{\mathrm{H\,I}} \sim 5.5 \times 10^5\,\mathrm{M}_\odot$ for this galaxy making it one of the gas-poor dwarfs in the Cen A group. Follow-up optical spectra were acquired for the group members. The Hα emission line was detected in NGC 5206. This emission line was used to measure the heliocentric velocity of $v_\odot = 571 \pm 10\mathrm{km\ s}^{-1}$ for the

galaxy, confirming its membership in the Cen A group. The nature of the Hα emission in NGC 5206 remains to be investigated.

NGC 3115 DW01

NGC 3115 DW01 is classified as a nucleated dE galaxy. This luminous ($M_B = -16.6$) and red ($B - R = 1.38$) dwarf galaxy is a companion of the S0 galaxy NGC 3115. The relative position of NGC 3115 DW01 to its larger companion can be seen in Fig. 2.7. The projected distance between the two galaxies is $17\farcm3$ which corresponds to $\sim$50kpc at the distance of $D \sim 9.8$Mpc. The optical morphology of NGC 3115 DW01 shows no signs of interaction with its larger companion (Durrell et al. 1996).

Hanes & Harris (1986) found that NGC 3115 DW01 possesses a very rich globular cluster (GC) system. They found that this dwarf galaxy has three times the number of clusters per luminosity compared to its parent galaxy NGC 3115. All the globular cluster candidates of Hanes & Harris (1986) may however not be "true" GCs as they could only be identified by their respective star counts on the photographic plates. The relative closeness of NGC 3115 DW01, together with its isolation and high SB, makes it an ideal target in which to study the formation of GCs in dwarf galaxies.

Durrell et al. (1996) carried out the first study of GCs in NGC 3115 DW01 using optical B- and V-band observations. True cluster candidates were defined as objects within $48''$ of the galaxy center having a V-band magnitude of $V < 23\fm2$. A total of 24 GCs were identified following these selection criteria. The $B - V$ colour of the GCs was used to determine the mean metallicity of the clusters. This was found to be $[\mathrm{Fe/H}]_{B-V} \sim -1.2$ which is comparable to the metallicities of GCs in the Galactic halo (van den Bergh & Mackey 2004).

The $B - V$ colour profile of NGC 3115 DW01 is shown in Fig. 2.8. The $B - V$ colour profile remains almost constant within a radius of $5'' \lesssim r \lesssim 50''$. The mean colour of the galaxy was found to be $B-V = 0.94 \pm 0.01$ in this radial range. Durrell et al. (1996) have also measured the $B - V$ colour of the galaxy nucleus. The colour of the nucleus was computed using the excess light above the best exponential fit to the SB profiles. This measurement was performed in a $7''$ aperture radius which gives $B - V = 0.90 \pm 0.03$ for the nucleus. The $B - V$ colour of the nucleus is very similar to that of the surrounding galaxy.

The GC luminosity function was used by Durrell et al. (1996) to derive a distance modulus of $(m - M)_V = 30.3^{+0.8}_{-0.5}$ for the galaxy. This places NGC 3115 DW01 at a distance of $D \sim 11^{+5}_{-2.3}$ which is consistent with the distance estimates for NGC 3115. This provided additional evidence for the dwarf galaxy being a companion of the NGC 3115. It should be noted that we have adopted the revised distance estimate based on the SBF method for NGC 3115 of 9.7Mpc (Parodi et al. 2002). The distance estimate for NGC 3115 DW01 given in Table 2.1 assumes its membership to the NGC 3115 galaxy system.

The kinematic properties of the GC system of NGC 3115 DW01 were investigated by Puzia et al. (2000). Seven GCs were confirmed as true cluster candidates based on their radial velocities. The mean radial velocity of the seven GCs is $v_{\mathrm{rad}} = 572 \pm 30$km s^{-1}. This value deviates by $\sim 1.6\sigma$ from the radial velocity of NGC 3115 DW01 ($v_{\mathrm{rad}} \sim 700$km s^{-1} Puzia et al. 2000). Puzia et al. (2000) point out that the deviation in the radial velocity can be biased by the incomplete spatial coverage of the small sample of GCs. A marginal

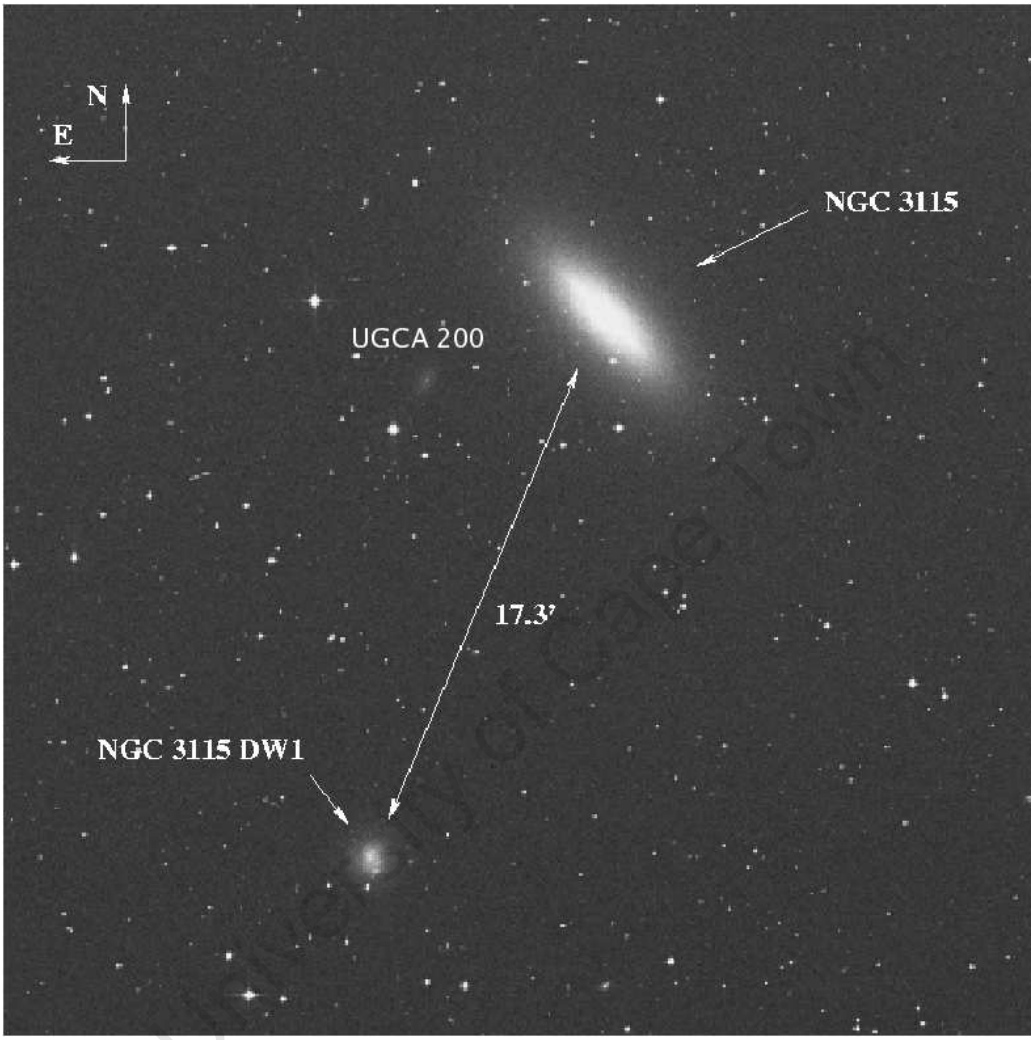

Figure 2.7 Relative position of the dwarf galaxy NGC 3115 DW01 to its parent galaxy NGC 3115 taken from Puzia et al. (2000). They measure a projected distance of 17.′3 (55kpc) between these two galaxies. The low surface brightness galaxy UGCA 200 is located East of the large SO galaxy. The size of the image is $30' \times 30'$.

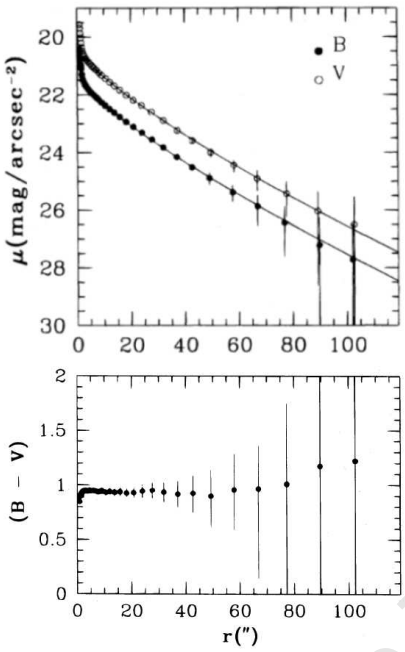

Figure 2.8 B- and V-band surface photometry results for NGC 3115 DW01 (Durrell et al. 1996). The radial surface brightness (*top*) and colour profiles (*bottom*) are shown.

net rotation of $v_{\rm rot} = 75 \pm 70$km s^{-1} is measured for the GC system. Correcting for the net rotation gives a line-of-sight velocity dispersion of $\sigma = 130 \pm 15$km s^{-1} for the GC system. The inner five clusters have a dispersion of $\sigma = 74 \pm 36$km s^{-1}. Puzia et al. (2000) provide two possible scenarios for the higher velocity dispersion of the outer GCs: the outer (halo) region of the galaxy could be dark-matter dominated or these clusters are being stripped by the nearby giant galaxy NGC 3115. A larger sample of GCs is however required to further explore the kinematical properties and effects of environment on this dwarf galaxy.

The seven GCs were used to obtain a rough mass estimate for NGC 3115 DW01. Assuming an isotropic orbit distribution for the GCs gives a lower mass limit of $(4.8 \pm 2.3) \times 10^{10}\,{\rm M}_{\odot}$ for the galaxy. The high mass of NGC 3115 DW01 together with the high velocity dispersion of the GCs are found to be more consistent with an elliptical galaxy. Given its absolute magnitude of $M_B = -16\overset{\rm m}{.}6$, the mass-luminosity relation of Dekel & Silk (1986) places this galaxy in the transition region between the luminous dEs and the low-luminosity elliptical galaxies. However, the large discrepancy between the mean radial velocity of the GCs and that of the galaxy argues against the determination of the mass of NGC 3115 DW01 from the seven GCs.

The combined spectrum of the seven GCs was used to measure the mean abundances (Puzia et al. 2000). The mean metallicity of the GC system was found to be [Fe/H] =

-0.97 ± 0.11 which is similar to those values obtained for GCs in the Milky Way. The B- and V-band observations from Durrell et al. (1996) were used to confirm the mean metallicity of the seven GCs. The colour-metallicity calibration of Couture et al. (1990) gives a photometric mean metallicity of [Fe/H] $= -0.93 \pm 0.11$ which is in good agreement with the value derived from spectroscopic measurements.

Deep B- and R-band imaging of NGC 3115 DW01 was obtained by Parodi et al. (2002). The surface brightness profiles of the galaxy are shown in Fig. 2.6. These observations allow for the light distribution of the galaxy to be traced out to a radius of $r \sim 100''$. A constant $B - R$ colour profile is observed similar to the earlier observations by Durrell et al. (1996). The mean $B - R$ colour in this wavelength range is $B - R \sim 1\overset{\mathrm{m}}{.}38$ indicating a dominant older population of stars.

An estimate of the H I mass for NGC 3115 DW01 is currently not available.

UGCA 200

UGCA 200 is a nucleated dE and is the faintest ($B \sim 16\overset{\mathrm{m}}{.}2$) dwarf galaxy in the sample. It is another dwarf companion of the lenticular (S0) galaxy NGC 3115. The relative position of UGCA 200 to the parent galaxy and second dwarf companion, NGC 3115 DW01, is shown in Fig. 2.7. The faint companion lies at a projected distance of $D \sim 15$kpc from NGC 3115.

B- and R-band imaging of UGCA 200 was obtained by Parodi et al. (2002). The SB profiles of the galaxy are shown in Fig. 2.6. Their deep observations allow for the SB profiles to be traced out to a radius of $r \sim 50''$. The $B - R$ colour profile was measured directly from the galaxy SB profiles. The $B - R$ colour profile of UGCA 200 is shown in Fig. 2.6. Parodi et al. (2002) measure a mean colour of $B - R \sim 1\overset{\mathrm{m}}{.}38$ which indicates that the galaxy contains an old stellar population. A gradual increase in the $B - R$ colour is observed towards the outskirts of the galaxy. However, it is not clear if this trend can be treated physically given the low S/N levels of the galaxy.

Summary

The main known optical properties of the dwarf galaxies observed with the IRSF are listed in Tables 2.1 and 2.2. The dwarfs have absolute B-band magnitudes in the range of $-17\overset{\mathrm{m}}{.}0 < M_B < -13\overset{\mathrm{m}}{.}0$. The distances of the galaxies vary from the nearby Cen A group ($D \sim 3.6$Mpc) to the boundaries of the LV ($D \sim 9.8$Mpc). Despite being members of the respective Cen A and Scl groups, the galaxies ESO 384-016, NGC 5206 and NGC 59 appear to be rather isolated. The more distant dwarfs show some degree of interaction with their nearest neighbours as suggested the tidal index Θ in Table 2.2. The dwarf galaxies range in morphological type from the gas deficient nucleated dE's to gas-rich dS0 galaxies. The different galaxy morphologies exhibit $B - R$ colours from that seen for typical older stellar populations ($B - R \gtrsim 1\overset{\mathrm{m}}{.}2$) to the colours observed for star-forming galaxies ($B - R \sim 1\overset{\mathrm{m}}{.}07$). The brightest galaxies ($M_B \lesssim -15\overset{\mathrm{m}}{.}7$) have a B-band angular extent of $D_{\mathrm{ext}} \gtrsim 1'.7$ which allows for the extraction of their SB profiles well beyond their effective radii of $R_{B,\mathrm{eff}} \lesssim 30''$. The faintest galaxy ($M_B \sim -13\overset{\mathrm{m}}{.}8$) in the sample, UGCA 200, has an effective SB of $\mu_{B,\mathrm{eff}} \sim 24$mag arcsec^{-2}. The dwarf galaxies span a range in central surface brightnesses from $\mu_{B,0} \sim 19.6$mag arcsec^{-2} for the dS0 galaxy NGC 59 to $\mu_{B,0} \sim 23.2$mag arcsec^{-2} for UGCA 200. The galaxies ESO 384-016 and NGC 59 are the only dwarfs in the sample for

Table 2.3. A comparison of the IRSF and 2MASS observing specifications.

	IRSF	2MASS
Aperture (m)	1.4	1.3
F-ratio	f/10	f/13.5
Bands	J H K_s	J H K_s
Wavelength (μm)	1.25 1.65 2.15	1.25 1.65 2.16
Detector	HgCdTe	HgCdTe
Size (pixels)	1024×1024	256×256
Pixel Scale (arcsec/pixel)	0.45	2
Field of view (arcmin)	7.8	7.7
Limiting magnitudes	20.6 19.4 19.1	16.5 15.8 15.0
Exposure (sec)	900	6×1.3

which reliable H I masses have been measured.

2.3 Data Acquisition

2.3.1 Telescope

Deep NIR imaging of the six dwarf galaxies was obtained with the 1.4m Infrared Survey Facility[2] (IRSF) telescope in Sutherland, South Africa (Glass & Nagata 2000). The *Sirius* detector of the IRSF telescope consists of three 1024×1024 HgCdTe arrays. The array system allows for simultaneous 3-channel J- (1.25μm), H- (1.65μm) and K_s-band (2.15μm) imaging. The individual CCDs give a total FoV of $7\farcm8 \times 7\farcm8$ together with a $0\farcs45$ pixel scale. The FoV of the *Sirius* detector complements the $8' \times 8'$ FoV of the SALT telescope. The radial extent of the follow-up longslit observations for the target galaxies with SALT will thus overlap with that seen in the NIR imaging.

The aperture size of the IRSF is closely matched to that of the 1.3m Two Micron All Sky Survey (2MASS) telescope. A comparison of the IRSF (Nagashima et al. 2002) and 2MASS (Skrutskie et al. 2006) detector systems is provided in Table 2.3. The f/10 focal ratio of the IRSF telescope compared to the f/13.5 of 2MASS results in deeper observations for the same exposure time. The ∼4 times better pixel scale of the *Sirius* detector exceeds the spatial resolution of the 2MASS images. These features make the IRSF telescope ideal for conducting deep NIR observations of faint extended sources such as dwarf galaxies.

The three brightest galaxies ($B < 13\fm4$) in our sample have been observed by 2MASS and are listed in the 2MASS Extended Source Catalog (Skrutskie et al. 2006). An example comparing the 2MASS and IRSF images of target galaxy NGC 5206 is shown in Fig. 2.9.

[2]A description of the telescope is found at http://www.z.phys.nagoya-u.ac.jp/∼telescop/index_e.html .

Figure 2.9 A comparison of the JHK_S-colour image of NGC 5206 observed by 2MASS (*left*) and the IRSF (*right*).

The smaller pixel scale of the *Sirius* detector results in a dramatic improvement in the spatial resolution of the galaxy images. This property together with the long exposure times allows for a more detailed mapping of the galaxy structure. The IRSF observations will also help probe the structure of the fainter galaxies in the sample which lie below the detection limit of 2MASS.

2.3.2 Observations

The NIR data were obtained during three different observing runs over the period of 2006–2007. The observations performed in February and June 2006 were carried out using shared telescope time. Single galaxy observations of NGC 3115 DW01 and NGC 59 were obtained during these respective observing runs. A further week in March 2007 was dedicated to the imaging of dwarf and low SB galaxies. Simultaneous J-, H- and K_s-band imaging of the other four galaxies was obtained during this observing run. Details of the galaxy observations are listed in Table 2.4. The total integration times for the galaxy observations vary from 60–132 minutes. All observations were performed during grey time under photometric conditions.

The aim of the NIR observations is to conduct a detailed photometric analysis of the dwarf galaxies out to at least the $\mu_{K_s} \sim 23$ mag arcsec^{-2} isophote. R. Metcalfe & M. McCall derived an exposure time for detecting nearby dwarf irregular (dIrr) galaxies down to the $\mu_{K_s} \sim 23$ mag arcsec^{-2} isophote using the IRSF telescope. The exposure time was calculated based on NIR observations of these galaxies with the 3.6m Canada-France-Hawaii (CFHT) and 2.1m OAN-SPM telescopes (Vaduvescu et al. 2005). They found a limiting magnitude of $\mu_{K_s} \sim 23$ mag arcsec^{-2} is reached in ∼70 minutes (R. Metcalfe, private communication).

The goal was therefore to observe each galaxy in principle for at least 70 minutes. An exception was made for the luminous galaxy NGC 59 which was only observed for 60 min-

Table 2.4. Near-infrared observations of 6 Local Volume dwarf galaxies

Galaxy	J2000 RA	J2000 DEC	Date	Filters	Exp (min)	Total Exp (min)
NGC 3115 DW01	10 05 41.6	−07 58 53	2006 Feb 14	JHK_s	48	132
			Feb 16	JHK_s	24	
			Feb 17	JHK_s	60	
NGC 59	00 15 25.1	−21 26 40	2006 Jun 11	JHK_s	60	60
LEDA 166099	09 12 29.3	−24 14 28	2007 Mar 08	JHK_s	96	96
ESO 384-016	13 57 01.4	−35 19 59	2007 Mar 08	JHK_s	24	84
			Mar 09	JHK_s	60	
UGCA 200	10 05 35.1	−07 45 00	2007 Mar 10	JHK_s	24	96
			Mar 11	JHK_s	24	
			Mar 13	JHK_s	48	
NGC 5206	13 33 44.0	−48 09 04	2007 Mar 10	JHK_s	48	60
			Mar 13	JHK_s	12	

utes on the shared night of June 11 2006. The low SB dwarf galaxies, LEDA 166099 and UGCA 200, were both observed for 96 minutes to ensure their detection (see Table 2.4).

The quality of deep NIR images is greatly affected by temporal and spatial variations in the sky background. An understanding of these variations is crucial to gain a proper estimate of the sky-level. A good estimate of the sky-level is particularly important when observing low SB dwarf galaxies such as LEDA 166099 and UGCA 200.

The NIR observing technique of Vaduvescu & McCall (2004) was employed to ensure an optimal extraction of the sky-level in the images. They propose an observing sequence of the form:

$$\text{sky} - \text{galaxy} - \text{sky} - \text{galaxy} - \text{sky} - \ .... \ - \text{sky} - \text{galaxy} - \text{sky} \ , \tag{2.1}$$

when observing faint extended sources in the NIR. Temporal variations in the sky-level were accounted for by allowing equal exposures for the galaxy and sky frames. A dithering step of $10''$ was applied to each new galaxy and sky exposure in the observing sequence. This was necessary for the removal of bad pixels and contaminants from the images.

The sequential sky and galaxy frames in (2.1) were exposed for 60 seconds each. Individual exposures were sub-divided into 3×20s non-dithered frames to avoid saturation of the pixel arrays. The background was sampled by choosing a sky region in close proximity to the galaxy that shows the least amount of stellar contamination. The sky-level was sampled $10'$ North or South of the galaxy center.

Twilight sky images were obtained in the evening and morning. A sequence of equal-duration exposures was taken as the twilight brightened or faded in each filter. These sky flats were used to remove the spatial variations in the images. A series of dark exposures were

taken every morning in the J-, H-, and K_s-bands for removal of the detector signature.

2.4 Data Reduction

The observational technique described in section 2.3.2 together with the long galaxy exposures results in an extensive number of frames in the NIR. For example, the 60 minute exposure of NGC 59 results in a total of 540 galaxy frames for the three wavelength bands. An automated routine was developed within the standard reduction package IRAF[3] to perform the reductions of the large data set more efficiently. Preliminary reductions consisting of the bias and dark current subtraction, as well as the flat-fielding was accomplished using tasks in the NOAO.CCDRED package. Various IRAF scripts were written to carry out the sky-subtraction of the galaxy images.

The first step in the reduction procedure involves the removal of the bias-level from the target images (i.e. sky flats, galaxy and sky exposures). Dark frames having the same exposure time as the target image were used to create a master dark frame. The dark current and hot pixels were eliminated from individual target exposures by subtracting the master dark frame.

The relative sensitivity of the CCD was measured by correlating the signal in any given pixel with the mean for all pixels. A master flat was created in each filter from a sequence of 30–40 equal-duration twilight sky exposures. These sky exposures were selected to have a mean count in the range of $J \sim 1300 - 7000$, $H \sim 6000 - 15000$ and $K_s \sim 3500 - 8000$ over the entire CCD. The twilight sky exposures in each wavelength band were combined using the FLATCOMBINE task. Division by the mode of the combined image then gives the normalized master flat. The master flat was used to correct for the pixel-to-pixel sensitivity in the sky and galaxy exposures.

The non-dithered 20sec galaxy (T_i) and sky (S_i) exposures were combined using the IMCOMBINE task. The resulting observational sequence takes the form:

$$S_1 - T_1 - S_2 - T_2 - S_3 - ... - S_i - T_i - S_{i+1} - ... - S_n - T_n - S_{n+1} \ , \tag{2.2}$$

where a dithered region of the sky S_i is sampled before and after each galaxy exposure T_i. This technique of straddling the sky frames allows for the interpolation of the background at the time of the galaxy observation. The sky subtraction procedure of Vaduvescu & McCall (2004) was followed in subtracting the background from the galaxy images. An outline of this procedure is given below:

1. The difference between straddling sky frames $(\Delta S)_i$ is computed for each galaxy exposure T_i:

$$(\Delta S)_i = S_i - S_{i+1} \ . \tag{2.3}$$

The dithering step of $10''$ between the consecutive sky frames ensures that a different region of the sky is sampled. Consequently, the stars in the sky frame S_i are positive sources in

[3]IRAF is distributed by the National Optical Astronomy Observatory, which is operated by the Association of Universities for Research in Astronomy, Inc., under cooperative agreement with the National Science Foundation.

the difference frame $(\Delta S)_i$ while those sources in S_{i+1} appear as negative residuals or "black holes".

2. Positive sources in the difference frame $(\Delta S)_i$ were identified using the DAOFIND algorithm. These sources were removed from the image using the IMEDIT task.

3. A smooth sky frame S_i' was created by filling in the "black holes" in the sky difference frame $(\Delta S)_i$. This was achieved by adding back the sky frame S_{i+1}:

$$S_i' = (\Delta S)_i + S_{i+1} \ . \tag{2.4}$$

4. A second sky difference frame was created by switching S_i and S_{i+1} in equation (2.3). Steps 2 and 3 were repeated to derive the contaminant-free sky frame S_{i+1}'.

5. The average of the sky frames S_i' and S_{i+1}' gives an approximation of the background at the time of the galaxy observation T_i:

$$S_i'' = (S_i' + S_{i+1}')/2 \ . \tag{2.5}$$

6. The target galaxies have small enough angular extent for the background level $T_{i,b}$ to be measured in the corners of the galaxy image. A comparison of the background measured in the galaxy frame, $T_{i,b}$, to that measured in the sky frame, $S_{i,b}''$, gives the adjusted sky image:

$$S_i''' = S_i'' + (T_{i,b} - S_{i,b}) \ . \tag{2.6}$$

7. The sky frame S_i''' was subtracted from the galaxy image T_i to give the background-free galaxy image.

The steps 1–7 were repeated for each galaxy image T_i given in the observational sequence (2.2). The dithered galaxy exposures were aligned using the IMALIGN task. The final galaxy image was created by taking the median of the aligned galaxy exposures.

To estimate the effectiveness of the sky subtraction technique, the uncertainty in the background level was measured in both the reduced and raw galaxy images. The IMEXAM task was used to measure the background level and corresponding uncertainty at various locations in the galaxy image. These measurements were carried out at a radius of $r \gtrsim 4'$ from the galaxy center to ensure that the results are not influenced by light from the galaxy itself. We find that the reduction method described above removes the sky to an accuracy of $\sim$0.02% in the K_s-band relative to the original signal.

The exposure time of the reduced galaxy images are listed in Table 2.5. Those galaxy exposures largely affected by atmospheric and telescopic defects were not used in creating the final images. This results in the different exposure times in the J-, H- and K_s-bands for a single galaxy observation. Defects in the images include extreme blurring due to changes in the observing conditions as well as problems with the CCD readout. The seeing in the final galaxy images varies from $1\farcs2$ in the K_s-band to $1\farcs6$ in the J-band.

The reduced J-, H- and K_s-band galaxy images are shown in Figs. 2.10–2.12. A distinct nucleus is seen in the galaxies NGC 3115 DW01, NGC 59, LEDA 166099 and NGC 5206. The brighter galaxies NGC 3115 DW01, NGC 59 and NCG 5206 show extended light profiles at least $1'$ beyond the nuclear component in the H-band. The NIR morphology of the dwarf galaxies coincides with those seen in the optical (see Fig. 2.1). The white features seen for

Table 2.5. Properties of the reduced NIR images

Name	Filter	Exp (min)	Ave seeing (arcsec)
NGC 3115 DW01	J	57	1.3
	H	57	1.2
	K_s	57	1.2
NGC 59	J	56	1.6
	H	57	1.5
	K_s	58	1.4
LEDA 166099	J	89	1.4
	H	93	1.3
	K_s	94	1.3
ESO 384-016	J	76	1.5
	H	83	1.5
	K_s	83	1.4
UGCA 200	J	74	1.5
	H	73	1.4
	K_s	81	1.4
NGC 5206	J	44	1.3
	H	44	1.3
	K_s	47	1.2

example in the NIR images of LEDA 166099 (Fig. 2.11) are negative residuals left behind by the sky subtraction. These features are observed in the crowded stellar fields where it is more challenging to obtain a smooth sky background.

The central region of the galaxy NGC 59 is shown in Fig. 2.13. Two intensity peaks aligned in the northeast-southwest direction can be distinguished in the center of this galaxy. The two peaks are separated by $\sim 2\farcs3$ with the northern component being more luminous in all three wavelength bands. The longslit galaxy kinematics along the major-axis of NGC 59 is explored in Chapter 3. These results indicate that the northern component is the dynamical center of the galaxy. This component is therefore assumed to be the nucleus of the galaxy in this chapter.

2.5 Photometric Calibrations

2.5.1 Image Alignment

The three CCDs of the *Sirius* detector are not physically aligned. To reduce the calibration procedure for each galaxy, a single astrometric solution was determined for the three wavelength bands. The reduced galaxy images in the J-, H- and K_s-bands were therefore transformed to the same physical coordinates before carrying out the astrometry.

This was achieved by identifying the pixel coordinates of 6–10 point sources in the K_s-band image of the galaxy. The positions of the point sources were then identified in the corresponding J- and H-band galaxy images. The pixel coordinates of the stars in the K_s-band were used as a reference in aligning the J- and H-band images. The GEOMAP task in IRAF was used to compute the coordinate transformation from the K_s-band image. The coordinate transformation for the J- and H-band galaxy images was applied with the GEOTRAN task.

The aligned J-, H- and K_s-band images were used to create a colour image of the galaxy. The JHK_s-colour images of the six dwarfs are shown in Fig. 2.14. These images reveal the distinct nuclei of the brighter galaxies NGC 3115 DW01, NGC 59 and NGC 5206. The remaining galaxies in the sample appear to be more diffuse stellar systems.

2.5.2 Astrometry

The galaxy images were transformed to the International Celestial Reference System J2000.0 using the CCMAP task. An astrometric solution was determined from ~ 10 point sources in the galaxy image. The pixel positions of the point sources were measured using the IMEXAM task. Their corresponding celestial coordinates were taken from the 2MASS Point Source Catalogue (Skrutskie et al. 2006). The astrometric positions of 2MASS catalogue stars are measured with an accuracy of $0\farcs07$–$0\farcs08$ for stars in the magnitude range of $9 \leq K_s \leq 14$. This uncertainty in the astrometric position can increase to $0\farcs2$–$0\farcs3$ for the faintest stars in the catalogue[4]. To reduce the uncertainty in the positions of stars, point sources in the magnitude range of $9 \leq K_s \leq 14$ were used to determine the astrometric solution for the galaxy images.

[4]See the 2MASS data release documentation at http://www.ipac.caltech.edu/2mass/releases/docs.html.

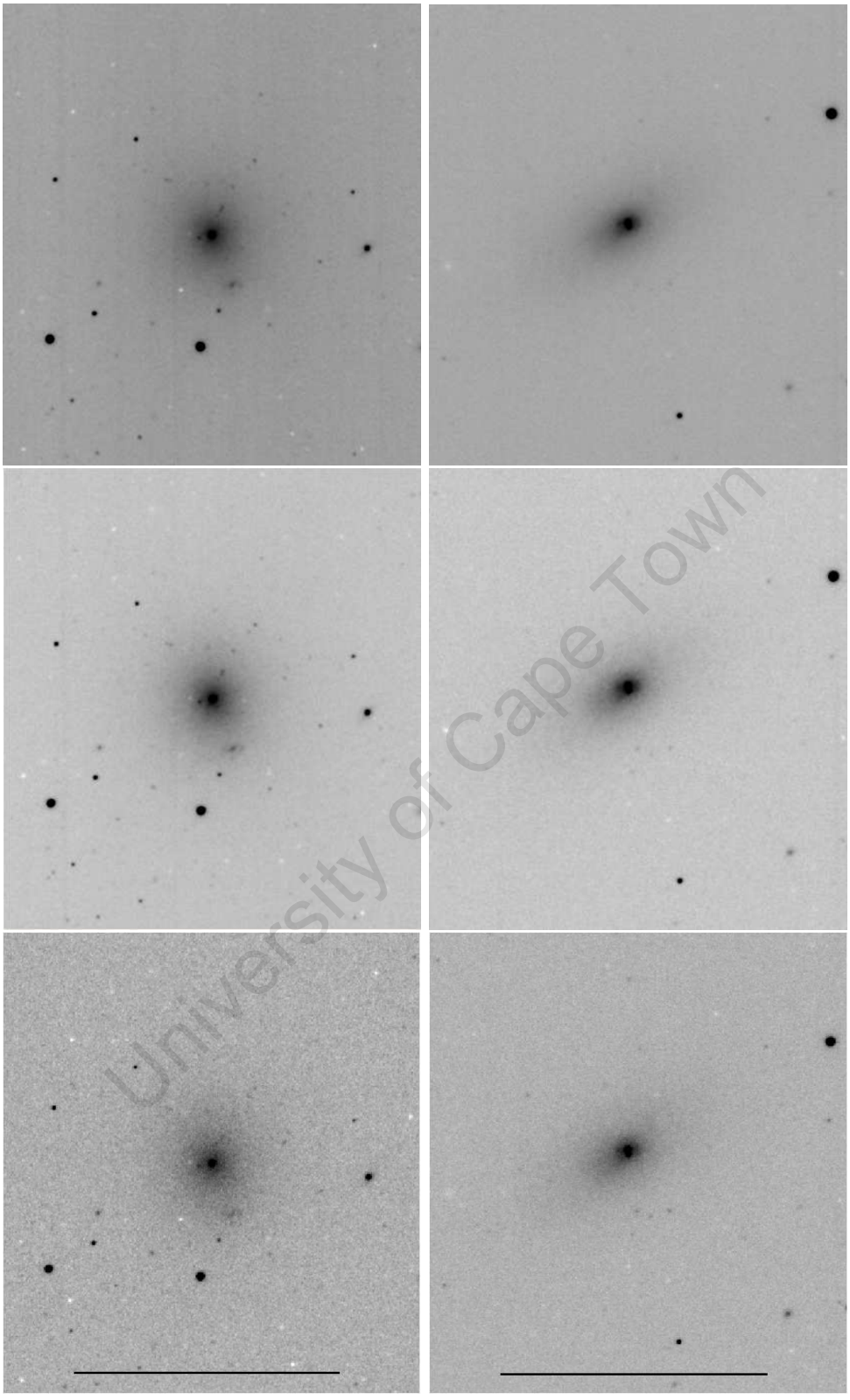

Figure 2.10 Reduced NIR images of the galaxies NGC 3115 DW01 (*left*) and NGC 59 (*right*). The galaxy images are shown in the J (*top*), H (*middle*) and K_s-bands (*bottom*). The horizontal bar in the K_s-band images indicates a scale of $2'$. North is up and East is left.

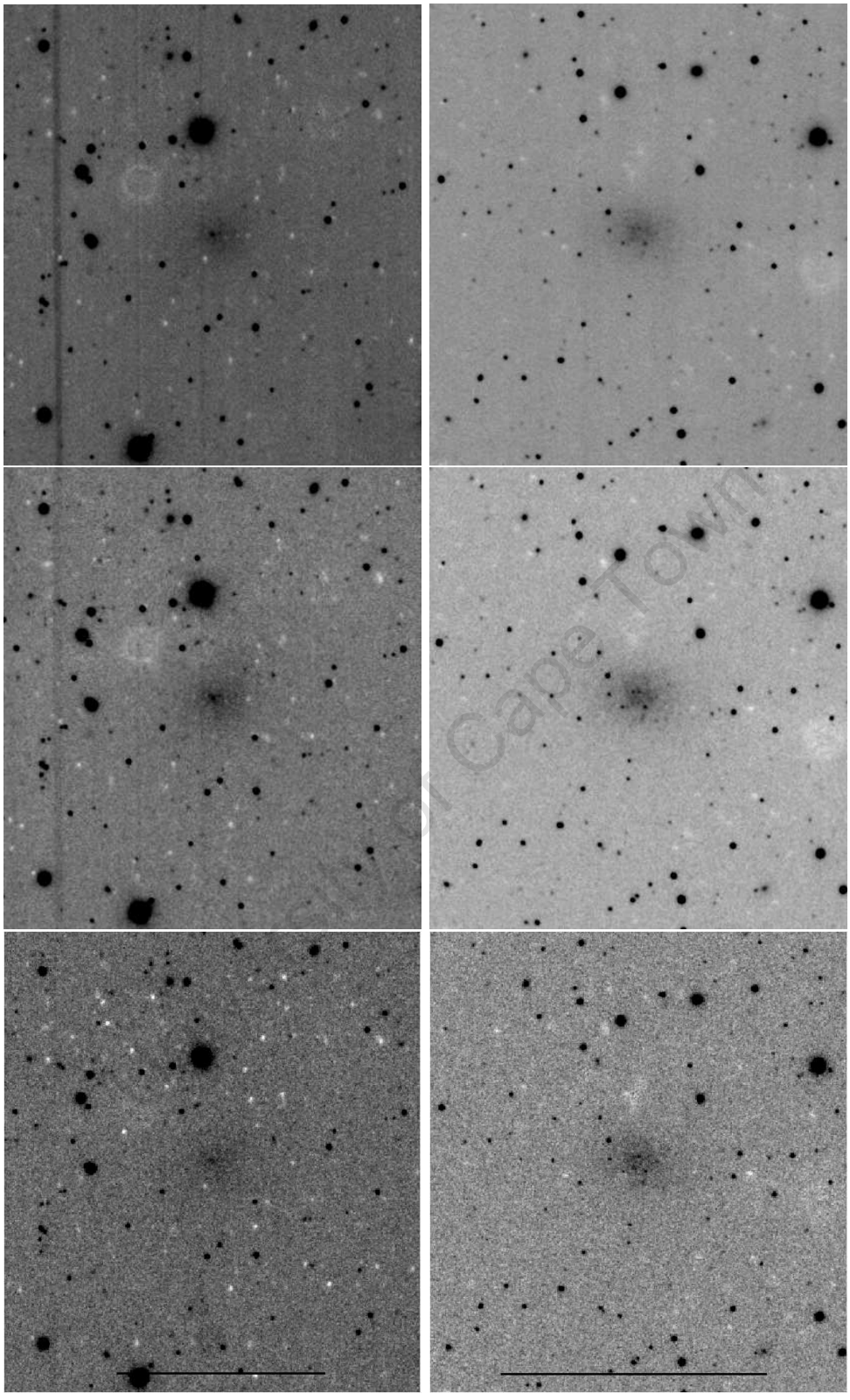

Figure 2.11 Reduced NIR images of the galaxies LEDA 166099 (*left*) and ESO 384-016 (*right*). The galaxy images are shown in the J (*top*), H (*middle*) and K_s-bands (*bottom*). The horizontal bar in the K_s-band images indicates a scale of $2'$. North is up and East is left.

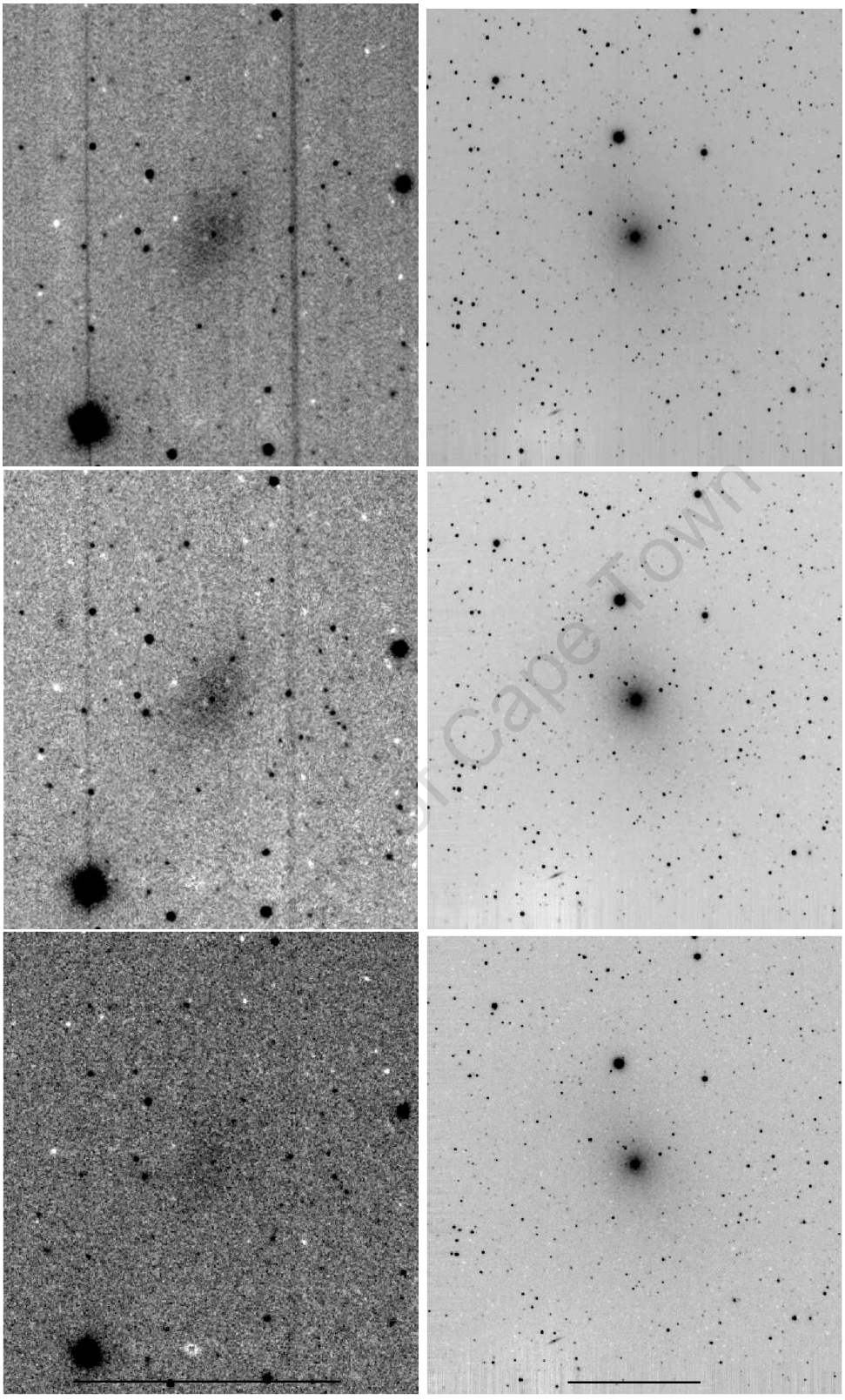

Figure 2.12 Reduced NIR images of the galaxies UGCA 200 (*left*) and NGC 5206 (*right*). The galaxy images are shown in the J (*top*), H (*middle*) and K_s-bands (*bottom*). The horizontal bar in the K_s-band images indicates a scale of $2'$. North is up and East is left.

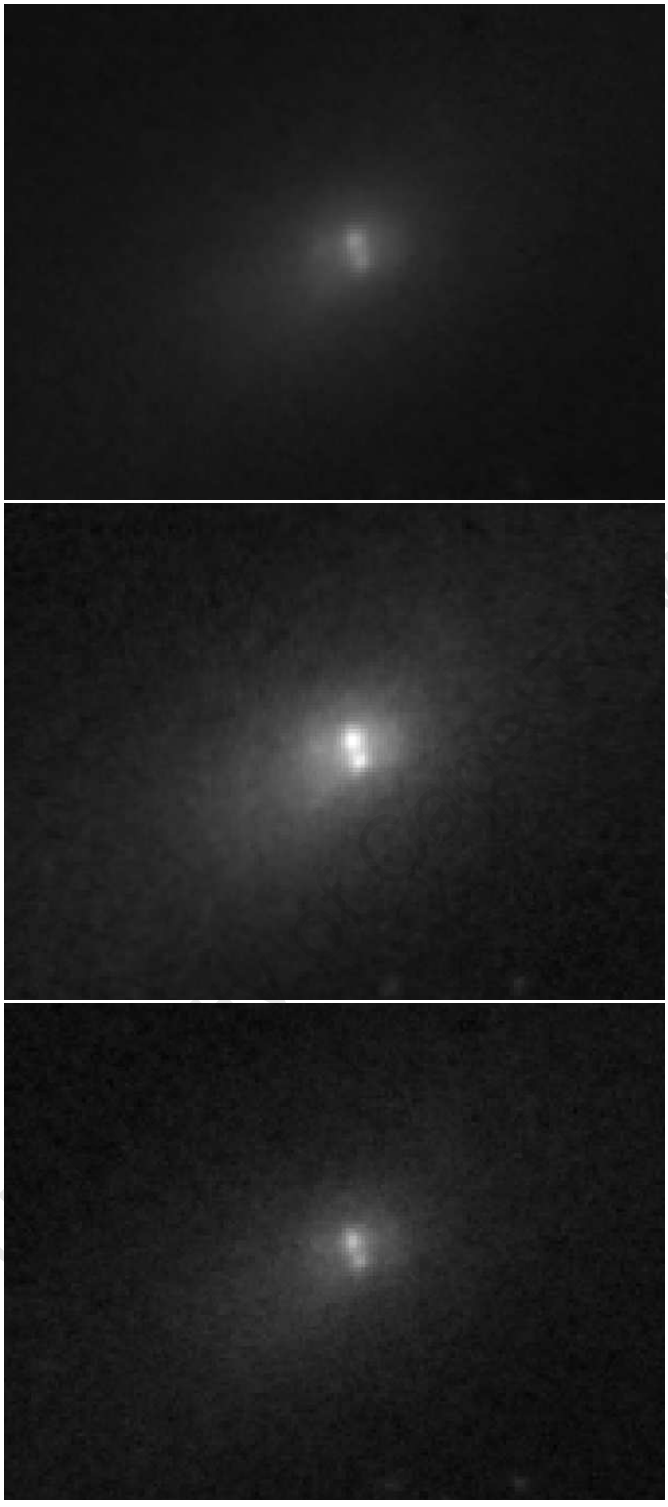

Figure 2.13 Double nuclear component of Scl group dwarf galaxy NGC 59 as seen in the J- (*top*), H- (*middle*) and K_s-bands (*bottom*). The two peaks are separated by $\sim 2\farcs3$. The image size shown is $68'' \times 58''$. North is up and East is left.

Figure 2.14 Reduced JHK_s-colour images of 6 dwarf galaxies acquired with the 1.4m IRSF telescope. *Top:* NGC 3115 DW01 (*left*) and NGC 59 (*right*); *middle:* LEDA 166099 (*left*) and ESO 384-016 (*right*); *bottom:* NGC 5206 (*left*) and UGCA 200 (*right*).

The CCMAP task computes the transformation between the pixel and celestial coordinates of the point sources. Assuming a tangent plane geometry for the sky projection gives an astrometric solution with RMS in the range of $0\farcs05$–$0\farcs08$ for the galaxy images. There are two sources of uncertainty in the absolute positions of the point sources: the accuracy of the 2MASS positions[5] and error in the coordinate mapping. These uncertainties give a maximum error of $0\farcs2$ in the astrometric positions of stellar sources in the galaxy images.

2.5.3 Calibration Method

We will follow the calibration procedure carried out by Kotze (2007) who observed the galaxy cluster, Abell S0423 (at redshift $z = 0.138$), using the IRSF. He showed that the apparent magnitudes of 2MASS point sources (Skrutskie et al. 2006) can be used directly in the photometric calibrations of the IRSF data. The transformations between the two photometric systems are given by equations (2.7)–(2.9) described later in this section. The photometric calibrations involve a direct comparison of the measured IRSF magnitudes to the apparent magnitudes given by 2MASS. A colour correction was applied to the IRSF magnitudes to account for differences in the filter systems.

The photometric filters of 2MASS[6] and the IRSF are shown in Fig. 2.15. It should be noted that the 2MASS K_s filter is centered on 2.16μm while the IRSF K_s filter is centered on 2.15μm. Slight differences are seen in the throughput of the two filter systems in the H- and K_s-bands. A broader J-band filter is seen for 2MASS compared to the IRSF. Kotze (2007) found that their independently calibrated IRSF magnitudes agree within $0\fm05$ to those magnitudes given by 2MASS. The dwarf galaxy images were therefore calibrated by comparing the instrumental magnitudes of the IRSF point sources to the corresponding 2MASS apparent magnitudes.

The point sources used to calibrate the galaxy images were selected from the 2MASS Point Source Catalogue (Skrutskie et al. 2006). The stellar sources were chosen to satisfy the following criteria:

1. Point sources should be brighter than the 2MASS completeness limit: $J \lesssim 15\fm8$, $H \lesssim 15\fm1$ and $K_s \lesssim 14\fm3$.

2. 'AAA' quality photometry is available for all stellar sources in the 2MASS catalogue. Point sources are rated as having 'AAA' quality photometry if they have a magnitude uncertainty of $\leq$10% in all three wavelength bands[7].

3. Saturated stellar sources were not used in calibrating the IRSF images. Given the long exposure time of the galaxy images, sources brighter than $10\fm0$ were found to be saturated in the IRSF observations.

The magnitudes of the 2MASS point sources were measured in a fixed $8''$ aperture or by performing aperture-corrected photometry. The photometric technique employed depends on

[5]The astrometric properties of the 2MASS point sources are described at http://www.ipac.caltech.edu/2mass/releases/allsky/doc/sec2_2.html#pscastrprop .

[6]The system transmission curves of 2MASS is found at http://www.ipac.caltech.edu/2mass/releases/allsky/doc/sec3_1b1.html .

[7]The criteria for selecting high-reliability point sources for the 2MASS catalogue are discussed at http://www.ipac.caltech.edu/2mass/releases/allsky/doc/sec1_6b.html#phuncptsour.

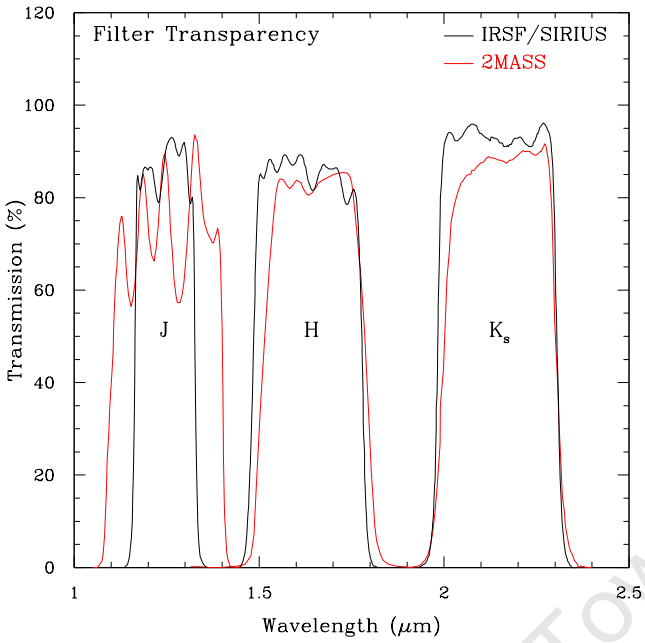

Figure 2.15 A comparison of the IRSF (*black*) and 2MASS (*red*) photometric filter systems. These curves represent the theoretical transmission curves of the detectors.

the flux from the point source. Generally, the total flux of a star is measured by defining large enough apertures that fully encompasses the stellar source. The noise contribution to the flux measurement however increases linearly with increasing aperture size. To overcome this effect, the aperture can be defined at some "intermediate" radius which requires an additional correction to the measured flux of the star. The magnitudes of selected point sources in the IRSF images were measured using aperture-corrected photometry. A variety of IRAF tasks in the DAOPHOT and PHOTCAL packages were employed to carry out the photometry.

The instrumental magnitudes of the stars were determined using the PHOT task in the DAOPHOT package. The flux of the point sources was measured in thirty different apertures. The apertures span a range of sizes about the Gaussian FWHM of the stars. A measurement of the background was obtained by interactively defining the sky annulus around a star. The sky annulus was chosen to have a width of 5–6pixels depending on the stellar crowding in the image.

The MKAPFILE task in the PHOTCAL package was used to determine the aperture correction for the individual galaxy images. The aperture correction was measured by fitting an analytical model stellar profile to the observed fluxes in each aperture. An example of the stellar profile fit (known as the *growth curve*) for point sources in the J-band image of NGC 59 is displayed in Fig. 2.16. A magnitude correction was calculated for each defined aperture using the stellar profile fit to the fluxes. This correction was defined as the difference between the total aperture magnitude from the stellar profile fit and the magnitude measured

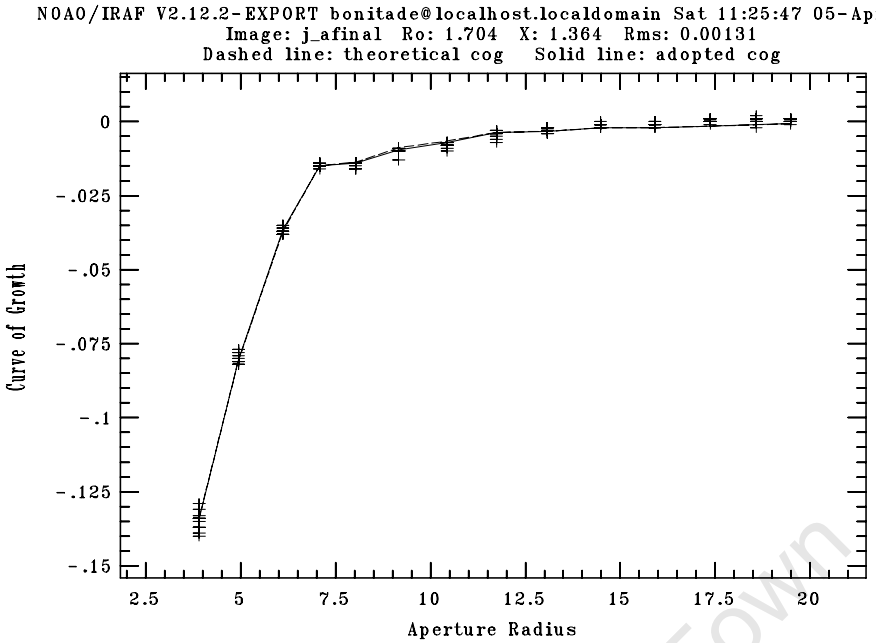

Figure 2.16 The stellar profile fit (or theoretical curve of growth) for a sample of 8 stars identified in the J-band image of NGC 59. The magnitude correction to be applied to 14 different apertures is shown. The aperture corrections were computed as the difference between the total aperture magnitude from the stellar profile fit, and the magnitude measured in any given aperture size.

in a given aperture size.

The next step involved choosing an appropriate aperture size to which the magnitude correction (determined by the MKAPFILE task) will be added. The aperture size depends critically on the seeing. It can be shown that ∼76% of the stellar flux is contained within the FWHM of a Gaussian fit to the light distribution. The Gaussian FWHM of the stellar flux distribution was thus used as a lower limit in defining the aperture size. The growth curve together with the final aperture size for the night of 14 Feb 2006 is illustrated in Fig. 2.17. The figures show that the aperture size for the three bands has been chosen to include most of the stellar flux. The growth curves for the remaining nights is displayed in Appendix B.1.

The aperture radius and corresponding magnitude correction to the stellar flux for the various nights are listed in Table 2.6. The aperture corrections are sufficiently small ($< 0^{\rm m}.25$) to ensure an insignificant noise contribution to the measured magnitudes. The aperture corrections listed in Table 2.6 were added to the magnitudes measured by the PHOT task. These magnitudes represent the "final" instrumental magnitudes of the point sources.

The offset between the instrumental and apparent magnitude (given by the 2MASS Point Source catalogue) was calculated for each of the point sources. The uncertainty in the magnitude offset is given by the square of the internal errors associated with the 2MASS and

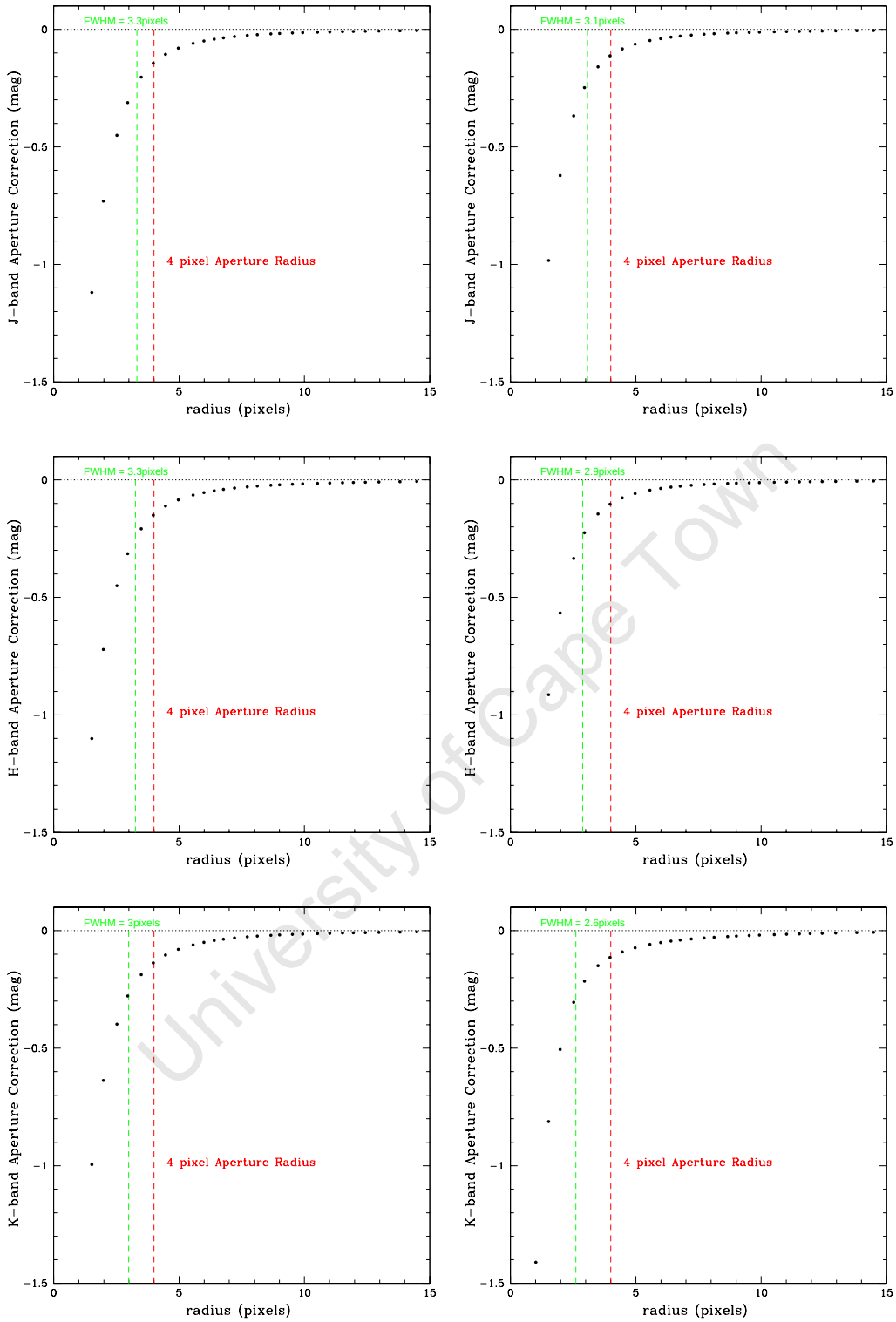

Figure 2.17 The magnitude correction as function of the aperture size for galaxy NGC 3115 DW01 observed on nights 14 Feb 2006 (*left*) and 16 Feb 2006 (*right*). The aperture corrections to be applied to the J- (*top*), H- (*middle*) and K_s-bands (*bottom*) are shown. The Gaussian FWHM of the flux distribution of point sources are indicated by the vertical green line. The chosen aperture radius to which the magnitude correction was applied is shown by the vertical red line.

Table 2.6. Aperture corrections applied to the magnitudes measured by the PHOT task.

		J Aperture		H Aperture		K_s Aperture	
Galaxy	Date	Radius (arcsec)	Correction (mag)	Radius (arcsec)	Correction (mag)	Radius (arcsec)	Correction (mag)
NGC 3115 DW01	2006 Feb 14	1.80	-0.14	1.80	-0.15	1.80	-0.14
	Feb 16	1.80	-0.11	1.80	-0.10	1.80	-0.11
	Feb 17	1.80	-0.12	1.80	-0.12	1.80	-0.11
NGC 59	2006 Jun 11	2.25	-0.12	2.25	-0.11	2.25	-0.11
LEDA 166099	2007 Mar 08	1.80	-0.21	1.80	-0.20	1.80	-0.20
ESO 384-016	Mar 08	1.80	-0.15	1.80	-0.15	1.80	-0.16
	Mar 09	1.80	-0.19	1.80	-0.17	1.80	-0.16
UGCA 200	2007 Mar 10	1.80	-0.16	1.80	-0.14	1.80	-0.14
	Mar 11	1.80	-0.11	1.80	-0.10	1.80	-0.12
	Mar 13	1.80	-0.22	1.80	-0.19	1.80	-0.18
NGC 5206	2007 Mar 10	1.80	-0.18	1.80	-0.15	1.80	-0.16

instrumental magnitudes, respectively. The magnitude offsets of the point sources show little scatter ($< 0^{\rm m}.05$) so that the nightly zero-point was taken as the mean magnitude offset between the IRSF and 2MASS point sources. The nightly zero-point j_1, h_1 and k_1 of the observations was determined for the J-, H- and K_s-bands, respectively.

The instrumental magnitudes of the point sources were transformed to apparent magnitudes using the equations:

$$j = J + j_1 + j_2(J - K_s) \ , \tag{2.7}$$

$$h = H + h_1 + h_2(J - H) \ , \tag{2.8}$$

$$k_s = K_s + k_1 + k_2(J - K_s) \ , \tag{2.9}$$

where J, H and K_s are the apparent magnitudes of the stars. The instrumental magnitudes are given by j, h and k_s in the J-, H- and K_s-bands, respectively. The nightly zero-points in the different wavelength bands are j_1, h_1 and k_1. The final term in equations (2.7)–(2.9) represents the colour correction to the magnitudes. The colour coefficients for the IRSF observations have been found to be $j_2 = -0^{\rm m}.018$, $h_2 = 0^{\rm m}.050$ and $k_2 = 0^{\rm m}.079$ (Kotze 2007) in the J-, H- and K_s-bands, respectively[8]. A correction for the airmass was not directly applied to the instrumental magnitudes. This calibration term is accounted for in the nightly zero-point correction derived from the 2MASS apparent magnitudes.

The nightly zero-points used in transforming the IRSF instrumental magnitudes to apparent magnitudes are listed in Table 2.7. The zero-points are observed to be stable across the period of the three observing runs. A maximum difference of $\Delta{\rm ZP} \sim 0^{\rm m}.2$ is measured in the zero-point value over the course of one year. The stability of the zero-point is observed in all three wavelength bands. The largest uncertainty in the zero-point is measured in the K_s-band which arises from the internal errors of the 2MASS magnitudes.

The apparent magnitudes of the IRSF point sources were determined using equations (2.7)–(2.9) together with the zero-points given in Table 2.7. The difference between the transformed IRSF apparent magnitudes and 2MASS apparent magnitudes (Δmag) is shown in Figs. 2.18–2.22 for the various nights. The magnitude difference is shown for the J-, H- and K_s-bands. A scatter of $\Delta{\rm mag} \lesssim 0^{\rm m}.1$ from the 2MASS apparent magnitudes is observed in the calibrated magnitudes. This scatter in the magnitudes allows the mean magnitude difference, $<\Delta{\rm mag}>$, to be used as a gauge of how well the 2MASS magnitudes are recovered.

The mean magnitude offset $<\Delta{\rm mag}>$ and 1σ deviation are shown in Figs. 2.18–2.22. A scatter of $\Delta{\rm mag} \lesssim 0^{\rm m}.2$ is measured about the mean magnitude offset. The scatter of the Δmag values does not increase significantly near the 2MASS magnitude limit due to the small photometric uncertainties ($\lesssim 10\%$ in the J, H and K_s-bands) in the 2MASS magnitudes of stars. The mean magnitude offset shows that the transformed IRSF apparent magnitudes agree within $0^{\rm m}.05$ with those given by 2MASS. This is in agreement with the findings of Kotze (2007). The J-band gives the best agreement of $<\Delta{\rm mag}> \lesssim 0^{\rm m}.002$ with the 2MASS

[8]The colour coefficients for the IRSF observations were obtained through private communication with J.P. Kotze. The coefficients were determined from the observation of Persson standard stars (Persson et al. 1998) at different airmasses. These stars are commonly used for the photometric calibration of the IRSF images.

Table 2.7. The magnitude zero-points for each night.

		Filter					
Date	Image	j_1 (mag)	j_1 Average (mag)	h_1 (mag)	h_1 Average (mag)	k_1 (mag)	k_1 Average (mag)
NGC 3115 DW01	2006 Feb 14	20.88 ± 0.037	20.87 ± 0.037	21.05 ± 0.041	21.03 ± 0.042	20.18 ± 0.041	20.16 ± 0.041
	Feb 16	20.86 ± 0.036		21.02 ± 0.042		20.14 ± 0.042	
	Feb 17	20.86 ± 0.037		21.03 ± 0.042		20.15 ± 0.041	
NGC 59	2006 Jun 11	20.79 ± 0.028		21.01 ± 0.025		20.22 ± 0.028	
LEDA 166099	2007 Mar 08	20.95 ± 0.034		21.13 ± 0.038		20.29 ± 0.040	
ESO 384-016	2007 Mar 08	20.92 ± 0.035	20.89 ± 0.036	21.11 ± 0.048	21.08 ± 0.048	20.29 ± 0.049	20.24 ± 0.047
	Mar 09	20.86 ± 0.037		21.04 ± 0.047		20.20 ± 0.044	
UGCA 200	Mar 10	20.91 ± 0.034	20.90 ± 0.034	21.09 ± 0.043	21.09 ± 0.043	20.16 ± 0.049	20.20 ± 0.049
	Mar 11	20.91 ± 0.032		21.11 ± 0.043		20.23 ± 0.049	
	Mar 13	20.89 ± 0.036		21.08 ± 0.043		20.21 ± 0.049	
NGC 5206	2007 Mar 10	20.95 ± 0.039		21.09 ± 0.048		20.26 ± 0.053	

magnitudes. A deviation of up to $<\Delta mag> = 0^{m}.033$ from the 2MASS magnitudes is observed in the H- and K_s-bands.

An average zero-point was calculated for those galaxies observed for more than one night (see Table 2.7). This proved sufficient as the zero-point values were shown to be stable for the different observing runs.

2.6 Star Subtraction

2.6.1 Overview

The near-infrared surface brightness profiles, photometric and structural parameters will be derived for each of the six target galaxies. To improve the accuracy of the surface photometry measurements, it is critical to remove the foreground stars in the galaxy images. The foreground contamination varies from one galaxy image to the next. In Fig. 2.14 it can be seen that the dwarf galaxy NGC 59 is least affected by contamination of foreground stars, whereas NGC 5206 is situated in a more star-crowded field. A careful removal of foreground stars is thus essential to obtain photometric results not influenced by resolved stellar sources.

The star subtraction routine of T. Nagayama (Kyoto University, private communication) was used in removing the foreground stars from the galaxy images. This routine was specifically developed for the removal of stellar contaminants in the star-crowded fields at low Galactic latitudes. The star subtraction routine builds the point spread function (psf) of the image by carrying out three iterative runs of the psf-fitting to the stars. This "automated" building of the psf distinguishes the star subtraction routine of Nagayama from the conventional KILLALL routine of Buta & McCall (1999). The KILLALL algorithm can only be successfully executed once a good model of the psf is established. This is contrary to the star subtraction method of Nagayama which incorporates the building of the psf into the algorithm itself, effectively reducing the computational time.

The star subtraction was carried out using two independent script files written in the IRAF command language. The first procedure script models the galaxy light distribution and removes it from the image. The star subtraction algorithm is implemented in the second script which creates the model psf using stars in the galaxy-free image. A detailed description of the technique used to remove the stellar contaminants is given below.

2.6.2 Galaxy Subtraction

The DAOPHOT.DAOFIND task was used to detect the stellar sources in the image. The DAOFIND task cannot easily distinguish between the intensity distribution of a star and that of a galaxy nucleus. This can lead to the galaxy center being used in the psf determination which is eventually removed with the stars in the image. It is thus necessary to remove the target galaxies from the image before conducting the star subtraction.

The intensity distribution of the target galaxy was measured using the ELLIPSE task. This task measures the intensity distribution of the galaxy by fitting elliptical isophotes at various radii along the semi-major axis of the galaxy. The integrated intensity is measured

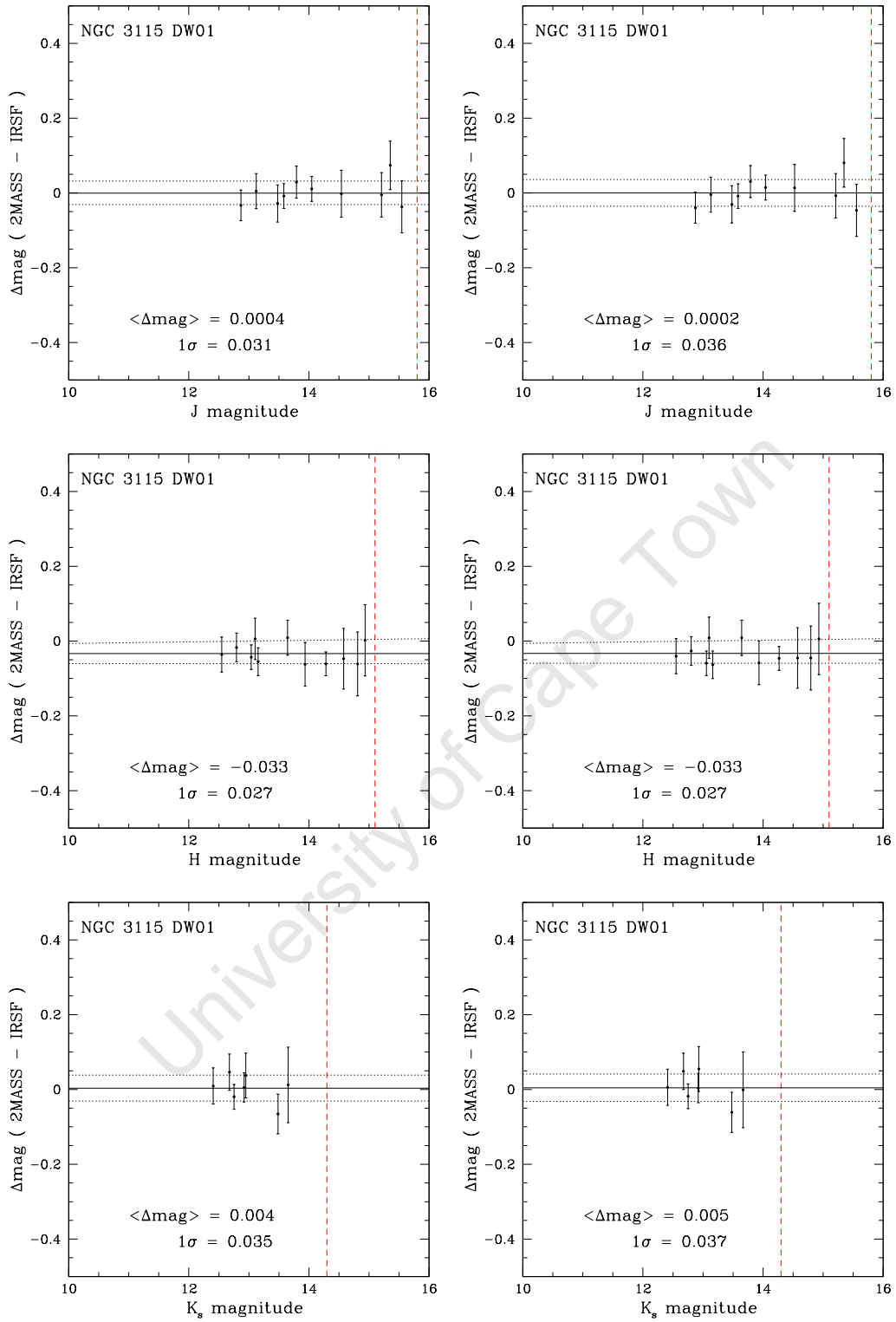

Figure 2.18 A comparison of the IRSF point source magnitudes with apparent magnitudes given by 2MASS for the nights 14 Feb 2006 (*left*) and 16 Feb 2006 (*right*). The galaxy observations are labeled at the top of each figure. The magnitude difference Δmag in the J- (*top*), H- (*middle*) and K_s-bands (*bottom*) is presented. The solid line shows the mean magnitude difference ($< \Delta\text{mag} >$) between the IRSF and 2MASS point sources. The horizontal dashed lines indicate the 1σ deviation from the mean magnitude difference. The completeness limit of the 2MASS observations is shown by the red vertical line.

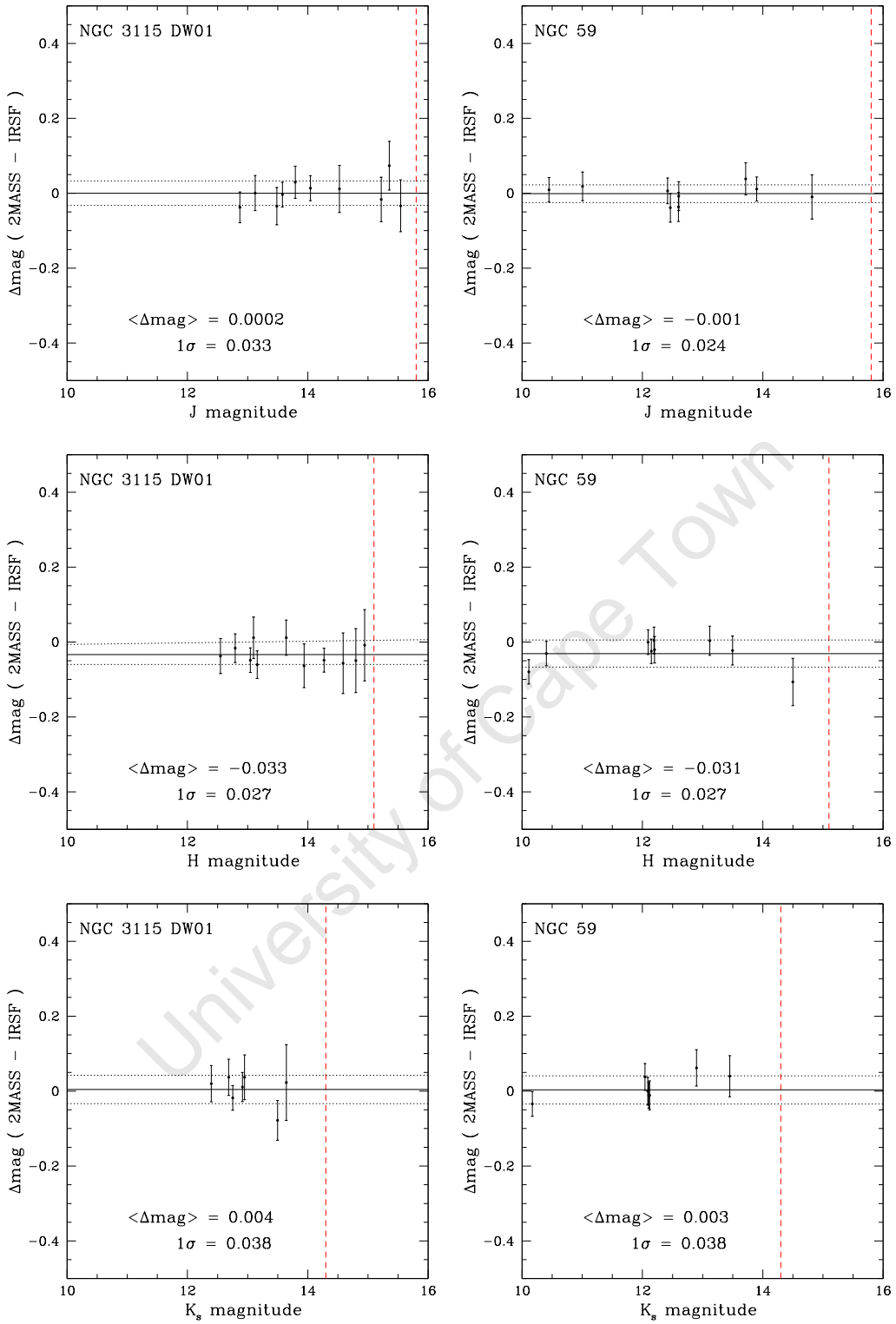

Figure 2.19 A comparison of the IRSF and 2MASS point source magnitudes for the nights 17 Feb 2006 (*left*) and 11 June 2006 (*right*); see caption for Fig. 2.18.

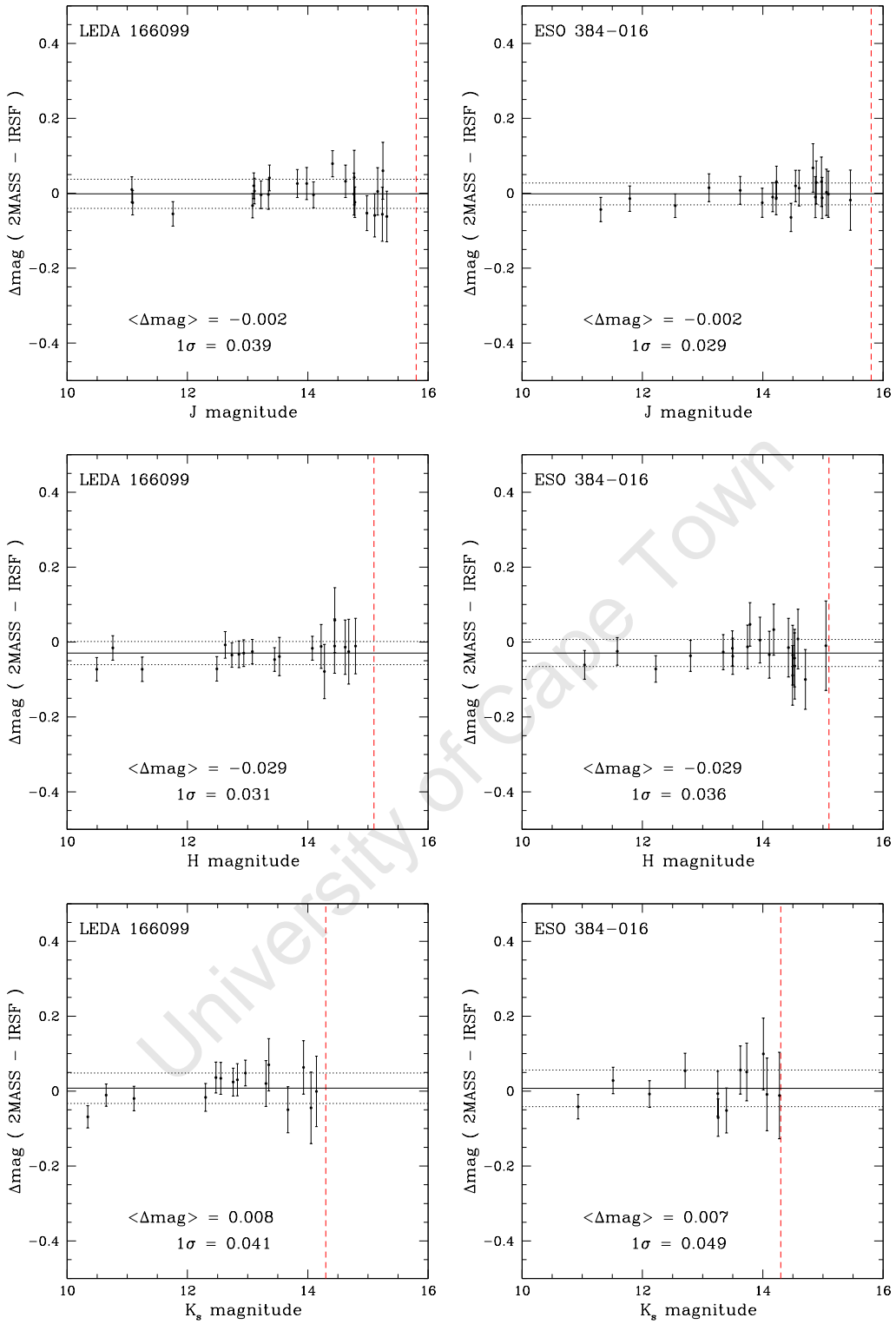

Figure 2.20 A comparison of the IRSF and 2MASS point source magnitudes for the night 8 March 2007; see caption for Fig. 2.18.

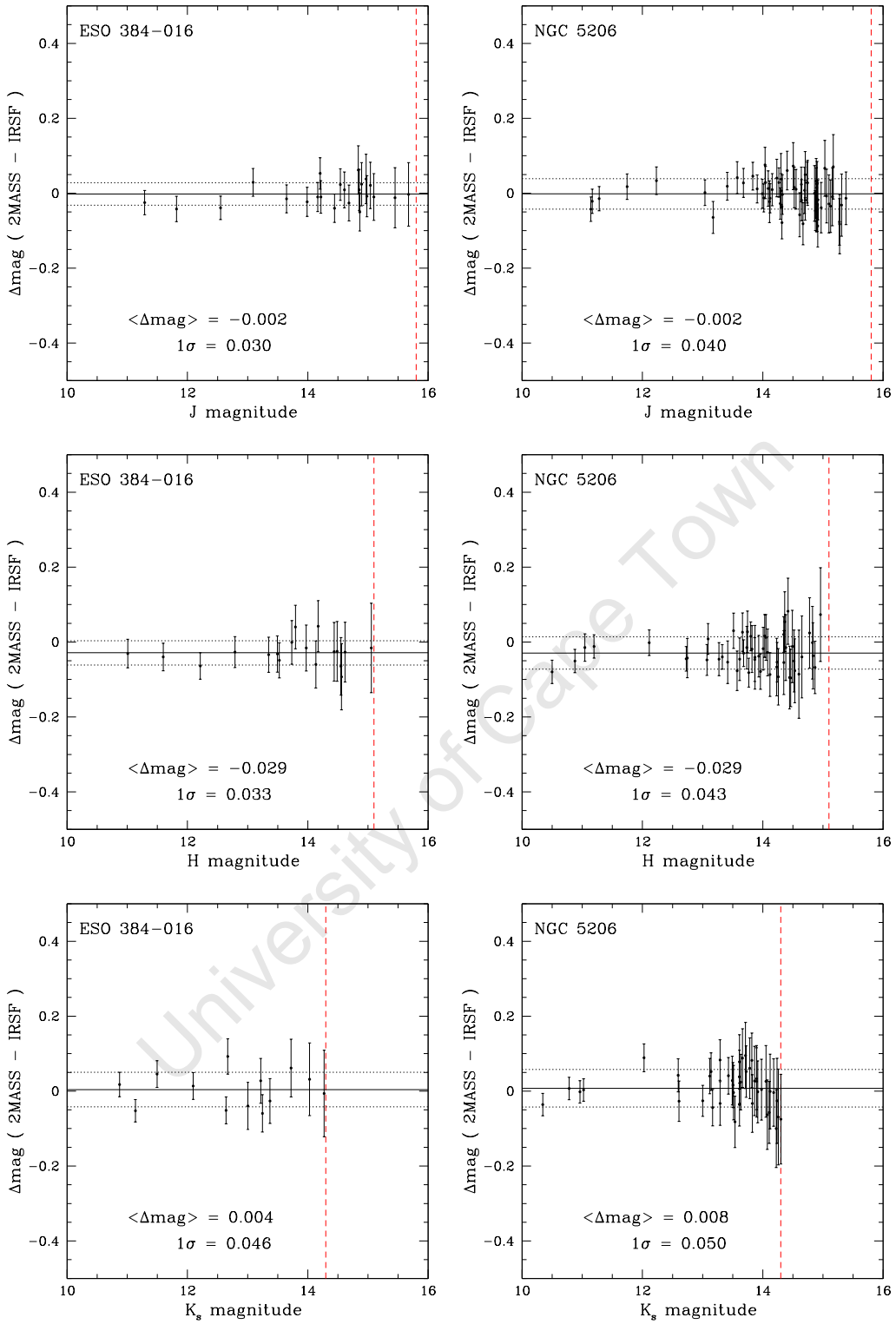

Figure 2.21 A comparison of the IRSF and 2MASS point source magnitudes for the nights 9 March 2007 (*left*) and 10 March 2007 (*right*); see caption for Fig. 2.18.

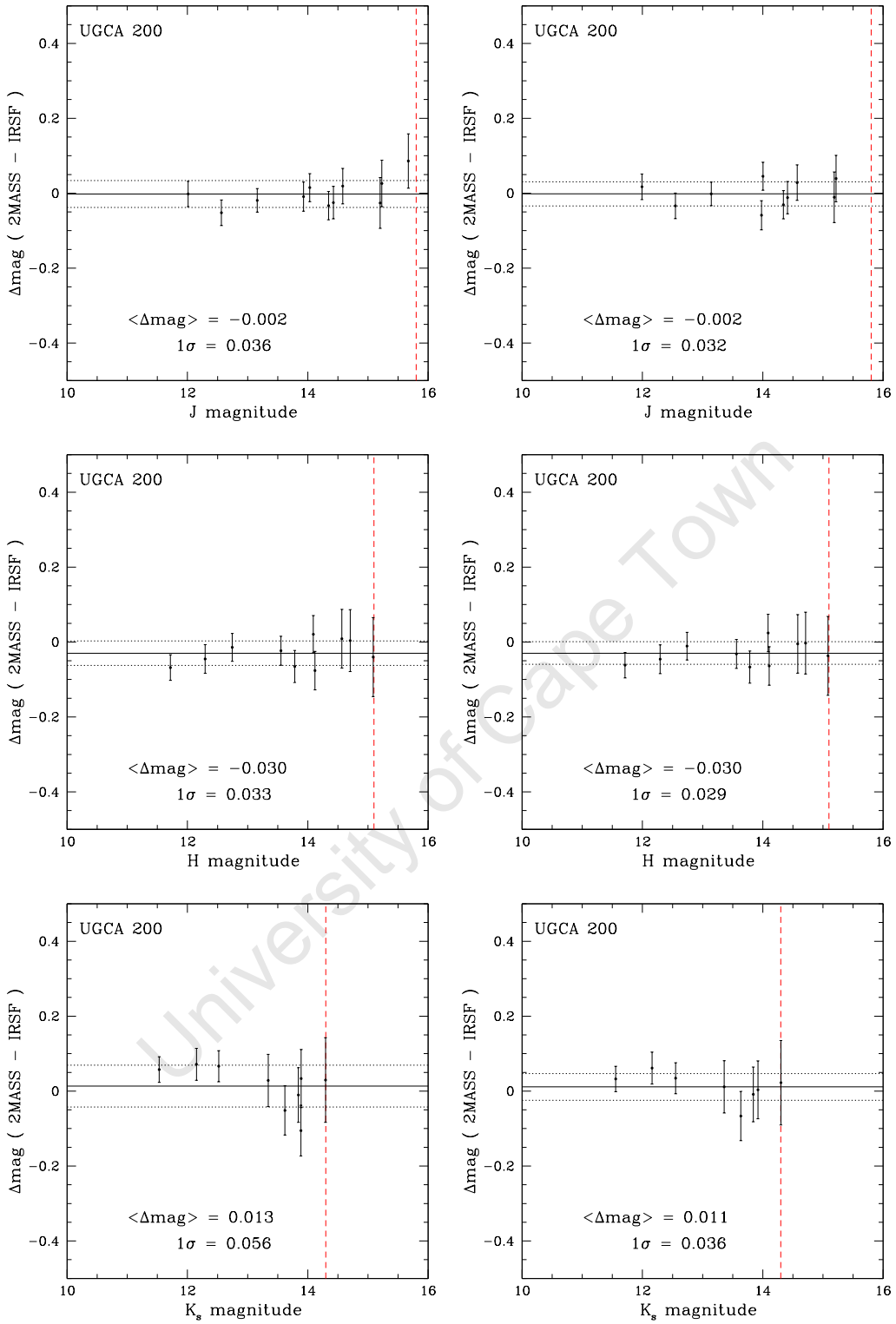

Figure 2.22 A comparison of the IRSF and 2MASS point source magnitudes for the nights 10 March 2007 (*left*) and 11 March 2007 (*right*); see caption for Fig. 2.18.

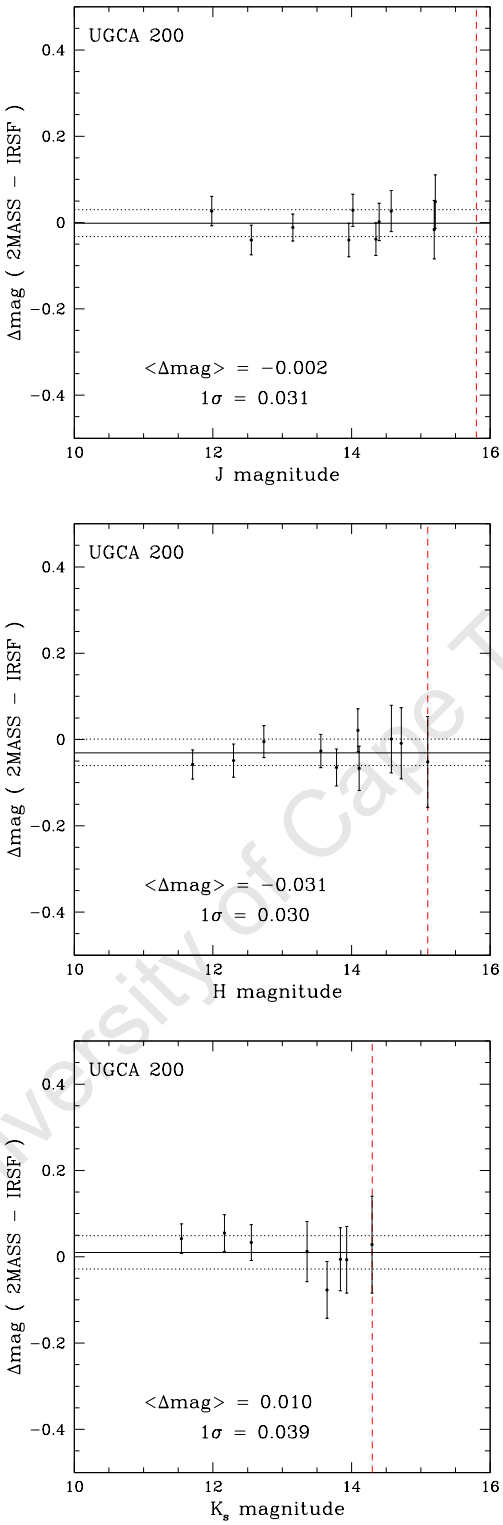

Figure 2.23 A comparison of the IRSF and 2MASS point source magnitudes for the night 13 March 2007; see caption for Fig. 2.18.

inside each of the elliptical isophotes. The central coordinates of the galaxy together with a defined maximum length for the semi-major axis serve as input parameters for the ELLIPSE task. The central coordinates of the galaxy were kept fixed throughout the fitting process. The ellipticity and position angle were however treated as free parameters during the fitting of the isophotes.

The ELLIPSE task generates a table containing the photometric parameters for each fitted isophote. These parameters were used in creating a two-dimensional, noise-free photometric model of the galaxy. The model galaxy was subtracted from the original galaxy image. The psf was determined from the stellar sources in the resulting galaxy-free image.

2.6.3 Star Subtraction Technique

The star subtraction routine of Nagayama is implemented as a procedure script file in IRAF. The routine employs various tasks in the DAOPHOT package to measure the psf and eventually remove the stars using the galaxy-free images. A step-by-step guide to the star subtraction process is provided below.

1. The DAOFIND task was used to detect stars above a 5σ threshold in the background-level. In this case, σ is an estimate of the background noise given by the SIGMA parameter in the DATAPARS definition file. The 5σ threshold allows for the detection of the brighter point sources in the galaxy-free image. The instrumental magnitudes of these sources were measured within a fixed aperture radius (corresponding to the FWHM of the stars) using the PHOT task.

2. The instrumental magnitude of the point sources measured by PHOT are given as

$$\mathrm{m_{instr}} = -2.5\log_{10}\left(\frac{\text{Total Counts } - \text{ Background Counts}}{\text{Exposure}}\right) . \tag{2.10}$$

A sample of point sources having instrumental magnitudes in the range of -14$^{\mathrm{m}}$.0 and -6$^{\mathrm{m}}$.5 were selected from the output photometry file. This magnitude range ensures that the faintest and saturated stars in the image will not be chosen as candidate stars in modeling the psf. The PSTSELECT task is used to select a maximum of 50 psf candidates from the sample stars. The PSTSELECT task requires the radius within which the psf model will be defined (DAOPARS.PSFRAD) and a psf-fitting radius for the stars (DAOPARS.FITRAD) as input parameters. The psf-fitting radius was chosen to be equal to the FWHM of the psf. The PSTSELECT task re-arranges the point sources in order of decreasing magnitude. The brightest sources in the sample that have no neighbouring stars within an aperture radius of

$$r = (\mathrm{PSFRAD} \ + \ \mathrm{FITRAD})/\mathrm{SCALE} \ + \ 1 \tag{2.11}$$

were selected as psf stars. The SCALE parameter is the pixel scale of the image. By setting the parameter SCALE to 1, r will be determined in units of pixels.

3. The PSF task builds the model psf of the image using the stars selected by PSTSELECT. The psf model is determined from the observed intensity distribution of the psf stars. The intensity distribution is a function of x and y which is stored as a two-component model of the psf. The first component approximates the light distribution in the cores of the psf stars

by a chosen analytic function. There are six functional forms for the analytical component of the psf model to choose from. The analytical component was computed using each of the six functions by setting the FUNCTION parameter to "auto". The function with the smallest standard deviation for the model fit of the psf was selected. The parameters of the analytic functions are then computed by fitting all the psf stars weighted by their signal-to-noise ratio.

The systematic variability of the psf across the image is specified by the empirical VARORDER parameter. The VARORDER parameter was set to +1 allowing the psf model to vary linearly across the image. This value for the VARORDER parameter generates a three-dimensional output image consisting of the computed psf model and two additional lookup tables. The first derivative of the psf with respect to x and y positions in the image are stored in the lookup tables. These lookup tables are used as additive corrections from the integrated analytic function to the actual observed psf.

4. The magnitudes of the stars detected in step 1 are re-measured using a psf-fitting photometry technique. This was accomplished with the ALLSTAR task. The ALLSTAR task fits the first iteration model psf (given by step 3) to individual stars in the photometry list. The stars which are successfully fitted with the model psf are subtracted from the galaxy-free image. The output image contains the residual point sources which could not be matched with the psf model. A tabular file containing the coordinates, magnitudes and fitting parameters of the subtracted stars is written to the output.

5. The DAOFIND task is used to detect stars above a 3σ threshold in the star-subtracted image generated in step 4. The lower threshold in the background allows the faint point sources in the image to be detected. The magnitudes of the point sources are measured with the PHOT task and stored in a photometry file. The stellar coordinates, magnitudes and sky values measured by the PHOT task are used as initial estimates in carrying out the psf-fitting photometry with the ALLSTAR task. The first iteration model psf is fitted to the point sources in the photometry file. The photometric results of the fitted stars are written to an output file. A master list of all point sources successfully fitted with the first iteration model psf is made.

6. A subsample of stars having instrumental magnitudes in the range of -12$^{\rm m}$.0 to -7$^{\rm m}$.0 were selected from the master list of psf-fitted point sources. These point sources will remain psf candidate stars in building the second and third iteration model psf.

7. The SUBSTAR task is used to remove the psf-fitted stars stored in the master list from the galaxy-free image. The subsample of psf candidate stars defined in step 6 are however retained in the galaxy-free image.

8. Following steps 2 and 3, the model psf is re-computed using the star-subtracted image. A maximum of 50 point sources are used in building the second iteration model psf. The ALLSTAR task is employed to fit the model psf to stars in the original galaxy-free image. The stars successfully fitted with the second iteration model psf are removed from the image. The psf candidate stars identified in step 6 are retained in the star-subtracted image. The resulting star-subtracted image is observed to have less residual stars compared to the previous iteration.

9. A third iteration of the psf is computed from the star-subtracted image given by step

8. The model psf is fitted to stars in the original galaxy-free image. Those stars successfully fitted with the third iteration model psf are removed from the image.

10. Finally, the DAOFIND task is used to detect point sources above a 2σ threshold in the star-subtracted image generated in step 9. The lower threshold allows for the detection of the residual point sources in the star-subtracted image. The third iteration model psf is fitted to these residual stars using the ALLSTAR task. The residual stars successfully fitted with the model psf are stored in an output file. A master list of all stars fitted by the third iteration model psf is constructed. The SUBSTAR task is used to subtract the point sources in the master list from the original galaxy image. The output image represents the final star-subtracted image of the galaxy.

The original and star-subtracted image of the galaxies NGC 5206 and NGC 59 are shown in Fig. 2.24. The residuals from saturated and bright point sources can be seen in the star-subtracted images. The effectiveness of the star subtraction routine is clearly demonstrated for NGC 5206 in which most of the stellar sources were cleanly removed. The residuals from background galaxies are also visible in the resulting images (e.g., see the edge-on spiral galaxy in the lower left corner of NGC 5206 image). The nuclei of these galaxies were removed together with the stars during the subtraction process.

The residuals from the background galaxies, bright and saturated stars were interactively removed using the IMEDIT task. The "cleaned" images of the target galaxies are shown in Figs. 2.25–2.30. The extended source seen south-west of the central component of NGC 3115 DW01 (Fig. 2.25) was not removed during the cleaning process. The NIR colour of this source was measured and found to be similar to that of NGC 3115 DW01. This provided some indication that the extended object is indeed a background galaxy which can be seen through the fairly bright central region of NGC 3115 DW01. The B-band image of NGC 3115 DW01 (see Fig. 2.1) from Parodi et al. (2002) reveals that this source is a background spiral galaxy. However, further information about this background galaxy is currently not available in the literature. The background galaxy was retained in the image of NGC 3115 DW01 to minimize the effect of smoothing on the light distribution of the galaxy. The surface photometry was carried out on the cleaned galaxy images shown in Figs. 2.25–2.30.

2.7 Surface Photometry

In this section, a photometric study of the underlying stellar component of the six dwarf galaxies is made based on the deep NIR observations. The photometric and structural properties are derived for the individual galaxies. These results will be used to gain more insight into the morphology and the evolutionary state of the galaxies.

2.7.1 Geometrical Parameters

The geometrical parameters governing the measurement of the galaxy SB profiles are its central coordinates (x_0, y_0), ellipticity (ϵ) and position angle (PA). By keeping these parameters fixed it is possible to measure the isophotes describing the intensity distribution of the galaxy

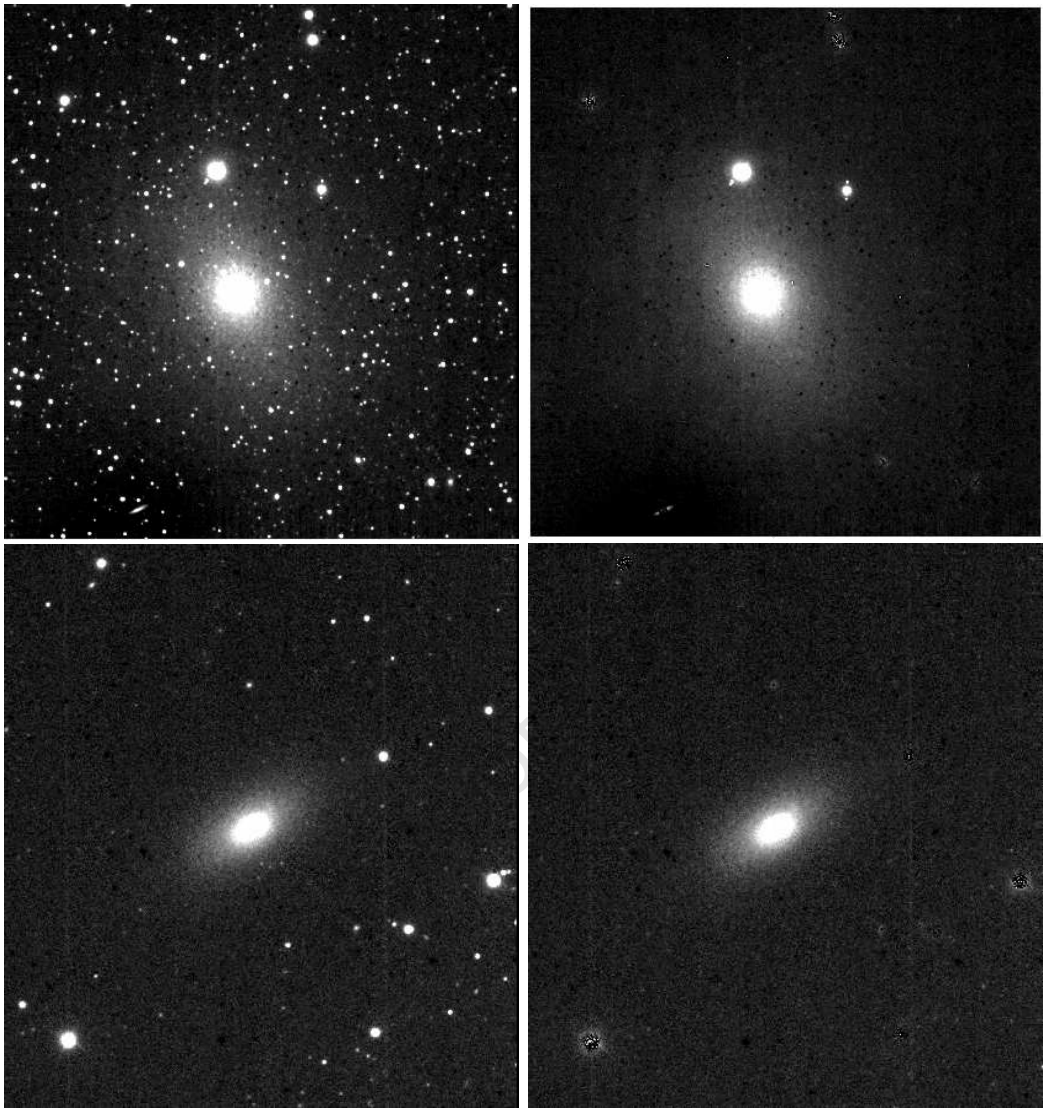

Figure 2.24 The original and star-subtracted H-band images of the galaxies NGC 5206 (*top*) and NGC 59 (*bottom*) are shown on the left and right, respectively. The residuals from background galaxies, saturated and bright stars in the images were removed manually using the IMEDIT task.

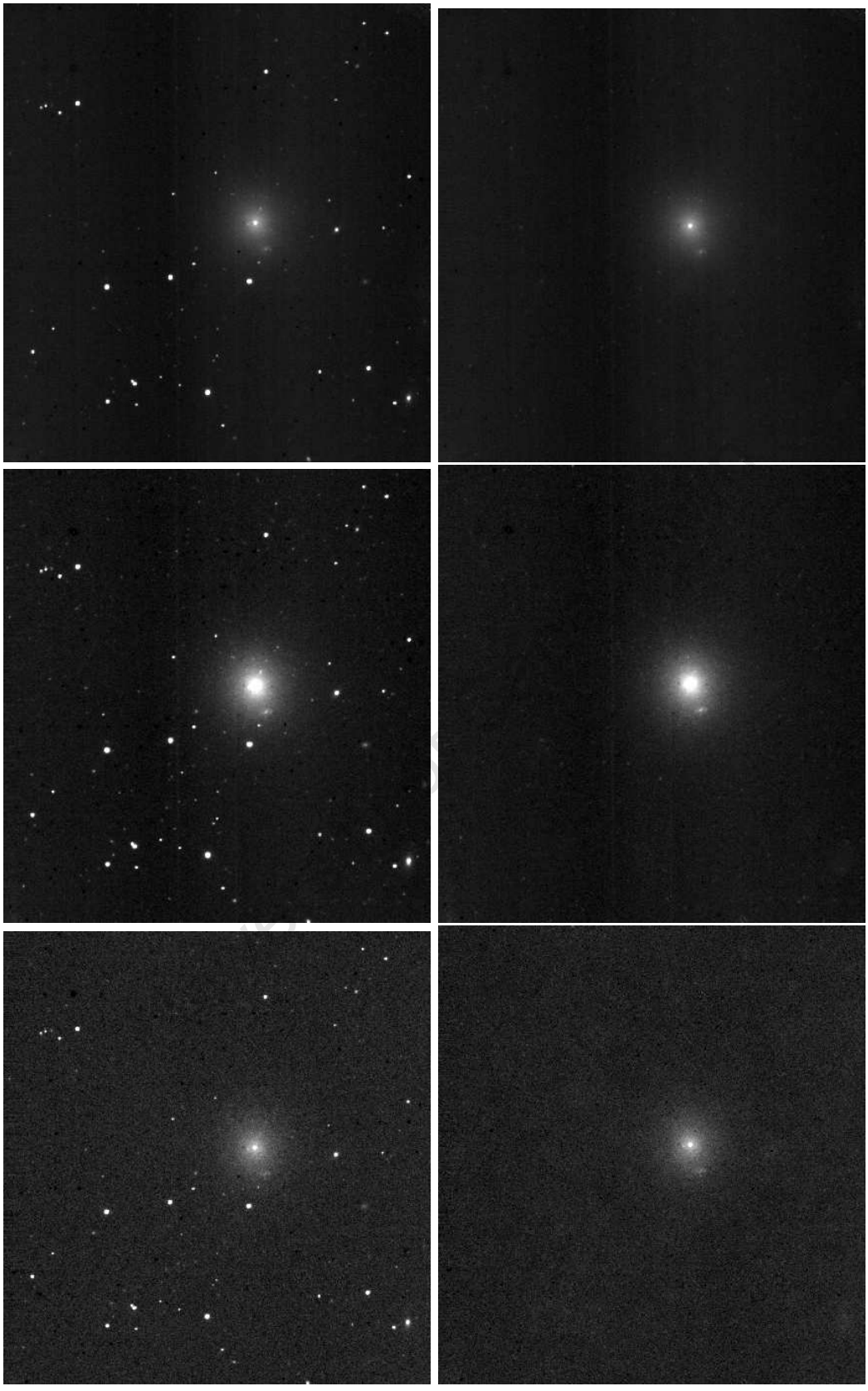

Figure 2.25 The original (*left*) and star-subtracted image (*right*) of the galaxy NGC 3115 DW01. The J- (*top*), H- (*middle*) and K_s-band (*bottom*) images are shown.

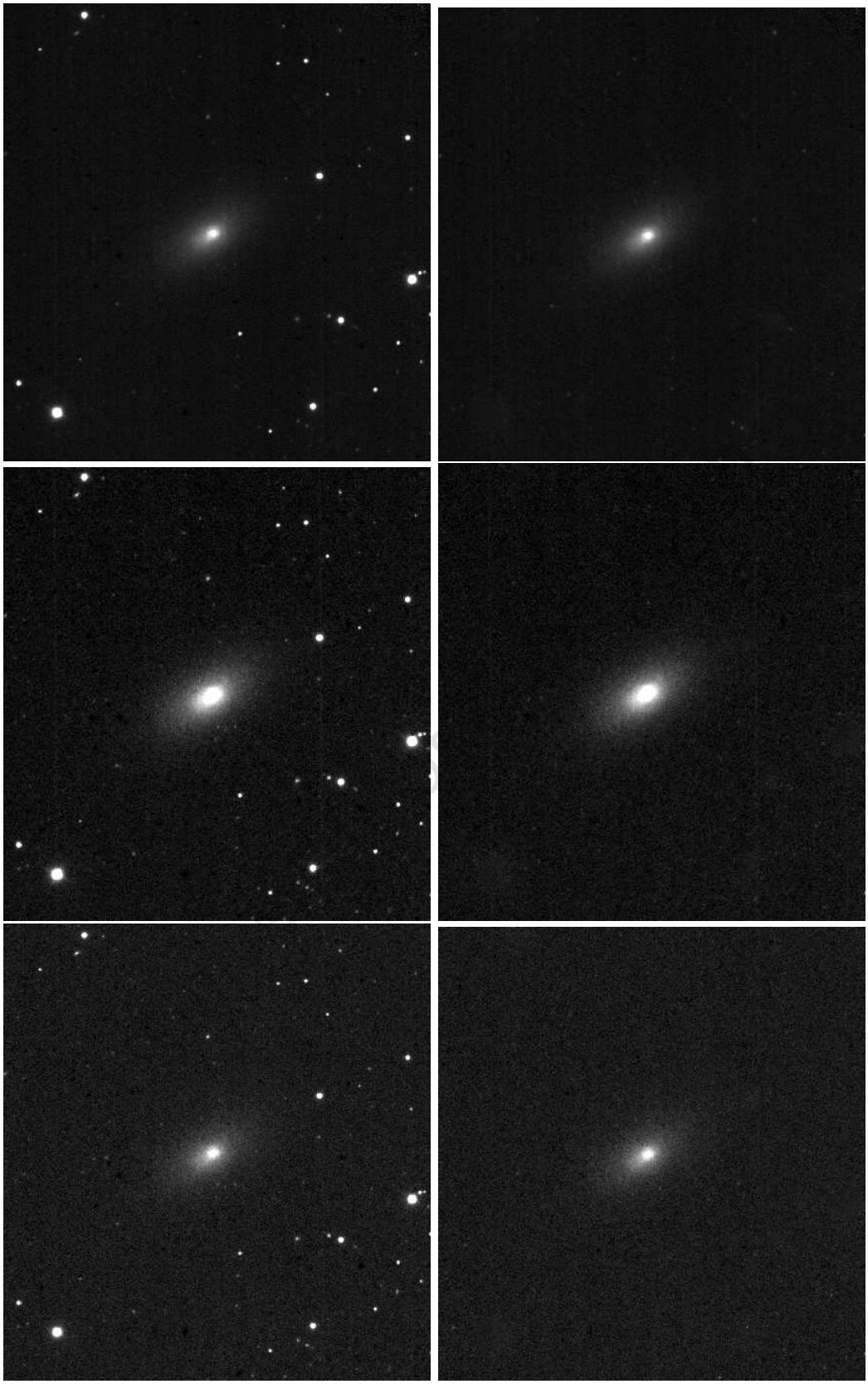

Figure 2.26 The original (*left*) and star-subtracted image (*right*) of the galaxy NGC 59. The J- (*top*), H- (*middle*) and K_s-band (*bottom*) images are shown.

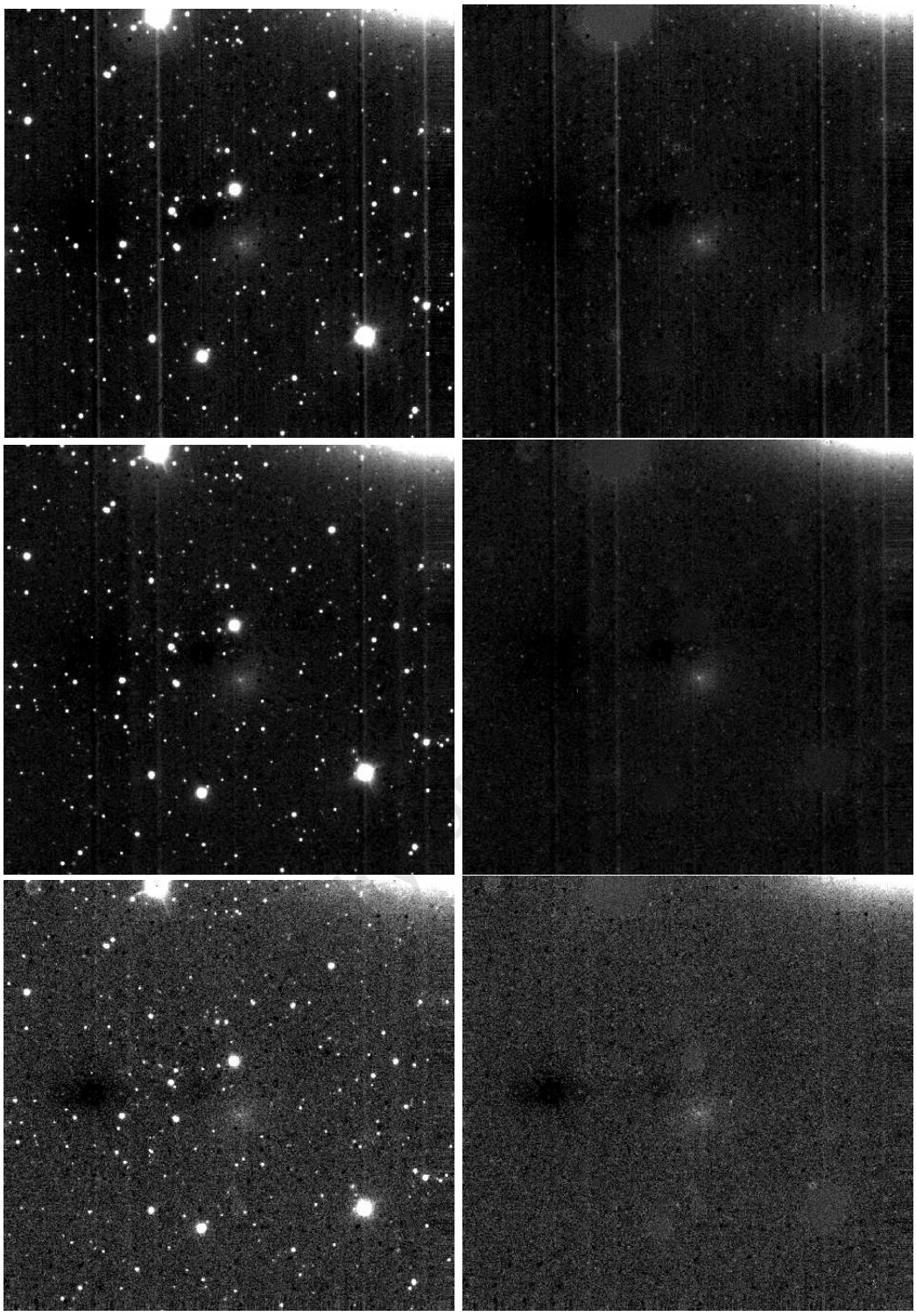

Figure 2.27 The original (*left*) and star-subtracted image (*right*) of the galaxy LEDA 166099. The J- (*top*), H- (*middle*) and K_s-band (*bottom*) images are shown. The vertical lines in the J- and H-band images are a result of "bleeding" from saturated foreground stars and the neighbouring galaxy NGC 2784.

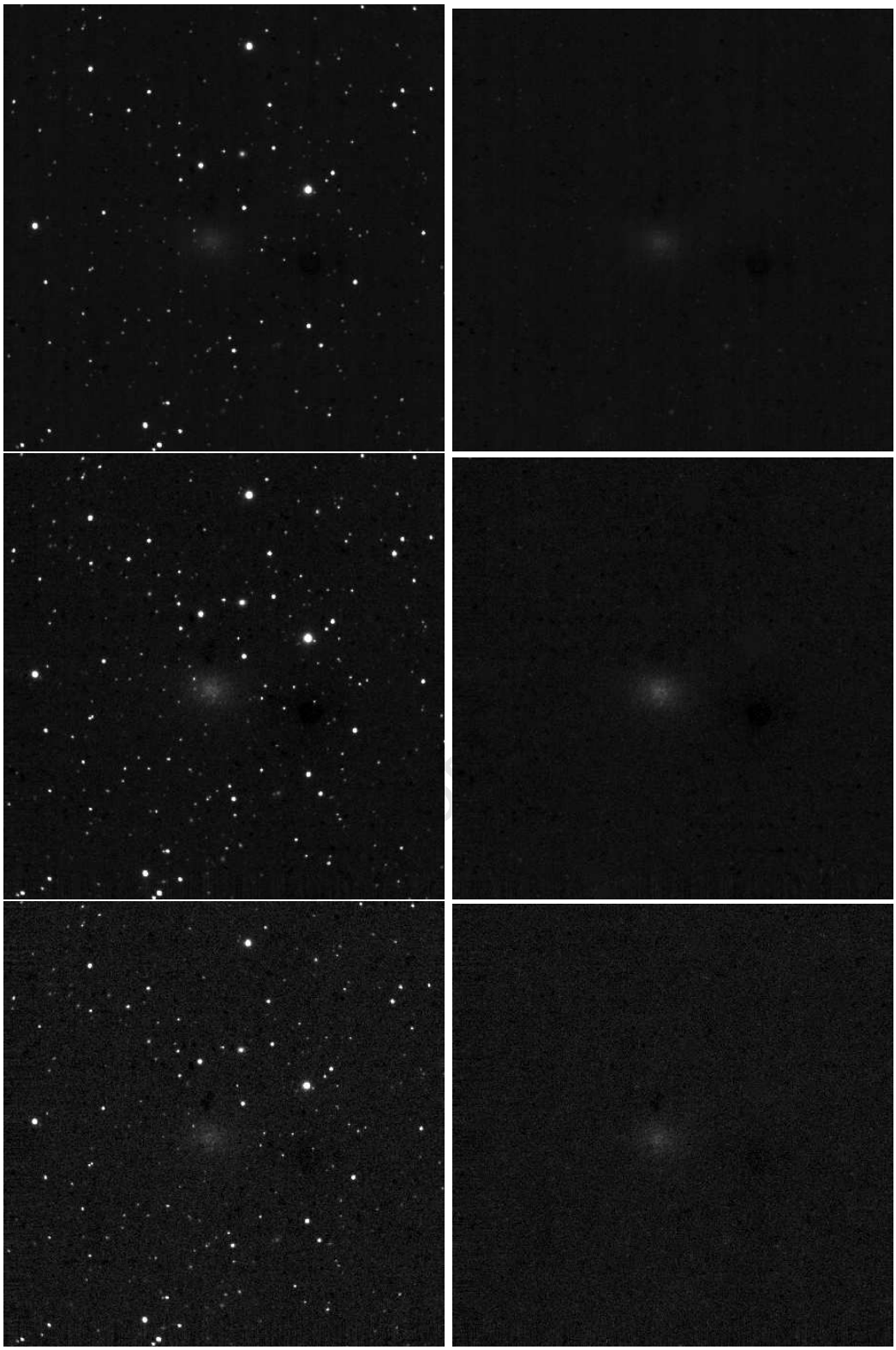

Figure 2.28 The original (*left*) and star-subtracted image (*right*) of the galaxy ESO 384-016. The J- (*top*), H- (*middle*) and K_s-band (*bottom*) images are shown.

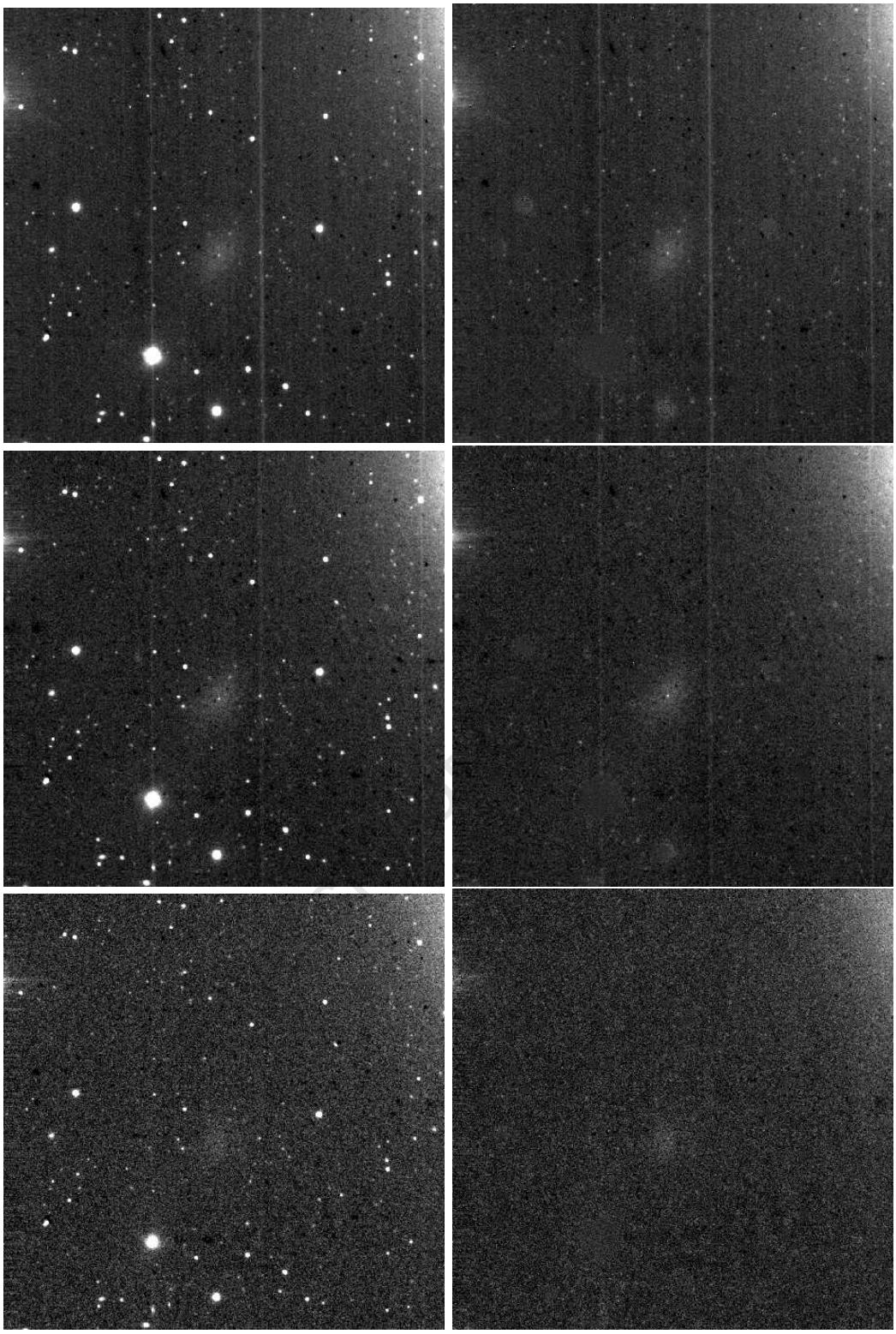

Figure 2.29 The original (*left*) and star-subtracted image (*right*) of the galaxy UGCA 200. The J- (*top*), H- (*middle*) and K_s-band (*bottom*) images are shown. The vertical lines in the J- and H-band images are a result of "bleeding" from saturated foreground stars and the neighbouring galaxy NGC 3115.

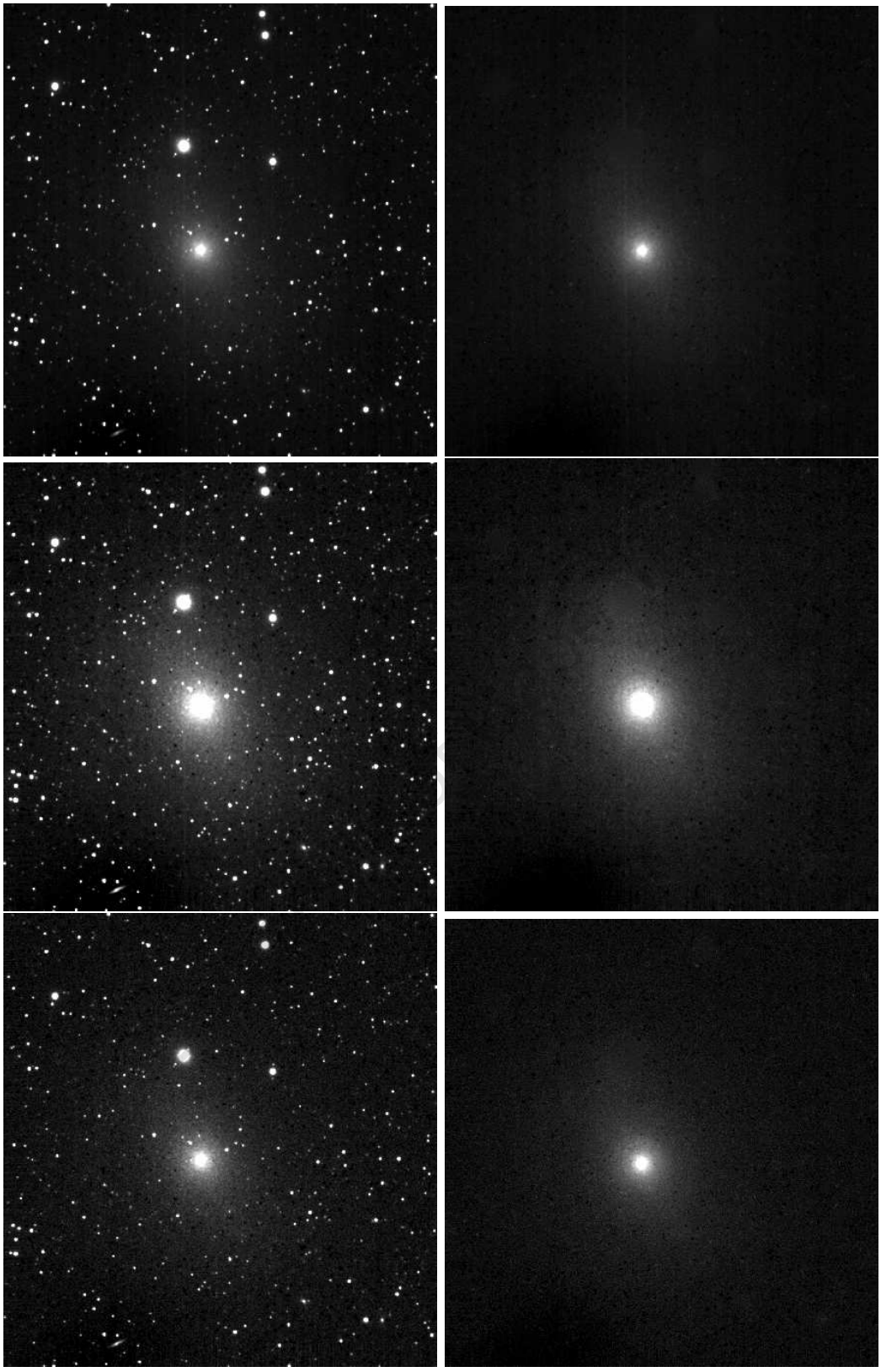

Figure 2.30 The original (*left*) and star-subtracted image (*right*) of the galaxy NGC 5206. The J- (*top*), H- (*middle*) and K_s-band (*bottom*) images are shown.

out to fainter levels. To achieve this, the SB profile of the galaxies was measured in two stages:

1. The parameters $x_0,\ y_0,\ \epsilon$ and PA were obtained by fitting elliptical isophotes to the light distribution of the galaxy. Initially, these parameters were allowed to vary freely with radius of the galaxy. The ellipticity and position angle are derived from the outer isophotes where the older stellar population is expected to set the overall geometry of the galaxy. These measurements assume that the galaxy does not strongly interact with its nearest neighbours which can introduce perturbations in its morphology.

2. The fitting process is repeated keeping the parameters $x_0,\ y_0,\ \epsilon$ and PA (as determined by the outer isophotes) fixed. Subsequently, the surface brightness is measured in fixed elliptical isophotes along the semi-major axis of the galaxy.

The isophotal fitting to the light distribution of the galaxy was carried out using the ELLIPSE task in IRAF. The ELLIPSE task requires an initial guess for the galaxy center, ellipticity and position angle but allows these parameters to vary freely with radius. The fitting was stopped once the noise levels in the background starts to dominate the isophotal fitting process.

The variation of the geometrical parameters ($x_0,\ y_0,\ \epsilon$ and PA) with galaxy radius (r) is shown in Figs. 2.31–2.33. The errors in the geometrical parameters are associated with the isophotal fitting process and are given by the ELLIPSE task. The parameters for the three brightest galaxies in the sample ($B < 13\overset{\mathrm{m}}{.}4$) can be seen in Figs. 2.31 and 2.32. The high surface brightness of these galaxies allows for their geometrical parameters to be traced out to $\mu_{K_s} \sim 23$mag arcsec^{-2} in all three wavelength-bands. These galaxies show little variation in the position angle ($\Delta\mathrm{PA} \lesssim 10^{\circ}$) outside the $r{\sim}10''$ radius. The galaxy NGC 5206 (Fig. 2.32) shows the largest gradient in ellipticity ranging from $\epsilon \sim 0.08$ at $r{=}10''$ to $\epsilon \sim 0.4$ at $r{=}100''$. The lower values of ellipticity near the center of NGC 5206 is due to the bulge component of the galaxy. The extended disk of the galaxy becomes the more dominant component at larger radii ($r \gtrsim 50''$).

Figure 2.33 shows the geometrical parameters for the two fainter galaxies ESO 384-016 and LEDA 166099. The parameters are traced out to $r{\sim}40''$ in both galaxies and are observed to be most stable in the H-band. A measure of the geometrical parameters for these fainter systems was thus obtained from the H-band images.

The variation of the geometrical parameters with radius could not be measured for the faintest galaxy ($B \sim 16\overset{\mathrm{m}}{.}2$) in the sample, UGCA 200. The low S/N levels of the galaxy caused the isophote fitting to end prematurely. The B-band value of the position angle and ellipticity given by Parodi et al. (2002) was adopted for this galaxy.

The ellipticity and position angle of each galaxy was defined by taking the mean of the respective data points beyond the $r{\sim}10''$ radius. The radial range used to measure these parameters is indicated by the vertical red lines in Figs. 2.31–2.33. The mean values of the ellipticity and position angle for the individual galaxies are listed in Table 2.11. For the brighter galaxies NGC 3115 DW01, NGC 59 and NGC 5206, the parameters were measured in the three wavelength bands. The error in ellipticity and position angle is given as the standard deviation of the mean value. Good agreement in the ellipticity ($\Delta\epsilon < 0.05$) and

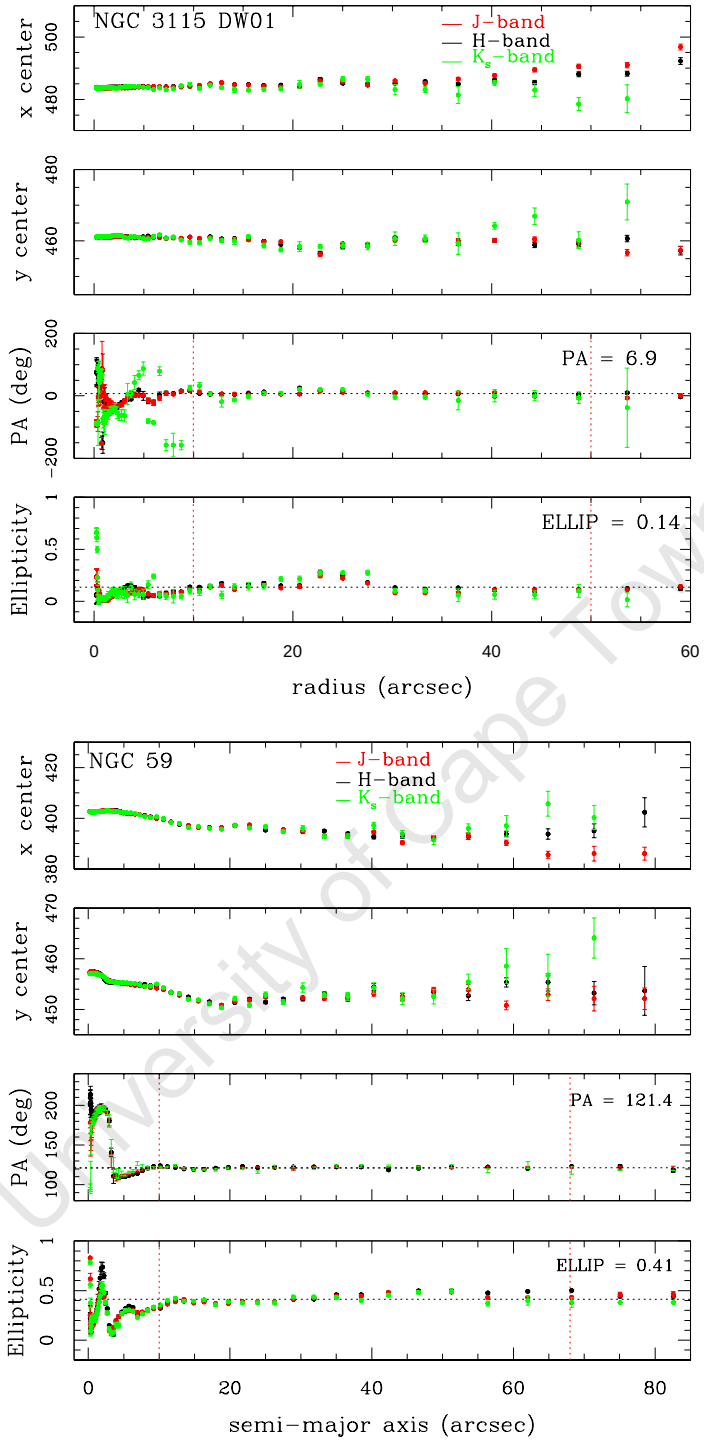

Figure 2.31 Geometrical parameters as a function of radius for the galaxies NGC 3115 DW01 (*top*) and NGC 59 (*bottom*). The galaxy central coordinates (x_0, y_0), position angle and ellipticity are plotted for the J- (*red*), H- (*black*) and K_s-bands (*green*). The vertical red lines indicate the radial range used to calculate the mean value of the ellipticity and position angle. These values are quoted above each plot of the ellipticity and position angle, respectively.

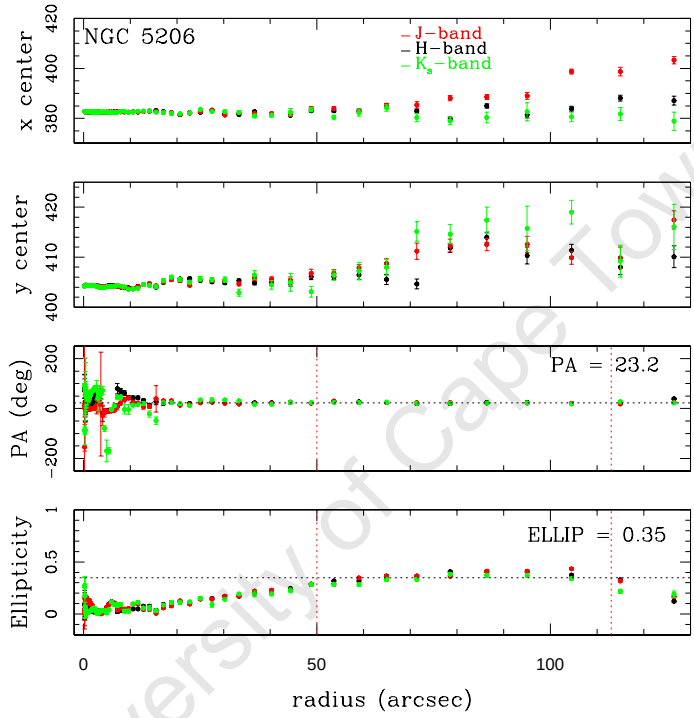

Figure 2.32 Geometrical parameters as a function of radius for galaxy NGC 5206. See caption for Fig. 2.31

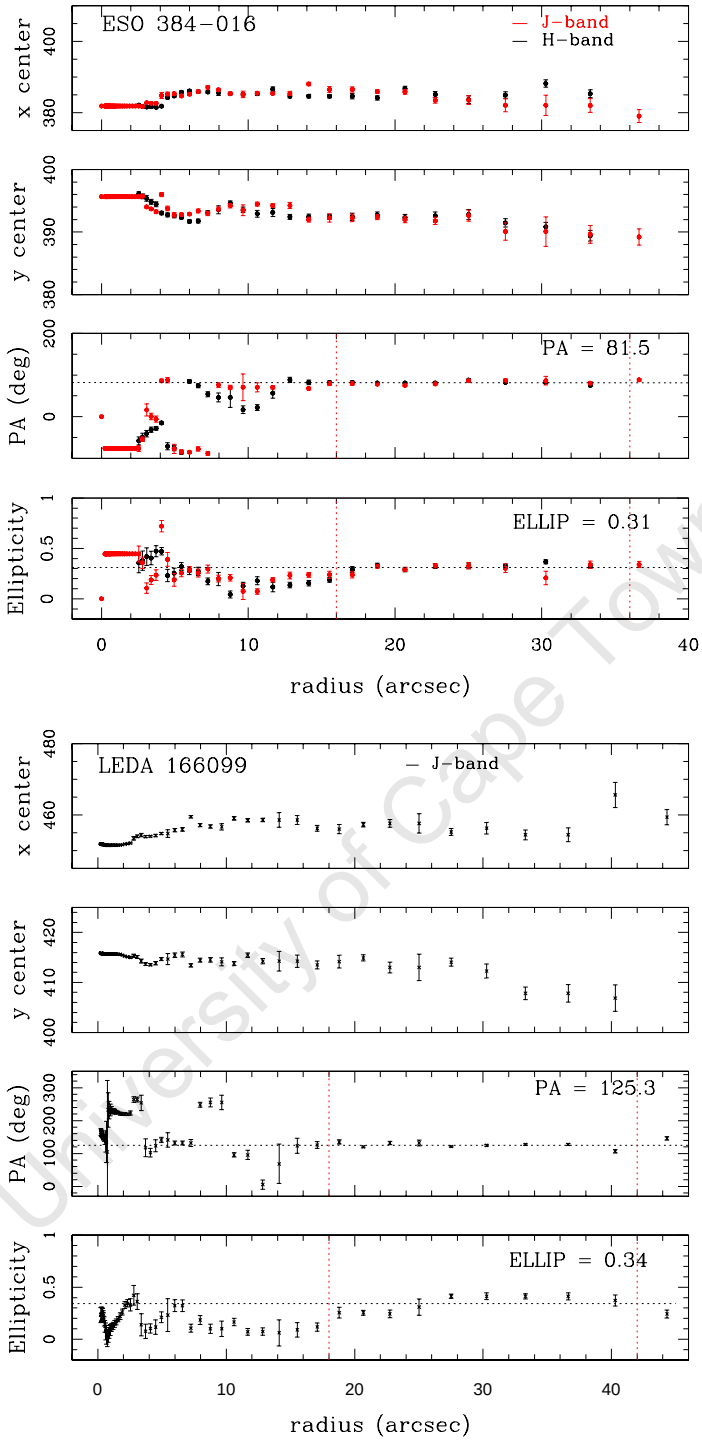

Figure 2.33 Geometrical parameters as a function of radius for the galaxies ESO 384-016 (*top*) and LEDA 166099 (*bottom*). The galaxy central coordinates (x_0, y_0), position angle and ellipticity are plotted for the J- and H-bands. The vertical red lines indicate the radial range used to calculate the mean value of the ellipticity and position angle. These values are quoted above each plot of the ellipticity and position angle, respectively.

position angle (ΔPA $< 1^{\circ}$) is observed for the three different bands.

The mean of the ellipticity and position angle of the galaxy ESO 384-016 was determined from the J- and H-bands. The K_s-band value for the ellipticity and position angle was computed as the average of the J- and H-band values. For LEDA 166099, the parameters could only be measured in the J-band. This value of the ellipticity and position angle was assumed to hold for the H- and K_s-bands.

The central coordinates of the galaxies were then measured as a function of radius keeping the ellipticity and position angle fixed. The centers of the galaxies NGC 3115 DW01 and NGC 5206 are given by the mean of the x_0 and y_0 data points within the $r \sim 10''$ radius. Only those data points larger than the Gaussian FWHM of stars in the image were used in defining the central coordinates of the galaxy. The centers of the remaining galaxies were measured interactively using the IMEXAM task. The central peak in the intensity distribution of the galaxy was defined as the "true" center.

The high spatial resolution of the NIR imaging reveals a resolved double nuclear component in the center of NGC 59 (see Fig. 2.13). This double nuclear component of NGC 59 was not detected in the B- and R-band observations of Jerjen et al. (2000b). It is expected that emission from the younger stellar population dominates the light contribution from the galaxy in the optical. The central features of NGC 59 could thus appear smeared out in the optical images resulting in just the detection of a single galaxy nucleus. An attempt was made to derive the photometric properties of the two nuclei independently (section 2.7.3), though this remains a challenge even for the deep well-resolved NIR photometry from the IRSF.

Based on the kinematical studies of NGC 59 (see Chapter 3), we have assumed that the northern component constitutes the nucleus of the galaxy. The detection of Hα in the center of NGC 59 (Skillman et al. 2003) is confirmed by the longslit spectroscopy in Chapter 3. It indicates that NGC 59 has experienced recent star formation activity in its center and it is thus possible that the second nuclear component is a star-forming knot in the galaxy center. This is supported by the fact that the secondary component is most luminous in the H-band (see Fig. 2.13). Based on the deep NIR imaging, it remains unclear, however, whether NGC 59 hosts a double nucleus or a star-forming region close to the galaxy nucleus. A detailed analysis of the NIR photometric properties of the central features in NGC 59 is explored further in section 2.7.3.

2.7.2 Surface Brightness Profiles

The ELLIPSE task was used to measure the intensity distribution along the semi-major axis of the galaxy. The galaxy center together with the geometrical parameters listed in Table 2.11 were kept fixed during the isophotal fitting. The SB profiles of the six dwarf galaxies are shown in Figs. 2.34–2.36. The SB profiles are measured out to $\sim$ 25mag arcsec^{-2} in the J- and H-bands. The galaxies are detected down to 23.5mag arcsec^{-2} in the K_s-band. The error associated with each point in the SB profile was computed as the RMS scatter in intensity given by the isophotal fitting.

The SB profile of NGC 3115 DW01 is displayed in Fig. 2.34. The location of the background galaxy detected in section 2.6.3 is indicated. The J and H-band profiles show a slight

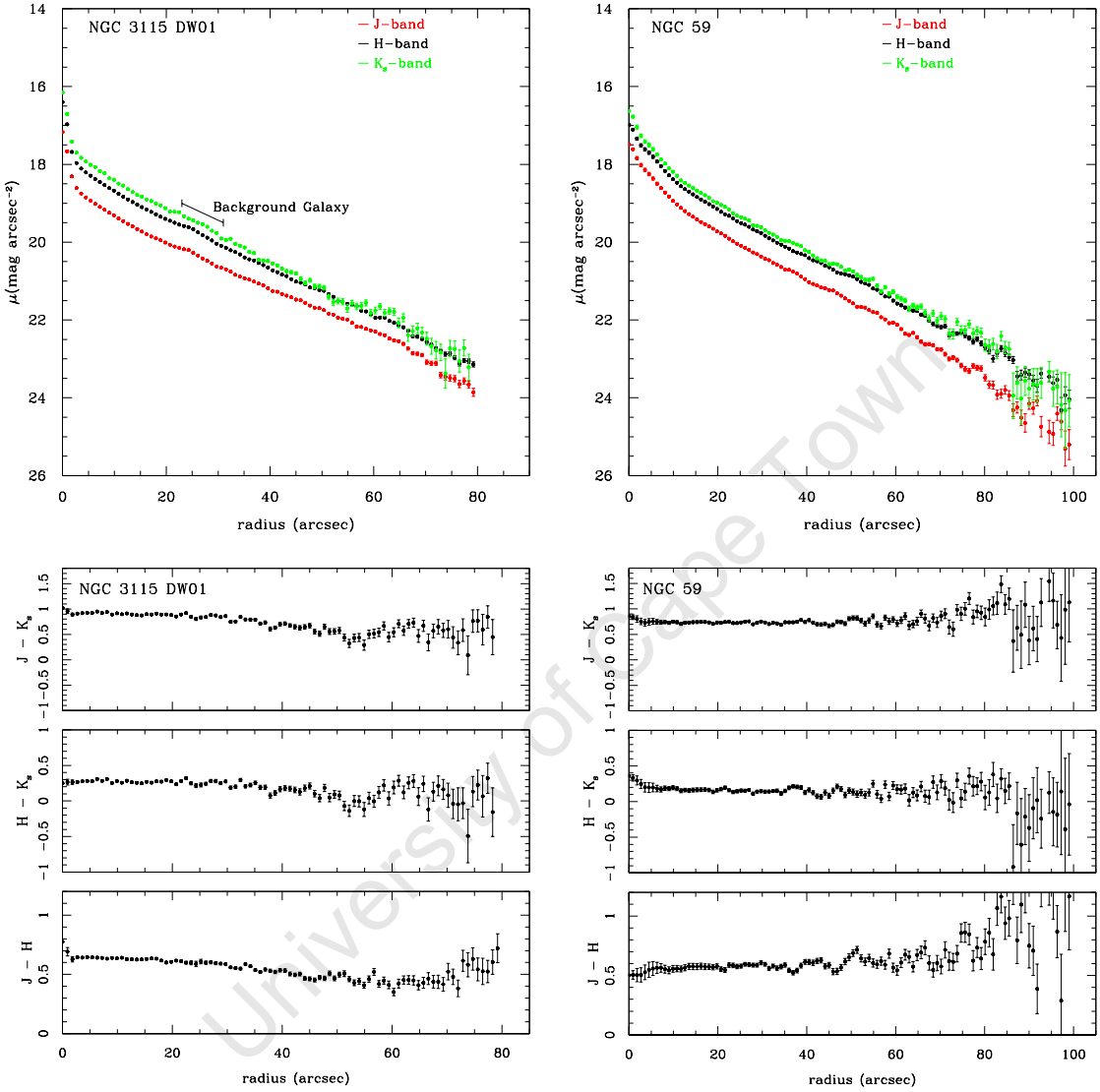

Figure 2.34 The near-infrared surface brightness profiles (*top*) and colour profiles (*bottom*) of the dwarf galaxies: *Left*: NGC 3115 DW01; *right*: NGC 59. The position of the background galaxy seen south-west of the center of NGC 3115 DW01 is shown.

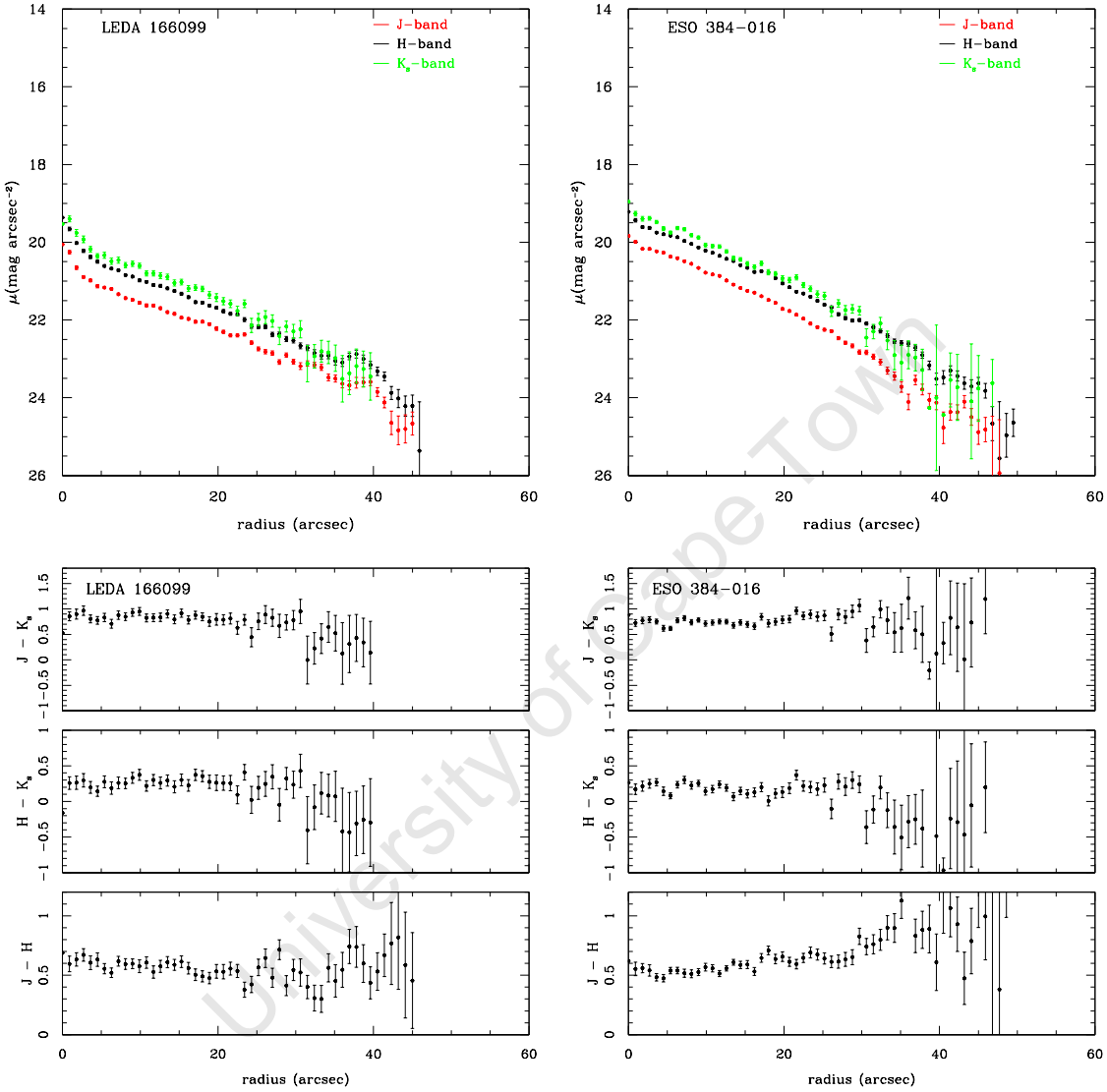

Figure 2.35 The near-infrared surface brightness profiles (*top*) and colour profiles (*bottom*) of the dwarf galaxies: *Left*: LEDA 166099; *right*: ESO 384-016.

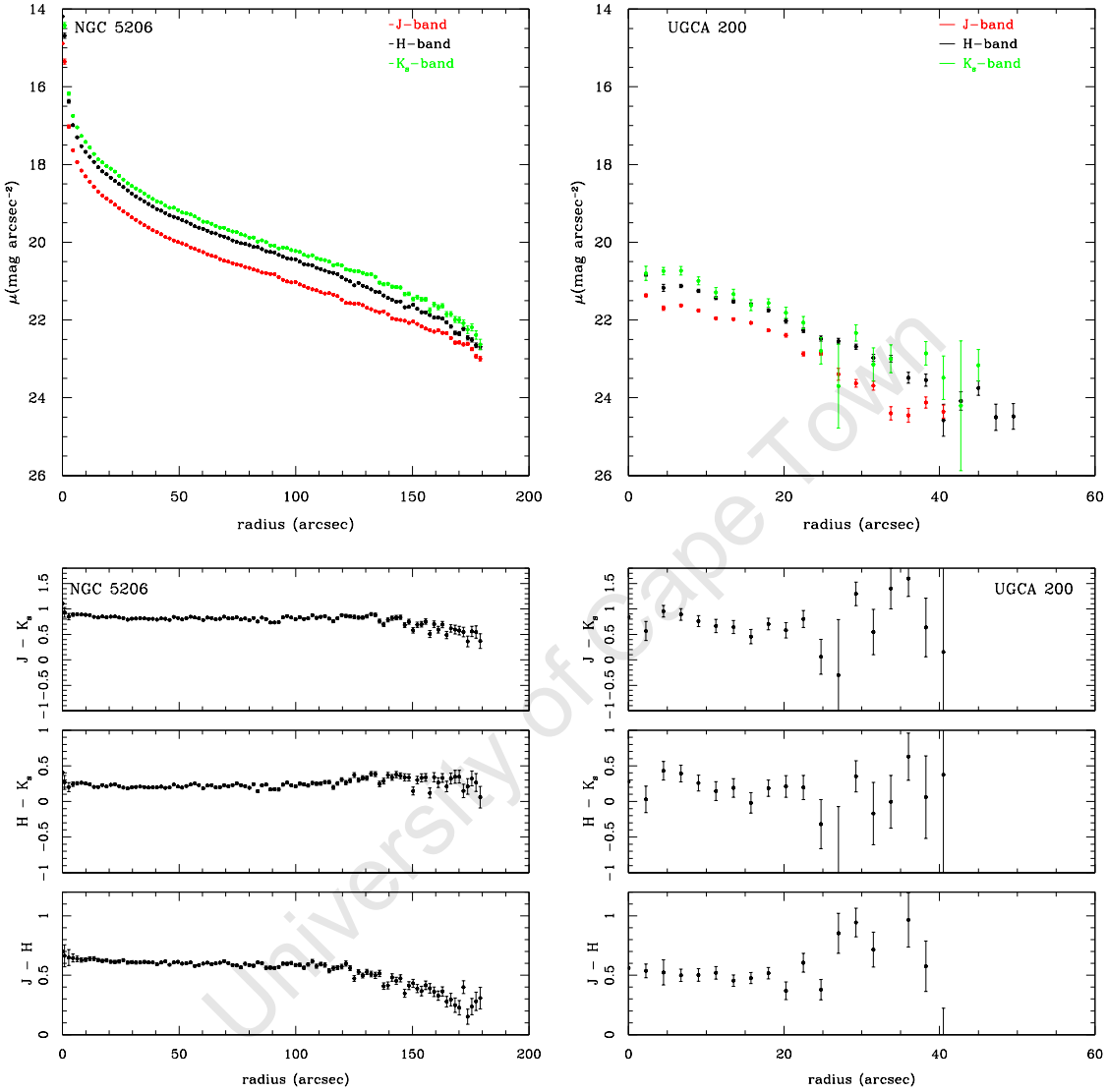

Figure 2.36 The near-infrared surface brightness profiles (*top*) and colour profiles (*bottom*) of the dwarf galaxies: *Left*: NGC 5206; *right*: UGCA 200.

increase in surface brightness at the location of the background galaxy. The background galaxy cannot, however, be easily distinguished in the K_s-band profile of NGC 3115 DW01 as a result of its low surface brightness in this band.

The SB profile of NGC 5206 is shown in Fig. 2.36. This galaxy was found to be quite spatially extended reaching the $\mu_J = 23$mag arcsec^{-2} isophote at a radius of $r{\sim}3'$. The SB profile of the faintest galaxy in the sample, UGCA 200, is also displayed in Fig. 2.36. The central SB component of this galaxy lies $\sim 1\overset{\mathrm{m}}{.}5$ above the NIR detection limit. The SB profile of UGCA 200 could be measured out to a radius of r=40–50″ despite its extremely low intensity levels.

The NIR light profiles of four of the galaxies in the sample can be divided into two components: the nuclear and low SB component. A steep increase in the SB profile of NGC 3115 DW01 and NGC 5206 is observed for the central $r \leq 5''$. The compact nuclei in these galaxies give rise to this central feature in the light profile (see Fig. 2.14). The SB profiles for both NGC 59 and LEDA 166099 indicate a distinct nucleus in these galaxies, whereas ESO 384-016 and UGCA 200 show pure exponential profiles. The central SB components of the galaxies NGC 3115 DW01, NGC 5206 and NGC 59 are significantly brighter (up to 4mag arcsec^{-2}) compared to those typically measured for dwarf galaxies (e.g., Vaduvescu et al. (2005) determine $\mu_{0,JK_s} \gtrsim 18$mag arcsec^{-2} for dIrr galaxies in the LG). The SB profiles of the six galaxies are observed to have the same shape as their optical counterparts shown in Figs. 2.4, 2.6 and 2.8. This suggests that these galaxies have similar morphologies in the NIR compared to the optical.

Vaduvescu et al. (2005) have carried out deep NIR observations of nearby ($D \lesssim 5$Mpc) dIrr galaxies ($-13\overset{\mathrm{m}}{.}5 \lesssim M_{K_s} \lesssim -19\overset{\mathrm{m}}{.}0$) in the J- and K_s-bands. These observations were performed with the 3.6m CFHT and 2.1m OAN-SPM telescopes. Their dwarf galaxies were detected down to the $\mu_{K_s} = 23$mag arcsec^{-2} and $\mu_J = 24$mag arcsec^{-2} isophotes. The dwarf galaxies presented in this chapter are traced to $0\overset{\mathrm{m}}{.}5$–$1\overset{\mathrm{m}}{.}0$ fainter SB levels than the NIR observations by Vaduvescu et al. (2005). These observations show that comparable or even better photometric results for nearby dwarfs were obtained with the smaller aperture IRSF telescope.

2.7.3 Near-Infrared Colour Profiles

The NIR colour profiles were derived by subtracting the SB profiles as function of radius in the respective wavelength bands. The $J - K_s$, $H - K_s$ and $J - H$ colour profiles are shown below each of the galaxy SB profiles in Figs. 2.34–2.36. It is evident that the galaxy colours remain almost constant for surface brightnesses of $\mu_{K_s} \lesssim 22$mag arcsec^{-2}. The noise levels dominate the K_s-band photometry measurements beyond this SB limit. The NIR colour of the extremely low SB galaxy, UGCA 200, shows the largest scatter from the mean colour of up to $0\overset{\mathrm{m}}{.}25$ within the $\mu_{K_s} \lesssim 22$mag arcsec^{-2} limit.

The mean colour of the galaxy was computed by averaging the data points above the $\mu_{K_s} \sim$ 22mag arcsec^{-2} detection limit. These mean NIR colours of the galaxies are listed in Table 2.8. Redder colours of $J - K_s > 0\overset{\mathrm{m}}{.}8$ are detected for the late-type galaxies NGC 3115 DW01 and NGC 5206, as well as for LEDA 166099. Similar NIR colours are measured for the early-type

Table 2.8. Mean colours of six dwarf galaxies.

Galaxy	$J-K_s$ (mag)	$H-K_s$ (mag)	$J-H$ (mag)	$B-R$ (mag)
NGC 3115 DW01	0.89 ± 0.09	0.27 ± 0.10	0.62 ± 0.09	1.38
NGC 59	0.73 ± 0.05	0.16 ± 0.05	0.58 ± 0.04	1.04
LEDA 166099	0.84 ± 0.09	0.27 ± 0.10	0.58 ± 0.07	1.16
ESO 384-016	0.74 ± 0.11	0.17 ± 0.12	0.57 ± 0.09	0.71
NGC 5206	0.82 ± 0.06	0.22 ± 0.07	0.61 ± 0.06	1.22
UGCA 200	0.71 ± 0.17	0.20 ± 0.17	0.50 ± 0.11	1.38

dwarfs NGC 59 and ESO 384-016. The optical observations of Jerjen et al. (2000b) for these two galaxies exhibit similar $B-R$ colour profiles (see Fig. 2.4). They reveal a significant colour gradient in the $B-R$ colour profiles towards the center of both galaxies. Bluer colours are measured in the center of these galaxies. No indication of central star-forming activity can, however, be seen in the NIR colour profiles of NGC 59 and ESO 384-016.

The NIR colours of the six dwarfs were compared to those measured for galaxies in the 2MASS Extended Source Catalogue (Jarrett 2000). The morphologies of the 2MASS galaxies were taken from NED which include (amongst others) elliptical, lenticular, spiral, irregular and dwarf galaxies. Their NIR colours were computed for different galaxy morphologies. Overall, the NIR colours of the six dwarfs are in good agreement with the colours measured for the 2MASS dwarf galaxies. The NIR colour distribution for the 2MASS dwarf galaxies are shown in Fig. 2.37. The dwarf galaxy sample of 2MASS includes dSph and low surface brightness dE types. The range in NIR colour for the six IRSF dwarfs is indicated by the red bins in Fig. 2.37. It can be seen that the IRSF dwarfs occupy those bins showing the largest number density of dwarf galaxies from the 2MASS sample. The IRSF dwarfs therefore exhibit typical NIR colours observed for dwarf galaxies. It should be noted that the flux loss in the 2MASS J- and K_s-bands are approximately equal. The $J-K_s$ colour is thus minimally affected by the underestimation of 2MASS galaxy magnitudes (see section 2.7.4).

The $B-R$ optical colours (Parodi et al. 2002; Lauberts & Valentijn 1989) for each galaxy are also listed in Table 2.8. The galaxies NGC 3115 DW01, LEDA 166099 and NGC 5206 are found to have redder colours of $J-K_s > 0\overset{\mathrm{m}}{.}8$, which is in agreement with the optical observations. These redder colours of $B-R > 1\overset{\mathrm{m}}{.}15$ were measured for the dwarf elliptical galaxies in the sample of Parodi et al. (2002). The optical colours of $B-R \leq 1\overset{\mathrm{m}}{.}04$ derived for the galaxies NGC 59 and ESO 384-016 hence reflect the presence of a younger stellar population. The crude age and metallicity determination by Jerjen et al. (2000a) shows that ESO 384-016 contains an old, metal-poor stellar population. However, faint and diffuse Hα emission has been detected near the galaxy center (Bouchard et al. 2009). These observations suggest that moderate star formation takes place in the central regions of ESO 384-016

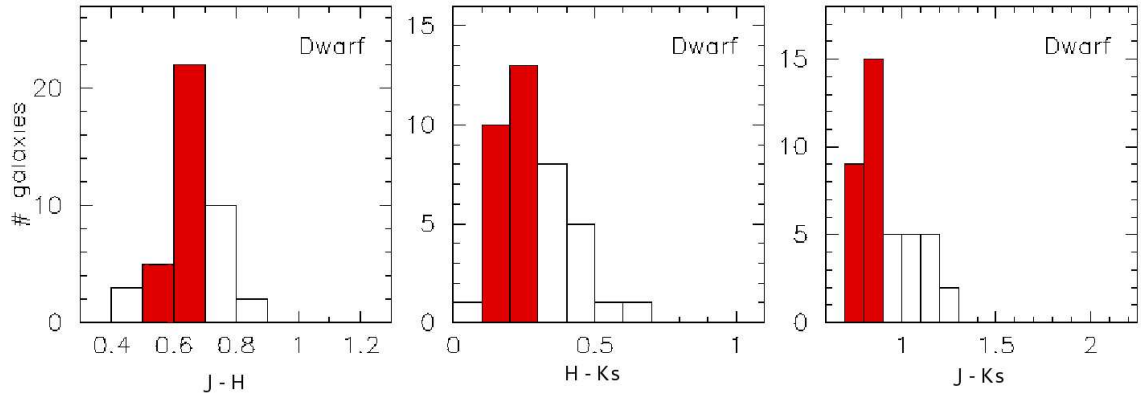

Figure 2.37 NIR colour distribution of dwarf galaxies detected by the 2MASS survey. The NIR colour range of the six IRSF dwarfs (as listed in Table 2.8) is indicated by the red bins.

resulting in the bluer colours. Similarly, the bluer colours for NGC 59 is a direct consequence of the star-forming activity close to the galaxy center (Skillman et al. 2003). A mean colour of $0\overset{\text{m}}{.}7 < J - K_s < 0\overset{\text{m}}{.}8$ is measured for these galaxies as well as for the low SB galaxy UGCA 200.

Double Nuclear Component of NGC 59

An increase of $\sim 0\overset{\text{m}}{.}2$ from the mean $J - K_s$ and $H - K_s$ colour is detected in the central r=5″ of the galaxy NGC 59. The J-, H- and K_s-band contour maps of NGC 59 are shown in Fig. 2.38. These maps clearly reveal the double nuclear component in the center of the galaxy. The star-forming knot (seen south-west of the center) is most luminous in the H-band. The contour maps show that the isophotal fitting fails to distinguish between the two nuclear components. This is mainly due to the high surface brightness levels in the galaxy center. It is not clear which regions of the galaxy are contaminated by light from the starburst. The SB profile of NGC 59 shows no marked change in its slope which could possibly indicate a transition between the star-forming region and low SB component of the galaxy. The colour variations observed in the center of NGC 59 must therefore be influenced by a combination of the light from the galaxy nucleus and the star-forming knot.

Aperture photometry was performed for the individual nuclear components of NGC 59 to avoid degeneracy in their respective colours. The photometric analysis was carried out for the nucleus and the star-forming knot using circular apertures of radius r=1.″6. The aperture radius was chosen to be at least as large as the seeing of the observations. The NIR colours of the two components were derived from these results and are listed in Table 2.9. In addition, the NIR colours of galaxies showing a distinct nucleus in our sample were derived for comparison. The photometric measurements were performed for the nuclei of the galaxies NGC 3115 DW01 and NGC 5206. The aperture radii and corresponding NIR colours of the galaxies are also listed in Table 2.9. The uncertainty in the NIR colours is a combination of the error in the instrumental magnitude given by IRAF, and the uncertainty in the nightly zero-point.

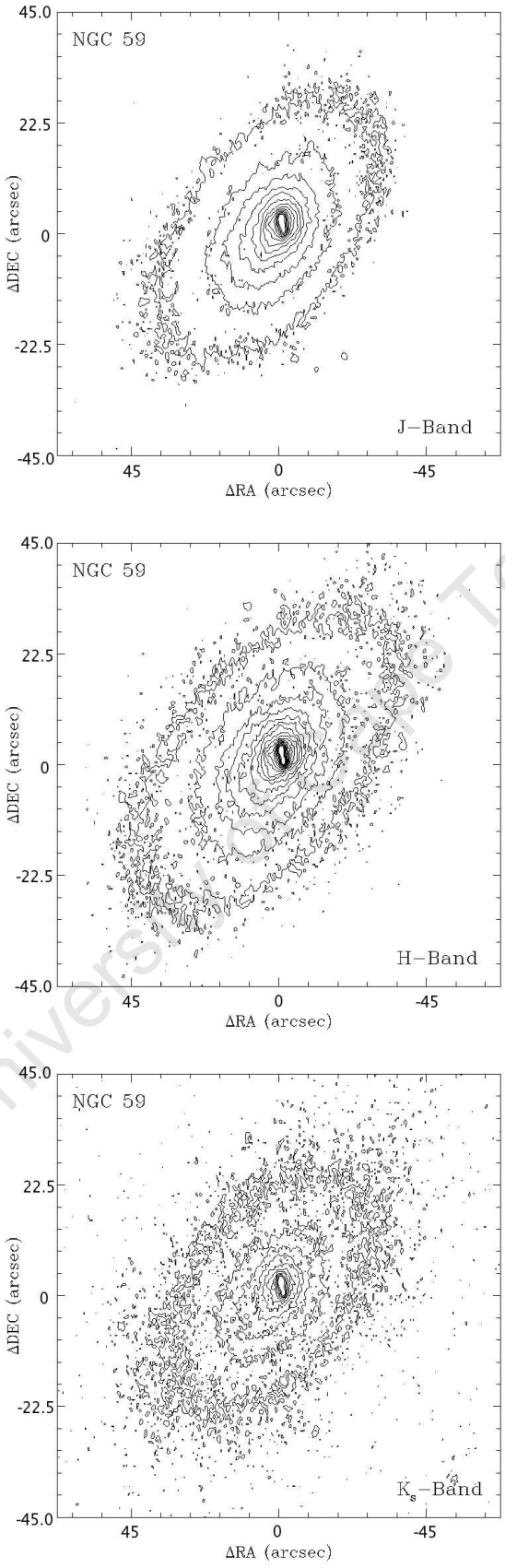

Figure 2.38 The J- (*top*), H- (*middle*) and K_s-band (*bottom*) contour maps of NGC 59. The contours are plotted down to the $\mu_J = 22$mag arcsec^{-2} surface brightness level.

Table 2.9. NIR colour of central features for the brightest sample galaxies.

Galaxy	Component	Aperture (arcsec)	$J-K_s$ (mag)	$H-K_s$ (mag)	$J-H$ (mag)
NGC 59	Nucleus	1.6	0.82 ± 0.04	0.41 ± 0.04	0.41 ± 0.04
	Knot	1.6	0.72 ± 0.04	0.16 ± 0.04	0.56 ± 0.04
NGC 3115 DW01	Nucleus	1.8	0.83 ± 0.06	0.22 ± 0.06	0.61 ± 0.06
NGC 5206	Nucleus	4.1	0.92 ± 0.07	0.27 ± 0.07	0.65 ± 0.06

The NIR colours of the galaxy nuclei resemble that of an evolved stellar population which is expected to have colours in the range $J-K_s \sim 0\overset{\mathrm{m}}{.}9$, $H-K_s \sim 0\overset{\mathrm{m}}{.}3$ and $J-H \sim 0\overset{\mathrm{m}}{.}7$ (Jarrett 2000). The $H-K_s$ and $J-H$ colours for the two nuclear components of NGC 59 differ by up to $\sim 0\overset{\mathrm{m}}{.}3$ from those values measured for galaxy nuclei. The star-forming knot is, however, observed to have very similar NIR colours as the mean values of the galaxy shown in Table 2.8. The seeing and proximity of the two nuclear components makes it difficult to isolate the NIR contribution from each individual source. This introduces a large uncertainty in the magnitude and colour measurements for the two central sources.

The $H-K_s$ and $J-H$ colours of the two nuclear components of NGC 59 are not indicative of an evolved stellar population. It is well known that the nebular emission in young starbursts is relatively strong in the NIR (e.g., Cairós et al. 2003). There are two contributions to the NIR emission in star-forming galaxies such as NGC 59: the underlying stellar component and an ionized gas contribution. The Hα observations of NGC 59 (Skillman et al. 2003) have detected ionized gas in the central $15''$ of this galaxy. The NIR emission of both nuclear components is therefore influenced by the presence of ionized gas. The NIR colours of the two central sources represent a combination of the underlying stellar and ionized gas component of the galaxy. It is suspected that the deviation in the NIR colours of NGC 59 from the values observed for the galaxy nuclei are caused by the ionized gas contribution. The total contribution of the ionized gas to the NIR emission can, however, not be accounted for given the J-, H- and K_s-band images of the galaxy.

Cairós et al. (2003) and Vanzi et al. (2002) have conducted deep NIR observations of blue compact dwarf (BCD) galaxies within the distance range of $D \simeq 10-65$Mpc. They have measured the NIR colours of individual star-forming knots for a sample of four BCDs. The photometry of the individual knots were performed using aperture radii in the range of r=0.8–2.0$''$. These measurements were not corrected for the ionized gas contribution. The NIR colours of the star-forming knots can therefore be directly compared to those values obtained for the nuclear sources of the IRSF dwarfs. The $J-K_s$ versus $J-H$ plot for the BCD star-forming knots are displayed in Fig. 2.39. The NIR colours of the nuclear sources for the three IRSF dwarfs (as listed in Table 2.9) have been added to this colour plot. The two nuclear components of NGC 59 are shown by the red points. The nucleus of NGC 59 shows

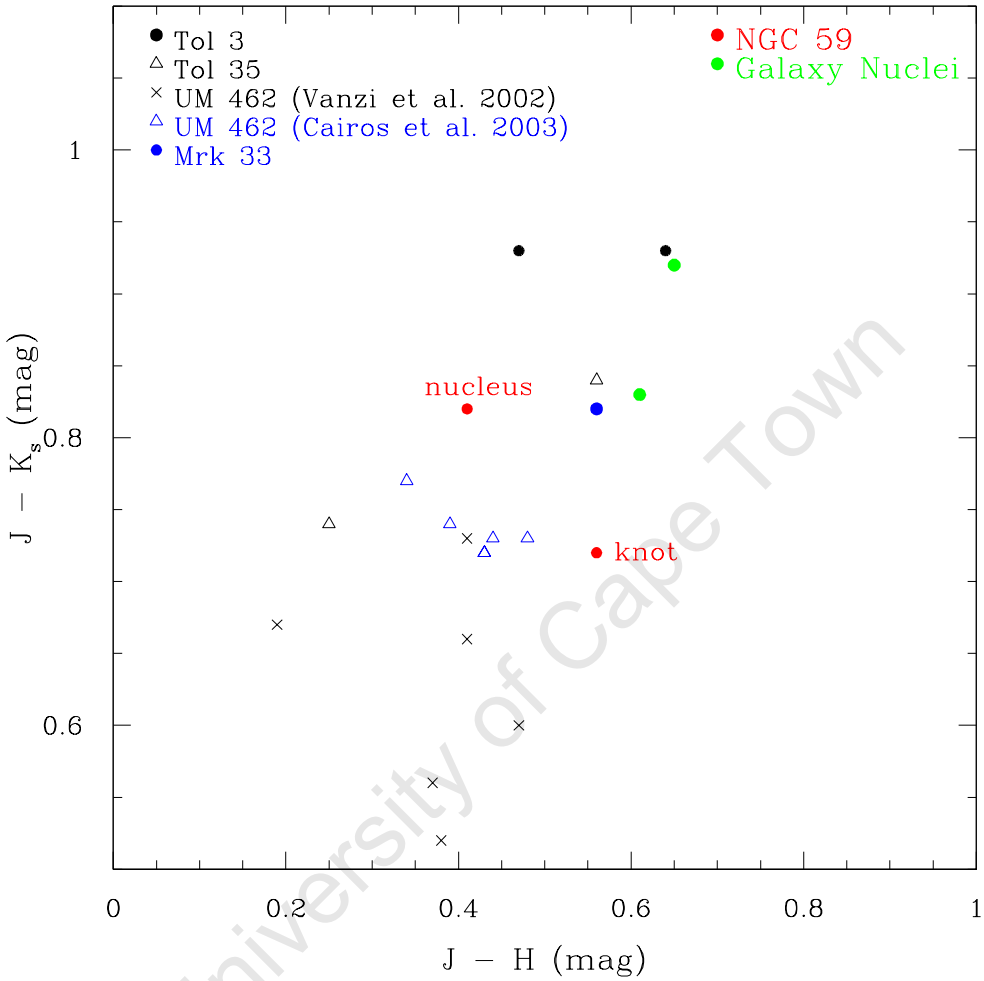

Figure 2.39 $J - K_s$ vs. $J - H$ plot for BCD star-forming knots and nuclear sources of IRSF galaxies. The nucleus and star-forming knot of NGC 59 are shown in red. The nuclei of the galaxies NGC 3115 DW01 and NGC 5206 are indicated by the green points. BCD galaxies from Vanzi et al. (2002) and Cairós et al. (2003) are shown in black and blue, respectively. The names of the BCDs for which the colours of their star-forming knots have been measured are shown at the top (*left*) of the plot.

redder $J-K_s$ colour which allows this component to be more closely grouped with the galaxy nuclei (green points). The secondary component shows bluer $J-K_s$ colours following the distribution of the majority of star-forming knots. This plot supports the initial assumption that the secondary component of NGC 59 is a star-forming knot.

The $J-H$ versus $H-K_s$ plot for the BCD star-forming knots and the IRSF galaxy sources are shown in Fig. 2.40. The two nuclear components of NGC 59 have bluer $J-H$ and $H-K_s$ colours than those measured for the galaxy nuclei. Consequently, the two sources lie well within the range of colours observed for the star-forming knots. The nucleus of NGC 59 is observed to have redder $H-K_s$ colours than its companion. Vanzi et al. (2002) point out a trend of redder $H-K_s$ colour for the brightest star-forming knot in the BCD galaxies. This trend is also observed for NGC 59 where the red $H-K_s$ colour is detected for the nucleus of the galaxy. Vanzi et al. (2002) interpret the decrease in the $H-K_s$ colour as a decrease in the gas fraction going from the brightest star-forming knot. This change in the gas fraction can also be interpreted as an age trend where the brightest knot is the younger component. Following the results for BCDs, the decrease in gas fraction together with the redder $J-H$ colour for the secondary component of NGC 59 implies that this component hosts an older stellar population than that seen in the nucleus. This argument holds if the nucleus has experienced a more recent starburst whose younger stellar population now dominates the NIR emission.

The nucleus of NGC 59 shows a red $H-K_s = 0\overset{\mathrm{m}}{.}4$ colour in contrast to the surrounding $H-K_s$ colour of $\sim 0\overset{\mathrm{m}}{.}2$ for the galaxy. For the case of BCDs, the red $H-K_s$ colour of the brightest knot is a signature of the presence of hot dust since there are no spectral signs of red supergiants (Vanzi et al. 2000). The longslit spectra of NGC 59 presented in Chapter 3 shows that unlike BCDs, the galaxy has a dominant older stellar population. The contribution of the old stellar population to the NIR emission of the nucleus can, however, not be determined with the current observations. The similarity between the NIR colours of the nucleus to those for the brightest knots in the BCDs does suggest a common evolutionary scenario for these sources. The NIR colours of the two central sources of NGC 59 indicate more recent star formation activity for the galaxy nucleus. This is reminiscent of a propagating star formation scenario in which the shock waves from supernovae in the older knot can trigger star formation in the nucleus of NGC 59. Further clues to the nature of the double nuclear component of NGC 59 will be gained in Chapter 3 in which the kinematics and chemical content of the galaxy is measured using the longslit spectroscopic observations.

2.7.4 Total Magnitudes

The galaxies NGC 3115 DW01, NGC 59 and NGC 5206 are listed in the 2MASS All-Sky Extended Source Catalogue[9]. These galaxies are the brightest dwarfs ($B \lesssim 13\overset{\mathrm{m}}{.}4$) in our sample for which NIR imaging and surface photometry measurements are available from 2MASS. A comparison of the IRSF and 2MASS galaxy images is shown in Fig. 2.41. The IRSF images show a striking increase in the spatial resolution and radial extent of the dwarf

[9]The 2MASS Extended Source Catalogue can be accessed online at http://irsa.ipac.caltech.edu/applications/Gator/.

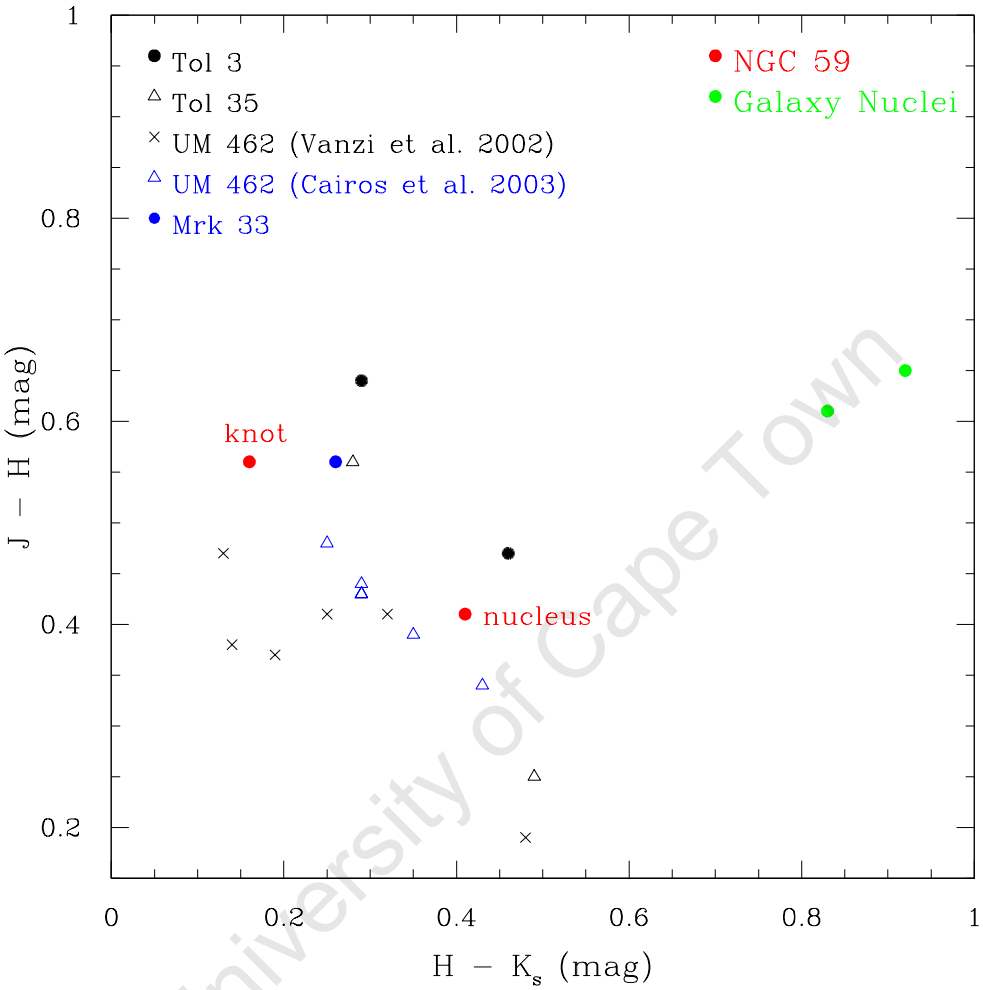

Figure 2.40 $J - H$ vs. $H - K_s$ plot for BCD star-forming knots and nuclear sources of IRSF galaxies. The nucleus and star-forming knot of NGC 59 are shown in red. The nuclei of the galaxies NGC 3115 DW01 and NGC 5206 are indicated by the green points. BCD galaxies from Vanzi et al. (2002) and Cairós et al. (2003) are shown in black and blue, respectively. The names of the BCDs for which the colours of their star-forming knots have been measured are shown at the top (*left*) of the plot.

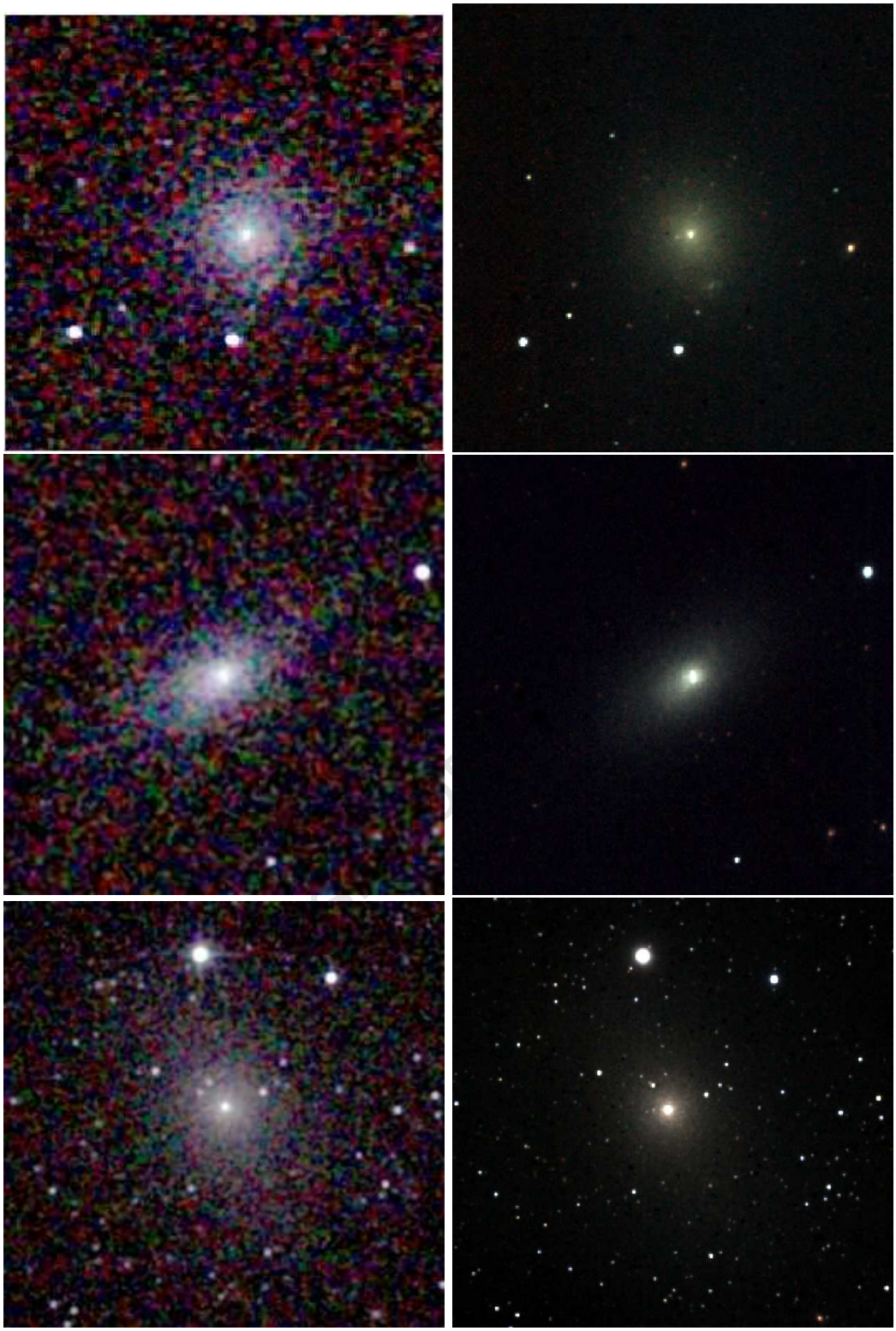

Figure 2.41 JHK_s-colour images of the dwarf galaxies obtained by 2MASS (*left*) and the IRSF (*right*). The three galaxies shown are NGC 3115 DW01 (*top*), NGC 59 (*middle*) and NGC 5206 (*bottom*). The image size of the galaxies NGC 3115 DW01 and NGC 59 is $3\farcm5\times3\farcm5$ while a total FoV of $4\farcm4\times4\farcm4$ is shown for NGC 5206. North is up and East is left.

galaxies compared to the 2MASS images. In particular, the central nucleus can be clearly distinguished from the extended low SB component of the galaxy. It is the four times higher spatial resolution of the IRSF images that allows for a much more detailed study of the structure and morphology of the dwarf galaxies. The NIR photometric properties of the individual galaxy components are measured in section 2.8.

The total apparent magnitude is given by the integrated flux within the detection limit of the galaxy. A growth curve was constructed for each galaxy by integrating the intensity in circular apertures. The apertures were defined at a radius step of $r = \sqrt{ab}$ where a and b are the respective major and minor axis of the galaxy. A plot of the measured intensities as a function of the equivalent radius r gives the integrated light profile of the galaxy. The total apparent magnitude, m_t, corresponds to the asymptotic intensity of the growth curve which is measured down to the background level of the image. A good measure of the background level was found by systematically varying the sky brightness in the image. The growth curve converges asymptotically to a flat background when the correct sky level is achieved.

The total magnitudes (m_t) of the six dwarf galaxies are listed in Table 2.10. The total magnitudes range from $K_s = 8\overset{\mathrm{m}}{.}1$ for NGC 5206 to $K_s = 13\overset{\mathrm{m}}{.}3$ for the faint galaxy UGCA 200. The accuracy of the total magnitudes depends on the data reduction and calibration procedures. The sky subtraction technique described in section 2.4 gives an uncertainty of $\lesssim 0\overset{\mathrm{m}}{.}02$ in the background level for the three wavelength bands. A larger source of uncertainty is introduced by the photometric calibrations of the images (see section 2.5.3). The accuracy in the measured zero points were found to vary from $0\overset{\mathrm{m}}{.}03$ in the J-band to $0\overset{\mathrm{m}}{.}09$ in the K_s-band. The total magnitudes are thus derived with an accuracy of $< 0\overset{\mathrm{m}}{.}1$ given the errors introduced through the reduction and calibration procedures.

The 2MASS total magnitudes of the galaxies NGC 3115 DW01, NGC 59 and NGC 5206 are listed in Table 2.10. These correspond to the extrapolated total magnitudes r_{ext} in the 2MASS Extended Source catalogue. The growth curve of the galaxies was determined by measuring the integrated flux within various elliptical isophotes along the major axis. The total integrated flux of the galaxy was measured down to the background level. The background was estimated by the asymptotic convergence of the growth curve towards a flat sky level. The aperture radii r_t in which the IRSF and 2MASS total magnitudes were measured are listed in Table 2.10. The deep observations of the dwarf galaxies allow for their detection out to larger radii compared to 2MASS. The difference in the IRSF and 2MASS aperture radii varies from Δr_t=10″ (for NGC 59) to Δr_t=66″ (for NGC 5206). The IRSF observations of NGC 5206 shows that this galaxy has an extended low SB component which was not completely detected by 2MASS.

The difference between the IRSF and 2MASS total magnitudes is given by the quantity Δm_t in Table 2.10. This comparison of the magnitudes reveals that 2MASS underestimates the flux of the three galaxies by up to $\lesssim 0\overset{\mathrm{m}}{.}5$. The largest deviation of $J = 0\overset{\mathrm{m}}{.}48$ from the 2MASS total magnitude is observed for the galaxy NGC 5206. The deep IRSF observations reveal the extended low SB component of this galaxy which is not seen in the 2MASS images. The higher SB galaxy NGC 59 shows the least deviation of $\leq 0\overset{\mathrm{m}}{.}05$ from 2MASS magnitudes in all three wavelength bands.

Table 2.10. Total apparent magnitudes of the six dwarf galaxies.

	IRSF					2MASS					
Galaxy	PA (deg)	ϵ	Filter	m_t (mag)	r_t (arcsec)	PA (deg)	ϵ	Filter	m_t (mag)	r_t (arcsec)	Δm_t (mag)
NGC 3115 DW01	6.87	0.14	J	10.70 ± 0.06	90	45	0.32	J	10.99	70.3	-0.29
			H	10.15 ± 0.07				H	10.15		-0.23
			K_s	9.94 ± 0.07				K_s	9.94		-0.11
NGC 59	121.4	0.41	J	10.84 ± 0.03	99	115	0.50	J	10.89	88.8	-0.05
			H	10.24 ± 0.03				H	10.26		-0.02
			K_s	10.07 ± 0.03				K_s	10.10		-0.03
LEDA 166099	125.3	0.34	J	13.72 ± 0.03	45	–	–				
			H	13.18 ± 0.04							
			K_s	12.95 ± 0.04							
ESO 384-016	81.5	0.31	J	13.12 ± 0.05	54	–	–				
			H	12.49 ± 0.07							
			K_s	12.35 ± 0.07							
NGC 5206	23.2	0.35	J	8.91 ± 0.04	180	45	0.16	J	9.39	114.3	-0.48
			H	8.35 ± 0.05				H	8.55		-0.20
			K_s	8.05 ± 0.05				K_s	8.49		-0.44
UGCA 200	-31	0.30	J	13.84 ± 0.06	45	–	–				
			H	13.32 ± 0.07							
			K_s	13.26 ± 0.09							

The deep H-band observations by Kirby et al. (2008) indicate that 2MASS can underestimate the total magnitudes of galaxies by $0\overset{\mathrm{m}}{.}2$ to $2\overset{\mathrm{m}}{.}5$. They also detect a significant loss of flux of up to $0\overset{\mathrm{m}}{.}5$ for some of the most luminous galaxies in their sample. This underestimation of the galaxy fluxes measured for 2MASS galaxies was also identified by Andreon (2002). He shows that the short exposures of 2MASS can result in a loss of the galaxy flux of up to 70%. Overall, the 2MASS survey fails to detect low SB galaxies, a finding observed by both Kirby et al. (2008) and Andreon (2002). The NIR photometric measurements for the low SB galaxies ESO 384-016, LEDA 166099 and UGCA 200 are therefore presented here for the first time. The deep NIR observations emphasize the serious selection biases of the 2MASS galaxy survey.

2.8 Surface Brightness Profile Fitting

A variety of models have been proposed in the literature to fit the SB profiles of galaxies. These include de Vaucouleurs profiles (de Vaucouleurs 1948), pure exponentials (Binggeli & Cameron 1993; Stiavelli et al. 2001), King models (King 1966), Sérsic profiles (Durrell 1997; Stiavelli et al. 2001) and Nuker laws (Rest et al. 2001; Ravindranath et al. 2001; Lauer et al. 2005). The de Vaucouleurs $r^{1/4}$ profile provides a good fit to SB profiles of dE galaxies while a pure exponential was found to describe the large-scale SB profiles of bright ellipticals very well. King profiles are based on specific dynamical models, and provide good fits to globular cluster SB profiles. It is parameterized by the central SB Σ_0, a core radius (where the SB is $\Sigma_0/2$) and tidal radius (where the brightness vanishes). An increase in the imaging resolution led to the introduction of the Nuker law which allows for a separate fit to the inner and outer SB profile of the galaxy. Basically, the Nuker law composes of a double power-law which is frequently used to model the SB profiles of early-type galaxies exhibiting a nuclear component (see below).

Generally, the standard Sérsic model (Sérsic 1968) provides an accurate description of the global SB profile for most galaxies. The Sérsic model has the form,

$$I(r) = I_0 \exp[-b_n(r/r_e)^{1/n}] \,, \tag{2.12}$$

where $I(r)$ is the SB (in intensity units) at radius r and I_0 is the central intensity. The parameter n controls the overall shape of the Sérsic profile which includes both the exponential ($n = 1$) and de Vaucouleurs ($n = 4$) functional forms. The parameter b_n is directly related to the shape parameter n and can be approximated by $b_n \simeq 1.9992n - 0.3721$ for $1 \lesssim n \lesssim 10$ (Caon et al. 1993). Given this definition of b_n, r_e is the effective radius of the galaxy which contains roughly half of the integrated light of the model. A single Sérsic model has been used to describe the SB profiles of a range of galaxy morphologies from giants (ellipticals and bulges) to dwarfs (e.g., Durrell 1997; Jerjen et al. 2000b; Kirby et al. 2008). These results contribute to the mounting evidence that the fundamental dichotomy between giant and dE galaxies (Kormendy 1985) may not be true (see e.g., Jerjen & Binggeli 1997; Graham & Guzmán 2003).

The availability of higher-resolution imaging (particularly with space-based telescopes such as HST) allows for the central structure of galaxies to be probed. Lauer et al. (2005),

Byun et al. (1996) and Faber et al. (1997) presented a detailed study of the central regions of early-type galaxies. They distinguished these galaxies into two classes: "power-law" galaxies, where the central SB increases into the limiting resolution with a steep power-law profile; and "core" galaxies, where the luminosity profile turns over at a fairly sharp "break" radius into a shallower power law. Given the higher-resolution of galaxy images, significant deviations from a Sérsic model can be detected in the central regions of the galaxy SB profile. These authors used the Nuker model to fit the central SB profiles of early-type galaxies. A Nuker model is composed of a double power-law with an adjustable transition region. The Nuker model fails, however, to provide a good fit to the outer parts of the galaxy SB profile which is generally well fitted by the Sérsic function. A detailed discussion of some of the systematic problems and ambiguities that can arise when using a double power-law model to fit galaxy light profiles was given by Trujillo et al. (2004). They suggest a new hypothesis and a new model that might resolve some of these problems. The "core-Sérsic" model was proposed by Graham et al. (2003) and Trujillo et al. (2004) as a better fit to the entire SB profile of a galaxy. This model consists of a power-law component in the inner region of the galaxy which breaks to a traditional Sérsic profile beyond some characteristic radius. This model has been extensively used by Côté et al. (2007) who detect a systematic progression from central light deficit (for galaxies having $M_B \lesssim -20\overset{\mathrm{m}}{.}0$) to excess ($-19\overset{\mathrm{m}}{.}5 \lesssim M_B \lesssim -15\overset{\mathrm{m}}{.}0$) along the luminosity function for their large sample of 143 early-type galaxies in the Virgo and Fornax Clusters. Côté et al. (2006) and Ferrarese et al. (2006) found that many galaxies in their sample (consisting of early-type galaxies from the Virgo Cluster) have compact sources at their centers. An additional King model was used to determine the properties of the nucleus of these galaxies while the global SB profile was adequately represented by a Sérsic or core-Sérsic model.

Deep B- and R-band imaging is available for five galaxies in our sample. The photometry of NGC 59 and ESO 384-016 were carried out by Jerjen et al. (2000b) while the optical properties of the galaxies NGC 3115 DW01, LEDA 166099 and UGCA 200 were measured by Parodi et al. (2002). The B- and R-band SB profiles of the galaxies were determined in both studies (see Figs. 2.4 and 2.6). A single Sérsic fit was used by Jerjen et al. (2000b) to derive the structural parameters of NGC 59 and ESO 384-016. These fits were found to give a good description of the overall SB profile of the galaxies. The structural parameters of NGC 3115 DW01, LEDA 166099 and UGCA 200 were derived by fitting an exponential function to their optical SB profiles. This functional form provides an excellent fit to the data at larger radii where the underlying stellar disk is believed to set the geometry of the galaxy.

The near-infrared SB profiles derived in section 2.7.2 reveal the intricate photometric structure of the dwarf galaxies. A distinct nuclear component is seen in the SB profiles of most galaxies in the sample. An improved understanding of the nature of the galaxy nucleus can be achieved by modeling the nuclear component of the SB profile separately from the galaxy disk. The SB profile of galaxies that show a nuclear component were therefore modeled using two functional forms: an exponential law for the underlying disk component of the galaxy and a Sérsic function to derive the nuclear properties. Based on the optical results, the exponential fit to the galaxy disk is known to provide an excellent fit to the outer

component of dE galaxies. The nuclei of galaxies in our sample are represented on kiloparsec scales which can accurately be fitted with a Sérsic model.

In this section, the NIR structural parameters will be derived for the individual galaxies in the sample. The structural parameters will be measured using two independent methods: (1) A one-dimensional (1D) function fitted to the galaxy SB profiles shown in Figs. 2.34–2.36; (2) A two-dimensional (2D) intensity distribution of the galaxy using the profile modeling algorithm GALFIT. The 2D modeling provides a better fit to the intensity distribution when high-enough spatial resolution is achieved for the galaxy to be decomposed into different components. In the 1D SB profile, the nuclear and disk component appear to merge smoothly which results in the degeneracy of the fitted parameters. This degeneracy between the two components is broken by the 2D modeling which allows the ellipticity to vary as a function of galaxy radius.

2.8.1 One-dimensional Fitting of SB Profiles

The 1D photometric decomposition was performed on the galaxy SB profiles derived in section 2.7.2. The analytic fits were carried out using the NFIT1D task in IRAF which employs a χ^2-minimization technique to find the best-fit solution. The galaxy SB profiles were fitted with the combination of a Sérsic and exponential function. The Sérsic law

$$I(r) = I_0 \exp[-(r/r_s)^{1/n}], \tag{2.13}$$

was adopted to describe the surface brightness of the nuclear component of the galaxy. The free parameters are the central SB μ_s (or central intensity I_0), scale length r_s, and shape parameter n. The disk component of the galaxy was assumed to follow an exponential law which is parameterized by the central SB μ_0 and scale length r_0 of the disk. An initial guess was specified for these free parameters after which the χ^2-minimization algorithm iterates to the best-fitting solution for the SB distribution of the galaxy.

The fits to the galaxy SB profiles in the J-, H- and K_s-bands are shown in Figs. 2.42–2.44. The galaxies NGC 3115 DW01, NGC 59, LEDA 166099 and NGC 5206 are best described by the sum of a Sérsic and exponential function. These are the galaxies in the sample showing a distinct nucleus. The transition between the nucleus and underlying low SB component can be seen as a definite change in the slope of the SB distribution. This transition, distinguishing the nuclear and low SB component of the galaxy, was observed to be greater than the seeing of the images. The combination of a Sérsic and exponential function gives a smooth transition between these two components. A single function was fitted to the SB profiles of galaxies ESO 384-016 and UGCA 200. The Sérsic law was found to best describe the gradual increase in the SB profile towards the center of the galaxy.

The residuals from the analytic fits are plotted as a function radius in the bottom panels of Figs. 2.42–2.44. A deviation of $< 0\overset{\mathrm{m}}{.}4$ from the observed profile is measured down to the ~ 23.5mag arcsec^{-2} isophote in the J- and H-bands. The same amount of scatter is observed in the K_s-band out to a magnitude limit of ~ 22mag arcsec^{-2}. Good agreement between the analytic fits and observed profiles is thus obtained out to the detection limit of the galaxies in all three wavelength bands.

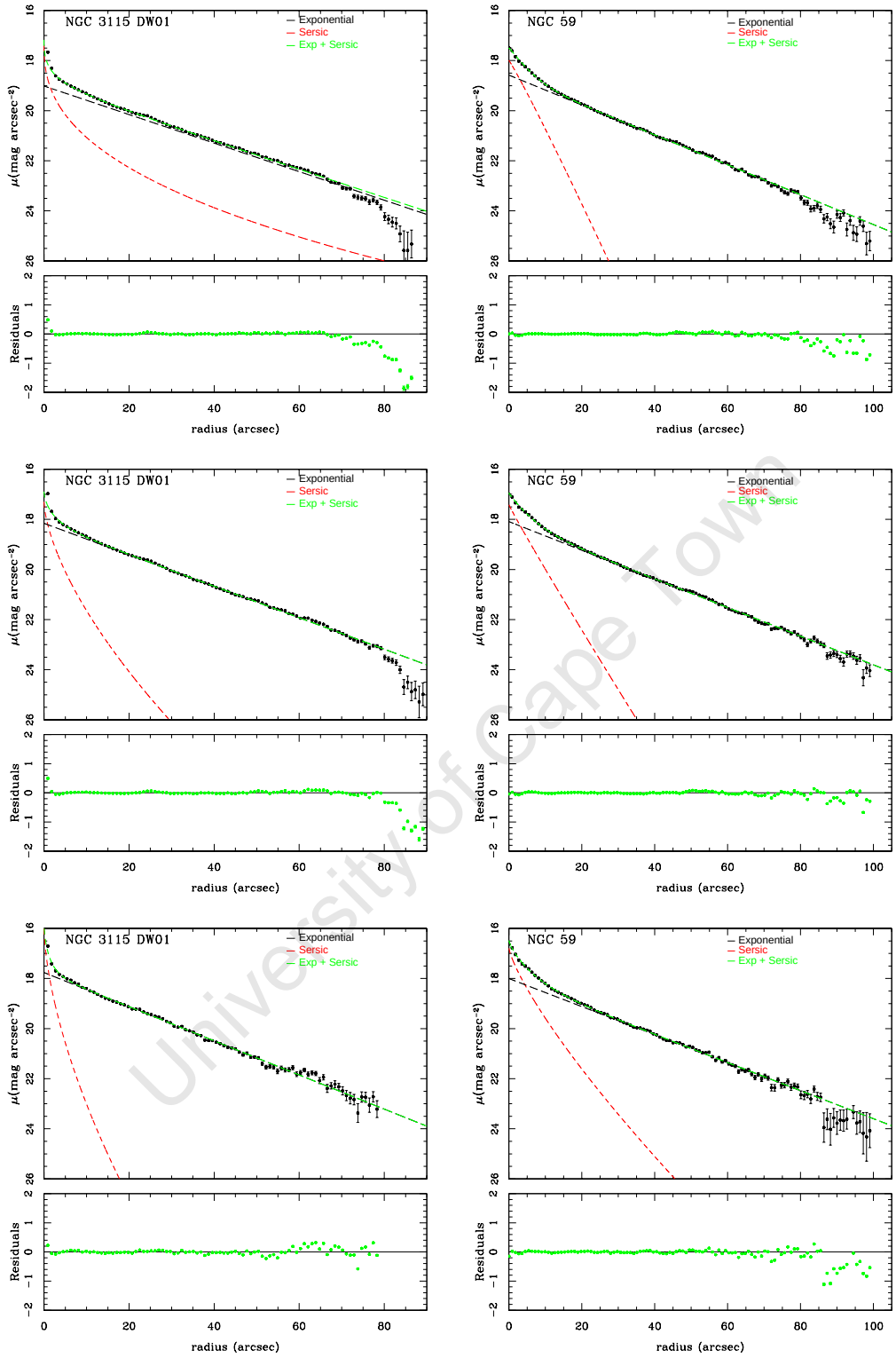

Figure 2.42 One-dimensional fits to the surface brightness profiles of NGC 3115 DW01 (*left*) and NGC 59 (*right*). The function fits in the J- (*top*), H- (*middle*) and K_s-bands (*bottom*) are shown. The dashed lines represents the Sérsic fit (red), exponential fit (black) and the combination of these two function fits (green). The residuals of the combined exponential and Sérsic fits from the measured surface brightness profile is shown in the inset below each figure.

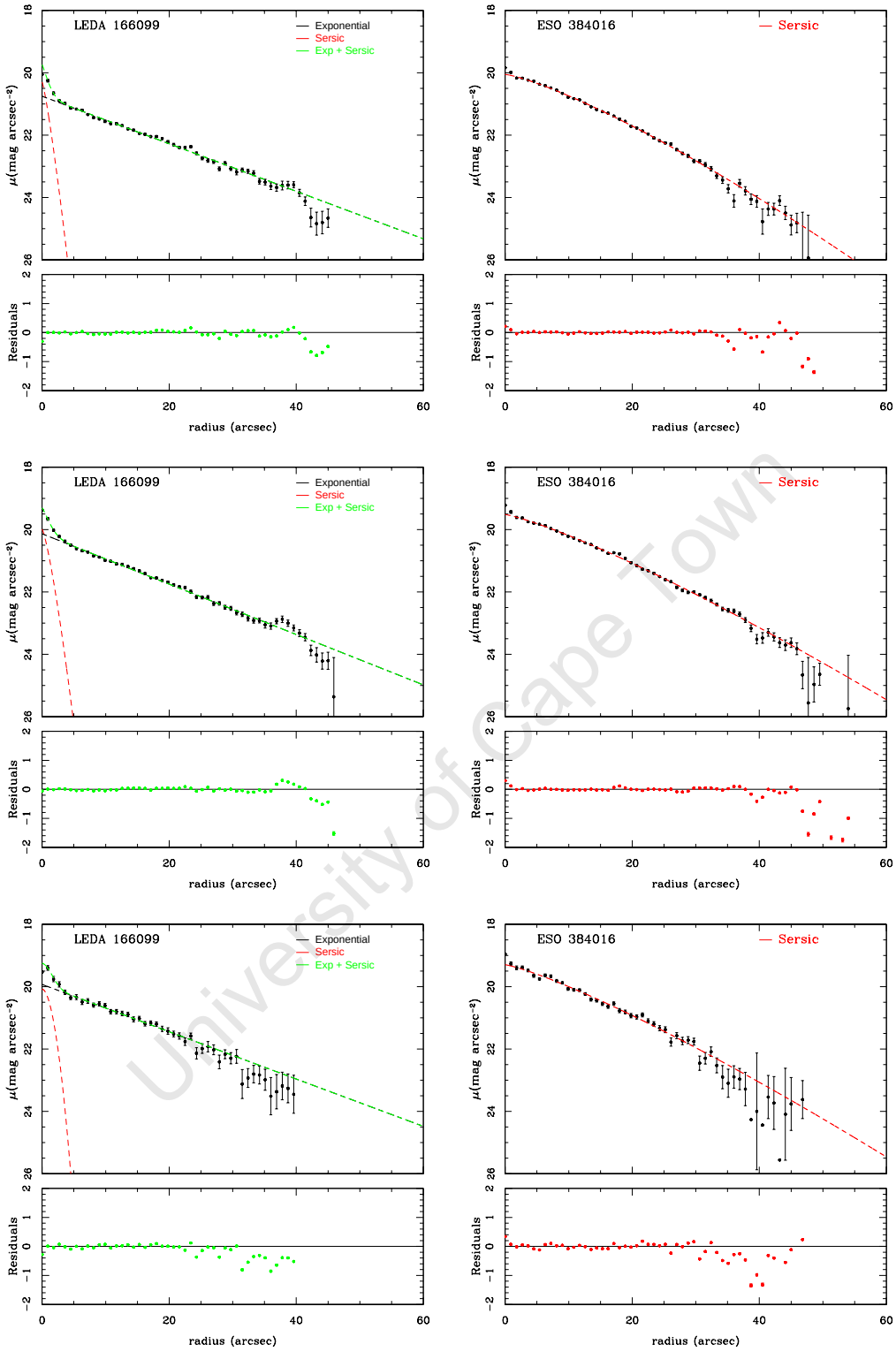

Figure 2.43 One-dimensional fits to the surface brightness profiles of LEDA 166099 (*left*) and ESO 384016 (*right*). The function fits in the J- (*top*), H- (*middle*) and K_s-bands (*bottom*) are shown. The dashed lines represents the Sérsic fit (red), exponential fit (black) and the combination of these two function fits (green). The residuals of the combined exponential and Sérsic fits from the measured surface brightness profile is shown in the inset below each figure.

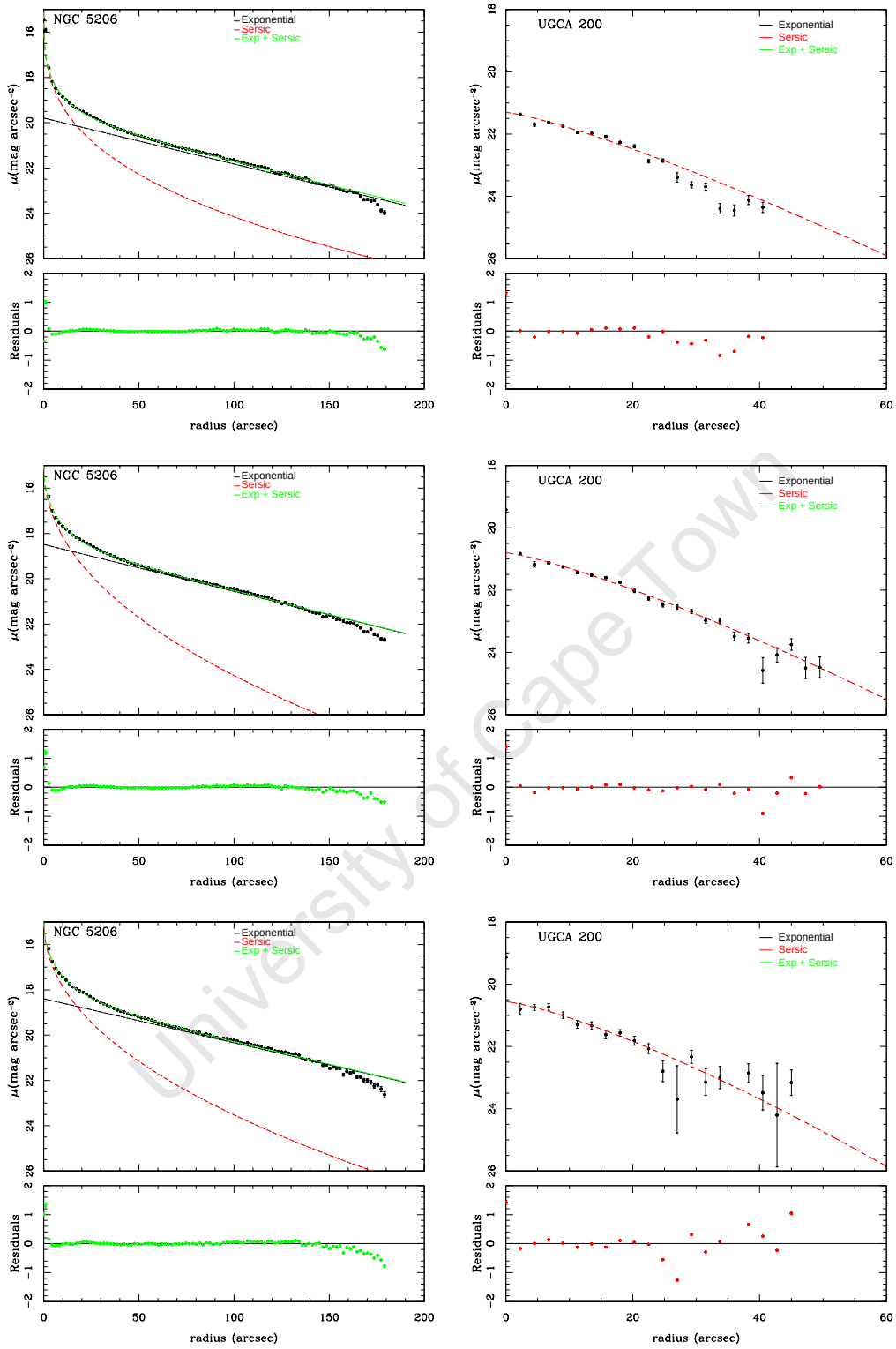

Figure 2.44 One-dimensional fits to the surface brightness profiles of NGC 5206 (*left*) and UGCA 200 (*right*). The function fits in the J- (*top*), H- (*middle*) and K_s-bands (*bottom*) are shown. The dashed lines represents the Sérsic fit (red), exponential fit (black) and the combination of these two function fits (green). The residuals of the combined exponential and Sérsic fits from the measured surface brightness profile is shown in the inset below each figure.

Table 2.11. Structural parameters of dwarf galaxies from one-dimensional fitting to measured surface brightness profile.

Galaxy	Filter	PA (deg)	ϵ	μ_s (mag arcsec^{-2})	r_s (arcsec)	n (mag)	μ_0 (mag arcsec^{-2})	r_0 (arcsec)	m_t
NGC 3115 DW01	J	7.1 ± 3.1	0.12 ± 0.01	17.38 ± 0.96	0.50 ± 0.34	2.45	19.02 ± 0.24	19.06 ± 1.85	10.70
	H	7.1 ± 2.5	0.14 ± 0.01	17.30 ± 0.61	1.15 ± 1.45	1.56	18.16 ± 0.07	17.29 ± 0.45	10.15
	K_s	6.4 ± 6.5	0.15 ± 0.03	15.96 ± 0.90	0.48 ± 0.93	1.63	17.76 ± 0.07	15.93 ± 0.61	9.94
NGC 59	J	121.4 ± 0.8	0.41 ± 0.01	17.99 ± 0.87	4.18 ± 2.76	0.94	18.58 ± 0.14	18.20 ± 0.52	10.84
	H	121.6 ± 0.8	0.42 ± 0.01	17.42 ± 0.38	4.07 ± 1.27	1.04	18.09 ± 0.10	18.99 ± 0.44	10.24
	K_s	121.2 ± 1.9	0.41 ± 0.02	16.79 ± 0.31	3.00 ± 0.95	1.27	18.00 ± 0.13	19.40 ± 0.45	10.07
LEDA 166099	J	125.3 ± 4.8	0.34 ± 0.04	20.30 ± 0.74	1.03 ± 0.60	0.82	20.75 ± 0.05	14.24 ± 0.47	13.72
	H			20.00 ± 1.03	1.30 ± 0.72	0.77	20.14 ± 0.04	13.44 ± 0.30	13.18
	K_s			20.08 ± 0.77	1.85 ± 0.57	0.53	19.93 ± 0.03	14.31 ± 0.23	12.95
ESO 384016	J	81.5 ± 4.9	0.29 ± 0.04	20.05 ± 0.13	14.33 ± 1.39	0.79	–	–	13.12
	H	81.6 ± 2.5	0.32 ± 0.02	19.52 ± 0.05	14.82 ± 0.56	0.82	–	–	12.49
	K_s	81.5	0.31	19.30 ± 0.14	14.32 ± 1.67	0.83	–	–	12.35
NGC 5206	J	22.9 ± 1.0	0.36 ± 0.01	15.10 ± 0.54	0.18 ± 0.34	2.99	19.79 ± 0.37	53.46 ± 3.62	9.53
	H	23.8 ± 0.8	0.36 ± 0.01	14.92 ± 0.34	0.94 ± 0.37	2.17	18.48 ± 0.39	52.41 ± 3.31	8.35
	K_s	22.9 ± 2.0	0.32 ± 0.02	14.84 ± 0.58	1.08 ± 0.80	2.18	18.39 ± 0.52	55.85 ± 7.31	8.05
UGCA 200	J	-31.0	0.30	21.31 ± 0.45	18.70 ± 5.82	0.81	–	–	13.84
	H			20.80 ± 0.11	18.68 ± 2.17	0.80	–	–	13.32
	K_s			20.56 ± 0.54	17.67 ± 6.98	0.77	–	–	13.26

The structural parameters given by the analytic fits to the SB profiles are listed in Table 2.11. The galaxies NGC 3115 DW01 and NGC 5206 were found to have a shape parameter in the range of $1.5 < n < 3.0$. The large value of n in these galaxies reflects the steep increase in the SB profile near its center. These galaxies have a scale length of r_s<1.″2 in the three wavelength bands which is comparable to the Gaussian FWHM of the observations. The 1D analytic functions are a direct fit to the SB profiles without any convolution with the PSF. For galaxies containing a nuclear component, this property can lead to a scale length which is smaller than the seeing of the observations. The scale lengths of NGC 3115 DW01 and NGC 5206 can thus not be interpreted physically. It is also worth noting that the structure parameter n for the nuclear component of the galaxy can vary up to $n \sim 0.9$ in the three wavelength bands. The central SB of these galaxies are measured $2 - 3$mag brighter than the underlying low SB component of the galaxy. This provides some evidence of the galaxies NGC 3115 DW01 and NGC 5206 harbouring compact nuclei at their centers.

The shape parameter n for the remaining galaxies in the sample are in the range $0.7 < n < 1.5$. These values are in the expected range measured for dwarf galaxies in the optical (e.g., Jerjen et al. 2000b; Stiavelli et al. 2001). Kirby et al. (2008) have measured the structural parameters of 8 dwarf galaxies in their sample. A Sérsic law was fitted to the H-band SB profiles of the galaxies. The best fit to the SB profiles have shape parameter in the range of $n \sim 0.5 - 1.8$ in good agreement with our measured values.

2.8.2 Two-dimensional Photometric Decomposition

The light distribution of the galaxies was modeled using the two-dimensional image decomposition program GALFIT. The GALFIT algorithm can be used to fit one or more analytic functions to the light profile of the galaxy. The algorithm implements a χ^2-minimization technique in determining the best-fit solution. Maximum flexibility of the fitting process is achieved by allowing multiple functions to be fit simultaneously to the light profile. The number of free parameters associated with each function can be conveniently adjusted to give a better fit. The free parameters are adjusted simultaneously to minimize the χ^2 residual between the galaxy image and model.

The light profile of the galaxy is measured using elliptical isophotes defined along the radial distance $r(x, y)$:

$$r = \left(|x - x_0|^{c+2} + \left| \frac{y - y_0}{q} \right|^{c+2} \right)^{\frac{1}{c+2}}, \tag{2.14}$$

where (x_0, y_0) are the central pixel coordinates of the galaxy. The major to minor axis ratio is given by q. The parameter c controls the diskiness/boxiness of the elliptical isophotes: $c = 0$ is a pure ellipse; isophotes become boxy (rectangular) for $c > 0$; disky or diamond-like isophotes are observed for $c < 0$. The radial distance r was oriented parallel to the major axis of the galaxy using the position angle parameter PA. The elliptical isophotes are characterized by five free parameters: x_0, y_0, q, c and PA. The central coordinates (x_0, y_0) of the galaxies obtained in section 2.7.1 were used during the fitting process. All other parameters were allowed to vary freely with radial distance.

The star formation knot identified in the center of NGC 59 (see section 2.7.3) was masked out before running the 2D fitting algorithm. The masking was carried out with the IMEDIT task in IRAF. The starburst component was masked using an aperture size of $2''$. This component was replaced with light from neighbouring pixels in the immediate vicinity of the galaxy nucleus.

Following the 1D fitting procedure, dwarf galaxies possessing a nuclear component were fitted with the combination of a Sérsic and exponential function. The light profile of ESO 384-016 was however fitted with a single Sérsic function. The diffuse galaxy, UGCA 200, was not detected by GALFIT due to its low S/N levels. The light profile models were convolved with a Gaussian PSF to account for atmospheric and optical effects of the telescope. Table 2.12 lists the various fits and corresponding parameters used in modeling the light profile of the galaxies. The GALFIT output parameters include the total integrated magnitude, m_t, which is a measure of the galaxy flux during the fitting process. The goodness of fit parameter, χ^2_ν, is given as:

$$\chi^2_\nu = \frac{1}{N_{\rm dof}} \sum_{x=1}^{nx} \sum_{y=1}^{ny} \frac{({\rm flux}_{x,y} - {\rm model}_{x,y})^2}{\sigma^2_{x,y}} \ , \tag{2.15}$$

where $N_{\rm dof}$ is the number of degrees of freedom in the fit, nx and ny are the image dimensions; and $\rm flux_{x,y}$ is the image flux at the pixel (x, y). The galaxy model,

$${\rm model}_{x,y} = \sum_{\nu=1}^{nf} f_{\nu,x,y}(\alpha_1, ..., \alpha_n) \tag{2.16}$$

is the sum of nf functions $f_{\nu,x,y}(\alpha_1, ..., \alpha_n)$, where $(\alpha_1, ..., \alpha_n)$ are the two-dimensional model parameters. The uncertainty as a function of pixel position $\sigma_{x,y}$ is the Poisson error at each pixel which is generated by the gain and readnoise of the galaxy image. Table 2.12 shows that the structural parameters for the galaxies are derived with $\chi^2_\nu < 1$ using the GALFIT software.

The light profile of NGC 5206 was modeled using three functional fits. An additional Sérsic fit was required to model the bulge component of this galaxy. The H-band residual image (galaxy–model) of the 2D galaxy fits are shown in Figs. 2.45–2.46. The Sérsic fits to the nuclear component of the galaxies NGC 5206 and NGC 3115 DW01 gives a shape parameter of $n > 4$. The point-like nuclei in the center of these galaxies are almost completely removed by this steep inner profile. Trujillo et al. (2001) proposed that larger n for galaxy bulges corresponds to a higher central light concentration. A correlation between light concentration and the mass of a central supermassive BH was found by Graham et al. (2001). They measure a shape parameter of $1 \lesssim n \lesssim 11$ for the bulge component of a sample of elliptical and spiral galaxies having reliable BH mass estimates. A shape parameter of $n \sim 4$ would correspond typically to a central BH mass of $M_{\rm BH} \simeq (5.1 \pm 0.2) \times 10^7\,{\rm M}_\odot$. Extrapolating the relation between the central light concentration and BH mass to dwarf galaxies, the large n values for NGC 3115 DW01, NGC 5206 and possibly LEDA 166099 are an indication of a massive nuclear component making these galaxies likely candidates for hosting a central BH. However, the large BH masses inferred from the relation of Graham et al. (2001) remains questionable for the dwarf galaxies. The extended disk component of the galaxies NGC 3115 DW01,

Table 2.12. Structural parameters of dwarf galaxies using the two-dimensional photometric decomposition software GALFIT.

Galaxy	Filter	Function	m_t (mag)	$r_{s,0}$ (arcsec)	n	q	PA (deg)	c	χ^2_ν
NGC 3115 DW01	J	Sérsic	14.68	3.92	4.35	0.94	-67.38	-0.15	0.02
		Exp	10.74	17.12	–	0.83	4.60	0.09	
	H	Sérsic	14.04	3.67	5.60	1.00	89.04	0.74	0.05
		Exp	10.18	16.46	–	0.85	10.05	-0.09	
	K_s	Sérsic	13.14	17.00	9.82	0.85	-68.57	-0.28	0.18
		Exp	9.96	16.10	–	0.86	9.85	-0.23	
NGC 59	J	Sérsic	13.69	4.91	1.17	0.91	-66.15	0.32	0.02
		Exp	10.86	18.25	–	0.58	-59.00	0.01	
	H	Sérsic	12.54	7.71	1.52	0.92	-67.86	0.49	0.10
		Exp	10.33	20.58	–	0.51	-57.38	0.01	
	K_s	Sérsic	13.34	7.30	1.80	0.99	-58.75	0.16	0.13
		Exp	11.17	19.63	–	0.52	-57.09	0.17	
LEDA 166099	J	Sérsic	17.82	5.00	4.21	0.82	-75.36	-1.20	0.17
		Exp	13.35	13.84	–	0.70	-40.98	1.93	
	H	Sérsic	17.41	6.93	2.41	0.99	-55.94	-1.65	0.75
		Exp	12.84	13.07	–	0.73	-42.02	1.35	
	K_s	Sérsic	18.24	1.26	0.07	0.62	-38.22	-1.00	0.42
		Exp	12.66	11.08	–	0.80	-37.98	1.19	
ESO 384016	J	Sérsic	13.06	16.11	0.77	0.71	83.62	0.48	0.02
	H	Sérsic	12.47	16.77	0.78	0.74	81.85	0.29	0.05
	K_s	Sérsic	12.32	15.99	0.75	0.78	80.58	-0.01	0.16
NGC 5206	J	Sérsic	12.19	4.50	5.54	0.89	4.92	-0.15	0.07
		Sérsic	12.13	13.30	0.55	0.89	-65.66	-0.03	
		Exp	9.02	44.98	–	0.69	24.34	-0.16	
	H	Sérsic	11.52	4.52	5.90	0.95	16.05	-0.15	0.25
		Sérsic	11.48	12.88	0.56	0.92	-55.62	-0.05	
		Exp	8.39	44.51	–	0.69	26.45	-0.10	
	K_s	Sérsic	11.32	4.48	7.57	0.93	56.77	0.25	0.26
		Sérsic	10.96	12.50	0.75	0.93	-25.57	0.04	
		Exp	8.08	47.93	–	0.71	27.42	-0.23	

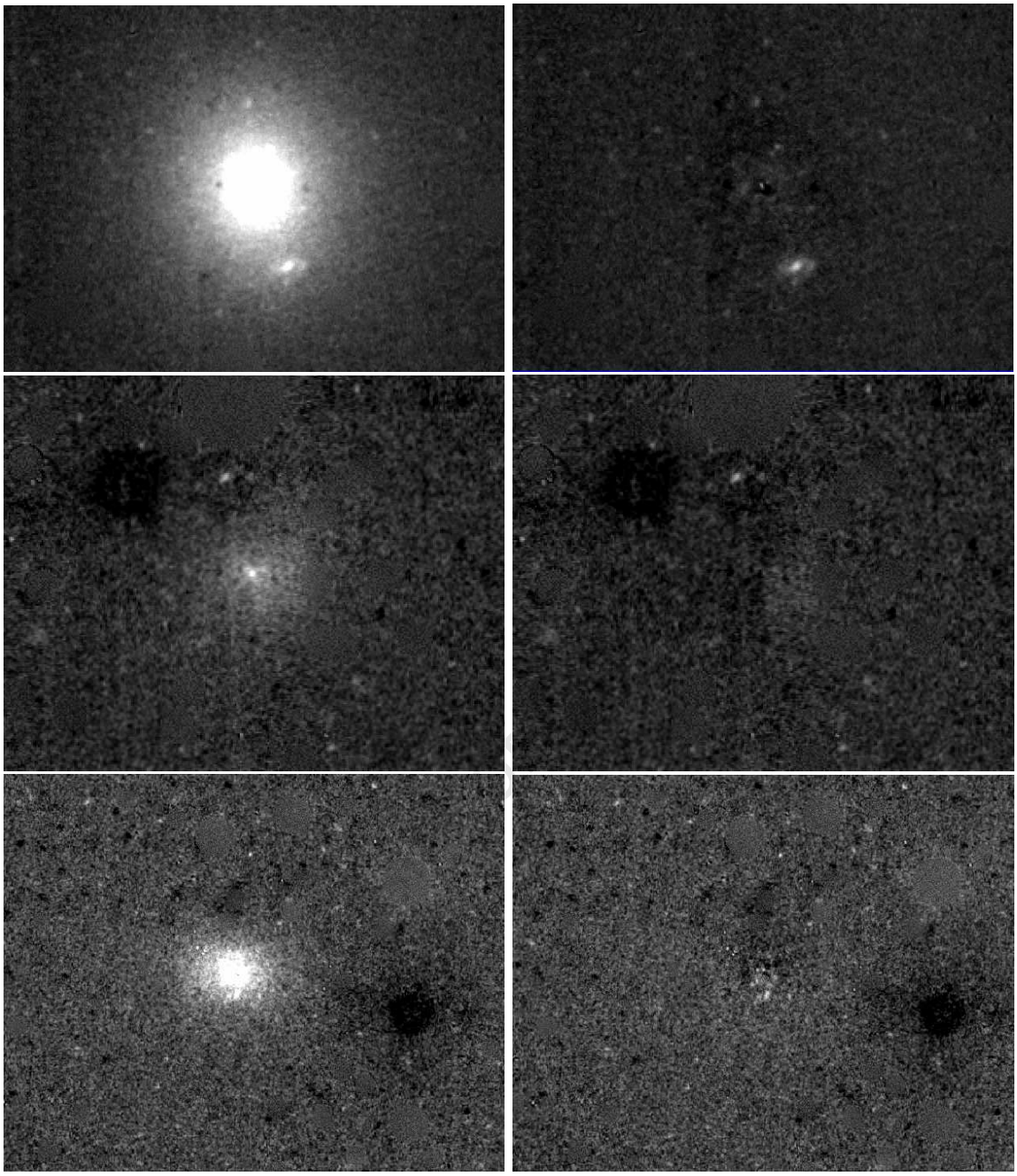

Figure 2.45 Surface brightness modeling of the dwarf galaxies NGC 3115 DW01 (*top*), LEDA 166099 (*middle*) and ESO 384016 (*bottom*) using GALFIT. The original galaxy image is shown on the left. The residual image after subtraction of the galaxy model is shown on the right.

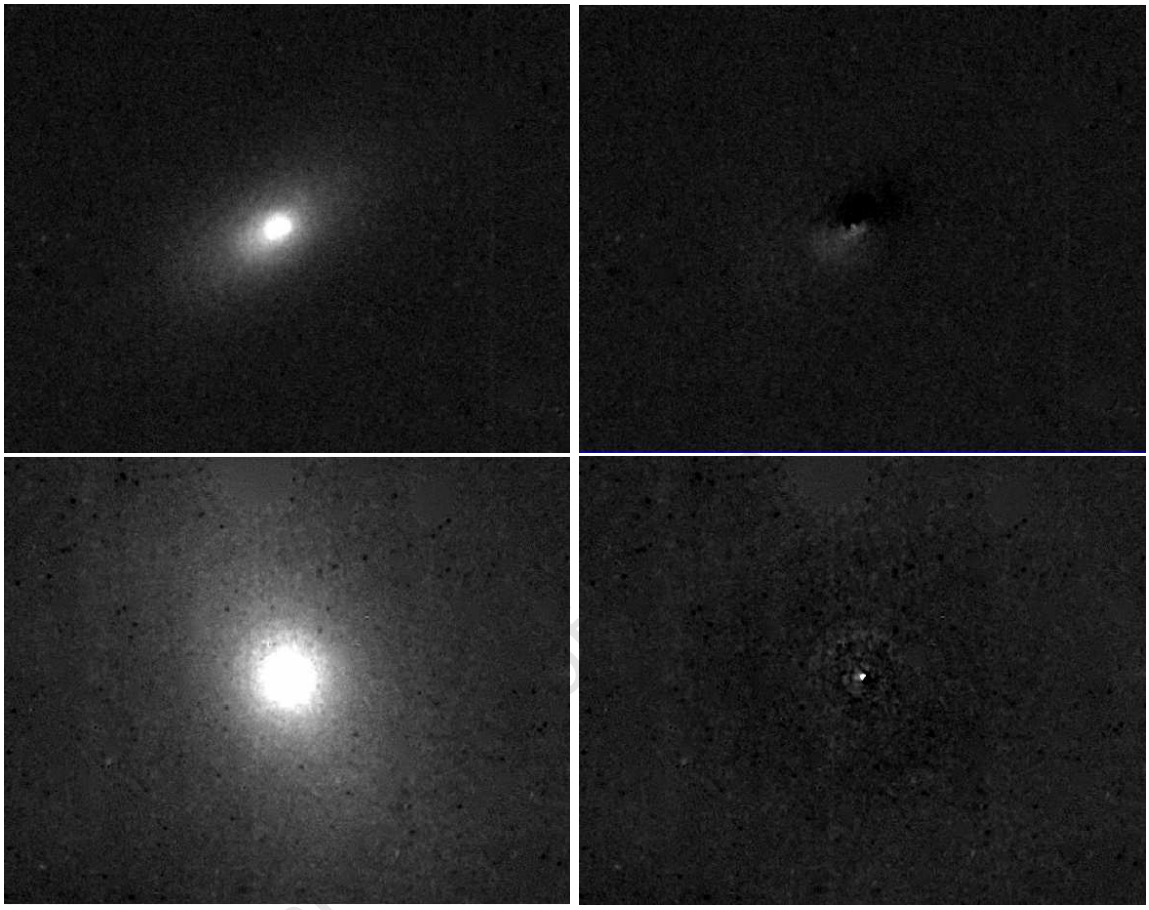

Figure 2.46 Surface brightness modeling of the dwarf galaxies NGC 59 (*top*) and NGC 5206 (*bottom*) using GALFIT. The original galaxy image is shown on the left. The residual image after subtraction of the galaxy model is shown on the right. The light excess from the galaxy nuclei can be seen in the residual images.

NGC 59, LEDA 166099 and NGC 5206 are well-described by an exponential law. The J-, H- and K_s-band value of the shape parameter for galaxy ESO 384-016 agrees within $n < 0.1$ with those values obtained from the 1D fitting.

Figure 2.46 shows the residual image of NGC 59. Excess light is seen near the galaxy center of the residual image. It is suspected that this light forms part of the star-forming region which is not fully accounted for by the removal of the point-like source near the galaxy nucleus. The excess light detected in the residual image suggests that the starburst region is extended beyond this point-like source. Additionally, an asymmetry in the light distribution of NGC 59 is detected just outside the bright core of the galaxy. This feature leads to an over-estimation in the measured flux of the galaxy seen north-west of the bright core in the residual image.

The Sérsic parameters (μ_s, r_s and n) are each plotted as a function of the H-band luminosity of the galaxy in Fig. 2.47. The absolute H-band magnitudes of the six IRSF dwarfs are listed in Table 2.13. These were computed using the individual galaxy distances given in Table 2.1 and the apparent magnitudes listed in Table 2.10. Reddening estimates from Schlegel et al. (1998) were used to obtain the extinction corrections A_λ also listed in Table 2.13. The structural parameters derived for the nuclear component are plotted for the galaxies NGC 3115 DW01, NGC 59, LEDA 166099 and NGC 5206. The parameters derived from the 1D Sérsic fit are shown for the low SB galaxy UGCA 200 (Table 2.11). For comparison, the structural parameters for the sample of LV galaxies ($D \lesssim 10$Mpc) by Kirby et al. (2008) are added to these plots. Their sample consists of deep H-band observations of 57 nearby galaxies ranging in morphological type from bright lenticulars to low SB (LSB) galaxies. The structural parameters of these galaxies were measured by fitting a single Sérsic function to their SB profiles.

A clear trend between the central brightness μ_s and H-band luminosity of the galaxies is evident in the top panel of Fig. 2.47. Generally, the brighter cores are observed for the more luminous galaxies. The nuclear component of NGC 5206 has comparable brightness to the cores of the luminous spiral galaxies. The galaxies NGC 3115 DW01 and NGC 59 bridge the gap between the luminous spirals/lenticulars and the dwarf galaxies which exhibit fainter central brightnesses. The starburst component in the center of NGC 59 leads to the detection of a brighter core compared to the values measured for the nearby dwarfs. It is known that the younger stellar component of this galaxy is most luminous in the H-band (section 2.7.3) which results in a higher SB for the nuclear component. The central component of NGC 59 is measured $\sim 0^{\rm m}.2$ brighter than the nucleus of NGC 3115 DW01 in the H-band. The central brightnesses of the galaxies ESO 384-016 and UGCA 200 are in good agreement with those measured for the nearby dwarfs. The nucleus of LEDA 166099, however, lies $\sim 0^{\rm m}.1$ below the dwarf galaxy sequence. The 2D decomposition of the SB profile for LEDA 166099 remains challenging due to its faintness and barely-resolved nuclear component. Some of the central flux forms part of modeling the galaxy disk which then leads to the underestimation of the central SB of this galaxy.

Figure 2.47 shows a continuity in the central SB from the luminous spirals ($M_H \sim -23$) to the fainter dwarf galaxies ($M_H \sim -14$). This continuous trend between the central SB

Table 2.13. Absolute magnitudes and extinction coefficients of the six dwarf galaxies.

Galaxy	M_J (mag)	A_J (mag)	M_H (mag)	A_H (mag)	M_{K_s} (mag)	A_{K_s} (mag)	M_B (mag)	A_B (mag)
NGC 3115 DW01	-19.23 ± 0.20	0.05	-19.78 ± 0.20	0.03	-19.99 ± 0.20	0.02	-16.32	0.23
NGC 59	-17.38 ± 0.16	0.02	-17.98 ± 0.16	0.01	-18.15 ± 0.16	0.01	-15.65	0.09
LEDA 166099	-16.24 ± 0.20	0.18	-16.78 ± 0.20	0.11	-17.01 ± 0.20	0.07	-13.61	0.85
ESO 384-016	-15.00 ± 0.13	0.07	-15.63 ± 0.13	0.04	-15.77 ± 0.13	0.03	-12.74	0.32
NGC 5206	-18.87 ± 0.20	0.11	-19.43 ± 0.20	0.07	-19.73 ± 0.20	0.04	-16.14	0.52
UGCA 200	-16.09 ± 0.20	0.04	-16.61 ± 0.20	0.03	-16.67 ± 0.20	0.02	-13.57	0.21

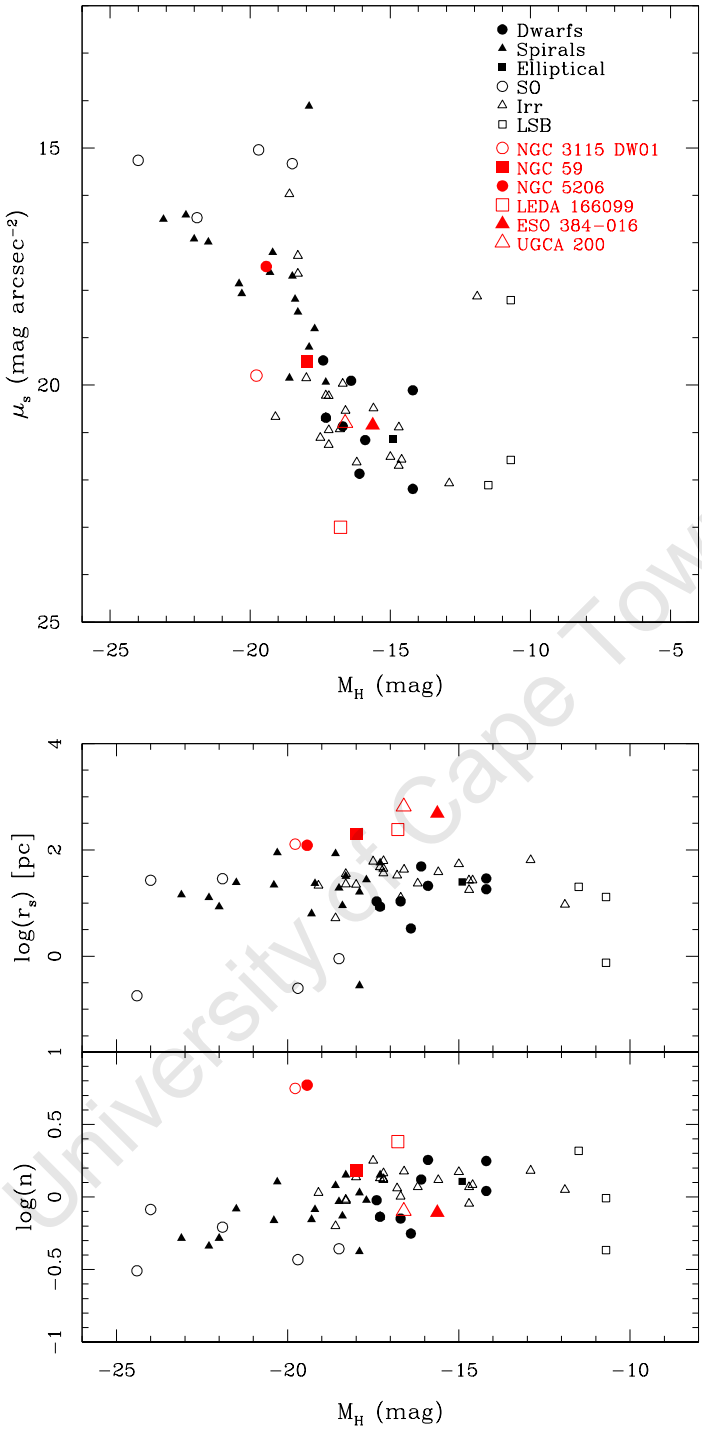

Figure 2.47 Sérsic parameters (μ_s, r_s and n) for the IRSF dwarfs (*red*) and nearby galaxy sample of Kirby et al. (2008) (*black*) are plotted against the absolute, reddening-corrected H-band magnitude. The structural parameters of the IRSF dwarfs correspond to the values obtained from the 2D decomposition fitting with GALFIT (with the exception of UGCA 200). Fittings to the nuclear component are thus shown for the galaxies NGC 3115 DW01, NGC 5206, NGC 59 and LEDA 166099. The morphological type of galaxies from the Kirby et al. (2008) sample are denoted by the different symbols indicated in the top panel.

and the absolute magnitude of galaxies is also observed in the optical (e.g., Karick et al. 2003). The same trend of brighter central surface brightnesses for the more luminous galaxies was detected in the B-band. Jerjen et al. (2000b) found that the continuum in all three Sérsic parameters are measured over a magnitude range of $15\overset{\mathrm{m}}{.}0$, from $M_B \sim -22\overset{\mathrm{m}}{.}0$ to $M_B \sim -7\overset{\mathrm{m}}{.}0$. The $M_H - \mu_s$ diagram in Fig. 2.47 shows that the continuous trend in the NIR spans a magnitude range similar to that seen in the optical ($\sim 14\overset{\mathrm{m}}{.}0$). Additionally, the $M_H - \mu_s$ relation appears to be linear down to an absolute magnitude of $M_H \sim -15\overset{\mathrm{m}}{.}0$, after which more constant values in the central SB are seen. The bending towards (on average) constant values in the central SB occurs at $M_B \sim -13\overset{\mathrm{m}}{.}0$ in the optical. Jerjen et al. (2000b) point out that this break is possibly a selection effect caused by the poor sampling of low surface brightness galaxies at the faint-end of this relation.

Overall, the continuous and linear relationship between M_H and μ_s suggests that the initial mechanism or mechanisms of galaxy formation is similar for the morphological types represented in Fig. 2.47. The significance of this result was illustrated by Jerjen & Binggeli (1997) for dE and elliptical galaxies. The earlier observations of Kormendy (1985) showed that dE and ellipticals form two distinct classes of galaxies based on the discontinuity of the $M_B - \mu_s$ relation at $M_B \sim -18\overset{\mathrm{m}}{.}0$. This finding was dubbed the dE-elliptical dichotomy and was an area of debate for many years. It was later found that the discontinuity was a direct consequence of the sample selection used by Kormendy (1985). There is now substantial evidence for a continuity between these two classes of galaxies (see Graham & Guzmán 2003, and references therein) which suggests that dE's are the low-luminosity representatives of giant ellipticals.

The central radius r_s and Sérsic index n of the galaxies are plotted on a logarithmic scale as a function of the H-band luminosity in Fig. 2.47. A linear trend with luminosity is observed for the Sérsic index with brighter galaxies exhibiting smaller values of $\log(n)$. This trend arises from the difference in the light profile shapes where an $R^{1/4}$-law (and subsequent smaller values of $\log(n)$) gives a better fit for the brighter galaxies having distinct cores. The optical observations of Jerjen et al. (2000b) indicate that both $\log(n)$ and $\log(r_s)$ decrease linearly with increasing galaxy luminosity. A similar trend is seen in the NIR for the shape parameter n. This trend is less clearly defined for the r_s parameter which shows more scattered points. The small number of luminous galaxies (and absence of ellipticals) in the Kirby et al. (2008) sample can result in a bias effect at the bright-end ($M_H \lesssim -20\overset{\mathrm{m}}{.}0$) of these relationships. The lack of luminous NIR galaxies in the sample can explain the poorly defined linear relationship for the n and r_s parameters.

Figure 2.47 shows that the Sérsic index of the galaxies ESO 384-016, LEDA 166099 and UGCA 200 fit well with those values measured for the nearby dwarf galaxies. The profile shape of NGC 59 is found on the periphery between the spirals and dwarfs. The steep nuclear profiles of NGC 3115 DW01 and NGC 5206 lead to the large deviation ($\log(n) \sim 0.5$) of these galaxies from the observed sequence for nearby galaxies. However, a Sérsic fit to the 1D SB profiles of these galaxies results in shape parameters in the range measured for the dwarf galaxies. The $M_H - \log(r_s)$ diagram shows that the three faintest galaxies ($M_H \gtrsim -18\overset{\mathrm{m}}{.}0$) in the sample may form an extension of the linear trend of larger central radii for low-luminosity galaxies. These

relations are, however, not well defined at low luminosities given the limited galaxy sample. It can also be seen that the nuclei of the brightest IRSF dwarfs have a radial extent similar to that measured for the cores of spiral galaxies. Overall, the structural parameters derived for the nuclei of these galaxies show a strong correlation with those parameters obtained for late-type spiral galaxies in the Kirby et al. (2008) sample. These results suggest that the galaxies NGC 3115 DW01, NGC 5206 and NGC 59 have massive nuclei and are more likely hosts of a central IMBH.

2.9 Discussion

2.9.1 $J - K_s$ colour-luminosity Relation

Variations in the broadband optical colours of galaxies can be interpreted as a change in the mean age of the stellar population. For most galaxies, red colours ($B - R \gtrsim 1^{\rm m}.2$) are a signature of an older generation of stars, whereas bluer colours ($B - R \lesssim 1^{\rm m}.0$) are identified with a younger stellar population. Other factors, such as dust, can strongly influence the optical colours of galaxies (see Bell & de Jong 2001). The dust extinguishes light from the stellar population making it appear dimmer and redder in the optical bands. With the exception of young starburst galaxies, the NIR colours are not affected by the presence of dust and are therefore a true representation of the underlying stellar population of the galaxy. Galaz et al. (2002) have shown that variations in the NIR colour of a galaxy are mainly driven by the metallicity of its stellar population. In particular, the $J - K_s$ colour index of a galaxy has been shown to be very metal sensitive with little dependence on the mean age of the stellar population.

The relation between the NIR colour and metallicity is demonstrated by the $J - K_s$ versus $B - V$ plot of Galaz et al. (2002) shown in Fig. 2.48. The stellar population synthesis models of Bruzual & Charlot (Liu et al. 2000a) are plotted for different mean metallicities ($0.005 - 2.5{\rm Z}_{\odot}$) and stellar ages (1–11Gyr). The models assume that the star formation started 12Gyr ago. The plot shows that for a single stellar metallicity, the maximum change in the $J - K_s$ colour is $\sim 0^{\rm m}.15$ over the entire range of mean stellar ages. A colour change of more than $\Delta(J - K_s) \sim 0^{\rm m}.15$ can therefore not be a result of an age gradient. Instead, colour changes of $\Delta(J - K_s) \gtrsim 0^{\rm m}.15$ are interpreted as a change in the mean metallicity of the galaxy.

The $J - K_s$ colour-magnitude diagram for the six IRSF dwarfs is shown in Fig. 2.49. The mean $J - K_s$ colours for the galaxies (listed in Table 2.8) are plotted against the absolute K_s-band magnitudes. Three different samples of galaxies were added to this plot for comparison. These include, early-type (dE, dS0 and dE/dS0) dwarf galaxies from the Virgo Cluster, the dIrr galaxies of Vaduvescu et al. (2005) and low surface brightness (LSB) galaxy sample of Galaz et al. (2002). The photometric data for dwarf galaxies in the Virgo Cluster were taken from the Goldmine database.[10] A mean distance of 15.8Mpc (Jerjen et al. 2004) was adopted for the Virgo Cluster. The galaxy sample of Galaz et al. (2002) consists of deep J- and

[10]The data for the Virgo Cluster can be accessed online at http://goldmine.mib.infn.it/.

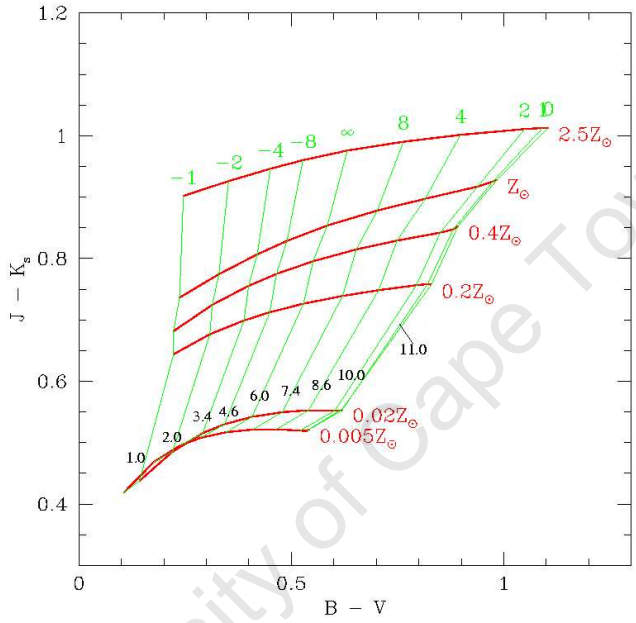

Figure 2.48 $J - K_s$ versus $B - V$ colour grid from Galaz et al. (2002) which shows different star formation rates and metallicities ($0.005 - 2.5Z_{\odot}$). The exponential star formation rates are shown by the top labels (∞ denotes a constant star formation rate). The mean ages in Gyr are indicated at the bottom. All models assume that star formation started 12Gyr ago.

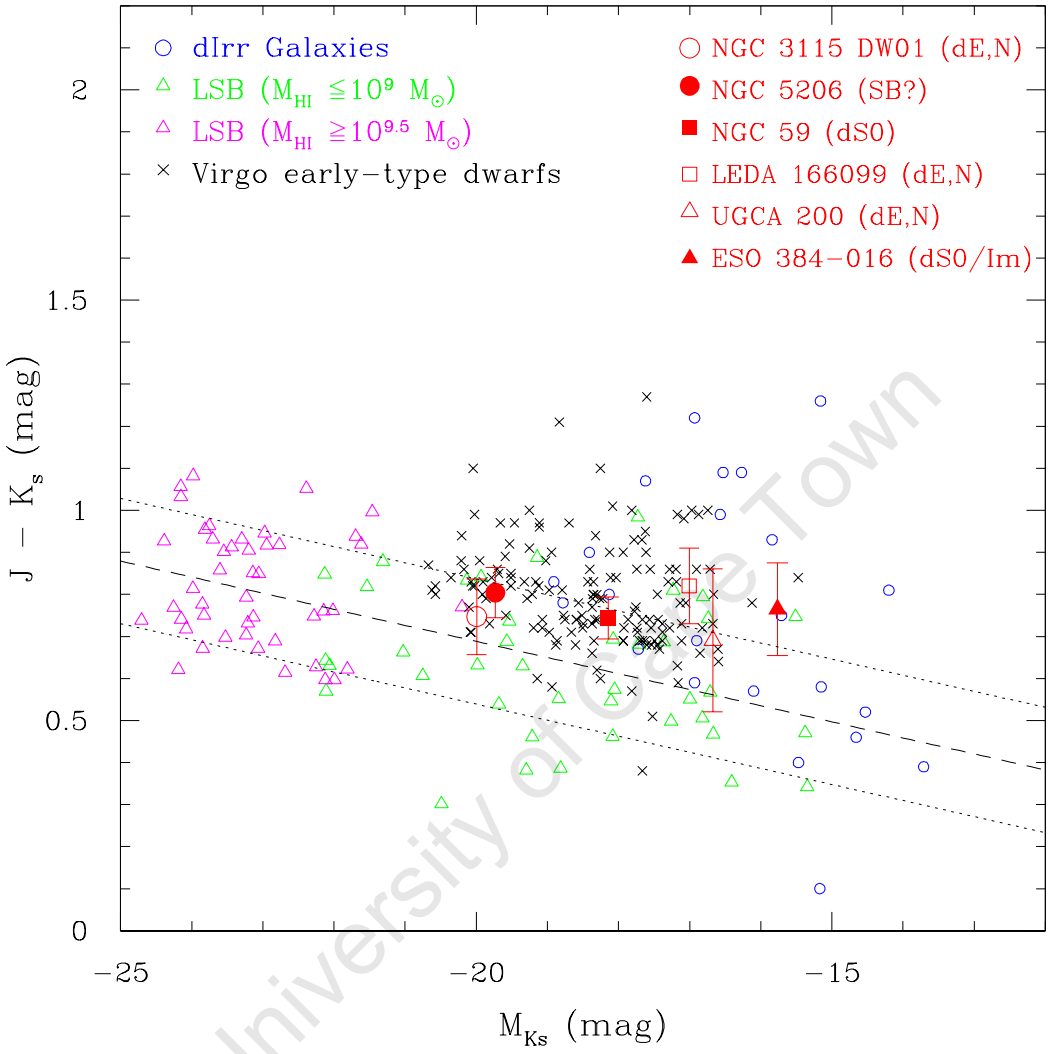

Figure 2.49 $J-K_s$ colour-magnitude diagram. The six IRSF dwarfs are shown in red where the filled symbols indicate those dwarfs which have been detected in H I. The early-type (dE, dS0 and dE/dS0) dwarf galaxies from the Virgo Cluster are shown by the black crosses. The LSB galaxies of Galaz et al. (2002) are plotted in green (low H I content, $7.5 \leq \log(M_{\rm H\,I}/M_\odot) \leq 9.0$) and magenta (high H I content, $\log(M_{\rm H\,I}/M_\odot) \geq 9.5$). The dIrr galaxies of Vaduvescu et al. (2005) are shown in blue. The linear least-squares fit to the sample of LSB galaxies and 1σ standard deviation is represented by the dashed and dotted lines, respectively.

K_s-band photometry for a large sample of LSB and spiral galaxies with redshifts $z < 0.1$. The majority of galaxies in their sample are LSB galaxies. The spiral galaxies span a wide range of Hubble types from Sa to Im. It should be noted that we refer to the full galaxy sample of Galaz et al. (2002) as LSB galaxies in this section. They have observed a total of 88 galaxies using the 1m Swope Telescope and 2.5m du Pont Telescope, both located at Las Campanas Observatory. A central SB cutoff of $\mu_0(B) = 22$mag arcsec^{-2} was imposed for galaxies observed with the 1m telescope and $\mu_0(B) = 23.5$mag arcsec^{-2} for galaxies observed with the 2.5m telescope. These galaxies were divided into two subsamples based on their H I content: 39 galaxies have $7.5 \leq \log(M_{\rm H\,I}/M_\odot) \leq 9.0$ (low H I gas content) and 49 galaxies have $\log(M_{\rm H\,I}/M_\odot) \geq 9.5$ (high H I gas content) which are shown by the respective green and magenta points in Fig. 2.49.

The absolute K_s-band magnitudes of the galaxies were not corrected for Galactic extinction. The absolute magnitudes and extinction coefficients A_λ (Schlegel et al. 1998) of the IRSF dwarf galaxies are listed in Table 2.13. The uncertainty in the absolute magnitudes are typically $\leq 0\overset{\rm m}{.}2$. The largest correction for galaxy reddening in the K_s-band is $0\overset{\rm m}{.}07$ for LEDA 166099. The k-correction for galaxy redshifts were not applied to the magnitudes of the IRSF dwarfs as well as the other galaxy samples. At redshifts of $z < 0.1$, the k-corrections are smaller than the photometric errors and can therefore be neglected. Figure 2.49 shows that the IRSF dwarfs overlap with the low H I mass LSB and dwarf galaxy samples. The early-type Virgo dwarfs span a $J - K_s$ colour range similar to that seen for the higher SB dIrr galaxies. Additionally, the early and late-type dwarf galaxies occupy a similar parameter space in this diagram where the early-type systems form the brighter extension to the dIrr galaxies. It can also be seen that the LSB galaxies do not necessarily have faint absolute magnitudes in the NIR. A number of these galaxies are as bright in the NIR as normal high SB galaxies which suggests that they have a significant older stellar population.

Figure 2.49 shows that there is little scatter [$\Delta(J-K_s) \lesssim 0\overset{\rm m}{.}2$] in the $J-K_s$ colours of the six IRSF dwarfs. The LSB galaxies, on the other hand, span a large range of $\Delta(J-K_s) \sim 0\overset{\rm m}{.}8$ in NIR colour. This wide range in the NIR colour cannot be due to changes in the mean stellar age of the galaxies as discussed earlier. The colour variation of $\Delta(J-K_s) \sim 0\overset{\rm m}{.}15$ for changes in the mean age of the stellar population is too small to explain the large range in $J - K_s$ colour for the LSB galaxies. Instead, the large gradient in the $J - K_s$ colour is a direct result of a change in the mean metallicity of the galaxies. Galaz et al. (2002) have imposed a limit on the metallicity distribution of their galaxy sample which assumes a maximum age spread of $\Delta(J - K_s) \sim 0\overset{\rm m}{.}15$. They argue that the metallicity of the LSB galaxies can vary by up to a factor of 100 in the $J - K_s$ colour range.

A systematic trend between the $J - K_s$ colour and stellar luminosity is observed for the LSB galaxies. Figure 2.49 shows that the redder $J - K_s$ colours are measured with increasing H I mass of the galaxies. The findings of Galaz et al. (2002) have extended these relations to include more significant trends between the $J - K_s$ colour and the stellar and baryonic mass of the galaxies. These relations suggest that the more massive galaxies tend to have more metal-rich stellar populations. To check if this correlation holds for the IRSF dwarfs, a linear least-squares fit was made to the data points for the LSB galaxies and is shown by the

dashed line in Fig. 2.49. The three brightest IRSF dwarfs ($M_{K_s} \lesssim -18\overset{\mathrm{m}}{.}0$) and UGCA 200 lie within the 1σ standard deviation (dotted line) of galaxies from the linear fit. The galaxies LEDA 166099 and ESO 384-016 show larger scatter [$\Delta(J-K_s) \lesssim 0\overset{\mathrm{m}}{.}3$] from the linear fit and seem to follow the red subclump of dwarf galaxies with absolute magnitudes in the range of $-19\overset{\mathrm{m}}{.}0 \lesssim M_{K_s} \lesssim -15\overset{\mathrm{m}}{.}0$. The dwarf galaxies in the subclump can appear up to $\Delta(J-K_s) \sim 0\overset{\mathrm{m}}{.}7$ redder than those galaxies following the $J-K_s$ colour-luminosity trend defined by the LSB galaxies.

The existence of the red subclump of dwarf galaxies in Fig. 2.49 suggests that the early and late-type dwarf systems may not follow the metallicity-luminosity trend observed for LSB galaxies. To improve our understanding of the relationship between the $J-K_s$ colour and stellar luminosity for dwarf galaxies, the colour-magnitude diagram for the early-type Virgo dwarfs and dIrr galaxies are shown separately in Fig. 2.50. The six IRSF dwarfs are indicated by the red points in these figures. A linear least squares fit was made to each sample of dwarf galaxies which is shown by the dashed line in Fig. 2.50. The 1σ standard deviation (dotted line) from the linear fit is also shown. The linear fit to the early-type dwarfs has a shallow slope of $m = -0.02 \pm 0.01$. This suggests that the early-type dwarf galaxies show almost constant $J-K_s$ colours independent of their luminosity. The six IRSF dwarfs are found to lie well within the 1σ deviation from the linear fit so that these nearby systems follow the trend observed for the Virgo early-type dwarfs. The almost constant $J-K_s$ colours implies that a weak correlation exists between metallicity and galaxy mass for early-type dwarf galaxies.

A slightly different linear relation has been determined for the dIrr galaxies of Vaduvescu et al. (2005). The slope of the linear fit is $m = -0.07 \pm 0.04$ for the dIrr's compared to $m = -0.04 \pm 0.01$ for the LSB galaxies. Vaduvescu et al. (2005) point out that redder $J-K_s$ colours are detected with increasing luminosity for the dIrr galaxies. This suggests that the dIrr galaxies show similar reddening trends to that seen for the LSB galaxies. However, the dIrr galaxies exhibit redder colours with increasing luminosity. The IRSF dwarfs are seen to lie within the 1σ deviation from the linear fit to the dIrr's. The redder $J-K_s$ colours with increasing luminosity are however not observed for the IRSF dwarfs who show more constant $J-K_s$ colours down to an absolute magnitude of $M_{K_s} = -15\overset{\mathrm{m}}{.}8$. The correlation of the $J-K_s$ colour with absolute magnitude M_{K_s} remains questionable for the low luminosity dIrr's ($M_{K_s} > -15\overset{\mathrm{m}}{.}5$). It is not clear if a selection effect results in the lack of low luminosity, red dIrr galaxies at the faint end of this relation. The detection of these galaxies can provide more convincing evidence of a distinguished red sub-population of dwarf galaxies as seen in Fig. 2.49.

Galaz et al. (2002) argue that the mean metallicity of galaxies is mainly determined by their H I gas content ($M_{\mathrm{H\,I}}/M_{\mathrm{baryonic}}$) which indicates the efficiency of star formation in the galaxy. The galaxies that have only recently begun creating stars have not enriched their gas reservoirs resulting in a low mean metallicity and blue $J-K_s$ colours. On the other hand, those galaxies which have experienced several generations of star formation would have greatly enriched their gas giving the higher metallicities and red $J-K_s$ colours. A comparison of the linear fits for the dIrr and early-type dwarf galaxy samples is illustrated in Fig. 2.50. It can be seen that the shallow slope for the early-type dwarfs may be a selection effect due to

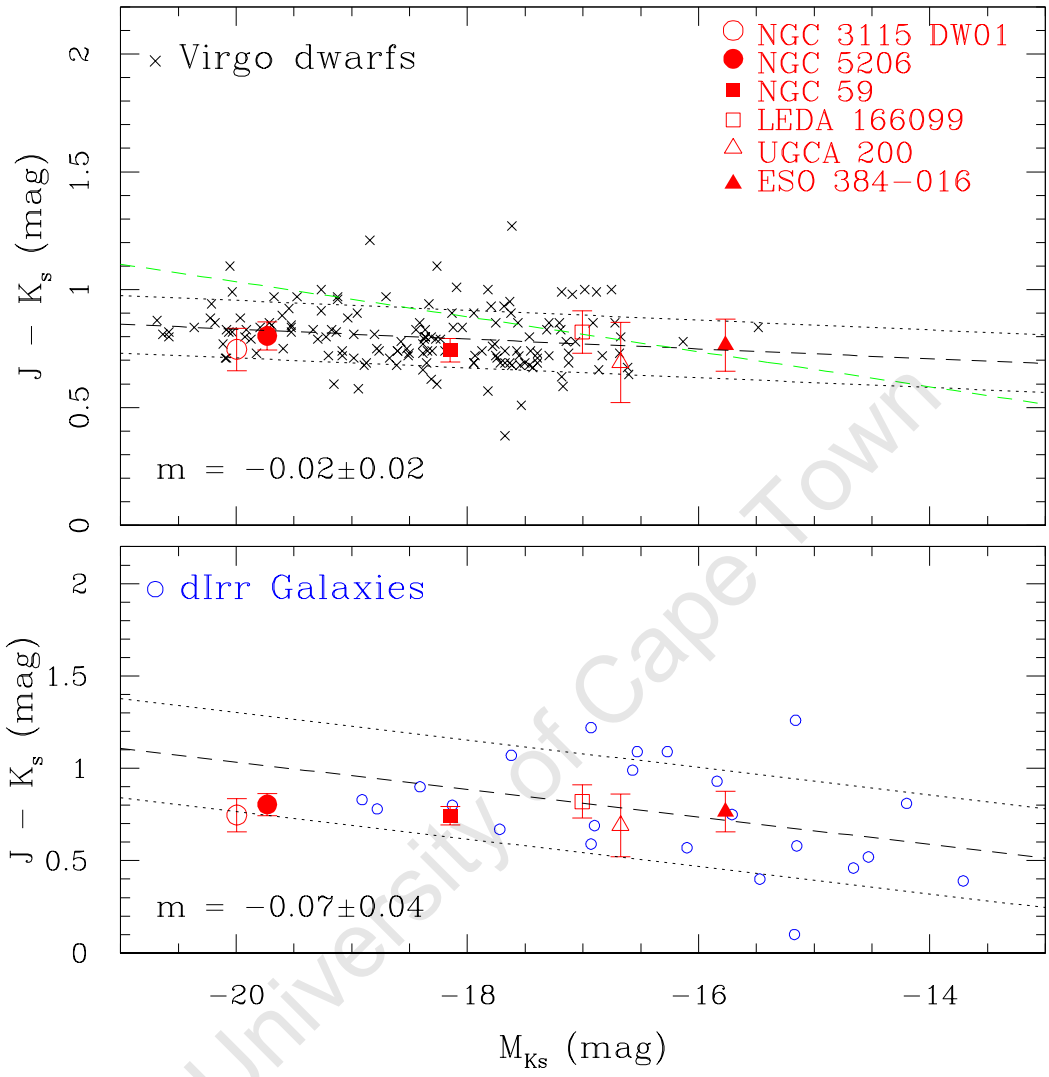

Figure 2.50 $J-K_s$ colour-magnitude diagram for the Virgo early-type (dE, dS0 and dE/dS0) galaxies (*top*) and dIrr's (*bottom*). The six IRSF dwarfs are shown in red where the filled symbols indicate those dwarfs which have been detected in H I. The linear least-squares fit and 1σ standard deviation for each galaxy sample are represented by the dashed and dotted lines, respectively. The slope m of the linear fit is indicated. For comparison, the linear fit for the dIrr galaxies is re-plotted in green in the top panel.

the absence of lower SB dwarfs at absolute magnitudes $M_{K_s} \gtrsim -17\overset{\mathrm{m}}{.}0$. If the $J-K_s$ colour-luminosity relation for dIrr's includes early-type dwarfs, then the galaxies NGC 3115 DW01 and NGC 5206 should contain more evolved, metal-rich stellar populations compared to the remaining dwarfs in our sample. These galaxies are known to host an older stellar population with a lack of H I gas (see section 2.2.2). It can be immediately implied that these galaxies have exhausted their gas content by undergoing several episodes of star formation. The galaxy NGC 59 bridges the gap in metallicity between the early and late-type dwarfs. The recent bursts of star formation in the center contribute to the enrichment of the gas content in this early-type dwarf. The element abundance of NGC 59 will be derived in chapter 3 where we show that the central regions of this galaxy have similar metallicity to that seen in nearby dIrr galaxies. Jerjen et al. (2000a) have found that the galaxy ESO 384-016 is composed of an old, metal-poor stellar population (see section 2.2.2). The lack of metals in this galaxy does provide some indication that ESO 384-016 follows the $J-K_s$ colour-luminosity trend.

The extremely red $J-K_s$ colours ($J-K_s \gtrsim 1$) for dwarf galaxies in the subclump are not well understood. Vaduvescu et al. (2005) give measurement uncertainties of $\lesssim 0\overset{\mathrm{m}}{.}1$ for the J- and K_s-band total magnitudes of the dIrr sample. This suggests that the extremely red $J-K_s$ colours are a real feature in these galaxies and are not simply due to the uncertainties in the photometric measurements. It is known that the heating of dust can play a significant role in metal-deficient, starburst galaxies. This process can result in the red NIR colours detected for dwarf galaxies in the subclump. Deep observations of a large sample of dwarf galaxies are however needed to further investigate the faint-end of the $J-K_s$ colour-luminosity relation.

2.9.2 Dwarf Galaxy Evolutionary Sequence and Morphology

The light profile of galaxies in the B-band is dominated by emission from young, massive stars. These observations can be strongly influenced by the presence of dust which results in reddening of the galaxies. Star formation activity can thus significantly distort the light profiles of galaxies in the optical. The NIR observations efficiently penetrate the dust associated with the interstellar medium to reveal the internal structure of galaxies. The NIR wavelengths are subsequently used to probe the structure of the underlying, massive component of the galaxy. An indication of the dominant stellar population can therefore be obtained by comparing the galaxy emission in the optical and NIR. In this section, the NIR photometric results for the six dwarf galaxies are combined with existing optical measurements to assess their evolutionary state and morphology.

The $B-K_s$ colour is known to be a good indicator of the galaxy morphological type (e.g., Jarrett et al. 2003). In Fig. 2.51, the $B-K_s$ colours of the six IRSF dwarfs are plotted against their corresponding K_s-band luminosity. The total apparent B-band magnitudes of the dwarfs (see Table 2.2) are taken from Karachentsev et al. (2004). For the faintest galaxies in the sample ($B \gtrsim 15\overset{\mathrm{m}}{.}2$), the total B-band magnitudes have been determined with an accuracy of $\sim 0\overset{\mathrm{m}}{.}5$. The $B-K_s$ colours were calculated as the difference between the total apparent B and K_s-band (Table 2.10) magnitudes of the galaxies. To gain more perspective of where the IRSF dwarfs are located relative to other galaxy morphologies, we have added four different galaxy samples to the $B-K_s$ colour-magnitude diagram: early-type dwarfs (dE, dS0, dE/dS0)

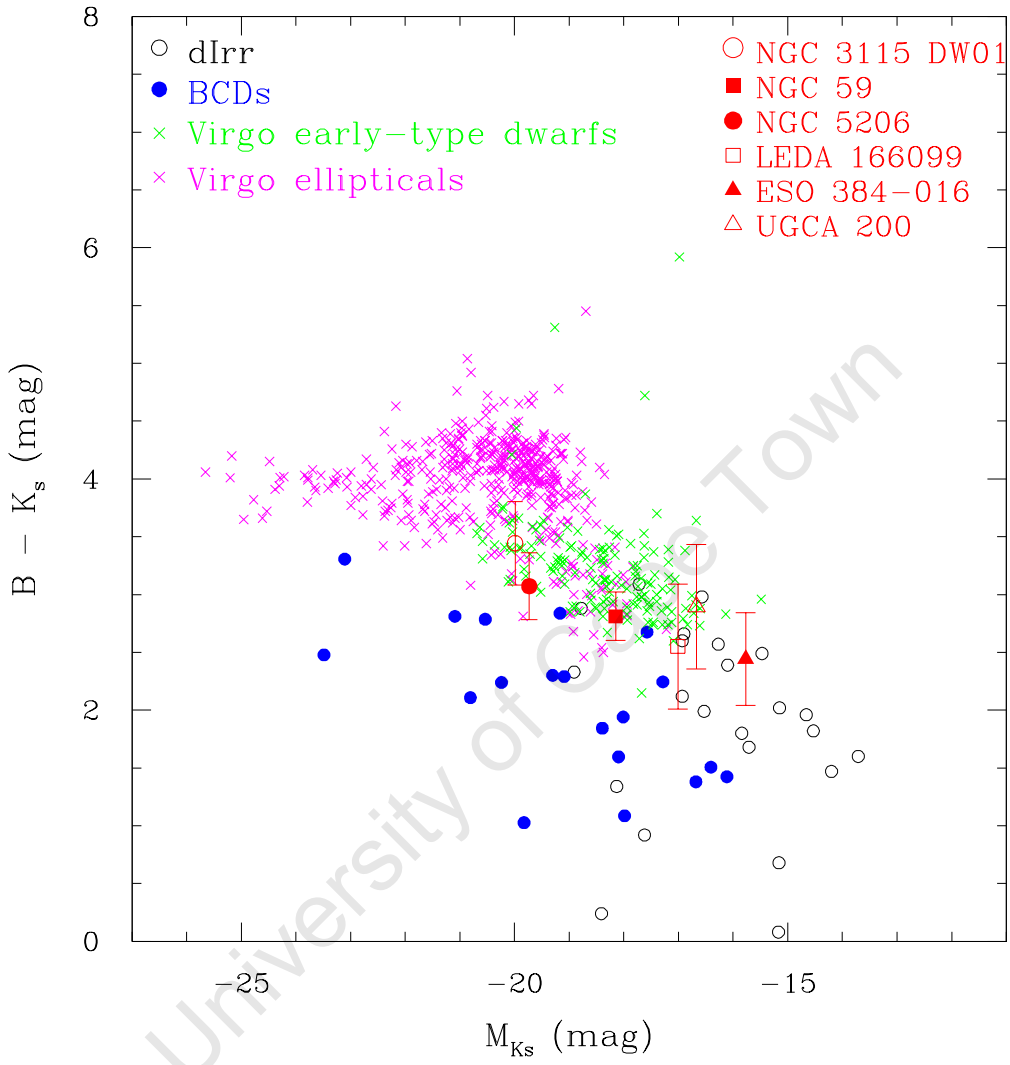

Figure 2.51 $B - K_s$ colour-magnitude diagram. The six IRSF dwarfs are shown in red where the filled symbols indicate those dwarfs which have been detected in H I. The elliptical and early-type dwarf galaxies from the Virgo Cluster are represented by the magenta and green points, respectively. The dIrr's (Vaduvescu et al. 2005) are indicated by the black points while the BCD galaxies from Cairós et al. (2003) and Noeske et al. (2003) are shown in blue.

and elliptical galaxies from the Virgo Cluster (taken from the the Goldmine database), dIrr galaxies from Vaduvescu et al. (2005), BCD galaxies from Cairós et al. (2003) and Noeske et al. (2003). The general trend shows redder $B-K_s$ colours for the elliptical galaxies while bluer colours are measured for both early and late-type dwarfs. An average $B-K_s$ colour of $\sim 4\overset{\mathrm{m}}{.}0$ was measured for early-type (E, S0) galaxies in the 2MASS Extended Source Catalog (Jarrett et al. 2003). The early-type dwarfs form a continuous sequence between the more luminous elliptical galaxies and late-type dwarfs. The emission from the BCD galaxies is dominated by the younger, starburst component indicated by the blue colours.

Figure 2.51 shows that the six IRSF dwarfs fit very well with the sequence of early-type dwarf galaxies. The slightly bluer colours of NGC 59 result in this galaxy occupying the transition range between the BCDs and the early-type dwarfs. The blue $B-K_s$ colour is an indication of a significant younger stellar population in this galaxy. NGC 59 shows similar $B-K_s$ colour to the redder BCDs. The overlapping $B-K_s$ colour of NGC 59 with that measured for BCDs provide further validity for the comparison of the NIR colours of their respective star-forming regions (see section 2.7.3).

A detailed study of the relationship between the B- and H-band luminosity of galaxies was made by Kirby et al. (2008). They found a tight correlation between the absolute B- and H-band magnitudes for their sample of nearby galaxies ($D \lesssim 10$Mpc). This correlation was extended to include more luminous galaxies such as the sample of spirals from Kassin et al. (2006) and galaxies from the Virgo Cluster (Gavazzi et al. 2003).

The B versus H-band luminosity diagram by Kirby et al. (2008) is reproduced in Fig. 2.52. The extinction-corrected, absolute B- and H-band magnitudes of the six IRSF dwarfs have been added to this plot for comparison. The photometric data for the Virgo Cluster were taken from the Goldmine database. The magnitudes were corrected for extinction using $A_B = 0\overset{\mathrm{m}}{.}13$ and $A_H = 0\overset{\mathrm{m}}{.}01$ for the respective bands. A mean distance of 15.8Mpc (Jerjen et al. 2004) was adopted for the Virgo Cluster. Kirby et al. (2008) performed a least squares fit to the Virgo Cluster data which gives the linear relation:

$$M_H = (1.14 \pm 0.02) M_B - (0.74 \pm 0.32) \ , \tag{2.17}$$

for these galaxies. The linear fit and 1σ uncertainty are shown by the dashed and dotted lines in Fig. 2.52, respectively. A strong correlation between the B- and H-band luminosity is observed for the IRSF dwarfs. The six dwarfs follow the linear relation defined for the Virgo Cluster galaxies quite closely and lie well within the 1σ uncertainty level. Kirby et al. (2008) point out that the scatter from the linear relation increases in the dwarf regime ($M_B \gtrsim -12\overset{\mathrm{m}}{.}0$) with a possible trend to redder colours. The three lowest luminosity galaxies ($-8\overset{\mathrm{m}}{.}0 \lesssim M_B \lesssim -7\overset{\mathrm{m}}{.}0$) in Fig. 2.52 are the dwarfs SC18, SC24 and SC45. It should be noted that these galaxies are commonly confused with H I clumps from the Magellanic Stream. They remain questionable LV objects even though their Hubble flow distances were obtained from HST observations (Karachentsev et al. 2004). The scatter of these galaxies from the linear $B-H$ relation may therefore be a consequence of the spurious absolute B-band magnitudes for these objects. The deviation of the slope in equation (2.17) from unity implies that dwarf galaxies are in general bluer than the more luminous galaxies. This trend is also observed in the $B-K_s$ colour-magnitude plot shown in Fig. 2.51.

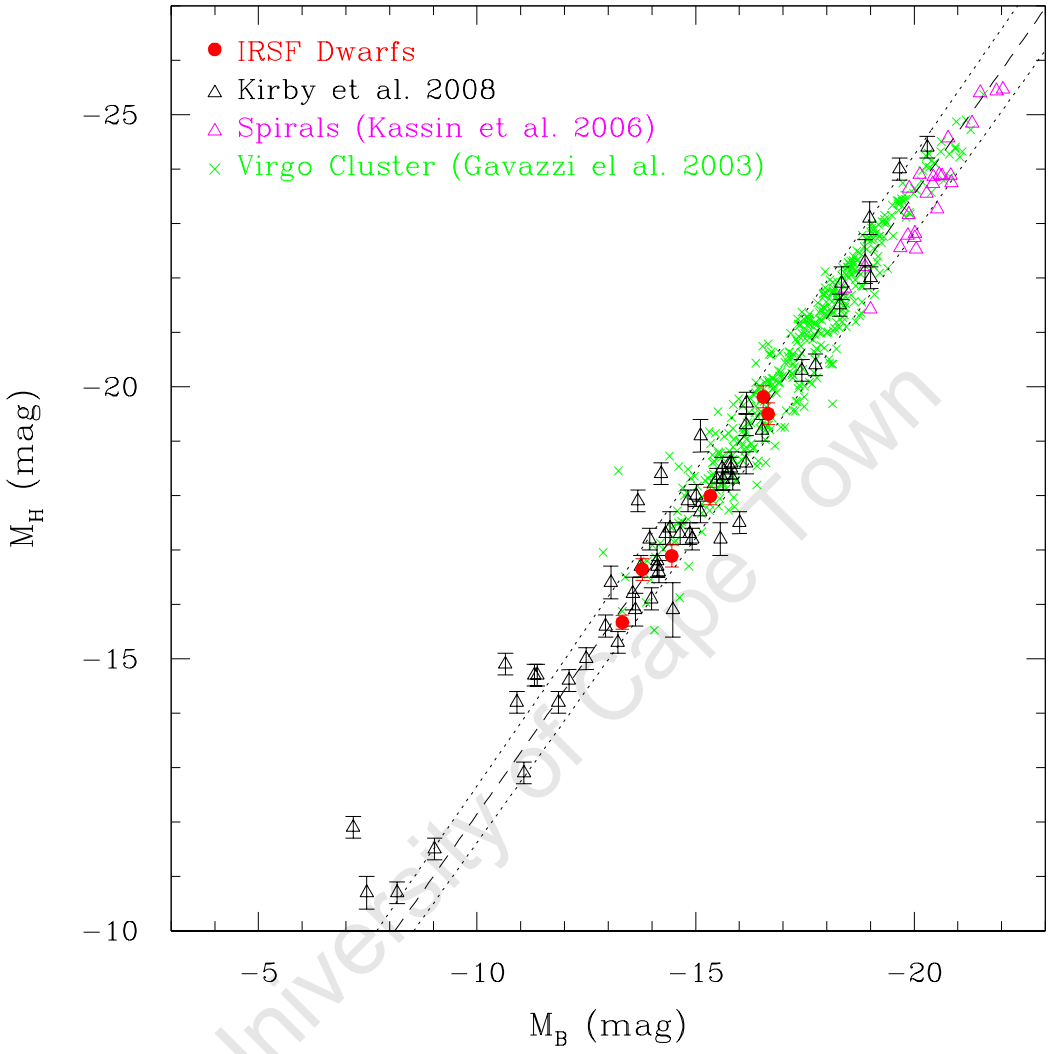

Figure 2.52 Correlation between the extinction-corrected, absolute H- and B-band magnitudes of galaxies. The sample of nearby galaxies ($D \lesssim 10$Mpc) by Kirby et al. (2008) is shown in black. The spiral galaxies of Kassin et al. (2006) and the Virgo Cluster data Gavazzi et al. (2003) have been added to this plot and are represented by the magenta and green points, respectively. The IRSF dwarfs are shown in red. The least-squares fit to the Virgo Cluster sample is indicated by the dashed line. The 1σ uncertainty in the fit is shown by the dotted lines.

Figure 2.52 reveals an unexpected linear relation between the B- and H-band luminosities of galaxies. The light profiles of galaxies in these two bands can be very different since they each sample disparate stellar populations. For galaxies experiencing star formation, the emission from young O and B stars dominate the B-band whereas the older stellar population emits at NIR wavelengths. The emission from the young stars can strongly influence the light profile of the galaxy which is set by the massive, underlying stellar component. For this reason, the structural parameters of galaxies have always been derived from NIR observations rather than in the optical. The tight correlation between the B- and H-bands in Fig. 2.52 suggests that the galaxies exhibit similar light profiles in the two bands. In particular, the correlation is strictly obeyed by the late-type galaxies. The light profiles of these galaxies are not distorted by dust which effectively results in similar galaxy morphologies in the NIR and optical. This argument can be applied to the IRSF dwarfs who closely follow the linear relation between the B- and H-bands. The correlation between the B- and H-bands for these galaxies implies that they are minimally affected by dust. This result is supported by the optical (Fig. 2.1) and NIR (Fig. 2.14) images of the dwarfs which have revealed similar galaxy morphologies.

2.9.3 The H-band Stellar Mass of Dwarf Galaxies

The dynamical mass-to-light (M/L) ratio of dwarf galaxies is largely uncertain. Observational M/L estimates for dwarf galaxies have mainly focused on the low SB dwarf spheroidal (dSph) galaxies of the Local Group (LG). The dynamical estimates of the M/L ratio for these galaxies are listed in the review by Mateo (1998). The M/L estimates were found to vary from $M/L \sim 1$ for NGC 147 (satellite galaxy of M31) to $M/L \sim 84$ for Draco, in solar units. A study of the stellar kinematics of the Draco dSph by Kleyna et al. (2002) gives a M/L ratio of ~ 440 for this galaxy. The discovery of numerous ultra-faint dSph galaxies around the Milky Way (MW) has placed further constraints on the M/L ratios (Simon & Geha 2007; Muñoz et al. 2006; Martin et al. 2007). Strigari et al. (2008) find a common mass of $\sim 10^7\,\mathrm{M}_\odot$ within the central 300pc for a sample of 18 MW dSph satellites. The common mass scale is found to be independent of the luminosity of the galaxies. This result suggests that the dynamical mass of dSph's is not correlated with the galaxy luminosity. An understanding of the mass-luminosity relation for dwarf galaxies can provide clues to the formation of these smaller systems. The high M/L estimates (approaching $1000(M/L)_\odot$) of the MW dSph's are confirmed by Strigari et al. (2008) which implies that these galaxies are strongly dark-matter (DM) dominated. They also provide convincing evidence for the existence of an extended DM halo (e.g., Evans et al. 2005). Based on the high M/L ratios, dSph's are believed to be the most DM-dominated members in the dwarf galaxy classification scheme. A more complete census of M/L estimates for various dwarfs is, however, needed to fully support these, as yet, preliminary claims.

To quantify the contribution from stars to the overall dynamics of galaxies, the stellar M/L ratio is needed. We have adopted the galaxy evolutionary models of Bell & de Jong (2001) in determining the stellar M/L ratio of the IRSF dwarfs. They have used spiral galaxy evolution models to investigate plausible trends in the M/L ratio with various galaxy properties (these include absolute magnitude, central SB, gas fraction and colour). The models are used to

construct the stellar M/L ratios for the integrated stellar populations by reproducing trends in the galaxy colour and its structural parameters. The M/L ratio shows significant trends with all four galaxy parameters in the optical and NIR passbands. These trends are however minimized in the NIR bands since these bands are less sensitive to the star formation history. A tight correlation is found between the stellar M/L and colour in all optical and NIR bands. Intuitively, this correlation is expected since the stellar M/L ratio and colour are both dependent on the star formation and chemical enrichment history of the galaxy. This correlation is robust to uncertainties in the stellar population, the galaxy evolution modeling, dust and small bursts of recent star formation. These factors give uncertainties of the order of $0.1 - 0.2$dex or less. The stellar initial mass function (IMF) is the primary uncertainty in modeling the M/L ratio. Galaz et al. (2002) have used the relations of Bell & de Jong (2001) to test the variations in the M/L ratio with $J - K_s$ colour for the Salpeter and Scalo IMF. They found the stellar masses of their sample of LSB galaxies do not vary by more than 7% between the two models. The choice of the IMF will thus not introduce uncertainties greater than 10% in the NIR stellar M/L ratio.

Bell & de Jong (2001) point out that the M/L-colour relation can break down when using colours that are strong metallicity tracers. For this reason, the M/L ratio of the IRSF dwarfs was determined using the $B-H$ colour rather than the $J-K_s$ colour. The linear coefficients given in Table 1 of Bell & de Jong (2001) were used to calculate the M/L ratio for each of the dwarf galaxies. These coefficients were measured by adopting a formation epoch model (with bursts) and a Salpeter IMF. The H-band stellar M/L ratio of the galaxies was then computed using the linear relation:

$$\Upsilon_H = a_H + b_H(B - H) \ . \tag{2.18}$$

The coefficients a_H and b_H were obtained from a linear combination of those values defined for the $B-V$ and $V-H$ colours. The stellar M/L ratio was calculated for each of the IRSF dwarfs by substituting their individual $B-H$ colour into equation (2.18). To increase the statistics by using a larger galaxy sample, the eight dwarfs from Kirby et al. (2008) were also used in calculating the M/L ratio. It should be noted that the dIrr galaxy AM 0521-343 in the Kirby et al. (2008) sample was excluded as the photometry of this galaxy is compromised by a bright foreground star. The average M/L ratios for the IRSF and Kirby et al. (2008) dwarf galaxy samples are $\Upsilon_H = 1.5 \pm 0.4$ and $\Upsilon_H = 1.3 \pm 0.5$, respectively. The errors in the M/L ratios represent the standard deviation of the mean. The M/L ratio of the full sample of dwarf galaxies was computed by taking the mean of the individual ratios obtained for the 13 dwarfs. This gives an H-band stellar M/L ratio of $\Upsilon_H = 1.4 \pm 0.4$ for the dwarf galaxies. Using the same formalism, Kirby et al. (2008) measured a stellar M/L ratio of $\Upsilon_H = 0.9 \pm 0.6$ for their sample of 57 galaxies (consisting mostly of irregular galaxies). The difference in the M/L ratios obtained for the dwarf and irregular galaxies arises from the different stellar populations in these systems. The larger M/L ratio for the dwarfs indicates that these galaxies host an older stellar population, on average, compared to that seen in the irregular systems.

The M/L ratio of $\Upsilon_H = 1.4 \pm 0.4$ was used to calculate the stellar mass of each of the IRSF dwarfs. The extinction-corrected, absolute H-band magnitudes M_H^0 of the galaxies were

Table 2.14. Total stellar masses (M_{stars}) of six IRSF dwarfs using the H-band M/L ratio of $\Upsilon_H = 1.4 \pm 0.4$.

Galaxy (1)	M_H^0 (mag) (2)	L_H ($\times 10^9 L_\odot$) (3)	M_{stars} ($\times 10^9 M_\odot$) (4)	$M_{\rm H\,I}$ ($M_\odot$) (5)	$M_{\rm H\,I}/M_{stars}$ (6)
NGC 3115 DW01	-19.81	1.84 ± 0.76	2.58 ± 1.17	–	
NGC 59	-17.99	0.34 ± 0.13	0.48 ± 0.21	1.5×10^7	0.031
LEDA 166099	-16.89	0.12 ± 0.05	0.17 ± 0.08	–	
ESO 384-016	-15.67	0.04 ± 0.01	0.06 ± 0.03	6.0×10^6	0.100
NGC 5206	-19.50	1.38 ± 0.57	1.93 ± 0.87	5.5×10^5	< 0.001
UGCA 200	-16.64	0.10 ± 0.04	0.14 ± 0.06	–	

Note. — Columns (2): Extinction-corrected, absolute H-band magnitudes; (5): H I masses of galaxies taken from the literature: NGC 59 and ESO 384-016 from Beaulieu et al. (2006); NGC 5206 from Côté et al. (1997). The upper H I mass limit is quoted for the galaxy NGC 5206.

converted into luminosity using the standard relation

$$L_H = 10^{0.4(M_{H,\odot} - M_H^0)} \tag{2.19}$$

where $M_{H,\odot} = 3^{\rm m}.35$ is the H-band luminosity of the sun (Colina et al. 1996). The total stellar masses of the galaxies are listed in Table 2.14. The two brightest dwarfs (NGC 3115 DW01 and NGC 5206) in the sample ($M_H^0 < -19^{\rm m}.0$), have the largest stellar masses. These are of the order of $10^9 M_\odot$. Puzia et al. (2000) measure $(4.8 \pm 2.3) \times 10^{10}$ M$_\odot$ as the lower mass estimate of NGC 3115 DW01 (see section 2.2.2). This mass estimate was obtained from the kinematics of seven GCs in the galaxy. We have derived an H-band stellar mass of $(2.6 \pm 1.2) \times 10^9$ M$_\odot$ for NGC 3115 DW01 which is ~ 25 times lower than the mass estimate imposed by the kinematics of the seven GCs. The dynamical mass of NGC 3115 DW01 is measured out to a projected radius of $r \simeq 2.7'$, making it almost twice as large as the radius in which the stellar mass of the galaxy was determined. This result suggests that NGC 3115 DW01 is a very DM dominated galaxy with no direct evidence of an extended DM halo (e.g., Kleyna et al. 2002). On the other hand, it is also possible that the GC system of Puzia et al. (2000) is not virialised around NGC 3115 DW01 giving the higher dynamical mass estimate for the galaxy.

Given the H I masses for the galaxies NGC 59 and ESO 384-016, we are able to derive the H I gas-to-star mass fractions for these systems (see Table 2.14). The H I mass of NGC 59 corresponds to $\sim$3% of its total stellar mass. This galaxy contains the largest amount of H I gas compared to other early-type dwarfs in the Scl group (Bouchard et al. 2005; Beaulieu

Table 2.15. Total stellar masses (M_{stars}) of six IRSF dwarfs using the H-band M/L ratio of $\Upsilon_H = 1.0 \pm 0.4$.

Galaxy (1)	M_H^0 (mag) (2)	L_H ($\times 10^9 L_\odot$) (3)	M_{stars} ($\times 10^9 M_\odot$) (4)	$M_{\rm H\,I}$ ($M_\odot$) (5)	$M_{\rm H\,I}/M_{stars}$ (6)
NGC 3115 DW01	-19.81	1.84 ± 0.76	1.84 ± 1.17	–	
NGC 59	-17.99	0.34 ± 0.13	0.34 ± 0.22	1.5×10^7	0.044
LEDA 166099	-16.89	0.12 ± 0.05	0.13 ± 0.08	–	
ESO 384-016	-15.67	0.04 ± 0.01	0.04 ± 0.03	6.0×10^6	0.150
NGC 5206	-19.50	1.38 ± 0.57	1.38 ± 0.87	5.5×10^5	< 0.001
UGCA 200	-16.64	0.10 ± 0.04	0.10 ± 0.06	–	

Note. — Columns (2): Extinction-corrected, absolute H-band magnitudes; (5): H I masses of galaxies taken from the literature: NGC 59 and ESO 384-016 from Beaulieu et al. (2006); NGC 5206 from Côté et al. (1997). The upper H I mass limit is quoted for the galaxy NGC 5206.

et al. 2006). The relatively large H I content of NGC 59 suggests that this galaxy is not a typical dS0 galaxy. Instead, this detection supports the claim of Bouchard et al. (2005) that this dwarf should rather be classified as dS0 pec based on its H I content and the detection of ionized gas in the galaxy center. The galaxy ESO 384-016 exhibits a larger gas fraction to that detected for the star-forming galaxy NGC 59. This correlates with the H I mass to B-band luminosity ratios measured by Beaulieu et al. (2006) where the lower H I gas fraction was measured for NGC 59. These were found to be $M_{\rm H\,I}/L_B = 0.21$ for ESO 384-016 while NGC 59 has $M_{\rm H\,I}/L_B = 0.07$. ESO 384-016 represents one of four mixed-type dwarfs in the Cen A group (Bouchard et al. 2007). Only two of the mixed-type dwarfs (including ESO 384-016) have been detected in H I. These galaxies show $M_{\rm H\,I}/L_B$ ratios similar to that found for mixed-morphology dwarfs in the LG (St-Germain et al. 1999; Bouchard et al. 2006). In addition, the H I distribution of ESO 384-016 (see Fig. 2.5) shows an eastern extension of the gas. Bouchard et al. (2007) suggest that the H I distribution of this galaxy is a result of mild ram pressure exerted by an intergalactic medium of density $\rho_{\rm IGM} \sim 10^{-3}{\rm cm}^{-3}$. They also find the Cen A environment to be much more efficient in removing gas from dwarfs than the Scl group. The upper H I mass limit for NGC 5206 was used to estimate the gas fraction of this dwarf. The stellar mass is the main contributor to the baryonic mass of this galaxy. The H I gas content of NGC 5206 is found to be less than 0.1% of the total stellar mass.

Kirby et al. (2008) have adopted a M/L ratio of $\Upsilon_H = 1.0 \pm 0.4$ which represents the weighted average of values obtained from galaxy observations (Bell et al. 2003) and theory

(de Jong 1996; Bell & de Jong 2001). The total stellar masses of the IRSF dwarfs were computed using the M/L ratio of $\Upsilon_H = 1.0$ and are listed in Table 2.15. This M/L estimate leads to a $\sim 30\%$ reduction in the total masses of the galaxies given in Table 2.14. These mass estimates do not significantly affect the H I gas-to-star mass ratios of the galaxies. The largest H I gas fraction of 15% of the stellar mass is measured for the galaxy ESO 384-016.

2.10 Summary of Results

Deep J-, H- and K_s-band imaging was obtained for six LV dwarf galaxies. The three most luminous ($M_B < -15^{\rm m}.5$) galaxies in our sample (NGC 3115 DW01, NGC 59 and NGC 5206) have been detected by 2MASS while the fainter galaxies were not. The total magnitudes of the three luminous dwarfs were compared to the corresponding magnitudes given by 2MASS. The results indicate that 2MASS underestimates the flux of these galaxies by up to $\lesssim 0^{\rm m}.5$ in agreement with findings of Andreon (2002) and Kirby et al. (2008). The 2MASS survey has failed to detect the three faintest galaxies, ESO 384-016, LEDA 166099 and UGCA 200, emphasizing the biases affecting the 2MASS catalogue at low luminosities and star densities.

The internal structure of the galaxies is revealed by the IRSF images which, apart from having much higher exposure times, have a four times better spatial resolution than the 2MASS images. This is most prominently seen in the luminous galaxies NGC 3115 DW01, NGC 59 and NGC 5206 where the bright nuclei can be dissociated from the stellar disks. The deep NIR observations allow for the extraction of the galaxy SB profiles out to the $\mu \sim 25$mag arcsec^{-2} in the J- and H-bands, and $\mu \sim 23.5$mag arcsec^{-2} in the K_s-band. The central structure of the galaxies is effectively seen in the SB profiles. To gain better understanding of the galaxy structure, a two-component (bulge-disk) decomposition of the light profiles was made. Steep profile shapes of $n > 4$ were measured for NGC 3115 DW01 and NGC 5206 indicating that these galaxies contain massive cores. The NIR structural parameters of the fainter galaxies ESO 384-016, LEDA 166099 and UGCA 200 are similar to those measured for nearby dwarfs. The structural parameters for NGC 59 show that this dwarf has features common to both spirals and low SB dwarf galaxies in the NIR. The IRSF dwarfs follow the trend of increasing central surface brightness μ_s with H-band luminosity which suggests that these galaxies have similar formation mechanisms.

The deep NIR images of NGC 59 reveal an intriguing double nuclear component in the center of the galaxy. Based on the kinematical studies of this galaxy (Chapter 3), the northern component is characterized as the "true" galaxy nucleus. The secondary component is assumed to be a star-forming knot given the presence of highly ionized gas in the central $15''$ of this galaxy. The NIR colours of the individual nuclear components are not indicative of an evolved stellar population. Instead, the colours represent a combination of the underlying stellar and ionized gas component of the galaxy. The two nuclear components show similar NIR colours to those measured for the star-forming knots in BCD galaxies. This suggests that both components have experienced recent star formation activity. The nucleus of NGC 59 is observed to have redder $H - K_s$ colour than the star-forming knot. The decrease in the $H - K_s$ colour going from the nucleus to star-forming knot corresponds to a decrease in the

gas fraction. This can simultaneously be interpreted as an age trend where the star-forming knot is the older component. The $H - K_s$ colours suggest that the nucleus of NGC 59 has experienced the most recent starburst which dominates the NIR emission of this component. The physical mechanism triggering the star formation in this relatively isolated galaxy is not understood. However, it is possible to adopt a propagating star formation scenario in which the shock waves from supernovae in the older knot trigger star formation in the nucleus of NGC 59.

The SB profiles of the galaxies were used to derive the NIR colours as a function of radius. The $J - K_s$, $H - K_s$ and $J - H$ colour profiles show little variation with galaxy radius. The mean colours of the galaxies were obtained by averaging these profiles. The redder colours of $J - K_s > 0\overset{\mathrm{m}}{.}8$ are measured for the galaxies NGC 3115 DW01, LEDA 166099 and NGC 5206. A mean colour in the range of $0\overset{\mathrm{m}}{.}7 < J - K_s < 0\overset{\mathrm{m}}{.}8$ is measured for the remaining dwarfs in the sample. The blue $J - K_s$ colour of NGC 59 is a reflection of the younger stellar population in its center. The galaxy ESO 384-016, however, shows no indication of star formation but contains an old, metal-poor stellar population. The relation between the $J - K_s$ colour and the absolute K_s-band magnitude was used to explore the metallicities of the galaxies. The six IRSF dwarfs show almost constant $J - K_s$ colours with increasing K_s-band luminosity. This is in agreement with the $J - K_s$ colour-luminosity relation observed for the early-type Virgo dwarfs. These galaxies show in general a weak correlation between the $J - K_s$ colour and metallicity for early-type dwarfs. The stellar content of the dwarfs were further investigated by deriving their $B - K_s$ colours. These colours show red, evolved stellar populations for the galaxies NGC 3115 DW01 and NGC 5206. The remaining galaxies are found to have bluer $B - K_s$ colours similar to those of dIrr galaxies. The star formation in the center of NGC 59 results in this galaxy having $B - K_s$ colour similar to BCDs.

A tight correlation is observed between the B- and H-band luminosities of the galaxies. This suggests that the dwarfs exhibit similar morphologies in the optical and NIR bands. The galaxies are therefore minimally affected by the presence of dust and star formation. This result is most surprising for the galaxy NGC 59 which has experienced a recent starburst. It is expected that the optical bands are dominated by emission from the younger stars. The younger stellar component is however found to contribute significantly to the NIR emission in the H-band. This allows for little scatter from the observed trend between the B- and H-band luminosities of the galaxies.

The total stellar masses of the IRSF dwarfs were derived using the H-band M/L ratio of $\Upsilon_H = 1.4 \pm 0.4$. The M/L estimate for the dwarf galaxies was obtained from the linear $B-H$ coefficients defined by M/L-colour relation of Bell & de Jong (2001). The two brightest galaxies ($M_H^0 < -19\overset{\mathrm{m}}{.}0$) in the sample are found to have stellar masses of $\gtrsim 10^9\,\mathrm{M}_\odot$. A stellar mass of $(2.6 \pm 1.2) \times 10^9\,\mathrm{M}_\odot$ was measured for the galaxy NGC 3115 DW01. This estimate of the stellar mass is ~ 25 times lower than the lower mass estimate of $(4.8 \pm 2.3) \times 10^{10}\,\mathrm{M}_\odot$ imposed by the kinematics of seven GCs in the galaxy. The radial distance in which the dynamical mass has been determined allows us to conclude that NGC 3115 DW01 is an extremely DM dominated galaxy. The H I gas-to-star mass fractions ($M_{\mathrm{H\,I}}/M_{stars}$) of 0.03 and 0.1 have been determined for the galaxies NGC 59 and ESO 384-016, respectively.

The relatively large amounts of H I gas in these galaxies allows them to be classified as mixed-morphology dwarfs rather than typical early-type systems. The elongation in the H I distribution of ESO 384-016 suggests that this galaxy could be experiencing gas loss due to ram pressure stripping in the Cen A group. The galaxy NGC 5206 is found to be gas deficient in H I with an H I gas fraction of $< 0.1\%$. This finding provides further evidence for NGC 5206 being an evolved dwarf galaxy which has exhausted its gas content by undergoing several episodes of star formation.

Chapter 3

A Detailed Study of Dwarf Lenticular Galaxy NGC 59 Based on Longslit and Deep Near-infrared Observations

3.1 Introduction

In this chapter, we present a pilot study of the search for intermediate-mass black holes (IMBHs) in the center of dwarf galaxies (see Chapter 1, section 1.2.1). These are BHs having masses in the range of $10^3\,\mathrm{M}_\odot \lesssim M_{\mathrm{BH}} \lesssim 10^6\,\mathrm{M}_\odot$ falling between the two familiar classes of BHs (i.e., supermassive and stellar-mass BHs). A single galaxy candidate was selected from the large sample of dwarf galaxies (see Appendix A, Table A.1) for this purpose. The kinematics of the galaxy was determined using longslit optical spectra from the 10m Southern African Large Telescope (SALT). These spectra were acquired during the Performance Verification phase of the Robert Stobie Spectrograph (RSS).

Longslit spectroscopic observations were obtained for the Sculptor (Scl) group dwarf galaxy, NGC 59. The relative high surface brightness ($\mu_{B,\mathrm{eff}} \sim 21.3\mathrm{mag\ arcsec}^{-2}$) of NGC 59 made this galaxy ideal for PV phase observations. In addition, the distinct nucleus of NGC 59 makes it a prime candidate for the search of a central IMBH. The kinematical analysis of NGC 59 will allow us to assess the feasibility of carrying out this ambitious project with the SALT telescope in the future. At the same time, a complete picture of the evolutionary state of the dwarf galaxy NGC 59 is constructed by combining the optical spectra with the near-infrared (NIR) results from Chapter 2. The kinematic results of NGC 59 will help answer some intriguing questions regarding the dynamics of the galaxy. These include: do the random motions of stars give any first clues of a possible IMBH in the center of NGC 59? Is NGC 59 a rotationally or pressure-supported system? What role does the environment play in the overall dynamics of this Scl group galaxy? These issues are fundamental in understanding the formation and evolution of dwarf galaxies.

Recent star formation activity was detected in the center of NGC 59 by Skillman et al. (2003). The young stars heat up the surrounding gas giving rise to regions of ionized gas (or H II regions) in the galaxy center. The presence of highly ionized gas is revealed by strong [O III] emission lines in the galaxy spectrum. The H II regions in the center of NGC 59 allow for the derivation of its chemical content. The element abundance ratios can be directly compared to the values obtained for dwarf galaxies in the field and group environments. The chemical analysis of NGC 59 provides another crucial piece of information that will be used to trace the evolutionary path of this galaxy.

The kinematic analysis of more dwarf galaxies from the large sample of Table A.1 will be

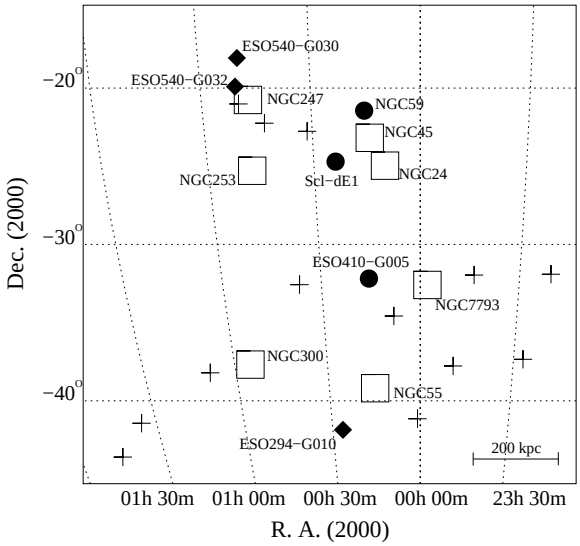

Figure 3.1 Sky distribution of all known galaxies of the Scl group taken from Bouchard et al. (2005). The different symbols denote galaxy type: squares – main group members; circles – early-type dwarfs; diamonds – mixed-type dwarfs; plus sign – late-type dwarfs. The scale of the figure (at a distance of 2Mpc) is indicated in the lower right corner.

carried out at a later stage. The galaxy observations will be optimized based on the findings of our pilot study. Not only will the large sample of dwarf galaxies allow for an investigation of the existence of a central IMBH in nearby galaxies, it will also give a detailed account of the effects of environment on the evolution of dwarf galaxies. Overall, these results can provide more clues to the formation and evolution of dwarf galaxies which still remains a largely debated topic in modern astrophysics.

3.2 Properties and Environment of NGC 59

3.2.1 Structure of the Sculptor Group

The Scl group consists of ∼26 galaxies with distances in the range of 1.5–4.4Mpc (Jerjen et al. 1998; Jerjen & Rejkuba 2001; Karachentsev et al. 2000b, 2003b). The sky distribution of all known members of the group taken from Bouchard et al. (2005) are shown in Fig. 3.1. The main members of the Scl group are seven late-type spiral galaxies: NGC 24, 45, 55, 247, 253, 300 and 7793. The remaining group members are dwarf galaxies which consist of 6 early-type (dS0, dE) and 13 late-type (dIrr) dwarfs.

Insight into the three-dimensional distribution of the Scl group galaxies is given by Jerjen et al. (1998) and Karachentsev et al. (2003b). The pseudo-three-dimensional plot of the major group members and 5 early-type dwarfs can be seen in Fig. 3.2 (taken from Jerjen et al. 1998). It should be noted that the late-type dwarf galaxies seen in Fig. 3.1 are not included

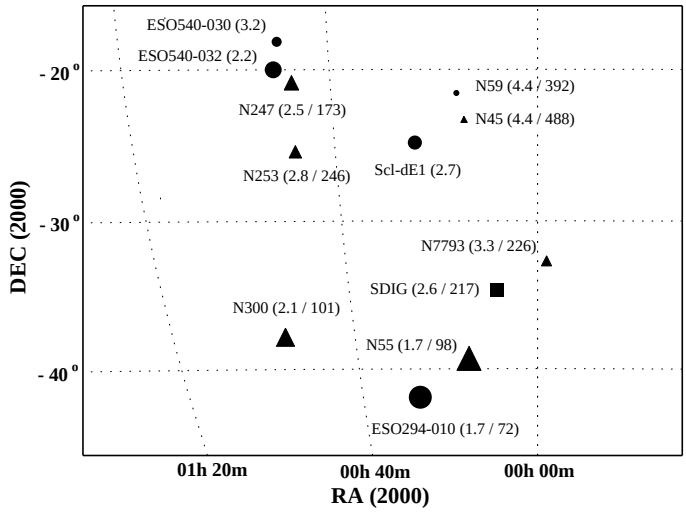

Figure 3.2 Sky distribution of the main group members (*triangles*) and 5 early-type dwarfs (*circles*) of the Scl group taken from Jerjen et al. (1998). The location of the Sculptor dwarf irregular galaxy (SDIG) is indicated by a square. The symbol size is inversely proportional to the galaxy distance to simulate a depth effect. The names, distances (in Mpc) and galactocentric velocities (if available) are indicated for each galaxy.

in this plot. The plot shows the sky distribution of the galaxies with their distances inversely proportional to the symbol size. Jerjen et al. (1998) found a close match in the distance of ESO 294-010 with NGC 55 at the near end (1.7Mpc), and of NGC 59 and NGC 45 at the far end (4.4Mpc) of the Scl group. They suggest that the two dwarf galaxies, ESO 294-010 and NGC 59, are bound companions to these major members. The dwarf galaxies are separated by < 200 kpc in projection from the main members and have a radial velocity difference of $\Delta v_{\odot} < 100$ km s^{-1}.

The Scl group consists of four subclumps centered on the galaxies NGC 55, NGC 253, NGC 7793 and NGC 45. The galaxies associated with the NGC 45 subclump have $v_{\rm LG} > 400$ km s^{-1} and are found on the outskirts of the group. The brightest spiral galaxy, NGC 253, together with its companions are considered to be the core of the Scl group (Karachentsev et al. 2003b). The more accurate distance estimates for NGC 253 ($D \sim 3.79$Mpc) and NGC 7793 ($D \sim 3.82$Mpc) from the tip of the red giant branch (TRGB), gives overlapping radial distances for these galaxies. The dIrr galaxies are not strongly associated with the main group members but are scattered over the entire volume of the group. This property is in agreement with the morphology-density relation for dwarf galaxies (Binggeli et al. 1990) in which dwarf irregulars are known to avoid high-density regions.

Jerjen et al. (1998) found that the overall shape of the Scl group takes the form of a cigar of length 3Mpc and thickness 1Mpc. An observer sees the Scl group pole-on since the Local Group (LG) lies near its end. The Hubble flow at the group shows no evidence for disturbance

due to the gravitational interaction between the main group members (Karachentsev et al. 2002b). They measure a large local Hubble constant of 119 km s^{-1} Mpc^{-1} using nine galaxies in the Scl group. A plausible explanation for the deviation from the global Hubble law ($H_0 \sim 70 \pm 1.3$ km s^{-1} Mpc^{-1}; Spergel et al. 2007) is given by the gravitational influence of the nearby, massive LG. Tidal forces of the LG can lead to a deceleration in the Hubble flow which is most effectively seen in the nearest Scl group galaxies. Jerjen et al. (1998) conclude that the LG and Scl group are not isolated in space. Instead, these groups are part of a large prolate cloud ($6 \times 2 \times 1$ Mpc^3 in size) of dIrr galaxies well defined in the Supergalactic plane.

The sparse distribution of galaxies in the Scl group allows for the study of dwarf galaxy evolution in a low-density environment. The majority of galaxies in the Scl group are in the late stages of evolution with depleted levels of neutral hydrogen gas (Côté et al. 1997; Bouchard et al. 2005). The six early-type dwarf galaxies show some indication of young blue stars in their central regions (Jerjen et al. 2000b; Karachentsev et al. 2000b; Jerjen & Rejkuba 2001; Karachentsev et al. 2003b). The mechanism triggering star formation in these relatively isolated systems of the Scl group is not well understood. It is expected that external factors such as ram pressure stripping or tidal interactions minimally affect the morphology of these galaxies. The absence of large-scale gravitational interactions in the Scl group provides an environment in which the intrinsic properties influencing dwarf galaxy evolution (e.g., supernova explosions, stellar winds) can be explored.

3.2.2 Properties of NGC 59

An extensive H I survey of dwarf galaxies in the Scl group (as well as the Cen A group) was conducted by Côté et al. (1997) using the 64m ATNF Parkes radio telescope. The group membership of the dwarfs was established based on their measured radial velocities. The H I detection limit of galaxies in the Scl group was $4 \times 10^6 M_\odot$. The dwarfs having an H I mass above this detection limit were confirmed as galaxies of the Scl group. Côté et al. (1997) measure a heliocentric radial velocity of $v_\odot \sim 367 \pm 2$km s^{-1} for NGC 59 which places this galaxy on the outskirts of the Scl group (see Fig. 3.2). They also measure an H I mass of $M_{\rm H\,I} \sim 5.4 \times 10^6\,M_\odot$ making NGC 59 one of the few early-type dwarfs in the Scl group having a substantial amount of H I gas.

Follow-up optical observations by Côté et al. (1997) revealed Hα line emission in the spectrum of NGC 59. This emission line indicates that NGC 59 must have experienced recent star formation activity. The Hα emission line allows for an independent measure of the galaxy's radial velocity. A heliocentric velocity of $v_\odot \sim 357 \pm 10$km s^{-1} was measured for NGC 59 using this optical emission line. The heliocentric velocity derived from the Hα line confirms that the detected H I gas is associated with NGC 59 and not with the high velocity clouds of the Galaxy. High velocity clouds are known to have velocities in the range of $70 - 450$km s^{-1} in the direction of the Scl group (Putman 2000).

The most recent H I observations of NGC 59 were carried out by Beaulieu et al. (2006) using the Australian Telescope Compact Array (ATCA). The dwarf galaxy NGC 59 was one of 10 dE/dS0 galaxies selected in the Scl and Cen A groups. The H I detection limit of the observations was $\sim 5.3 \times 10^5 M_\odot$. NGC 59 was the only Scl group early-type dwarf detected

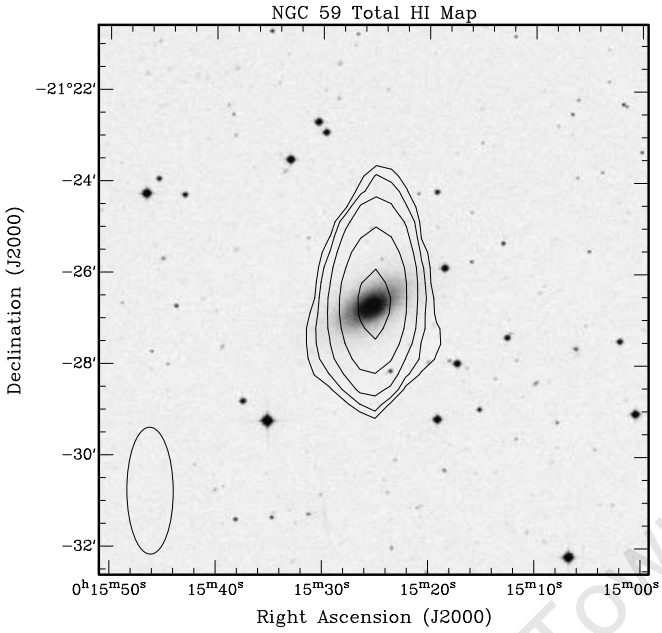

Figure 3.3 Total H I map of NGC 59 from Beaulieu et al. (2006) superimposed on the DSS optical image. The beam size of ATCA is shown in the lower left corner.

above this H I mass limit. The H I map of NGC 59 can be seen in Fig. 3.3 which shows that the distribution of neutral hydrogen gas is barely resolved with the beam size of ATCA. Beaulieu et al. (2006) measure a heliocentric velocity of $v_{\odot} \sim 359$km s^{-1} for the galaxy. This value is in good agreement with the measurements of Côté et al. (1997). Beaulieu et al. (2006) measure an H I mass of $M_{\rm H\,I} \sim (1.5 \pm 0.3) \times 10^7 {\rm M}_{\odot}$ for NGC 59 providing additional support that this galaxy is one of the most gas-rich dwarfs in the Scl group. The reservoir of neutral hydrogen gas is believed to be fueling the star formation activity at the galaxy center. The relatively large gas content of NGC 59 distinguishes this galaxy from the gas-poor dE systems. An H I mass-to-light ratio of $M_{\rm H\,I}/L_B \sim 0.07$ was measured for NGC 59 which lies closer to those values obtained for dIrr or normal spiral galaxies (see e.g., Broeils & Rhee 1997).

Optical imaging of the dwarf galaxy NGC 59 is available from the ESO/SERC sky survey. The optical morphology of the galaxy reveals a disc component which led Karachentseva & Karachentsev (1998) to classify NGC 59 as a dwarf lenticular (dS0) galaxy. An extended stellar disc is also observed in the NIR images presented in Chapter 2. This feature can clearly be seen in the combined JHK_s-band image of NGC 59 shown in Fig. 3.4. The disc component separates the morphology of NGC 59 from those of "classical" dE galaxies.

Deep B- and R-band imaging of NGC 59 was obtained by Jerjen et al. (1998). Employing the surface brightness fluctuation technique of Tonry & Schneider (1988), a distance of 4.4Mpc was measured for the galaxy which corresponds to $v_{\rm LG} = 431$km s^{-1} ($H_0 = 73$km sec^{-1} Mpc^{-1}; Karachentsev & Makarov 1996). The absolute magnitude of

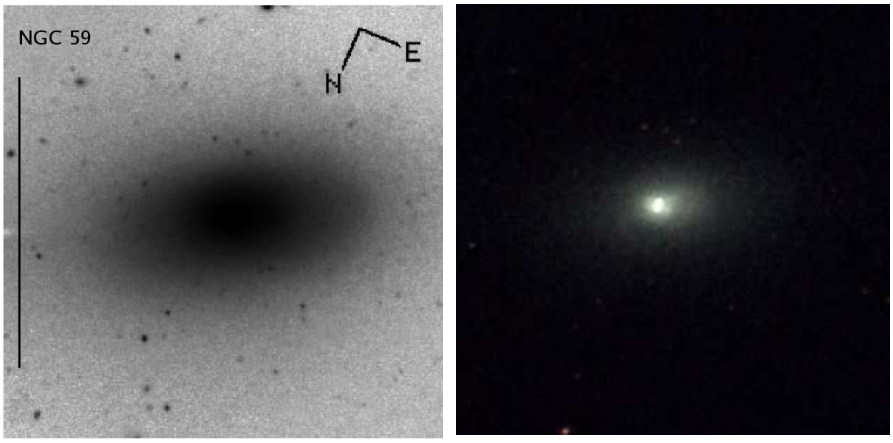

Figure 3.4 Comparison of the R-band (*left*) and JHK_s-color image (*right*) of NGC 59. Optical imaging of the galaxy was carried out by Jerjen et al. (2000b) while the NIR imaging was obtained using the IRSF telescope (Chapter 2). The vertical bar in the optical image indicates a scale of $2'$. The orientation and size of the NIR image is the same as the optical image.

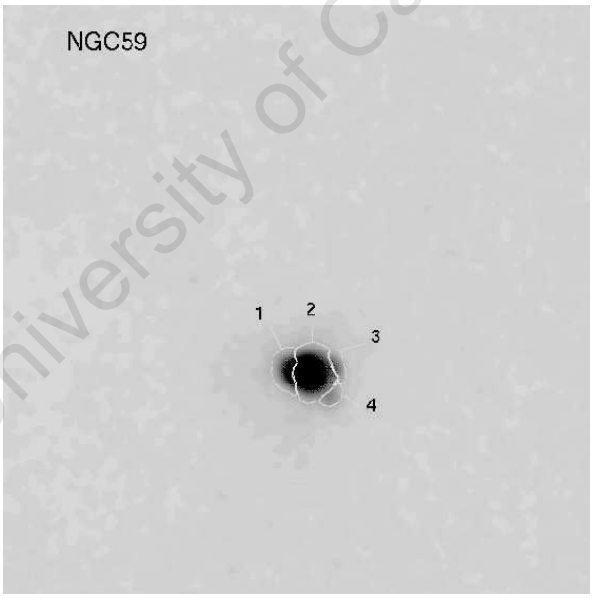

Figure 3.5 Continuum (i-band) subtracted Hα image of NGC 59 taken from Skillman et al. (2003). The H II regions in the galaxy center are labelled. The image size is $1\farcm96 \times 1\farcm96$. North is up and East is left.

NGC 59 is $M_B = -15^{\rm m}.3$ making it one of the brightest dwarf galaxies in the Scl group. The B- and R-band imaging of NGC 59 was later used by Jerjen et al. (2000b) to derive the $B-R$ color profile of the galaxy (see Fig. 2.4 in Chapter 2). A decrease of $1^{\rm m}.5$ in the $B-R$ color is observed towards the center of the galaxy. The bluer colors towards the galaxy center together with the Hα detection of Côté et al. (1997), served as a first indication of a younger stellar population residing in the central regions of NGC 59.

Skillman et al. (2003) carried out narrow-band Hα imaging of NGC 59. The continuum (i-band) subtracted Hα image of NGC 59 is shown in Fig. 3.5. Ionized gas was detected in the central $15''$ of the galaxy. Skillman et al. (2003) decomposed the ionized gas into four H II regions, each of which has a distinct peak in the Hα emission. These regions are separated by contours of constant Hα surface brightness level. The Hα flux from the central H II region (labeled No. 2 in Fig. 3.5) is at least five times greater than its neighbouring counterparts. The relation of Kennicutt et al. (1994) was used to convert the total Hα luminosity from all H II regions to a current star formation rate. This relation has been derived for normal spiral galaxies with a modified Salpeter initial mass function. A star formation rate of $3.1 \times 10^{-3}\,{\rm M}_{\odot}\ {\rm yr}^{-1}$ was determined for NGC 59. This moderate star formation activity is detected in most dIrr galaxies of the Scl group (Skillman et al. 2003). A summary of the properties of NGC 59 is given in Table 3.1.

The complementary NIR and optical data sets presented in this thesis will contribute to our current knowledge of this galaxy. In particular, the dominant older stellar population was used to explore the NIR morphology of NGC 59 (see Chapter 2). Further insight into the processes governing the evolution of NGC 59 can be gained from the optical spectra. These investigations include a detailed mapping of the stellar and ionized gas kinematics along the major axis of the galaxy. The stellar kinematics will indicate whether the galaxy is supported by rotation or anisotropic pressure, while the velocity dispersion of stars can give the first indication of a possible BH in the galaxy center (see e.g., Geha et al. 2002). The chemical content of NGC 59 is also derived in this chapter, which will provide more vital clues as to how this galaxy has evolved.

3.3 SALT Longslit Observations of NGC 59

The stellar component of galaxies outside of the LG is observed as a continuum of light from the individual stars. The determination of the galaxy kinematics using individual stars at these distances remains an impossible task with current ground and space-based telescopes. Instead, the kinematics of galaxies beyond the LG are derived by measuring the average motions of stars along a particular line-of-sight. One of the observational techniques to measure the bulk motions of stars about a defined axis is by means of longslit spectroscopy. By positioning the slit along the semi-major axis, the global motions of stars are obtained leading to an overall view of the kinematics of the galaxy.

Longslit spectroscopic observations of the dwarf galaxy NGC 59 were carried out with the Robert Stobie Spectrograph[1] (RSS; Burgh et al. 2003; Kobulnicky et al. 2003) on the 10m

[1]See http://www.salt.ac.za/telescope/instrumentation/pfis/ for an overview of the design of the Robert

Table 3.1. Known properties of NGC 59 from the literature

Parameter			Comment	References
Optical	RA (J2000)	00 15 25.1		1
	DEC (J2000)	-21 26 40.0		1
	M_B (mag)	-15.3		2
	Classification	dS0	Part of the ESO/SERC sky survey.	3
	Distance (Mpc)	4.39 ± 0.15	R-Band imaging. SBF method.	2
	$B-R$ (mag)	1.04	Extinction-corrected $B-R$ color.	2
	A_B (mag)	0.09	Galactic extinction using dust maps of Schlegel et al. (1998).	2
	SFR ($M_\odot$ yr^{-1})	3.1×10^{-3}	Star formation rate from Hα imaging.	6
	$v_\odot$(km s^{-1})	357 ± 10	Heliocentric velocity from Hα emission line	4
H I	$v_\odot$(km s^{-1})	367 ± 2	Telescope: 64m Parkes. RMS noise: 30mJy $beam^{-1}$.	4
	$v_\odot$(km s^{-1})	359	Telescope: ATCA. RMS noise: 2.6mJy $beam^{-1}$.	5
	Mass ($M_\odot$)	$(1.5 \pm 0.3) \times 10^7$		5
	M_{HI}/L_B	0.07		5

Note. — REFERENCES–(1) NASA/IPAC Extragalactic Database (NED); (2) Jerjen et al. (1998); (3) Karachentseva & Karachentsev (1998); (4) Côté et al. (1997); (5) Beaulieu et al. (2006); (6) Skillman et al. (2003)

SALT telescope[2] (Buckley et al. 2006; O'Donoghue et al. 2006). The RSS spectrograph is expected to have a nearly constant throughput between the wavelength range of 4000–6500 Å. It is this high sensitivity of the RSS in the blue which distinguishes SALT from other large aperture telescopes. The blue sensitivity of the SALT/RSS can therefore be fully exploited by carrying out longslit observations of the dwarf galaxies in the blue wavelength range. Here, the Ca II K and H absorption lines, as well as multiple strong Balmer lines can be used to trace the kinematics of the galaxies.

The stellar population in the dwarf galaxies in our sample (given by the $B-R$ colour in Table A.1) varies significantly from one galaxy to the next. The choice of the observational configuration (and consequently the wavelength range) will therefore depend on whether the galaxy hosts an older or younger stellar population. The spectral resolution in the blue and red wavelength ranges are comparable, placing no additional constraints on the observational configuration for the galaxies. The longslit observations of the dwarf galaxy NGC 59 were mainly carried out in the blue as this galaxy is known to host a younger stellar population in its center. Additional longslit observations of NGC 59 were, however, obtained in the red spectral range for comparison of the kinematic results.

A list of all the data obtained with the SALT/RSS instrument is given in Table 3.2. The spectra were acquired during the Performance Verification (PV) phase of the telescope (May–August 2006). The observations were performed during grey time with an average seeing of $1\farcs5$ in clear weather conditions. The galaxy NGC 59 was observed using three different spectral gratings: the GR3000 (3882–4619Å with spectral resolution of 0.23Å/pix), GR2300 (4780–5770Å with spectral resolution of 0.31Å/pix) and GR0900 (3640–6740Å with spectral resolution of 0.98Å/pix) gratings. These are the spectra that will be used to determine the kinematics and chemical content of NGC 59.

Stobie Spectrograph. A detailed description of the RSS spectrograph and its capabilities are provided at http://www.sal.wisc.edu/%7eebb/pfis/observer/.

[2]The website for the Southern African Large Telescope can be found at http://www.salt.ac.za/.

Table 3.2. SALT/RSS longslit spectroscopic observations of NGC 59 using the 1.″5 slit.

Date	Object	RA (J2000)	DEC (J2000)	Type	Grating	Wavelength Range (Å)	Exp (s)
2006 May 29	Arc	–	–	CuAr	GR3000	3882 – 4619	40
	HD 1116	00 15 15.1	-40 05 45.5	K0 III	GR3000	3882 – 4619	5
	NGC 59	00 15 25.1	-21 26 40.0	–	GR3000	3882 – 4619	300
	Arc	–	–	CuAr	GR3000	3882 – 4619	60
	HD 1461	00 18 41.9	-08 03 10.8	G0 V	GR3000	3882 – 4619	5
	Arc	–	–	CuAr	GR3000	3882 – 4619	60
2006 May 30	HD 1116	00 15 15.1	-40 05 45.5	K0 III	GR3000	3882 – 4619	60
	HD 1116	00 15 15.1	-40 05 45.5	K0 III	GR3000	3882 – 4619	30
	Arc	–	–	CuAr	GR3000	3882 – 4619	60
	NGC 59	00 15 25.1	-21 26 40.0	–	GR3000	3882 – 4619	900
	NGC 59	00 15 25.1	-21 26 40.0	–	GR3000	3882 – 4619	900
	Arc	–	–	CuAr	GR3000	3882 – 4619	60
	HD 1461	00 18 41.9	-08 03 10.8	G0 V	GR3000	3882 – 4619	10
	Arc	–	–	CuAr	GR3000	3882 – 4619	60
2006 May 31	HD 1116	00 15 15.1	-40 05 45.5	K0 III	GR3000	3882 – 4619	30
	HD 1116	00 15 15.1	-40 05 45.5	K0 III	GR3000	3882 – 4619	30
	Arc	–	–	CuAr	GR3000	3882 – 4619	60
	NGC 59	00 15 25.1	-21 26 40.0	–	GR3000	3882 – 4619	1200
	NGC 59	00 15 25.1	-21 26 40.0	–	GR3000	3882 – 4619	1200
	Arc	–	–	CuAr	GR3000	3882 – 4619	60
2006 June 03	LTT 6248[1]	15 38 59.7	-28 35 36.9	–	GR0900	3640 – 6740	60
	LTT 6248	15 38 59.7	-28 35 36.9	–	GR0900	3640 – 6740	60
	NGC 59	00 15 25.1	-21 26 40.0	–	GR0900	3640 – 6740	600
	NGC 59	00 15 25.1	-21 26 40.0	–	GR0900	3640 – 6740	600
2006 June 04	HD 1116	00 15 15.1	-40 05 45.5	K0 III	GR2300	4780 – 5770	10
	Arc	–	–	CuAr	GR2300	4780 – 5770	60
	NGC 59	00 15 25.1	-21 26 40.0	–	GR2300	4780 – 5770	900
	NGC 59	00 15 25.1	-21 26 40.0	–	GR2300	4780 – 5770	900
	NGC 59	00 15 25.1	-21 26 40.0	–	GR2300	4780 – 5770	900
	Arc	–	–	CuAr	GR2300	4780 – 5770	120
2006 June 05	HD 1116	00 15 15.1	-40 05 45.5	K0 III	GR3000	3882 – 4619	5
	Arc	–	–	Ar	GR3000	3882 – 4619	60
	NGC 59	00 15 25.1	-21 26 40.0	–	GR3000	3882 – 4619	1200

Table 3.2 (cont'd)

Date	Object	RA (J2000)	DEC (J2000)	Type	Grating	Wavelength Range (Å)	Exp (s)
	NGC 59	00 15 25.1	-21 26 40.0	–	GR3000	3882 – 4619	1100
	Arc	–	–	CuAr	GR3000	3882 – 4619	60

Note. — (1) LTT 6248 is a spectrophotometric standard star which is used for the relative flux calibrations of the low-resolution (GR0900) spectra of NGC 59.

The detector system of the SALT/RSS consists of three CCD chips of 2048×4102 pixels, each having two amplifiers. The gain and readnoise therefore vary from one CCD to the next. These differences in the gain and readnoise were corrected for during the pre-reductions of the spectra. The 2×2 binning of the spectra yields a spatial scale of $0\farcs256$ per binned pixel.

All galaxy observations were carried out with the $1\farcs5 \times 4\farcm0$ slit. The position of the slit on the galaxy is shown in Fig. 3.6. The observations were performed with the slit along the major-axis of the galaxy. We have used the V-band position angle of 120 degrees (measured from North to East) as given in Lauberts & Valentijn (1989) to align the slit with the galaxy. The dwarf galaxy NGC 59 has small enough angular diameter ($< 3'$ in the V-band) to be fully sampled by the $4\farcm0$ slit length.

To obtain medium-resolution blue spectra of NGC 59, the 3000 lines mm^{-1} volume phase holographic (VPH) grating (GR3000) together with the hoyaUV-34 order-blocking filter were used. The blue spectra cover the wavelength range of 3882–4619Å which includes the Ca II K and H absorption line features at λ3933 and λ3968, respectively. In the red, the galaxy NGC 59 was observed using the 2300 lines mm^{-1} grating (GR2300). The wavelength range of these spectra sample the Mg Ib triplet absorption lines ($\lambda\lambda$5167, 5173, 5184). Both the red and blue spectra will be used in the extraction of the galaxy kinematics (see section 3.5 for further details).

A quick inspection of the raw data revealed prominent emission lines in the red and blue spectra of NGC 59. These emission lines can be used to measure the abundances of the various elements in the interstellar medium (ISM) of the galaxy. Additional longslit spectroscopic observations of NGC 59 were therefore obtained using the low-resolution 900 lines mm^{-1} grating (GR0900). The chemical composition of the galaxy was derived from these spectra which sample the full-optical wavelength range of 3640–6740Å. An investigation of the chemical evolution of NGC 59 is presented in section 3.6 of this chapter.

All of the observations of NGC 59 were guided. This was achieved with an auto-guider which uses a single star in the field-of-view (FoV) to maintain the position of the slit. However, it should be noted that the guiding system was not functioning optimally during the PV phase

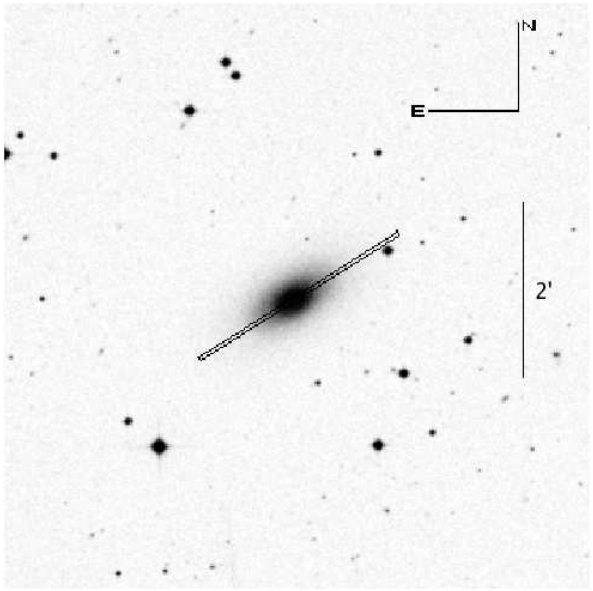

Figure 3.6 Digitized Sky Survey (DSS) image of the dwarf lenticular galaxy NGC 59. The alignment of the slit (not drawn to scale) with the major-axis of the galaxy is shown. The slit width has been exaggerated due to the small spatial scale of the DSS image.

of the SALT/RSS instrument. A V-band image of the galaxy position in the slit allowed monitoring of additional drifts of the field while the observations were performed. A nudge of $1\farcs5$ was applied to the telescope to compensate for these drifts in the field. It should be noted that there are no records of when this "nudge" was applied to the observations.

A minimum signal-to-noise (S/N) ratio of ∼10 is needed to unambiguously extract the galaxy kinematics. We estimated that this minimum S/N is required to accurately recover velocity dispersions down to an instrumental resolution of $\sigma_{\rm instr} \sim 40$km s^{-1}. An optimal exposure time for the galaxy was estimated with the SALT/RSS exposure time tool. As the earlier version of the exposure time tool was restricted to point sources, an interpolation of these exposure times to include extended sources was made using the exposure calculator of the Very Large Telescope[3] (VLT). The FOcal Reducer and low dispersion Spectrograph 2 (FORS2) is optimized for observations in the blue[4]. The exposure time calculator of this instrument was therefore used to calculate the correction for galaxy extent in the blue wavelength range. A similar observational setup to that of the SALT/RSS was chosen for these calculations. The corrections for galaxy extent were applied to the output exposure times given by the SALT/RSS tool which assumes that galaxy observations are sky-limited.

The calculations of the exposure time indicated that NGC 59 can be detected down to the $\mu_B = 23$mag arcsec^{-2} isophote in 1hr30min. However, the first observations in the PV

[3]The exposure time calculators for the various instruments of the European Southern Observatory (ESO) can be found at http://www.eso.org/observing/etc/.

[4]Further information about the FORS instruments are available at http://www.eso.org/sci/facilities/paranal/instruments/fors/.

phase displayed a significantly lower (30–40%) throughput at the blue end of the spectrum than predicted. After a series of tests by the SALT astronomers, this drop in the throughput was found to be a result of the mirror coatings. Further corrections to the exposure time were then applied to account for this steep drop in throughput observed in the blue wavelength range.

A detailed log of the observations is given in Table 3.2. The total exposure time of NGC 59 in the blue wavelength range was 1hr45min which consists of individual 15- to 20-minute exposures to facilitate the removal of cosmic rays. The total exposure time in the blue corresponds to a 16% rather than 30–40% correction in the exposure time for the drop in throughput since this was the maximum time that could be allocated to this project during the PV phase. In the red wavelength range, a total exposure time of 45 minutes (3×15min) was obtained. The galaxy was observed for 20 minutes using the low-resolution 900 lines mm^{-1} grating of the SALT/RSS.

The observations of radial velocity standard stars (or template stars) are necessary for fitting kinematic line-profile shapes to the galaxy spectra. A K0 III giant and a G0 V star were chosen as stellar templates for the kinematic modeling. The K0 III template star represents the dominant older stellar population and will therefore provide a better match to the absorption features in the galaxy spectrum from which the kinematics is derived. To compare the kinematic results from different template stars, a G0 V star was also selected for observation. On most nights, a radial velocity standard star was observed before and after the galaxy observations (see Table 3.2). The radial velocity templates were observed with the same instrumental setup and position angle as the galaxy.

A CuAr or Ar comparison arc lamp spectrum was taken before or after each galaxy and template star observation in order to derive the wavelength solution.

3.4 Reductions of the SALT/RSS Spectra

Standard reductions of the data were performed by the SALT astronomers at the South African Astronomical Observatory[5] (SAAO). Pre-reductions of the individual frames of the SALT/RSS detector include: bias subtraction, overscan correction and trimming, gain correction, and corrections for amplifier cross-talk. The reductions were carried out using the SALT package in IRAF[6]. This package has been specifically developed for the reduction of data obtained with the SALT/RSS instrument. The reduced image consists of the mosaiced CCD with interpolation across the CCD gaps.

The SALT astronomers found that the internal calibration unit flats obtained during the PV phase increased the pixel-to-pixel sensitivity variation of the CCD by $\lesssim 1\%$. We have chosen *not* to use these flats in flatfielding the spectra. This was done to avoid increases in the noise levels of the reduced galaxy spectra. The cosmic rays in the images were most effectively removed using the FILTER/COSMIC task in MIDAS[7].

[5]The webpage of the South African Astronomical Observatory (SAAO) is found at http://www.saao.ac.za/.

[6]The Image Reduction and Analysis Facility is distributed by the National Optical Astronomy Observatory which is operated by the Association of Universities for Research in Astronomy.

[7]Munich Image Data Analysis System (MIDAS) is distributed by the European Southern Observatory

The SALT/RSS spectra were calibrated following the procedure outlined by Massey et al. (1992)[8]. The wavelength calibrations of the spectra were performed using various IRAF tasks in the TWODSPEC package. Neither the red nor blue optical spectra have been flux-calibrated as this is not required for the extraction of the galaxy kinematics. Relative flux calibrations were performed for the low-resolution galaxy spectra.

3.4.1 Wavelength Calibrations of the Blue Spectra

The galaxy and template star spectra were wavelength-calibrated using the comparison lamp spectrum closest in time to the actual target observation. The wavelength solutions for the lamp spectra were determined using the IDENTIFY and REIDENTIFY tasks in IRAF. The wavelengths of 30–50 emission lines were identified over the entire spectral range of the CuAr lamp spectrum. These emission lines were used to measure the wavelength solution across the three CCDs. A fifth-order polynomial[9] was fitted to the positions of the arc lines. This typically gave a dispersion solution with an RMS ≤ 0.05Å for all the lamp spectra. The residuals and non-linear component of the wavelength solution for the individual lamp spectra can be found in Appendix C.1. A stable dispersion solution was measured throughout the period of the observing run.

During one night a single Ar comparison lamp spectrum was obtained. For this spectrum, a lack of strong emission lines is observed in the blue. The dispersion solution of the Ar lamp was therefore determined from ~ 20 emission lines in the spectrum. Most of the emission lines were identified on the second (4150–4390Å) and third CCDs (4399–4619Å) of the detector (see Fig. C.4 in Appendix C.1). A fifth-order polynomial was fitted to the measured wavelengths for the Ar spectrum. The largest scatter of up to $\Delta\lambda \simeq 0.06$Å in the dispersion solution was measured for the first CCD. The dispersion solution over the entire wavelength range of the Ar spectrum was determined with an RMS $\simeq 0.03$Å.

A two-dimensional (2D) wavelength solution for the CCD array was determined using the FITCOORDS task. This task gives a 2D mapping of the wavelength solution as function of position along the slit. The 2D wavelength solution for the comparison lamps were applied to the respective galaxy and template star spectra. The optical effect of geometric distortions was corrected for by performing the 2D wavelength calibration. The properties of the wavelength-calibrated spectra are shown in Table 3.3. The blue spectra sample the wavelength range of 3881–4619Å. The spectral dispersion of 0.233Å pixel^{-1} gives a velocity resolution of $\sim$ 17.8km s^{-1} pixel^{-1} at the Ca II K(λ3933) absorption line. A Gaussian FWHM of $\Delta\lambda \sim$ 1.32Å was measured from the emission lines in the comparison lamp spectra. This gives an instrumental resolution of $R \simeq 2974$ for the blue spectra. The velocity dispersion of the dwarf galaxies can therefore be detected down to $\sigma_{\rm instr} \sim 43$ km s^{-1} using the $1\farcs5$ slit and blue spectral grating.

(ESO).

[8]The manual "A User's Guide to Reducing Slit Spectra with IRAF" can be found at http://iraf.noao.edu/docs/spectra.html.

[9]It should be noted that the polynomial orders in the thesis refer directly to those which have been specified in IRAF e.g., a fifth-order polynomial fit in IRAF would actually correspond to a fourth-order fit.

Table 3.3. Properties of the wavelength-calibrated SALT/RSS spectra

Date	Object	Exp (sec)	Wavelength Range (Å)	Spectral Dispersion (Å pixel^{-1})	Velocity Resolution (km s^{-1} pixel^{-1})	Dispersion RMS[1] (Å)
2006 May 29	HD 1116	5	3881 – 4619	0.233	17.8	0.03
	NGC 59	300	3881 – 4619	0.233	17.8	0.04
	HD 1461	5	3881 – 4618	0.233	17.8	0.02
2006 May 30	HD 1116	60	3881 – 4619	0.233	17.8	0.03
	HD 1116	30	3881 – 4619	0.233	17.8	0.03
	NGC 59	900	3882 – 4619	0.233	17.8	0.02
	NGC 59	900	3882 – 4619	0.233	17.8	0.02
	HD 1461	10	3881 – 4618	0.233	17.8	0.02
2006 May 31	HD 1116	30	3882 – 4619	0.233	17.8	0.02
	HD 1116	30	3882 – 4619	0.233	17.8	0.02
	NGC 59	1200	3882 – 4619	0.233	17.8	0.02
	NGC 59	1200	3882 – 4619	0.233	17.8	0.02
2006 June 03	LTT 6248	60	3648 – 6742	0.979	56.5	0.11
	LTT 6248	60	3648 – 6742	0.979	56.5	0.11
	NGC 59	600	3648 – 6742	0.979	56.5	0.11
	NGC 59	600	3648 – 6742	0.979	56.5	0.11
2006 June 04	HD 1116	10	4780 – 5770	0.313	18.2	0.04
	NGC 59	900	4780 – 5770	0.313	18.2	0.04
	NGC 59	900	4780 – 5770	0.313	18.2	0.06
	NGC 59	900	4780 – 5770	0.313	18.2	0.06
2006 June 05	HD 1116	5	3881 – 4618	0.233	17.8	0.03
	NGC 59	1200	3881 – 4618	0.233	17.8	0.03
	NGC 59	1100	3881 – 4618	0.233	17.8	0.02

Note. — (1) RMS in the wavelength solution using a fifth-order polynomial fit. These correspond to the central row in the comparison lamp spectrum.

The sky-level in the spectrum was estimated using the outer regions of the galaxy's spatial profile. These regions were carefully selected as not to include light from the galaxy. The sky-level in the galaxy spectrum was measured and subtracted using the BACKGROUND task. A low-order polynomial was fitted to the outer regions of the galaxy spatial profile. The polynomial fit defines the sky-level which was subtracted from the galaxy spectrum.

The resulting wavelength-calibrated spectrum of the galaxy NGC 59 is shown in Fig. 3.7. The displayed spectrum corresponds to one 20-minute galaxy exposure and covers the wavelength range of 3882–4616Å. The emission lines seen throughout the galaxy spectrum are: He I(λ3889), [Ne III](λ3968), Hϵ(λ3970), Hδ(λ4101), Hγ(λ4341), [O II](λ4364) and He I(λ4471). A broad Ca II K(λ3933) absorption line is seen on the first CCD. The [Ne III] and Hϵ emission lines are superimposed on the dominant Ca II H(λ3968) absorption line feature. It can also be seen that the hydrogen absorption lines are well visible underneath the corresponding hydrogen emission line features.

3.4.2 Calibrations of the Red and Low-resolution Spectra

The wavelength calibrations of the red medium-resolution (4780–5770Å) and low-resolution (3640–6740Å) spectra of NGC 59 were performed in the same manner as for the blue spectra. The residuals and non-linear component of the wavelength solution for both gratings are given in Appendix C.1. The fifth-order polynomial fit to the measured wavelengths results in a dispersion solution with RMS $\leq$ 0.1Å for the comparison lamp spectra. A total of 64 emission lines were used to determine the wavelength solution of the low-resolution spectra. The largest scatter in the dispersion solution (RMS $\simeq$ 0.1Å) is observed when fitting the full optical range of 3640–6740Å.

Two exposures of the comparison lamp were obtained with the red spectral grating (see Fig. C.5 in Appendix C.1). A CuAr and Ar spectrum was acquired before and after the galaxy observations of June 4, respectively. The number of emission lines used to determine the wavelength solution for the CuAr and Ar spectra are 29 and 37, respectively. The fifth-order polynomial fit to the measured wavelengths gives a slightly larger scatter (RMS $\simeq$ 0.06Å) for the CuAr spectrum. It was found that the CuAr lamp was not sufficiently heated before the exposure which resulted in the weaker emission lines in the comparison spectrum. This leads to the larger errors of up to $\Delta\lambda \simeq$ 0.1Å in the measured wavelengths of the emission lines. The dispersion solution for the Ar spectrum excludes the wavelength range of 5250–5400Å which does not contain strong emission lines.

An additional check of the wavelength solutions for the red spectra is provided by the sky emission line at λ5577. The wavelength of the λ5577 night-sky emission line was measured at the location of the galaxy in the slit. The wavelength of the sky emission line was measured using a Gaussian fit to the line-profile. The wavelength of this line does not vary with slit position which indicates that the 2D wavelength solution is well determined for the individual galaxy spectra. The first galaxy spectrum showed an offset of 11km s^{-1} with respect to the rest wavelength of the λ5577 emission line. A smaller offset of $\lesssim$ 3km s^{-1} is observed for the two remaining galaxy spectra. The uncertainties in the measured wavelength of the λ5577 line are $\epsilon <$ 2km s^{-1}. An offset of $\sim$ 3km s^{-1} from the rest wavelength of the sky emission

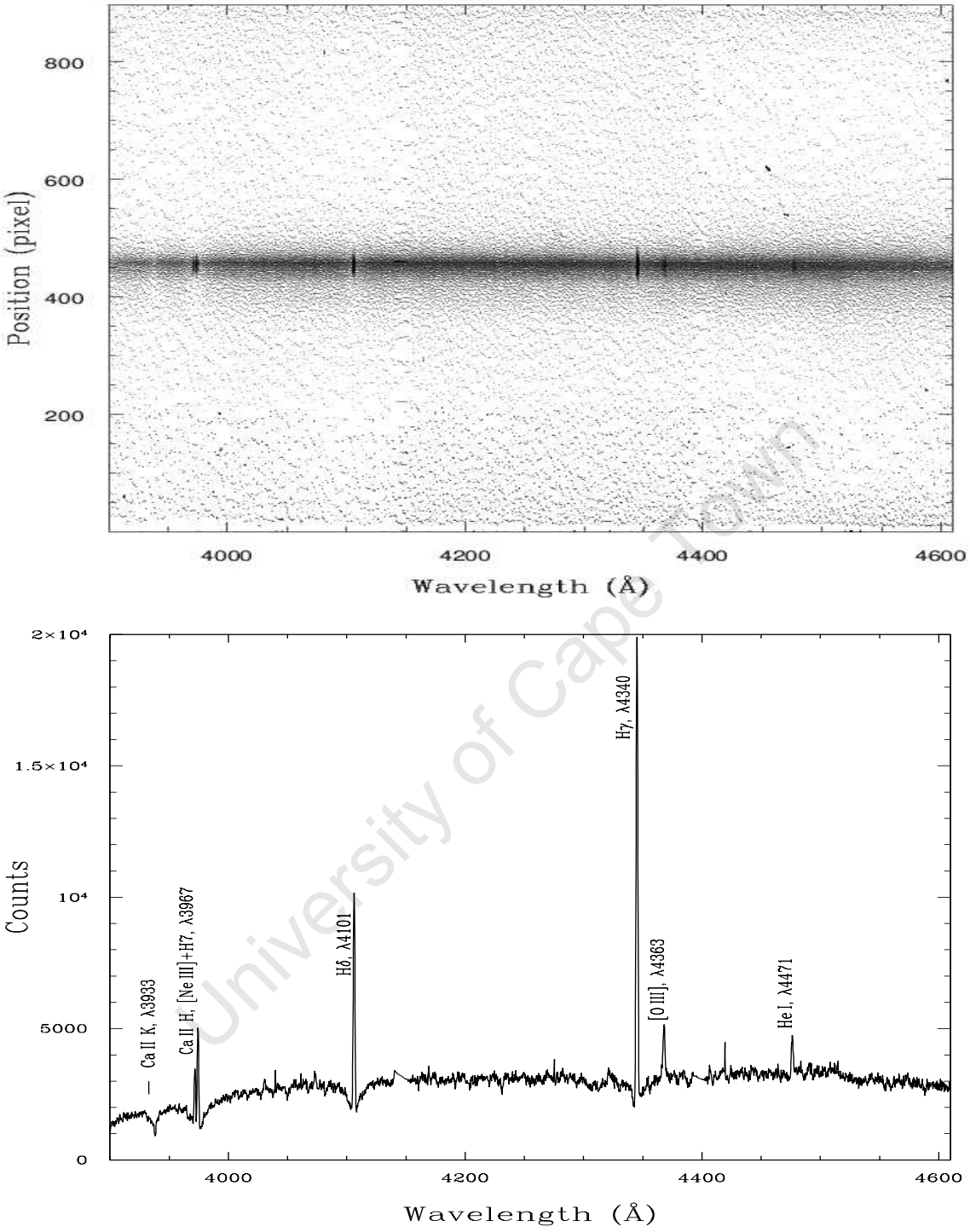

Figure 3.7 *Top*: Two-dimensional spectrum of NGC 59 taken with the blue (GR3000) grating. The spectrum corresponds to a 20-minute galaxy exposure. *Bottom*: The one-dimensional spectrum of NGC 59 obtained by summing the rows of the 2D galaxy spectrum (top) out to the background level. Observed emission lines in the spectrum (from left to right) are: [Ne III] and Hϵ(λ3968), Hδ(λ4101), Hγ(λ4341), [O III](λ4364) and He I(λ4471). The Ca II K and H absorption features at λ3933 and λ3968, respectively, are seen on the first CCD. The hydrogen absorption lines are also seen underneath the corresponding hydrogen emission lines in the spectrum.

corresponds to less than a quarter of the pixel scale. We therefore did not apply any correction for this offset in carrying out the wavelength calibrations of these spectra.

The wavelength-calibrated spectrum of NGC 59 obtained with the red grating is shown in Fig. 3.8. The strong H$\beta(\lambda 4861)$ and [O II]$(\lambda\lambda 4959, 5007)$ emission lines are the most dominant features in the spectrum. The observational configuration of NGC 59 was set up such that the Mg Ib$(\lambda\lambda 5167, 5173, 5184)$ absorption lines lie on the second chip of the CCD. The Mg Ib absorption lines of the galaxy are shown in Fig. 3.9. These features are almost indistinguishable from the galaxy continuum.

Relative flux calibrations were performed for the galaxy spectra acquired with the low-resolution GR0900 grating. The sensitivity curve of the detector was derived from the spectrophotometric standard star LTT 6248. The observed spectral energy distribution of the standard star was fitted with a low-order polynomial. The Sutherland extinction curve (Jones 1980) was adopted in determining the sensitivity curve.

The one-dimensional galaxy spectra were extracted using the APALL task in IRAF. The galaxy spectra obtained with the low-resolution grating were averaged. The final combined spectrum of NGC 59 is shown in Fig. 3.10. Strong emission lines are seen throughout the optical spectral range of 3648–6742Å. The presence of highly ionized gas at the center of the galaxy is revealed by the dominant [O III] emission lines in the spectrum. These emission lines will be used to measure the physical and chemical properties of the ISM (see section 3.6 for details).

3.5 Kinematical Data Analysis

The stability of the SALT/RSS spectrograph in performing long-exposure observations was not thoroughly investigated during the PV phase. The observations of NGC 59 were used to explore some of the scientific capabilities of the spectrograph which include a qualitative study of the stability of the SALT/RSS during long-exposure observations. The results can be used to place important constraints and limitations on the science projects to be carried out with the spectrograph. The outcome of this study will be crucial for the planning of future observational projects with the SALT/RSS instrument.

An initial test of the stability of the SALT/RSS consisted of the measurement of the systemic velocity of NGC 59 from the individual galaxy exposures. The absorption and emission lines in the spectrum were used independently to measure the heliocentric velocity as a function of the radius of the galaxy. This mapping of the heliocentric velocity with radius defines the velocity profile of the galaxy. The systemic velocity of the galaxy was determined from the resulting velocity profiles in each galaxy spectrum. The measured velocities were then compared to the literature value of the systemic velocity for NGC 59 (Beaulieu et al. 2006). We find a good agreement between the measured velocities and the literature value for most nights. A systematic change in the velocity profile shapes is however detected for consecutive galaxy exposures acquired on the same night.

Note that the kinematic analysis of the blue spectra has been restricted to the first CCD (3881–4137Å) only. This was done to avoid possible systematic errors in the measured veloc-

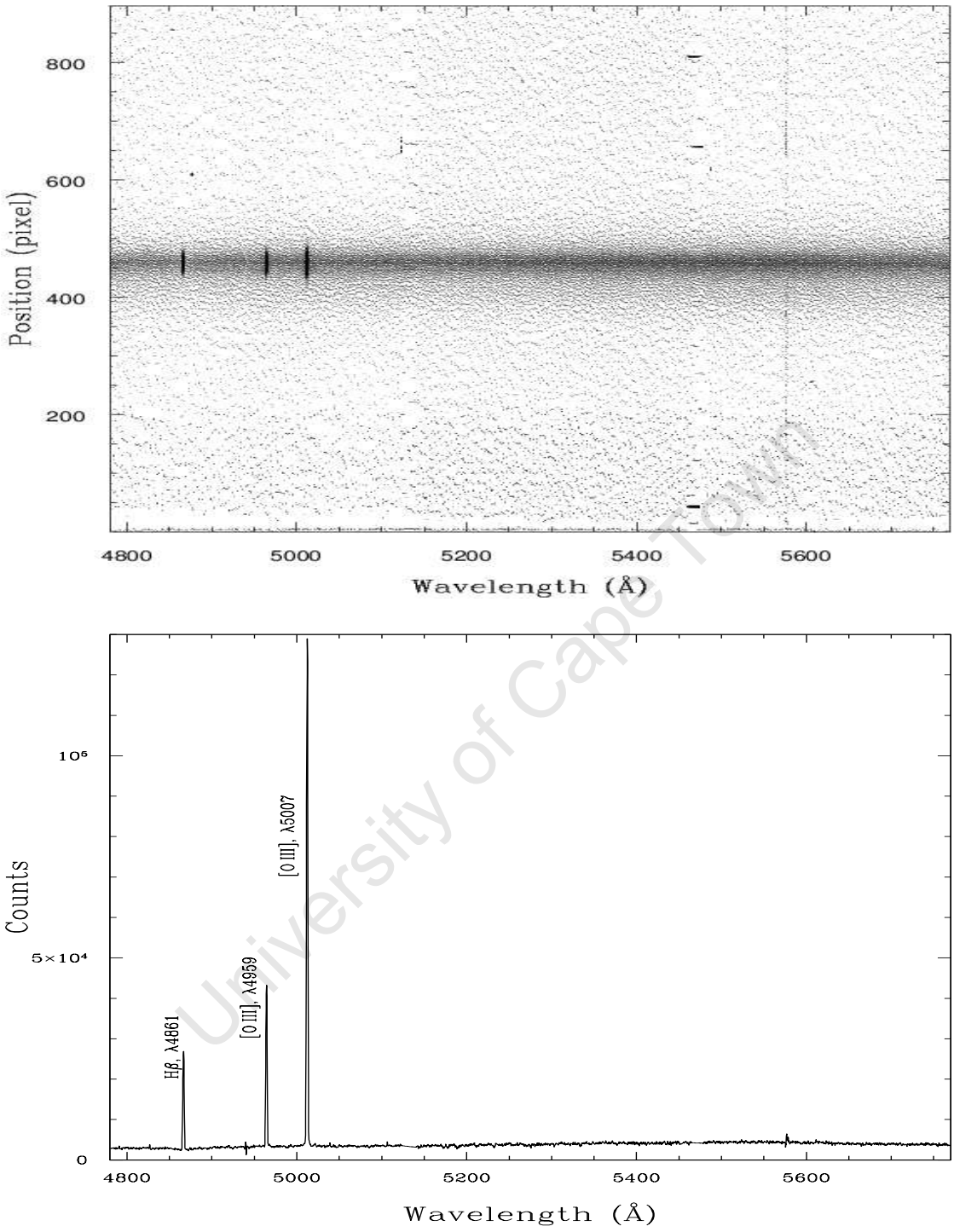

Figure 3.8 *Top*: Two-dimensional spectrum of NGC 59 taken with the red (GR2300) grating. The spectrum corresponds to a 15-minute galaxy exposure. The λ5577 sky emission line can also be seen. *Bottom*: The one-dimensional spectrum of NGC 59. The prominent emission lines in the spectrum are the H$\beta(\lambda 4861)$ and [O III]$(\lambda\lambda 4959, 5007)$ lines.

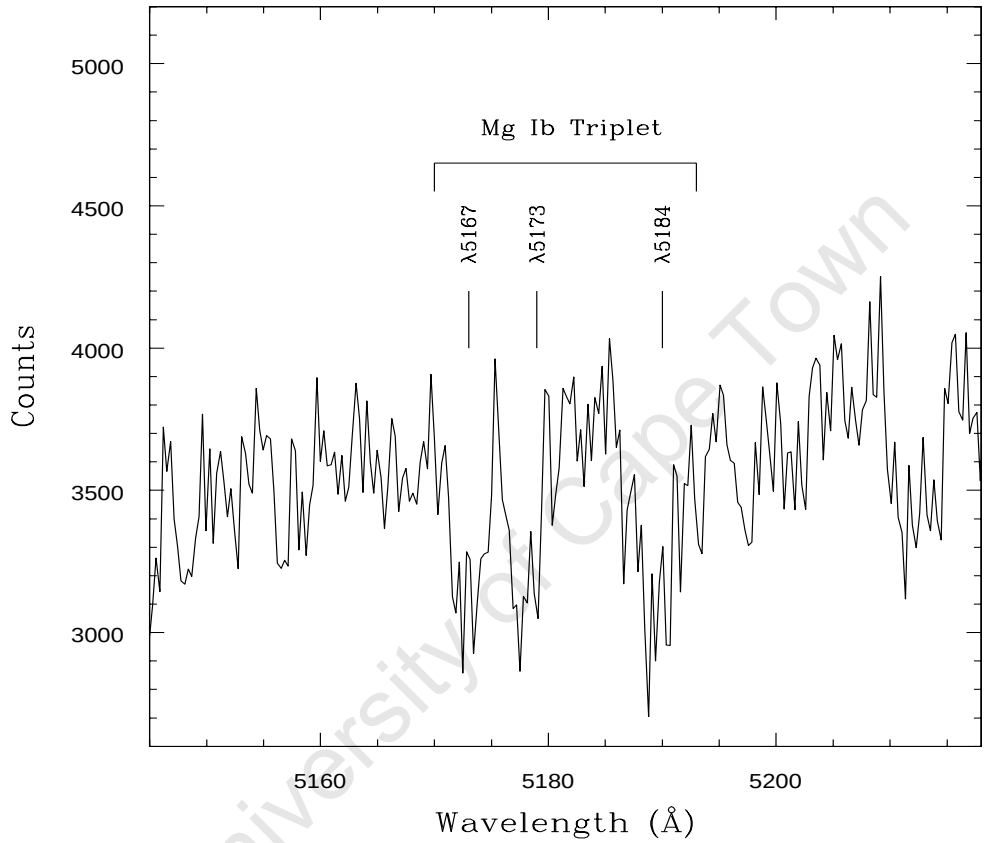

Figure 3.9 The Mg Ib triplet absorption feature of the galaxy NGC 59. The spectrum corresponds to a 15-minute galaxy exposure. The wavelength range of 5145–5218Å is shown. The rest wavelength of the Mg Ib features are indicated above each of the absorption lines.

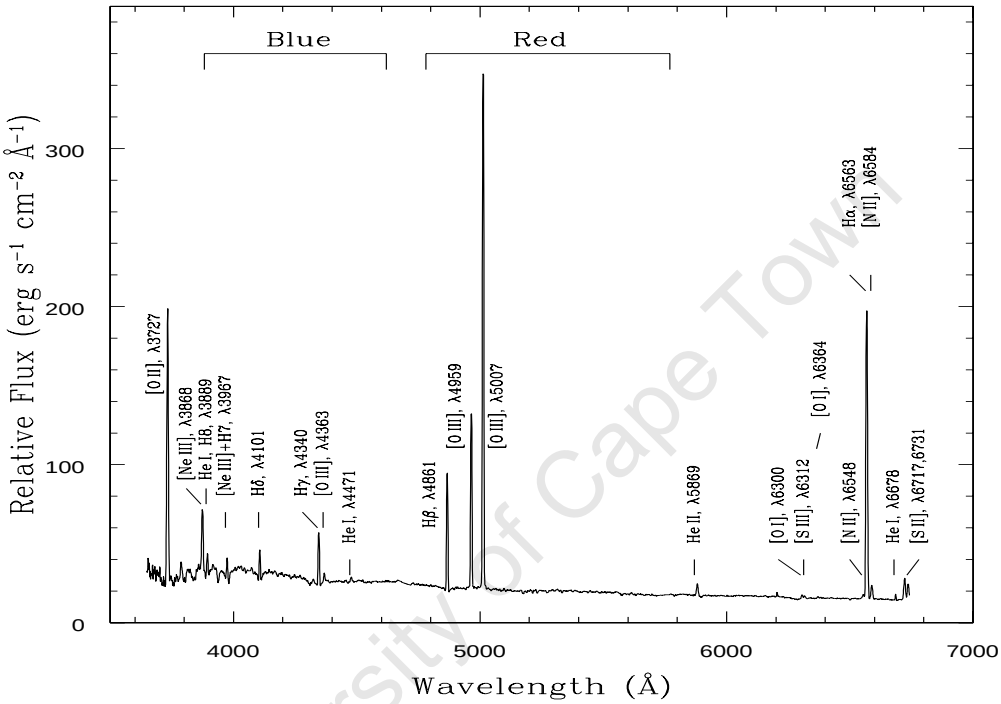

Figure 3.10 Low-resolution spectrum of NGC 59 acquired with the GR0900 grating. The spectrum corresponds to a 20-minute galaxy exposure. The low-resolution spectrum covers the wavelength range of 3648–6742Å. The wavelength range sampled by the blue (GR3000) and red (GR2300) gratings are indicated above the spectrum. The emission lines in the full-optical range are labeled.

Table 3.4. Properties of wavelength-calibrated blue spectra used in the kinematic analysis of NGC 59

Date	Object	Exp (sec)	Wavelength Range (Å)	Spectral Dispersion (Å pixel^{-1})	Velocity Resolution (km s^{-1} pixel^{-1})
2006 May 29	HD 1116	5	3882 – 4138	0.253	19.3
	NGC 59	300	3881 – 4137	0.253	19.3
	HD 1461	5	3881 – 4137	0.253	19.3
2006 May 30	HD 1116	60	3881 – 4138	0.253	19.3
	HD 1116	30	3881 – 4138	0.253	19.3
	NGC 59	900	3881 – 4138	0.253	19.3
	NGC 59	900	3881 – 4138	0.253	19.3
	HD 1461	10	3881 – 4137	0.252	19.2
2006 May 31	HD 1116	30	3882 – 4138	0.252	19.2
	HD 1116	30	3882 – 4138	0.252	19.2
	NGC 59	1200	3882 – 4138	0.252	19.2
	NGC 59	1200	3882 – 4138	0.252	19.2
2006 June 05	HD 1116	5	3881 – 4137	0.233	17.8
	NGC 59	1200	3881 – 4137	0.233	17.8
	NGC 59	1100	3881 – 4137	0.252	19.2

ities caused by fitting the wavelength solution over the entire spectral range. The individual CCDs were re-calibrated by fitting a third-order polynomial as the wavelength solution. A dispersion solution was found using a minimum of 14 emission lines in the comparison lamp spectrum. The polynomial fit yields a dispersion solution with RMS $\lesssim 0.1$Å. The wavelength solutions for all the comparison lamp spectra can be found in Appendix C.2. The RMS scatter in the wavelength solutions for the first CCD is comparable to that obtained for the full wavelength range (3882–4619Å). However, the lack of strong emission lines on the first CCD of the Ar lamp spectrum results in a poorly measured wavelength solution. The calibrations of the first CCD were therefore not carried out for this comparison lamp spectrum. Instead, the wavelength solution fitted over the entire spectral range was used (see Appendix C.1). The resulting wavelength range and dispersion of the blue galaxy and the template star spectra are listed in Table 3.4. The kinematics of NGC 59 will be derived from these spectra.

3.5.1 Measurement of the Radial Velocities of Template Stars

The velocity profile of NGC 59 was determined using the Fourier cross-correlation method (Tonry & Davis 1979). The cross-correlation procedure requires the radial velocity of the template stars. The heliocentric velocity of the galaxy is measured relative to the radial

velocity of the template star. The Doppler shift technique was employed to measure the radial velocity of the template stars. This technique involves the identification of strong absorption lines in the template spectrum. A Gaussian fit to the absorption line-profile gives the central wavelength of the line which was then used to derive the radial velocity of the template star.

The one-dimensional (1D) spectrum of the template stars was extracted using the APALL task in IRAF. An example of the 1D wavelength-calibrated spectrum of the K0 III and G0 V template stars of May 29 is shown in Fig. 3.11. The 1D spectra of the template stars for the remaining nights are given in Appendix D. A total of four prominent absorption lines were used to measure the radial velocity of the template stars: these include the Ca II K(λ3933) and H(λ3968), Fe I(λ4046) and Hδ(λ4101) absorption line features. The wavelength of these absorption lines was measured by a Gaussian fitting to the line-profile shape. The central wavelength of the Gaussian fit was used to calculate the radial velocity given by each of the absorption line features.

The radial velocity determined from the Hδ(λ4101) line was found to be systematically smaller by $\Delta v_{\rm rad} \lesssim 30$ km s^{-1} compared to the ones measured for the other three absorption lines. The velocity offset of the Hδ(λ4101) line is most pronounced for the K0 III template stars. This offset in the velocity is due to blending of the Hδ(λ4101) line with other absorption features. The blending of absorption/emission line features in the spectrum can lead to an incorrect measurement of the effective wavelength of the line which in-turn gives a spurious radial velocity. The deviation of the velocity from the Hδ(λ4101) line compared to the other absorption features has automatically led to the exclusion of this line from the radial velocity measurements. The radial velocity of the template stars were therefore exclusively derived from the Ca II K(λ3933), Ca II H(λ3968) and Fe I(λ4046) absorption features. The radial velocities of the template stars and their corresponding literature values (Kharchenko et al. 2004) are listed in Table 3.5. They agree well for the nights May 30, May 31 and June 5 and lie within 1σ of the literature values. A large offset of $\Delta v_{\rm rad} \sim 30 - 50$km s^{-1} is however measured for the template stars acquired on the first night (May 29) of the observations. It should be noted that the wavelength solutions obtained for the night May 29 were found to have an RMS < 0.1Å (see Appendix C.1) so that these offsets in the velocity cannot be a consequence of a poorly fitted wavelength solution. Similar offsets in the velocity have been measured from template star spectra acquired later in the PV phase of the SALT/RSS spectrograph (see results for the globular cluster study in Appendix E). The source of these offsets are not understood which led us to exclude the template star observations of May 29 from the kinematical analysis of NGC 59. Overall, the radial velocities of the template stars can be accurately recovered within the observational uncertainities.

3.5.2 The Velocity Profiles and Systemic Velocity of NGC 59 from Blue Spectra

For the kinematical analysis, we have only used the galaxy spectra that have exposure times longer than ten minutes. This was done to ensure high-enough S/N-levels were achieved in the single galaxy exposures. All the spectra obtained on the nights of May 30, May 31 and

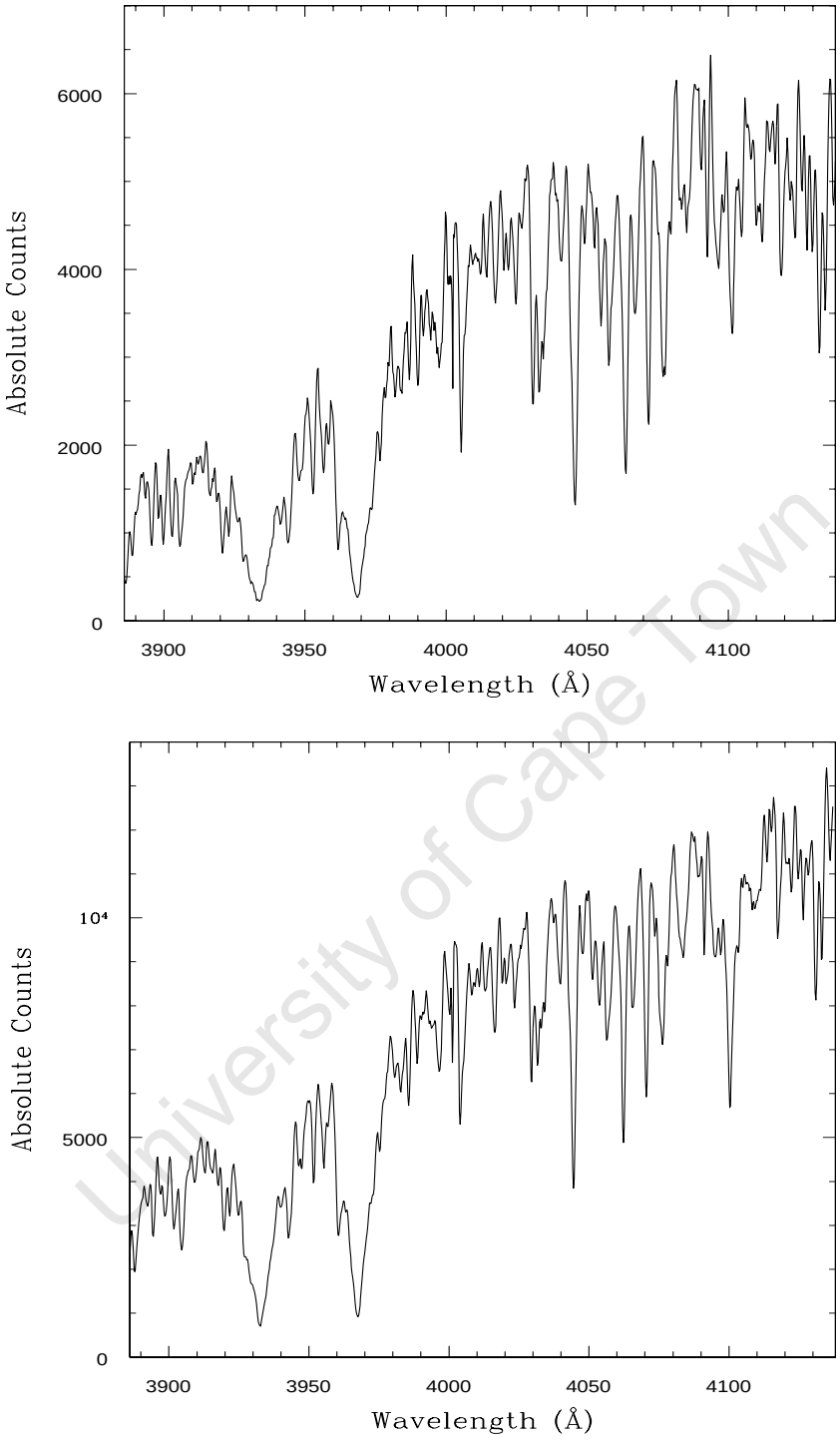

Figure 3.11 Wavelength-calibrated spectra of template stars acquired on May 29. *Top*: HD 1116 (spectral type K0 III); *bottom*: HD 1461 (spectral type G0 V). The prominent absorption lines seen throughout the spectrum include: Ca II K(λ3933Å) and H(λ3963), Fe I(λ4046) and Hδ(λ4101).

Table 3.5. Measured radial velocities of template stars

Date	Template	Type	Exp (s)	Radial Velocities $v_{\rm rad}$ Literature[1] (km s^{-1})	Doppler shift[2] (km s^{-1})
2006 May29	HD 1116	K0 III	40	-11.9 ± 2	$+26.0 \pm 6.9$
	HD 1461	G0 V	5	-10.7 ± 2	-61.5 ± 6.9
2006 May30	HD 1116	K0 III	60	-11.9 ± 2	-14.6 ± 7.0
	HD 1116	K0 III	30	-11.9 ± 2	-10.6 ± 5.4
	HD 1461	G0 V	10	-10.7 ± 2	-11.1 ± 7.4
2006 May31	HD 1116	K0 III	30	-11.9 ± 2	-11.5 ± 5.4
	HD 1116	K0 III	30	-11.9 ± 2	-8.8 ± 6.7
2006 Jun05	HD 1116	K0 III	5	-11.9 ± 2	-11.2 ± 5.6

Note. — (1) Literature values of the radial velocity are taken from Kharchenko et al. (2004). (2) The mean radial velocity derived from the Ca II K, H($\lambda\lambda$3933,3968) and Fe I(λ4046) lines using the Doppler shift technique. The errors in the radial velocities were calculated as the standard deviation of the mean.

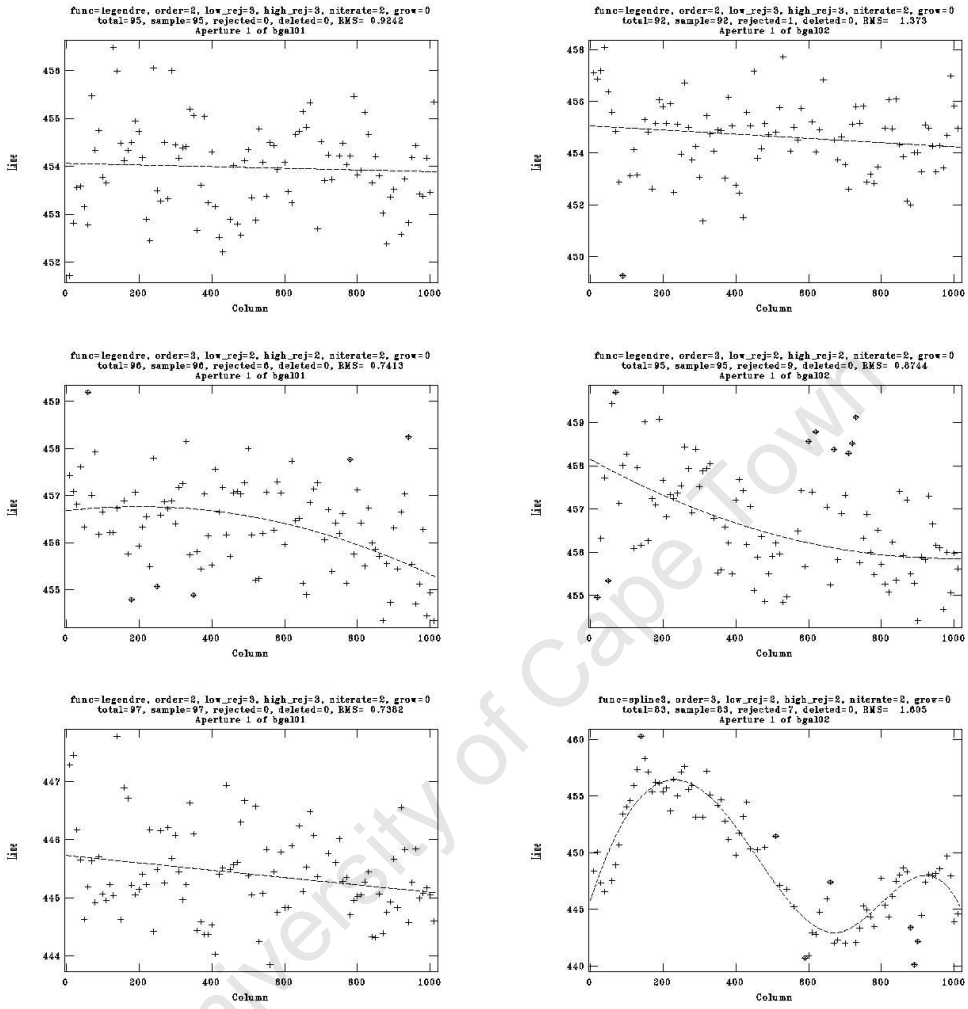

Figure 3.12 Functional fits to the trace of the peak intensity along the galaxy dispersion axis. *Top*: Trace for the night May 30 was best fit with a linear function; *middle*: Galaxy trace for May 31 was fit with a third-order Legendre function and; *bottom*: Trace of two galaxy exposures for the night June 5 were fit with a linear (*left*) and third-order cubic spline (*right*), respectively. The trace of the second galaxy exposure shown on the right encompasses 20 rows of the CCD.

June 5 were therefore used in studying the kinematics of NGC 59 while the five minute galaxy exposure of May 29 was excluded.

The two-dimensional (2D) galaxy spectra were aligned with the rows of the CCD using the APALL task in IRAF. This task allows for the peak in the intensity profile to be traced along the dispersion axis. Figure 3.12 shows the functional fit to the trace of the individual galaxy spectra. A linear or third-order polynomial fit was used to trace the peak of the intensity profile in the galaxy exposures. A wavy appearance is seen in the trace of the second galaxy exposure obtained on June 5. The trace of this galaxy exposure encompasses ~ 20 rows of the CCD. A third-order cubic spline fit to the trace was not effective in aligning this spectrum with the CCD rows. Tracing was thus not performed for this galaxy spectrum.

The resulting 2D galaxy spectra of the individual exposures are illustrated in Figs. 3.13–3.18. The prominent emission line features evident in the galaxy spectra are He I(λ3889), [Ne III](λ3967), Hϵ(λ3970) and Hδ(λ4101). A rotation-like signal is observed in the emission line features of four spectra, i.e. the first galaxy spectrum of the nights May 30 (Fig. 3.13) and June 5 (Fig. 3.17), and in both spectra obtained on May 31 (Figs. 3.15–3.16). However, closer inspection of these emission lines indicates that the observed rotation varies from one galaxy exposure to the next (see the inset of Figs. 3.13–3.18). This change in rotation for the individual spectra will be investigated when extracting the galaxy kinematics in the following sections.

Independent measurements of the heliocentric velocity as a function of the galaxy radius were made from the absorption and emission lines in the spectrum. A set of 1D apertures were defined along the spatial axis each consisting of the sum of six rows (or $1\farcs54$) in the galaxy spectrum. The aperture size was chosen to be greater than the FWHM ($\sim 1\farcs5$) of the observations. The heliocentric velocity was measured in each of these apertures to give the velocity profile of the galaxy. It should be noted that the continuum in each spectrum was used to determine the galaxy center by fitting a Gaussian to the spatial profile.

NGC 59 Velocity Profiles from Absorption Lines

Using the Fourier cross-correlation technique (Tonry & Davis 1979), the heliocentric velocity was measured from absorption lines in the galaxy spectrum. The FXCOR task in IRAF was employed to measure the velocities at each defined aperture. The cross-correlation analysis was performed for the galaxy and template star spectra acquired on the same night. The spectral range used for the cross-correlation analysis was selected interactively in the FXCOR task. An example of the wavelength range used for the cross-correlation analysis of the galaxy and the K0 III template star spectra of May 31 is shown in Fig. 3.19. The analysis was carried out using the Ca II K absorption feature and regions free of emission lines in the galaxy spectrum. By excluding the emission lines, the heliocentric velocity of the stellar component of the galaxy is measured. The spectral range of the K0 III template, shown in the bottom panel of Fig. 3.19, overlaps with the wavelength regions selected for the galaxy spectrum. The continuum in the galaxy and template star spectra was subtracted using a low-order polynomial. In addition, the spectra were filtered to remove high-frequency noise components and the low-frequency spectral variations not removed by the continuum subtraction.

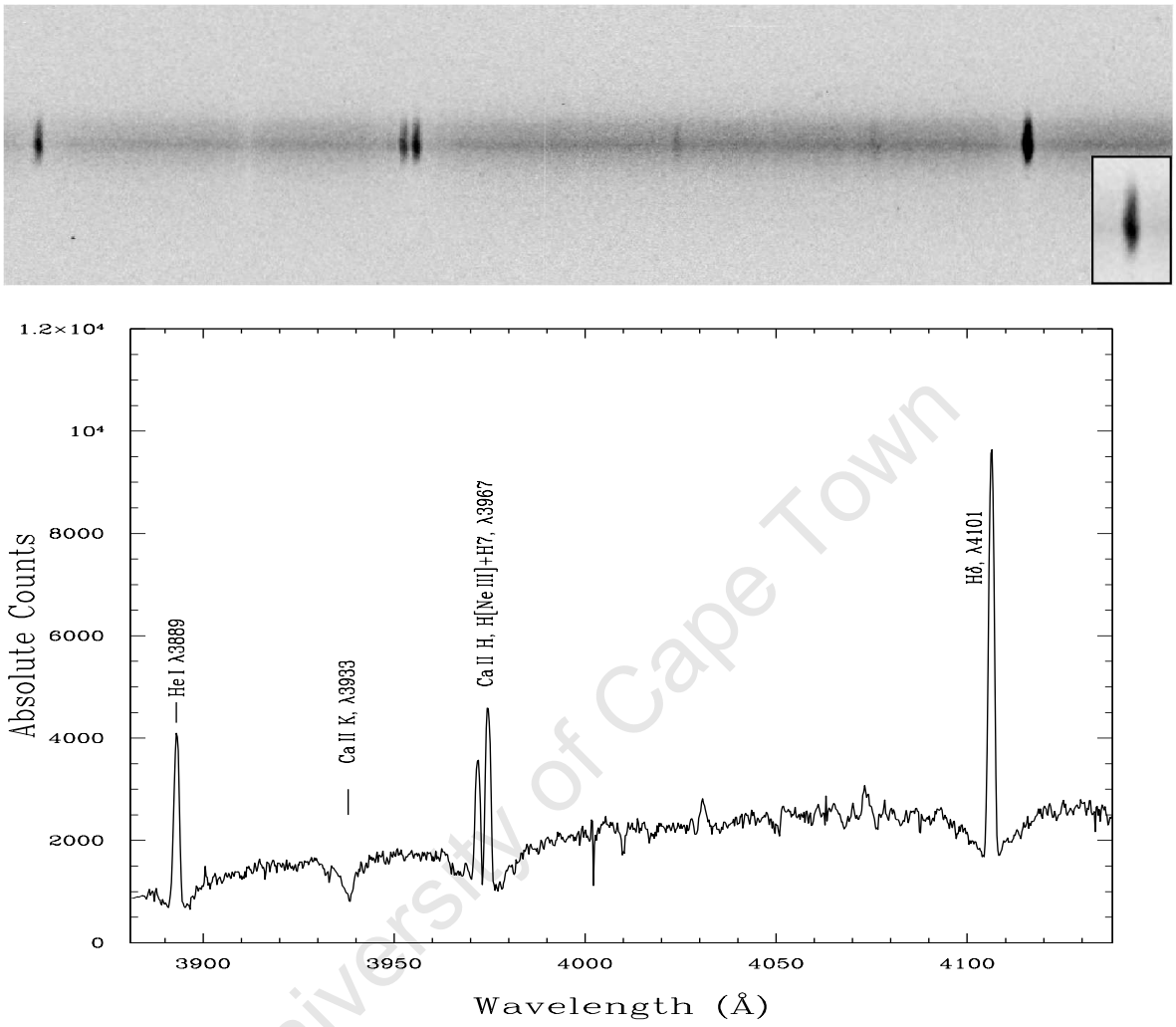

Figure 3.13 First exposure of NGC 59 obtained on May 30. The spectrum corresponds to a 15-minute galaxy exposure and shows the first CCD (3881–4137Å). *Top*: The two-dimensional galaxy spectrum. The spatial axis of the galaxy is in the vertical direction. The dispersion axis is in the horizontal direction with wavelength range corresponding to the 1D galaxy spectrum shown below. The inset in the right corner magnifies the Hδ(λ4101) emission line to show its structure. *Bottom*: The one-dimensional spectrum of NGC 59. Absorption and emission line features in the spectrum are labeled.

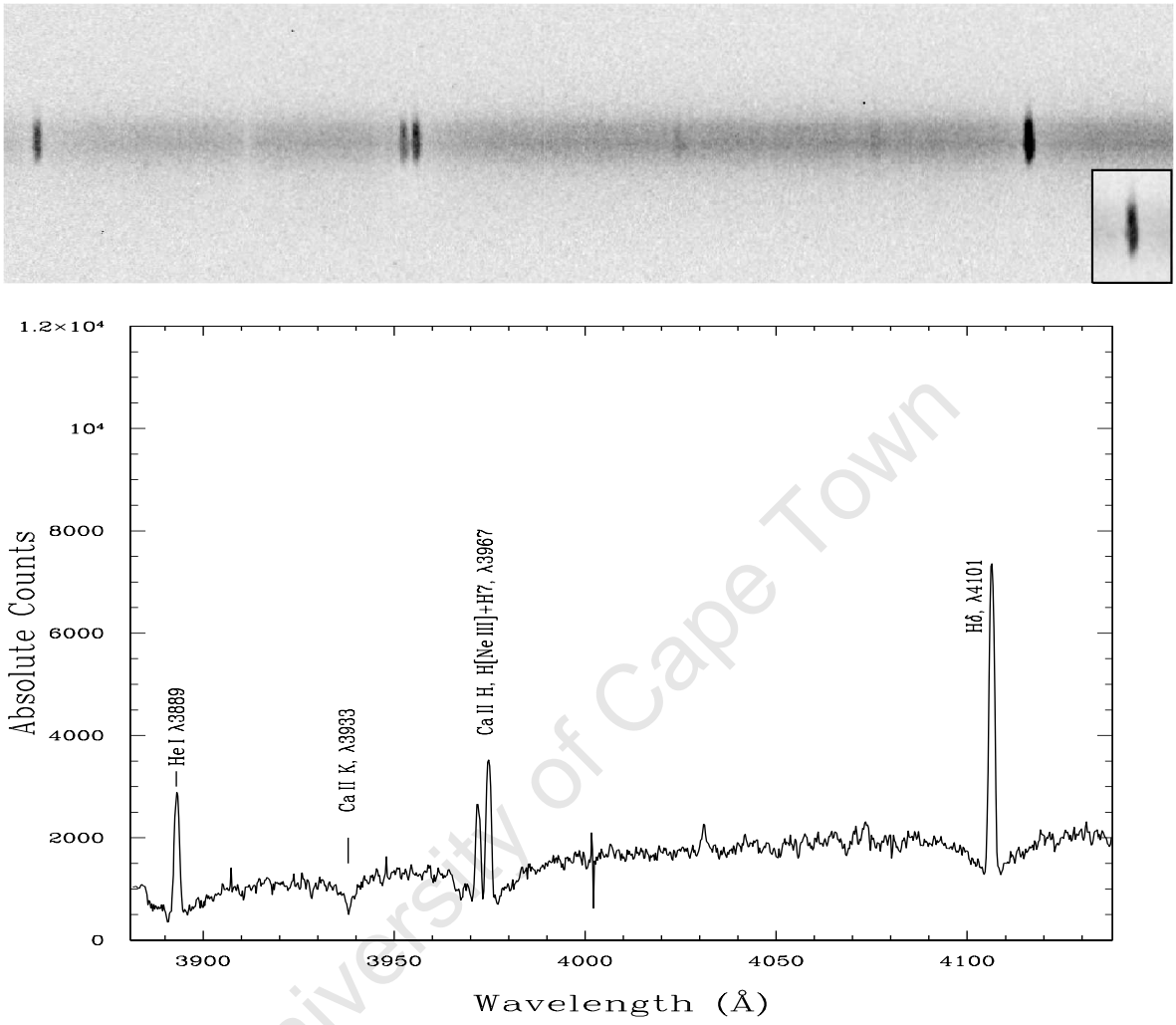

Figure 3.14 Second exposure of NGC 59 obtained on May 30. The spectrum corresponds to a 15-minute galaxy exposure and shows the first CCD (3881–4137Å). *Top*: The two-dimensional galaxy spectrum. The spatial axis of the galaxy is in the vertical direction. The dispersion axis is in the horizontal direction with wavelength range corresponding to the 1D galaxy spectrum shown below. The inset in the right corner magnifies the Hδ(λ4101) emission line to show its structure. *Bottom*: The one-dimensional spectrum of NGC 59. Absorption and emission line features in the spectrum are labeled.

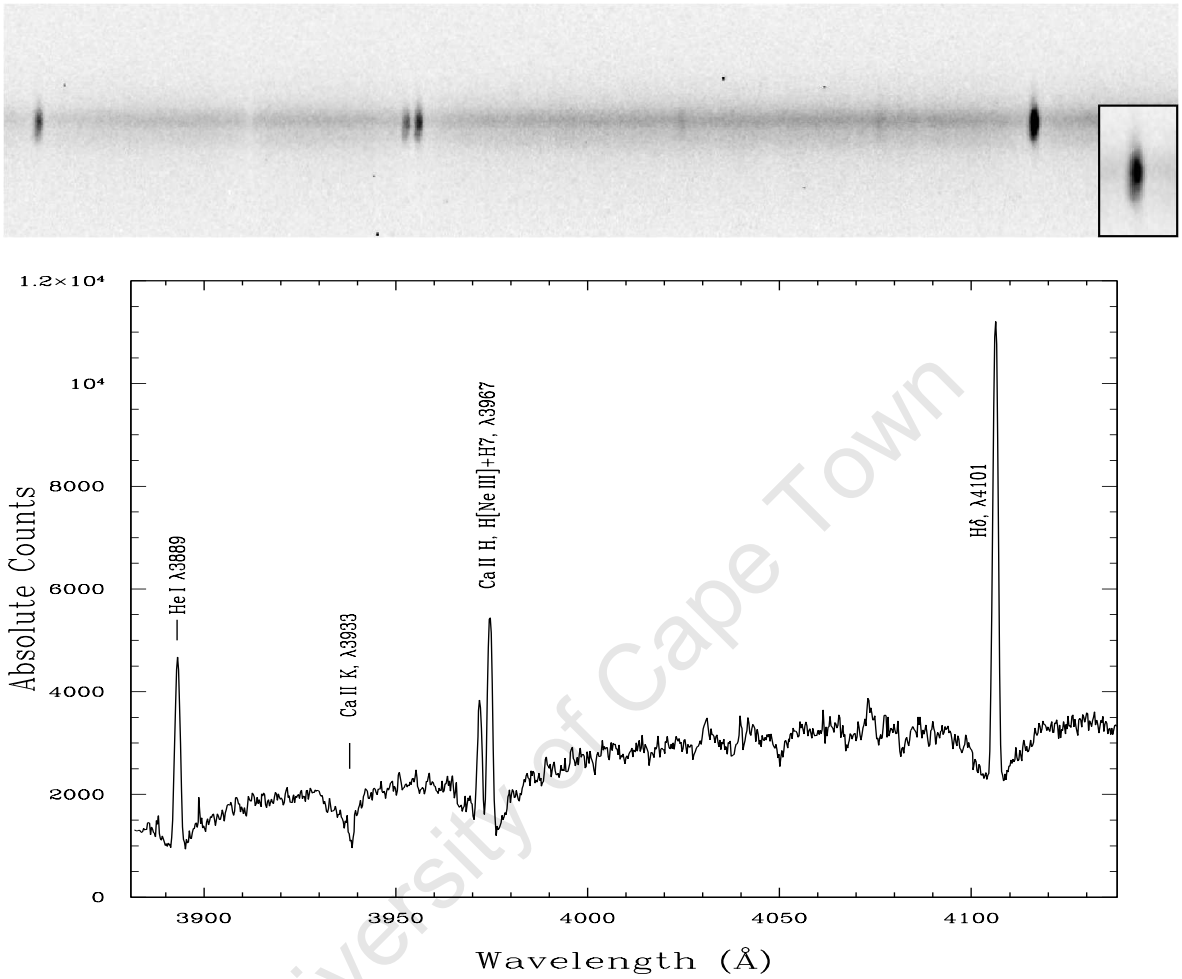

Figure 3.15 First exposure of NGC 59 obtained on May 31. The spectrum corresponds to a 20-minute galaxy exposure and shows the first CCD (3881–4137Å). *Top*: The two-dimensional galaxy spectrum. The spatial axis of the galaxy is in the vertical direction. The dispersion axis is in the horizontal direction with wavelength range corresponding to the 1D galaxy spectrum shown below. The inset in the right corner magnifies the Hδ(λ4101) emission line to show its structure. *Bottom*: The one-dimensional spectrum of NGC 59. Absorption and emission line features in the spectrum are labeled.

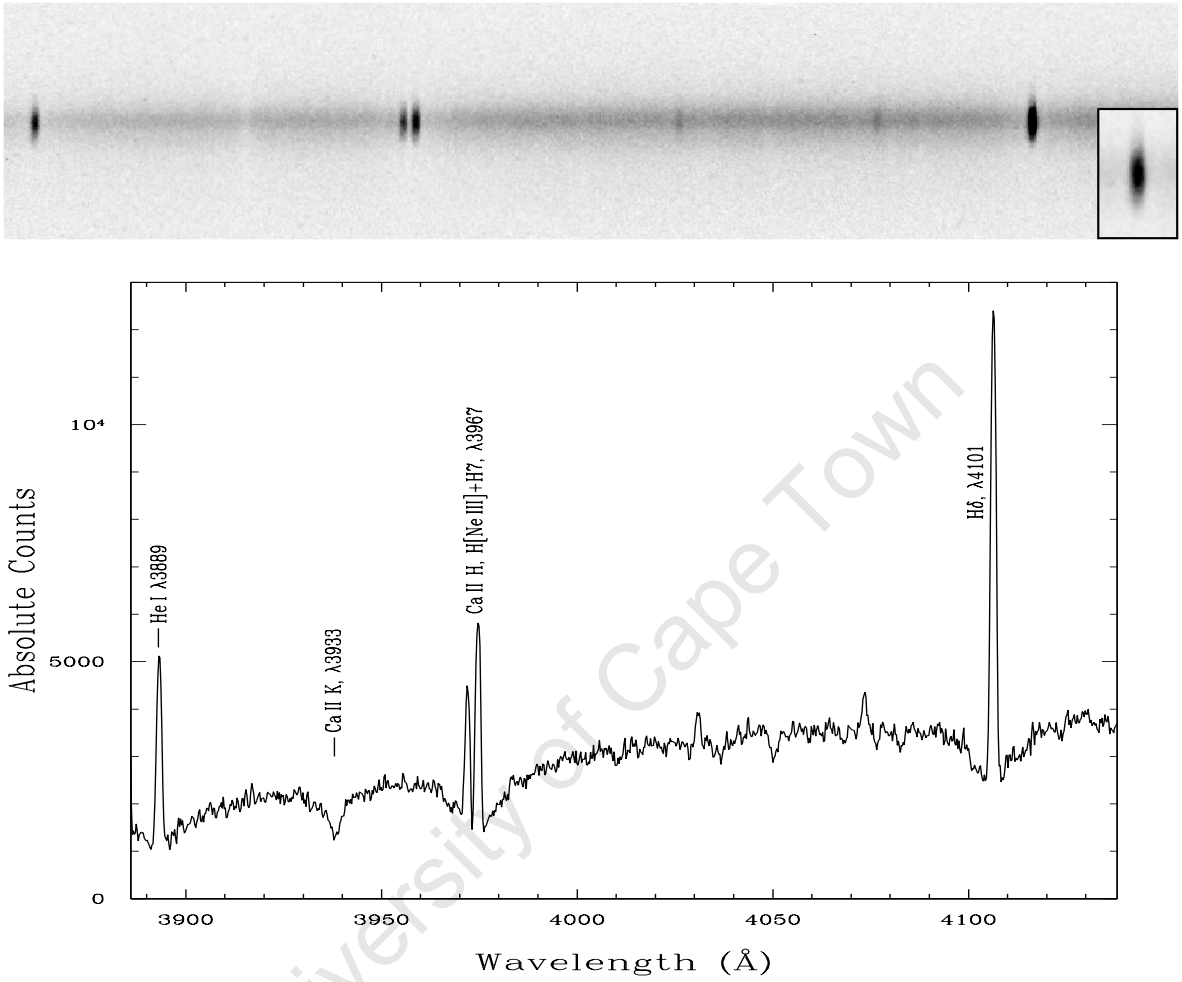

Figure 3.16 Second exposure of NGC 59 obtained on May 31. The spectrum corresponds to a 20-minute galaxy exposure and shows the first CCD (3881–4137Å). *Top*: The two-dimensional galaxy spectrum. The spatial axis of the galaxy is in the vertical direction. The dispersion axis is in the horizontal direction with wavelength range corresponding to the 1D galaxy spectrum shown below. The inset in the right corner magnifies the Hδ(λ4101) emission line to show its structure. *Bottom*: The one-dimensional spectrum of NGC 59. Absorption and emission line features in the spectrum are labeled.

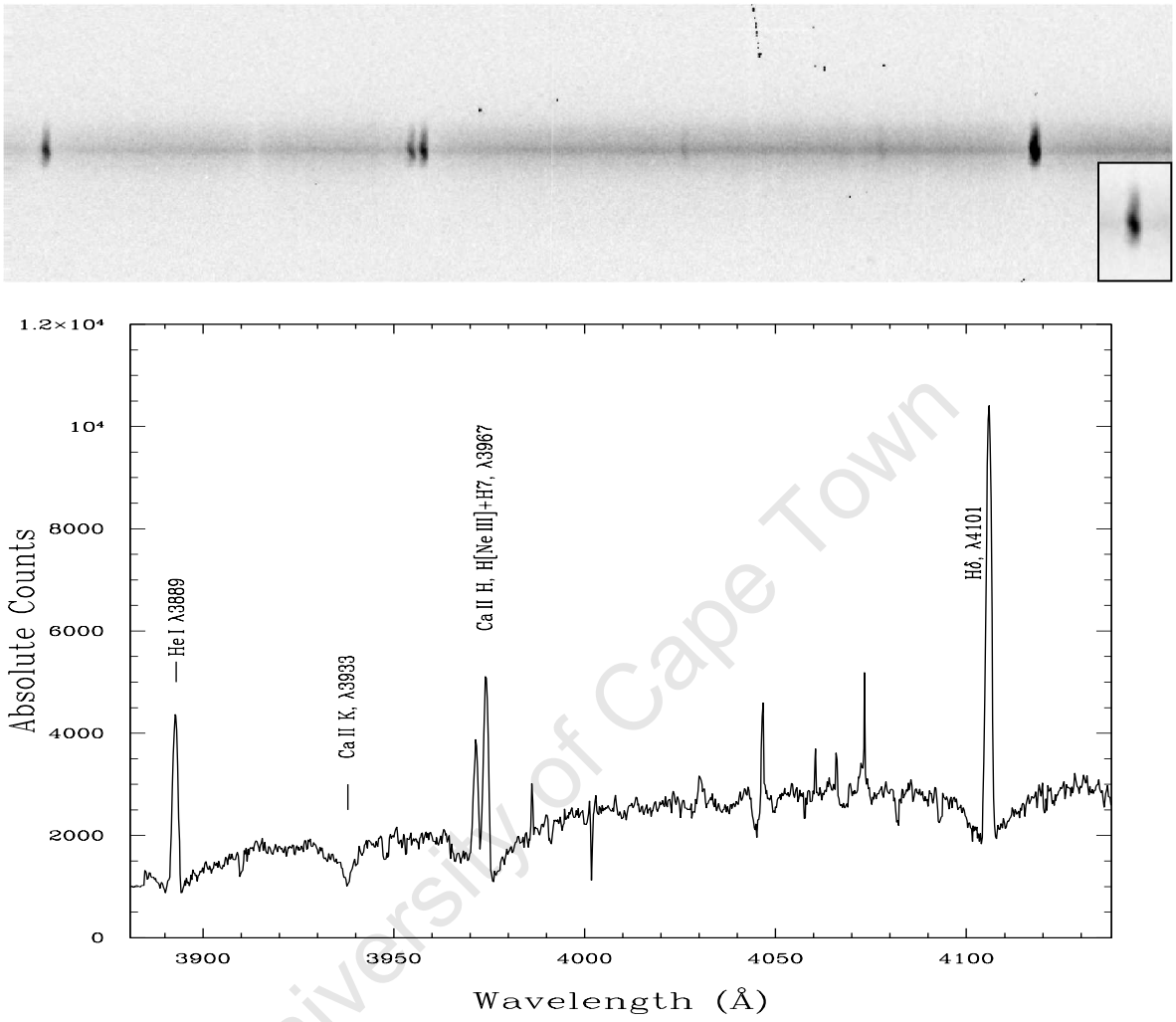

Figure 3.17 First exposure of NGC 59 obtained on June 5. The spectrum corresponds to a 20-minute galaxy exposure and shows the first CCD (3881–4137Å). *Top*: The two-dimensional galaxy spectrum. The spatial axis of the galaxy is in the vertical direction. The dispersion axis is in the horizontal direction with wavelength range corresponding to the 1D galaxy spectrum shown below. The inset in the right corner magnifies the Hδ(λ4101) emission line to show its structure. *Bottom*: The one-dimensional spectrum of NGC 59. Absorption and emission line features in the spectrum are labeled.

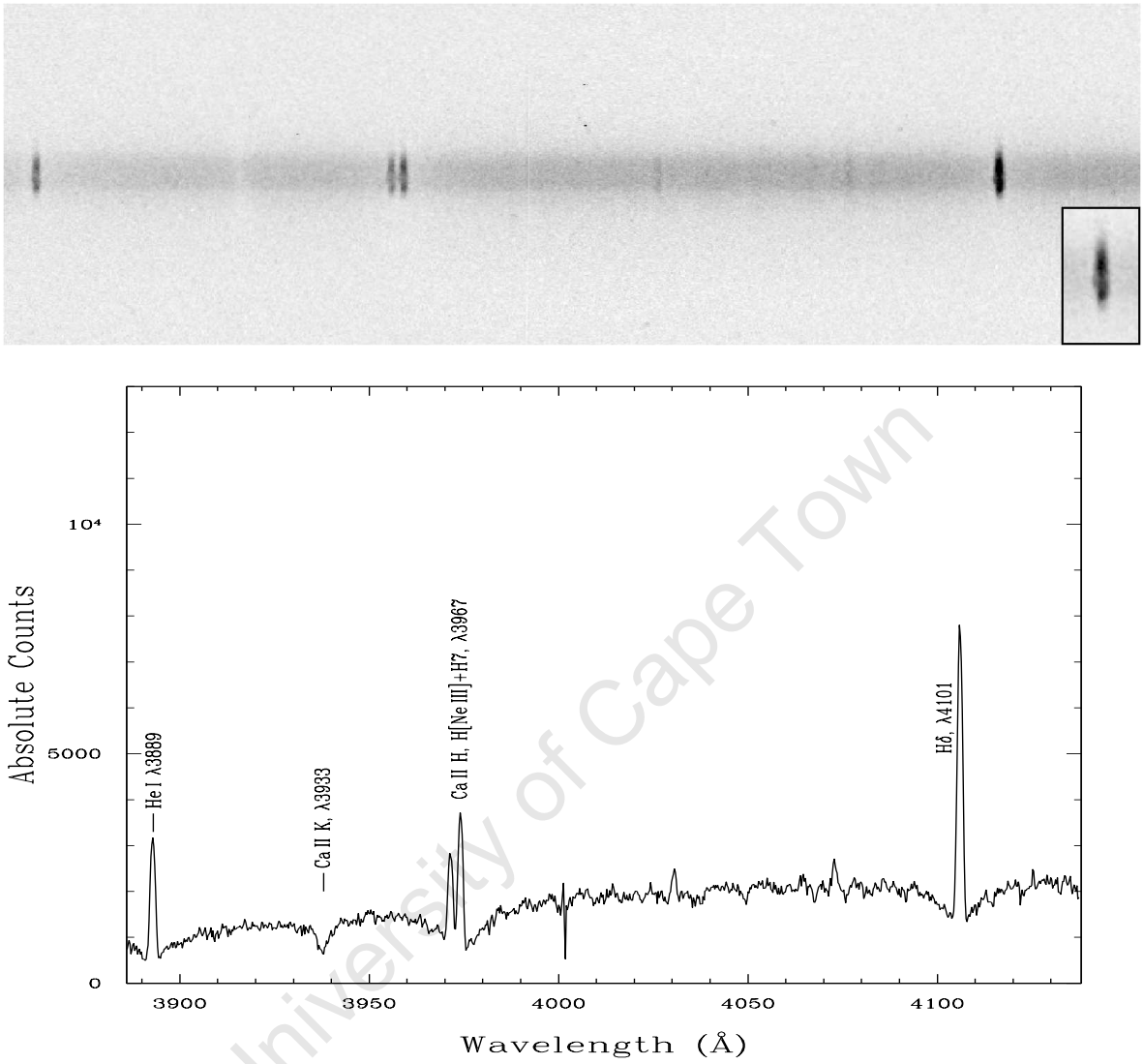

Figure 3.18 Second exposure of NGC 59 obtained on June 5. The spectrum corresponds to a 18 minute galaxy exposure and shows the first CCD (3881–4137Å). *Top*: The two-dimensional galaxy spectrum. The spatial axis of the galaxy is in the vertical direction. The dispersion axis is in the horizontal direction with wavelength range corresponding to the 1D galaxy spectrum shown below. The inset in the right corner magnifies the Hδ(λ4101) emission line to show its structure. *Bottom*: The one-dimensional spectrum of NGC 59. Absorption and emission line features in the spectrum are labeled.

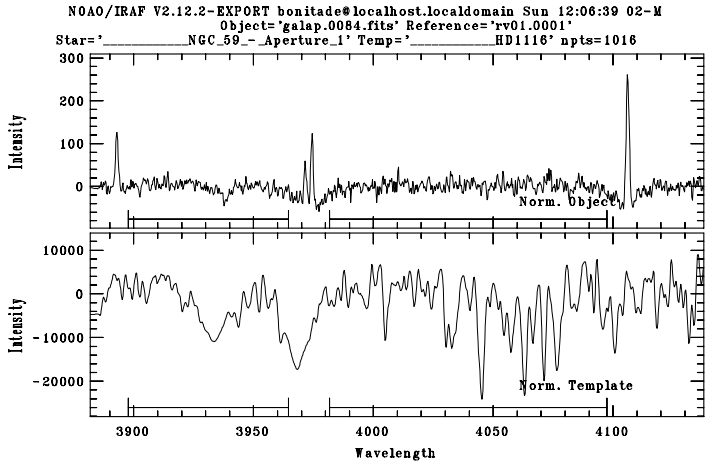

Figure 3.19 Interactive display of the FXCOR task which shows the spectrum of NGC 59 (*top*) and KO III template star (*bottom*) for a given aperture. The spectra were continuum-subtracted and filtered before conducting the Fourier cross-correlation analysis. The wavelength regions in the galaxy and template star spectra that were cross-correlated are indicated by the solid lines below each spectrum. The emission lines in the galaxy spectrum are essentially masked by choosing emission-free regions for the cross-correlation analysis.

The resulting cross-correlation function (CCF) of the galaxy with the K0 III template star is displayed in Fig. 3.20. The entire CCF is displayed in the top panel of Fig. 3.20. The maximum of the highest peak occurs at the redshift of the galaxy. The dashed vertical lines are the limits of the expanded plot (bottom panel of Fig. 3.20) which is centered on the peak of the CCF. The normalized CCF shows at most 25% correlation between the K0 III template and the galaxy spectrum. It should be noted that the best correlation with the galaxy spectrum was achieved using the K0 III template rather than the G0 V template star. The redshift (and subsequent heliocentric velocity) of the galaxy is given by the position of the maximum of the CCF. The velocity of the galaxy was measured relative to the template star using the radial velocities listed in Table 3.5. The CCF function was fitted with a weighted Gaussian distribution in measuring the heliocentric velocity of the galaxy. The velocity errors were computed from the fitted peak height of the Gaussian and the antisymmetric noise component of the CCF as described by Tonry & Davis (1979).

The heliocentric velocity profiles of the six galaxy spectra obtained in the blue are shown in Figs. 3.21–3.23. The points in the heliocentric velocity profile are separated by $0\farcs76$ which corresponds to an aperture step of three rows in the galaxy spectrum. This aperture step introduces a smoothing effect in the velocity profiles as each point is not independent. The different colors of the velocity profiles represent the results obtained from various template star exposures for the same night. The velocity profiles derived from the different template stars are in good agreement with each other. However, the large error (up to $\Delta\epsilon_{\odot} \sim 60\mathrm{km\ s^{-1}}$) in the velocity at each aperture makes it extremely difficult to obtain an accurate measure

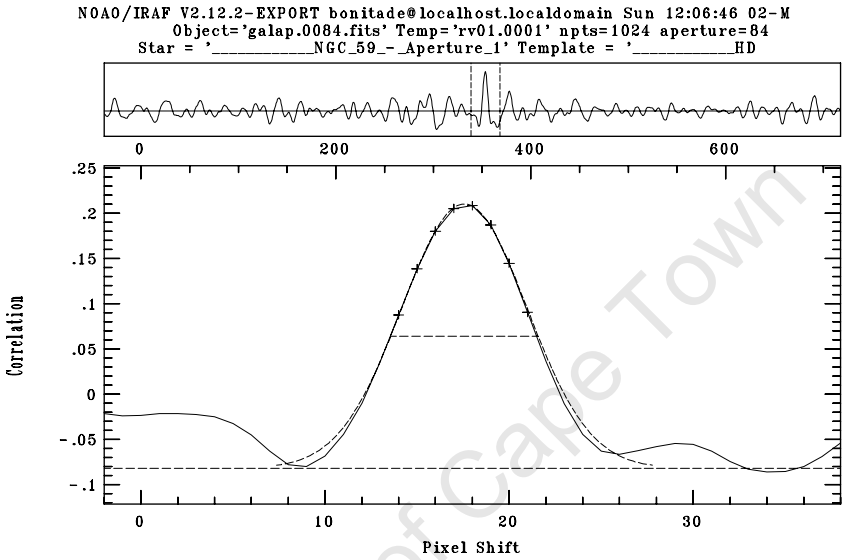

Figure 3.20 Fourier cross-correlation function (CCF) of the spectrum of NGC 59 with the KO III template star for a single aperture. The entire CCF is shown in the top panel which includes the antisymmetric noise component of the function. The vertical dashed lines show the limits of the highest peak of the CCF displayed in the bottom panel. The offset (in pixels) of the galaxy spectrum relative to the template star is shown along the bottom axis. This is converted into the relative velocity scale shown by the top axis. The best-fit Gaussian to the CCF is drawn.

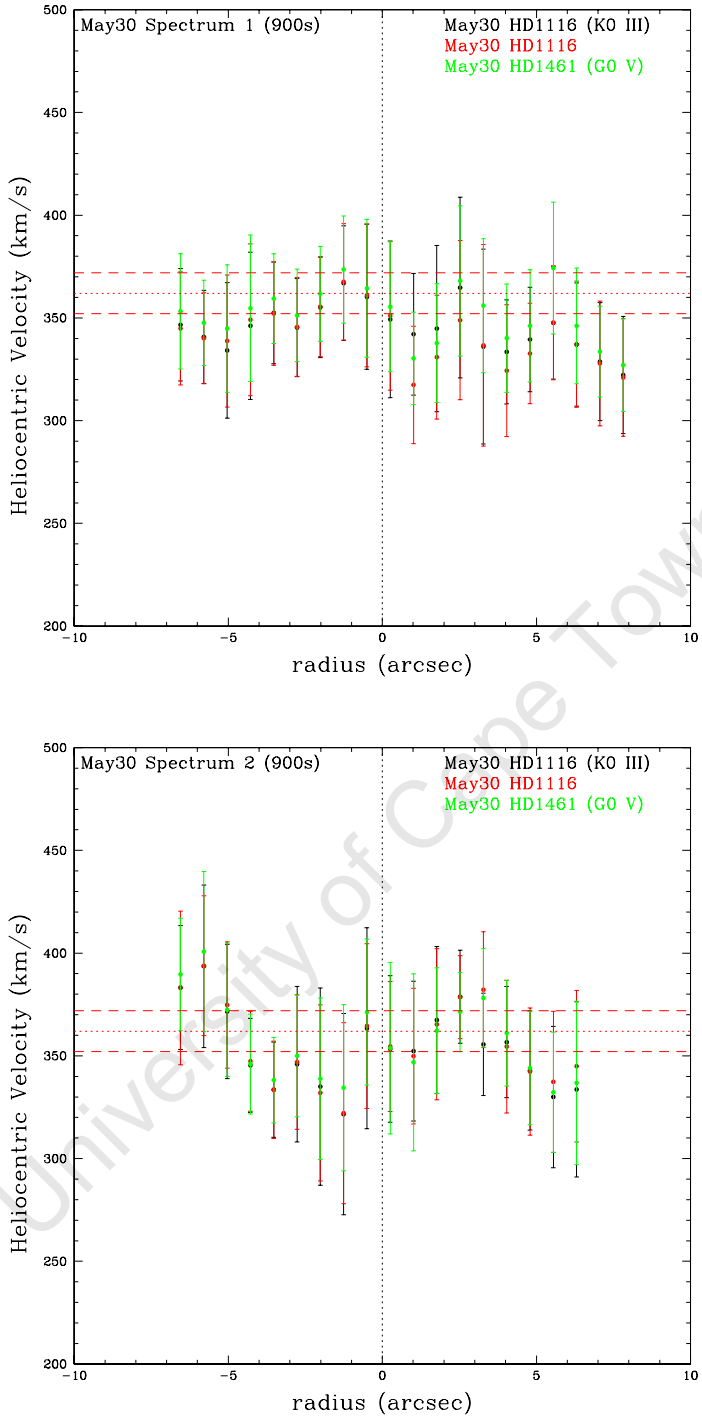

Figure 3.21 Heliocentric velocity profiles of NGC 59 derived from absorption lines in the spectra. The velocity profiles from the first (*top*) and second galaxy exposures (*bottom*) of May 30 are shown. The different colors represent velocity profiles obtained from the various template star exposures which are indicated at the top of each figure. The literature value of the heliocentric velocity and 1σ deviation from optical observations are shown by the horizontal dotted and dashed lines, respectively. The vertical line indicates the galaxy center.

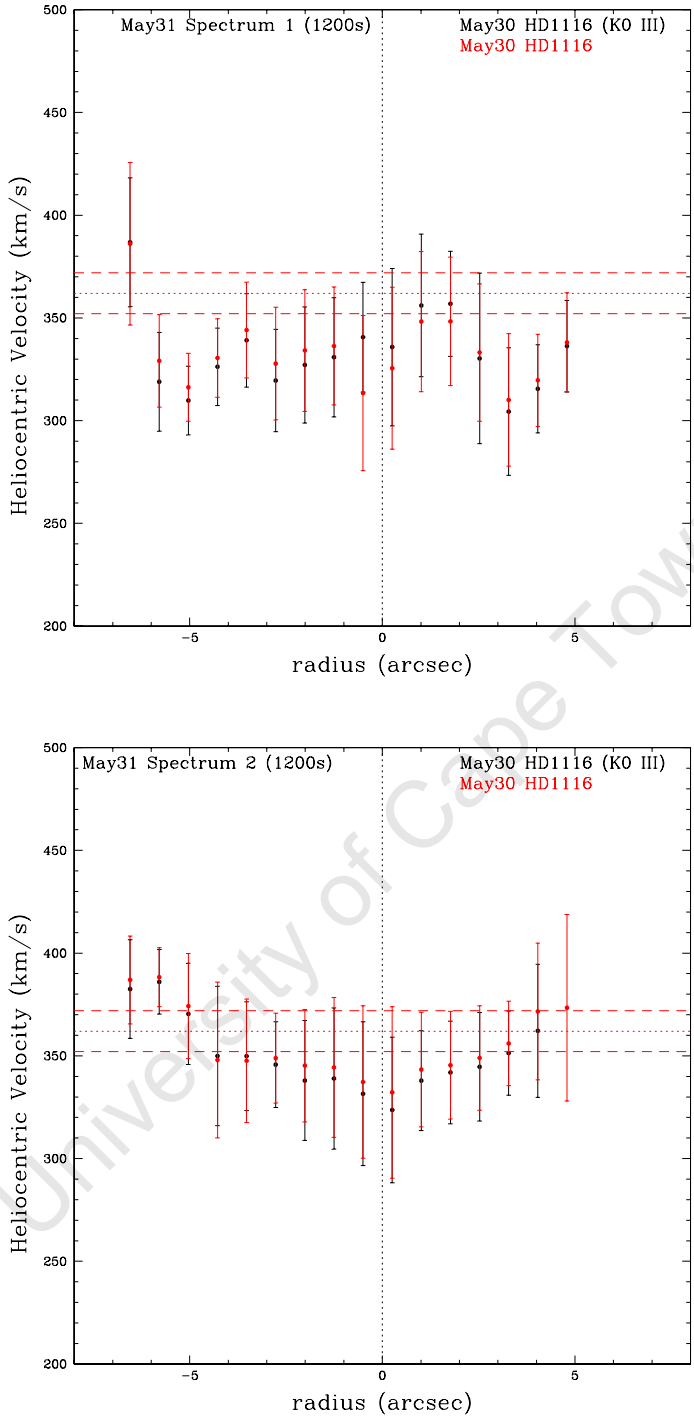

Figure 3.22 Heliocentric velocity profiles of NGC 59 derived from absorption lines in the spectra. The velocity profiles from the first (*top*) and second galaxy exposures (*bottom*) of May 31 are shown. The different colors represent velocity profiles obtained from the various template star exposures which are indicated at the top of each figure. The literature value of the heliocentric velocity and 1σ deviation from optical observations are shown by the horizontal dotted and dashed lines, respectively. The vertical line indicates the galaxy center.

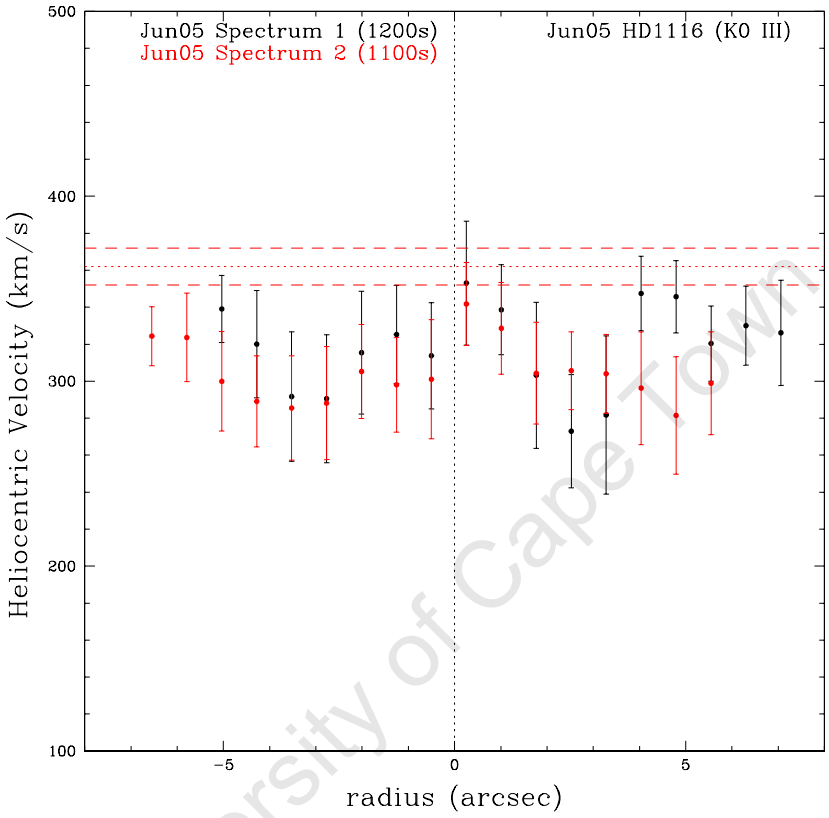

Figure 3.23 Heliocentric velocity profiles of NGC 59 derived from absorption lines in the spectra. The velocity profiles from the first (*black*) and second galaxy exposures (*red*) of June 5 are shown. The Fourier cross-correlation was performed with the single template star acquired on this night. The literature value of the heliocentric velocity and 1σ deviation from optical observations are shown by the horizontal dotted and dashed lines, respectively. The vertical line indicates the galaxy center.

of the heliocentric velocity. The velocity profiles of NGC 59 were compared to the literature value of the heliocentric velocity from optical observations (Beaulieu et al. 2006) which gives $v_{\odot} = 362 \pm 10$km s^{-1}. The literature value of the heliocentric velocity and 1σ deviation are indicated by the dotted and dashed lines, respectively, in Figs. 3.21–3.23. The velocity profiles for the nights May 30 and May 31 overlap with the literature value of the heliocentric velocity. The velocity profiles of both galaxy spectra obtained on June 5 are on average $\Delta v_{\odot} \sim 40$km s^{-1} lower than the literature value. The shape of the velocity profiles does give some indication of rotation in the galaxy. However, this remains inconclusive given the large errors associated with the heliocentric velocity measurements.

The systemic velocity $v_{\rm sys}$ of NGC 59 was measured from the individual galaxy spectra. An average-1D galaxy spectrum was created for each exposure (Figs. 3.13–3.18) by summing all rows along the spatial axis. The systemic velocity of the galaxy was determined using the Fourier cross-correlation technique. The 1D galaxy spectra were cross-correlated with the template stars acquired on the same night. The systemic velocity of the galaxy was measured using the FXCOR task as described for the single apertures. The systemic velocity of NGC 59 derived from the individual 1D galaxy spectra are listed in Table 3.6. The galaxy velocities measured for the nights May 30 and May 31 are in good agreement with the literature value of the heliocentric velocity. There is consistency in the galaxy velocities measured from the different template star exposures. Slightly higher velocities (of the order of a few km s^{-1}) are obtained from the G0 V template star which is a result of a template mismatch. The K0 III template is therefore a better representation of the overall stellar population of the galaxy. The degree of template mismatch is given by the height of the CCF, i.e. the best matching stellar template corresponds to the CCF with the highest amplitude. The largest deviation of up to $\Delta v_{\rm sys} \sim 30$km s^{-1} is measured for the galaxy spectra of June 5. The systemic velocity of the galaxy from these spectra are found to be within $\sim 3\sigma$ of the literature value. It is not clear what gives rise to the lower values of the galaxy systemic velocity for this night.

NGC 59 Velocity Profiles from Emission Lines

The presence of strong emission lines in the spectrum of NGC 59 allowed for an independent derivation of the heliocentric velocity profiles. These profiles will give more insight to the kinematics of the ionized gas component of the galaxy. The Doppler shift technique was used to measure the heliocentric velocity from the emission lines. The velocity profiles of the galaxy were derived from the four prominent emission lines on the first CCD i.e. the He I(λ3889), [Ne III](λ3967), Hϵ(λ3970) and Hδ(λ4101) lines. The RVIDLINES task in IRAF was used to determine the heliocentric velocity at each defined aperture. This task measures the heliocentric velocity from the individual lines where the rest wavelengths have been specified. The wavelengths of the emission lines were determined from a Gaussian fit to the line profile. The [Ne III] and Hϵ lines were deblended before measuring the velocities of these lines.

The velocity profiles from the individual emission lines are shown in Figs. 3.24–3.26 for the various nights. The profiles derived from the individual lines are represented by different colors in these figures. The heliocentric velocities measured from the hydrogen lines (Hϵ and Hδ) are found to be $\Delta v_{\odot} \sim 20 - 30$km s^{-1} larger than those measured from the He I and [Ne III] lines. The velocities from the two hydrogen lines are within 1σ of the H I heliocentric

Table 3.6. Systemic velocity of NGC 59 from individual galaxy spectra in the blue wavelength range. Literature value of the systemic velocity[1] is $v_{sys} = 362 \pm 10$km s^{-1}.

Date	Exp (s)	Template[2]	Type	Exp ID[3]	Systemic Velocity Absorption[4] (km s^{-1})	Systemic Velocity Emission[5] (km s^{-1})
May30	900	HD 1116	K0 III	1	$+368.6 \pm 10.5$	$+366.8 \pm 5.6$
	900			2	$+369.8 \pm 14.1$	$+372.2 \pm 7.4$
		HD 1116	K0 III	1	$+368.4 \pm 11.7$	
				2	$+370.4 \pm 13.9$	
		HD 1461	G0 V	1	$+376.9 \pm 8.4$	
				2	$+374.5 \pm 11.9$	
May31	1200	HD 1116	K0 III	3	$+351.8 \pm 11.4$	$+341.8 \pm 6.6$
	1200			4	$+372.0 \pm 10.9$	$+359.2 \pm 5.9$
		HD 1116	K0 III	3	$+350.4 \pm 11.7$	
				4	$+371.1 \pm 10.6$	
Jun05	1200	HD 1116	K0 III	5	$+331.3 \pm 11.7$	$+323.1 \pm 5.3$
	1100			6	$+336.1 \pm 10.7$	$+328.8 \pm 7.4$

Note. — (1) Systemic Velocity of NGC 59 measured from optical observtions (Beaulieu et al. 2006); (2) Template star used in Fourier cross-correlation analysis. Radial velocities of template stars are listed in Table 3.5; (3) Galaxy exposure reference number; (4) Systemic velocity of NGC 59 measured using Ca II K absorption line and emission-free regions of the galaxy spectrum; (5) Systemic velocity of NGC 59 measured from the emission lines: Hζ, [Ne III], Hξ, Hγ and Hδ.

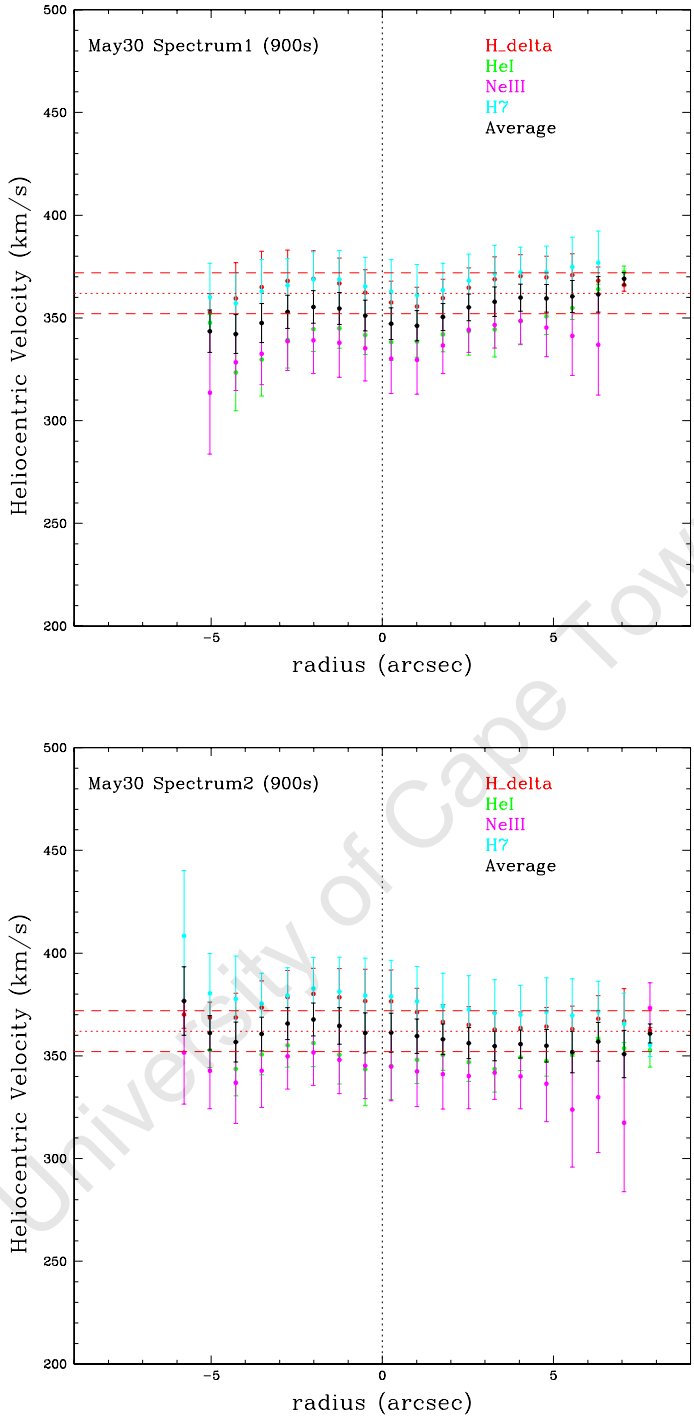

Figure 3.24 Heliocentric velocity profiles of NGC 59 measured from emission lines: Hδ (*red*), He I (*green*), [Ne III] (*magenta*) and Hϵ (*cyan*). The velocity profiles from the first (*top*) and second galaxy exposures (*bottom*) of May 30 are shown. The average heliocentric velocity from emission lines is represented by the black points. The literature value of the heliocentric velocity and 1σ deviation from optical observations are shown by the horizontal dotted and dashed lines, respectively. The vertical line indicates the galaxy center.

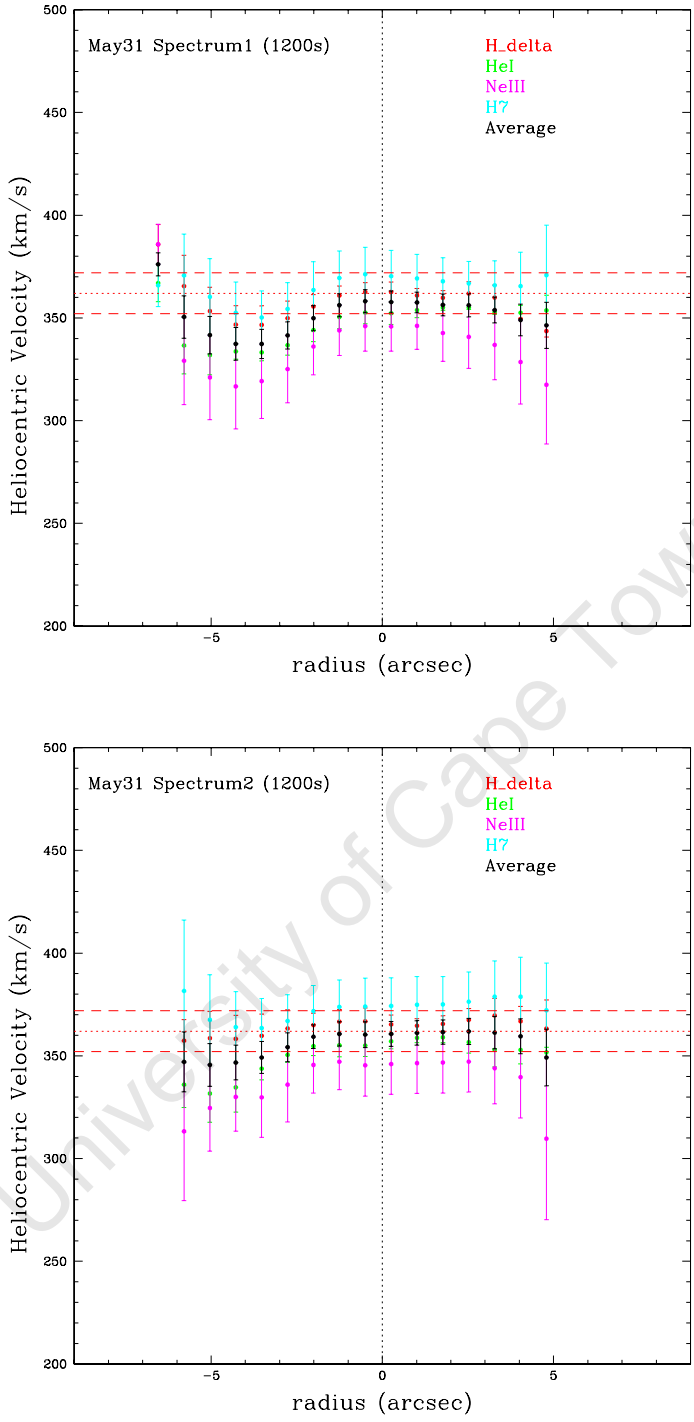

Figure 3.25 Heliocentric velocity profiles of NGC 59 measured from emission lines. The velocity profiles from the first (*top*) and second galaxy exposures (*bottom*) of May 31 are shown. See caption for Fig. 3.24.

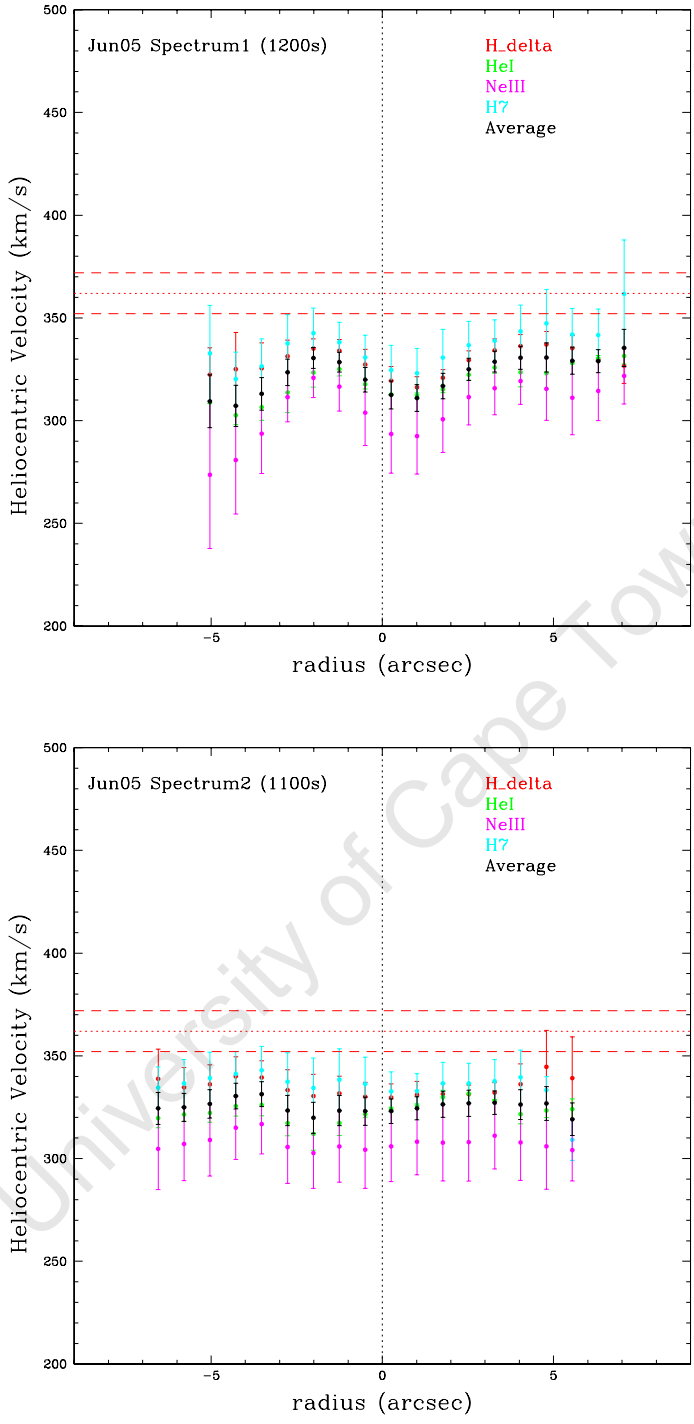

Figure 3.26 Heliocentric velocity profiles of NGC 59 measured from emission lines. The velocity profiles from the first (*top*) and second galaxy exposures (*bottom*) of June 5 are shown. See caption for Fig. 3.24.

velocity of NGC 59 (see Table 3.1) from Beaulieu et al. (2006). The heliocentric velocities have a typical RMS error of $\Delta\epsilon_{\odot} \sim 10 - 20$km s^{-1} for the different emission lines. Three times better accuracy in the heliocentric velocity measurements is therefore obtained from the emission lines in the galaxy spectrum compared to those derived from the absorption lines (see previous section). This increase in the precision of the velocities allows for the detection of any rotation-like signature that may be present in the galaxy spectrum.

A rotation-like signature of $v_{\rm rot} \sim 20$km s^{-1} is detected within the central $\sim 15''$ of the galaxy (see Figs. 3.24–3.26). This signature is more clearly identified in the velocity profiles derived from the first galaxy exposures of each night. A more flattened profile is measured from the second galaxy exposures. The shape of the velocity profiles from the individual emission lines is found to be similar. The heliocentric velocity of each galaxy exposure was therefore calculated as the non-weighted average of the velocities measured from the individual emission lines. The average velocity profiles from the emission lines are shown in Figs. 3.27–3.29 for the three nights. The uncertainty in the average velocity profiles was computed from the wavelength RMS for individual lines. The wavelength RMS is converted into a velocity RMS and then weighted by the number of lines to give the uncertainty in the mean velocity. These profiles were compared to the literature value (Beaulieu et al. 2006) of the heliocentric velocity with the 1σ deviation shown by the dotted and dashed lines, respectively. The derived velocity profiles for the nights May 30 and May 31 are found to be in good agreement with the literature value of the heliocentric velocity. Again, a systematic offset of $\Delta v_{\odot} \sim 30$km s^{-1} from the literature value is observed for the velocity profiles of June 5.

Figures 3.27–3.29 show the velocity profiles measured from consecutive galaxy exposures for each of the three nights. For the nights May 30 and June 5, the profile shapes are seen to vary from one galaxy exposure to the next. The velocity profiles derived from the first galaxy exposures show a rotation-like signature while the second exposures appear to be more flattened. A comparison of the velocity profiles derived for these two nights is shown in Fig. 3.30. The velocity profiles measured from the first and second galaxy exposures, respectively, are grouped together. These figures illustrate the similarity of the profile shapes derived from the respective galaxy exposures. A rotation is observed in the velocity profiles from the first galaxy exposures which is then lost in the profiles derived from the second exposures. This trend is also observed in the 2D galaxy spectra (Figs. 3.13–3.18) where the rotational signature can be seen in the emission lines of the first exposures of these nights (Figs. 3.13 and 3.17). Emission lines with less defined rotational structure is detected in the second galaxy exposures (Figs. 3.14 and 3.18). Similar velocity profiles are observed for the two galaxy exposures of May 31 with both profiles showing a slight rotation. The rotational signature in these spectra is however different from that measured for the nights May 30 and June 5. We suspect that the differences in the velocity profiles are an observational effect which is caused by a change in the slit position along the galaxy. A detailed investigation of these effects is given in section 3.5.4.

The systemic velocity of NGC 59 was derived from the four emission lines in the blue wavelength range. The 1D galaxy spectra, created in the previous section, were used to determine the velocities. The heliocentric velocity of the galaxy was derived from the individual

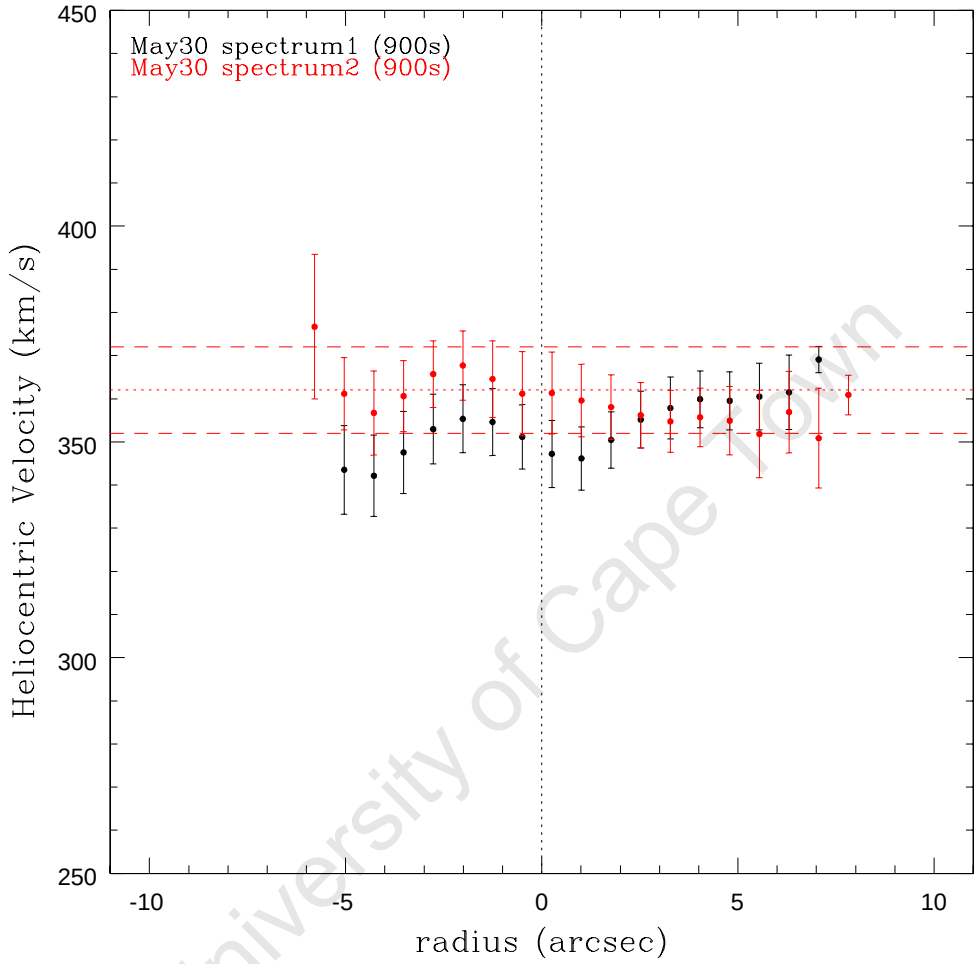

Figure 3.27 Average heliocentric velocity profile measured from emission lines for night May 30. Velocity profiles obtained from the first and second galaxy spectrum are shown in black and red, respectively. The literature value of the heliocentric velocity and 1σ deviation from optical observations are shown by the horizontal dotted and dashed lines, respectively. The vertical line indicates the galaxy center.

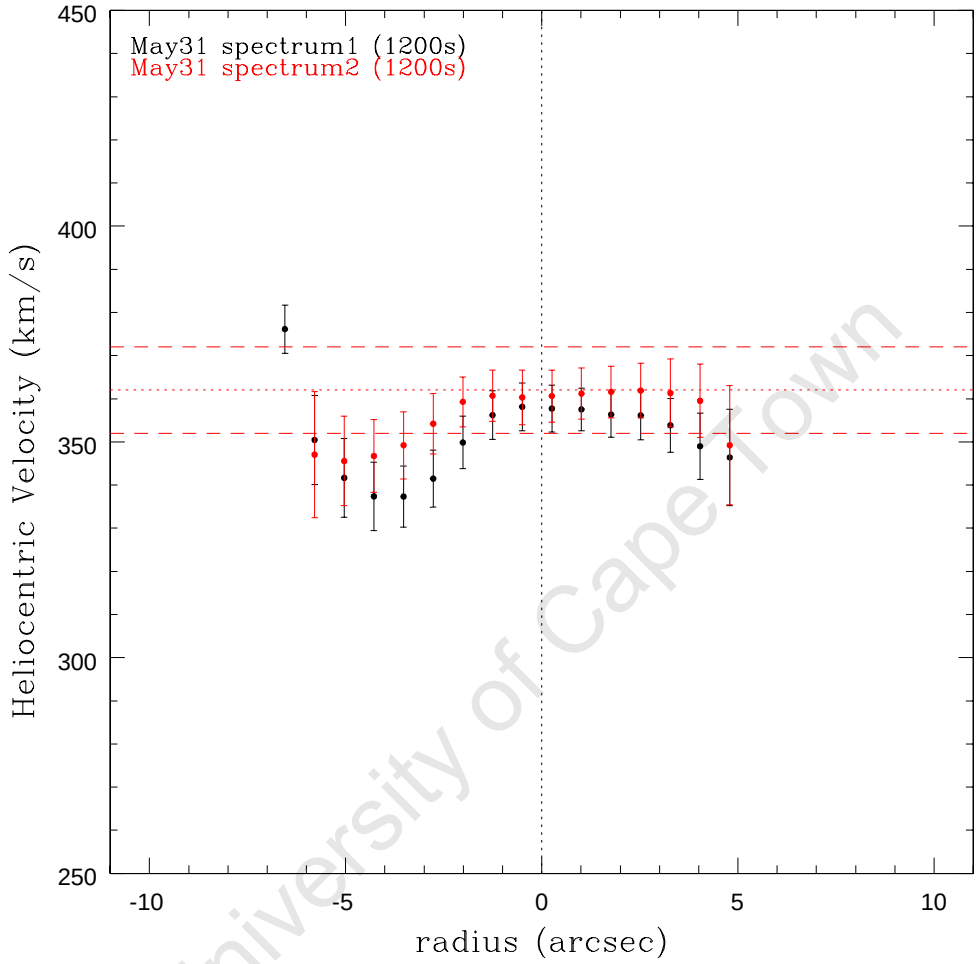

Figure 3.28 Average heliocentric velocity profile measured from emission lines for night May 31. Velocity profiles obtained from the first and second galaxy spectrum are shown in black and red, respectively. The literature value of the heliocentric velocity and 1σ deviation from optical observations are shown by the horizontal dotted and dashed lines, respectively. The vertical line indicates the galaxy center.

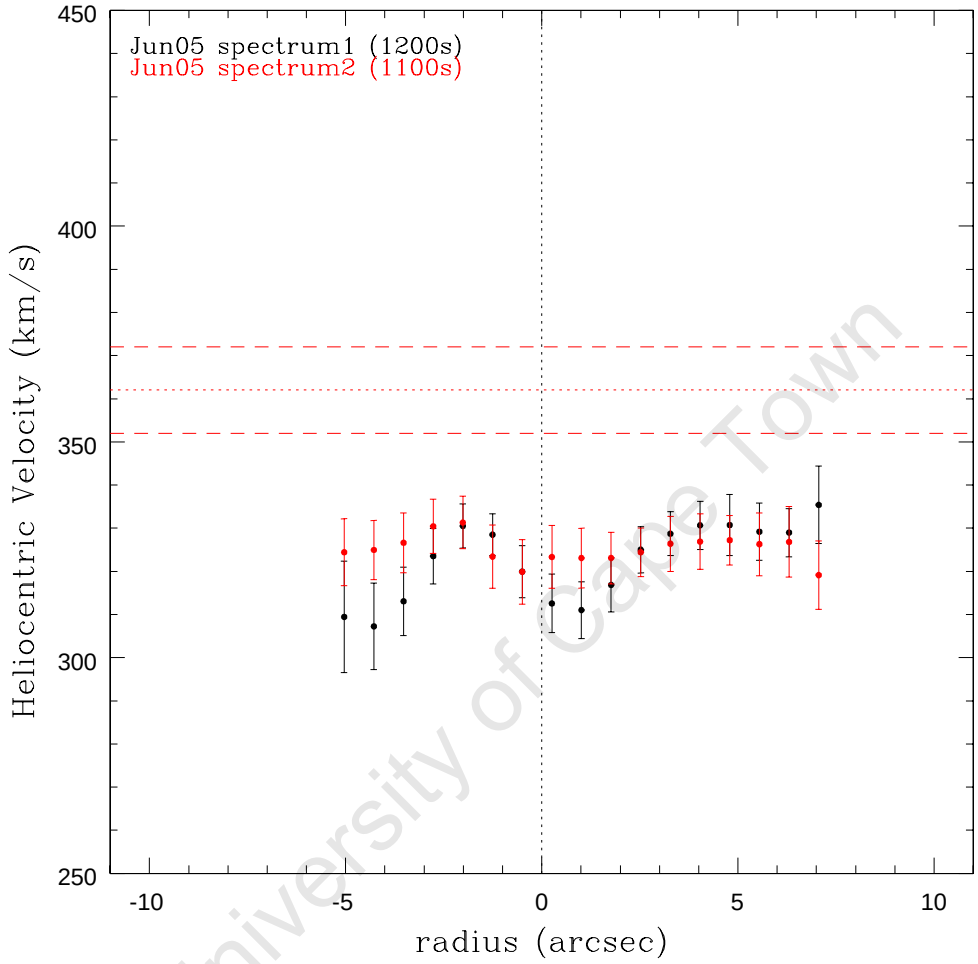

Figure 3.29 Average heliocentric velocity profile measured from emission lines for night June 5. Velocity profiles obtained from the first and second galaxy spectrum are shown in black and red, respectively. The literature value of the heliocentric velocity and 1σ deviation from optical observations are shown by the horizontal dotted and dashed lines, respectively. The vertical line indicates the galaxy center.

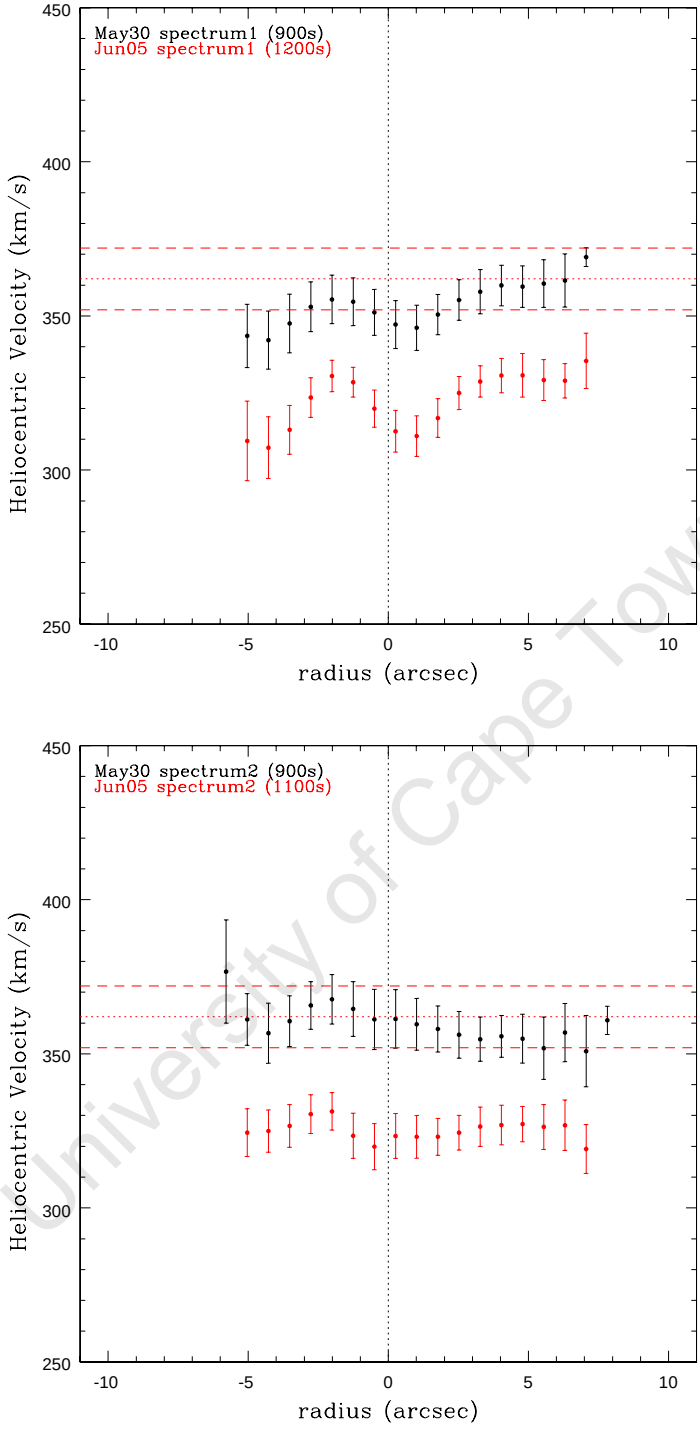

Figure 3.30 A comparison of heliocentric velocity profiles obtained for the nights May 30 and June 5. The profiles derived from the first (*top*) and second (*bottom*) galaxy exposures of the respective nights are plotted. The literature value of the heliocentric velocity and 1σ deviation from optical observations are shown by the horizontal dotted and dashed lines, respectively. The vertical line indicates the galaxy center.

emission lines using the RVIDLINES task. The systemic velocity of the galaxy is given as the average velocity obtained from these lines. The derived velocities for the six galaxy spectra are listed in Table 3.6 together with those values obtained from the absorption lines. There is a good agreement between the systemic velocities obtained from the emission and absorption lines. The lower velocities of $\Delta v_{\rm sys} \sim 30$km s^{-1} from the literature value of the systemic velocity are again measured for the galaxy spectra acquired on the night June 5.

3.5.3 NGC 59 Velocity Profiles from Emission Lines in Red Spectra

The red spectrum of NGC 59 (Fig. 3.8) shows three prominent emission lines on the first CCD (4750–5150Å): the H$\beta(\lambda 4861)$ and [O III]$(\lambda\lambda 4959, 5007)$ emission lines. The heliocentric velocity profiles of the galaxy were extracted from these dominant emission lines using the same Doppler shift technique as described for the blue spectra (see previous section).

A total of 27 apertures were defined along the spatial axis of the galaxy. Each aperture was created by combining six rows in the galaxy spectrum which gives an aperture size of $\sim 1\farcs54$. The heliocentric velocity from the emission lines was then measured in each aperture using RVIDLINES task. The velocity profile of the galaxy was calculated as the (non-weighted) average heliocentric velocity from the three emission lines. The velocity profiles derived from the individual red galaxy spectra are displayed in Fig. 3.31. The strong emission lines in the red galaxy spectra allows for the velocity profiles to be measured out to at least a radius of $r \sim 10''$. This radial range corresponds to the central region of the galaxy in which the Hα emission (Skillman et al. 2003) is detected (see Fig 3.5). The heliocentric velocities at each aperture are determined with an RMS error of $\lesssim 10$km s^{-1} which leads to the well-defined profile shapes.

Figure 3.31 shows that the resulting velocity profiles are in good agreement with the literature value of the heliocentric velocity. The rotational structure is clearly seen in the velocity profile derived from the first galaxy exposure. This profile is symmetrical about the galaxy center and gives a maximum rotational velocity of $v_{\rm rot} \sim 20$km s^{-1} for the ionized gas component of the galaxy. The highest degree of rotation is seen in the first galaxy spectrum. The velocity profiles tend to become more flat in the spectra that immediately follow the first galaxy exposure. This effect is very similar to that seen in the blue spectra (see section 3.5.2). The 2D galaxy spectra obtained in the red are displayed in Fig. 3.32. A rotation-like signature is not quite apparent in the emission lines of these spectra. A closer look at the velocity profiles from the second and third galaxy exposures reveals that the rotation is maintained for $r < -1''$. For these spectra, the rotational structure in the profiles seems to disintegrate for $r > -1''$. The velocity profile from the final galaxy exposure is flatter than that derived from the previous exposure which suggests that the rotational structure degrades with time. The different profile shapes obtained from the red galaxy spectra indicate that the slit position has changed over the course of the observations. The possible cause of the degradation of the velocity profiles is explored in section 3.5.4.

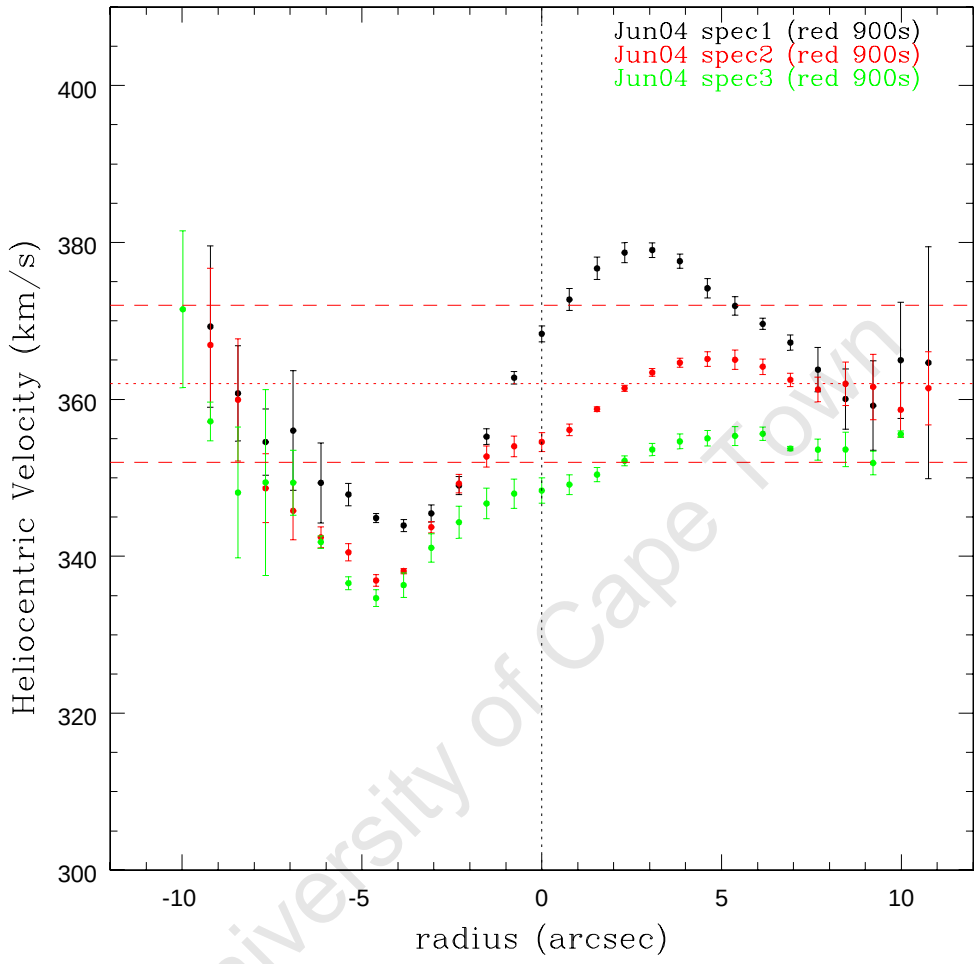

Figure 3.31 Heliocentric velocity profiles measured from emission lines in the red spectra of NGC 59. The velocity profiles derived from the three galaxy spectra of June 4 are displayed. The first, second and third galaxy exposures are shown in black, red and green, respectively. The literature value of the heliocentric velocity and 1σ deviation from optical observations are shown by the horizontal dotted and dashed lines, respectively. The vertical line indicates the galaxy center.

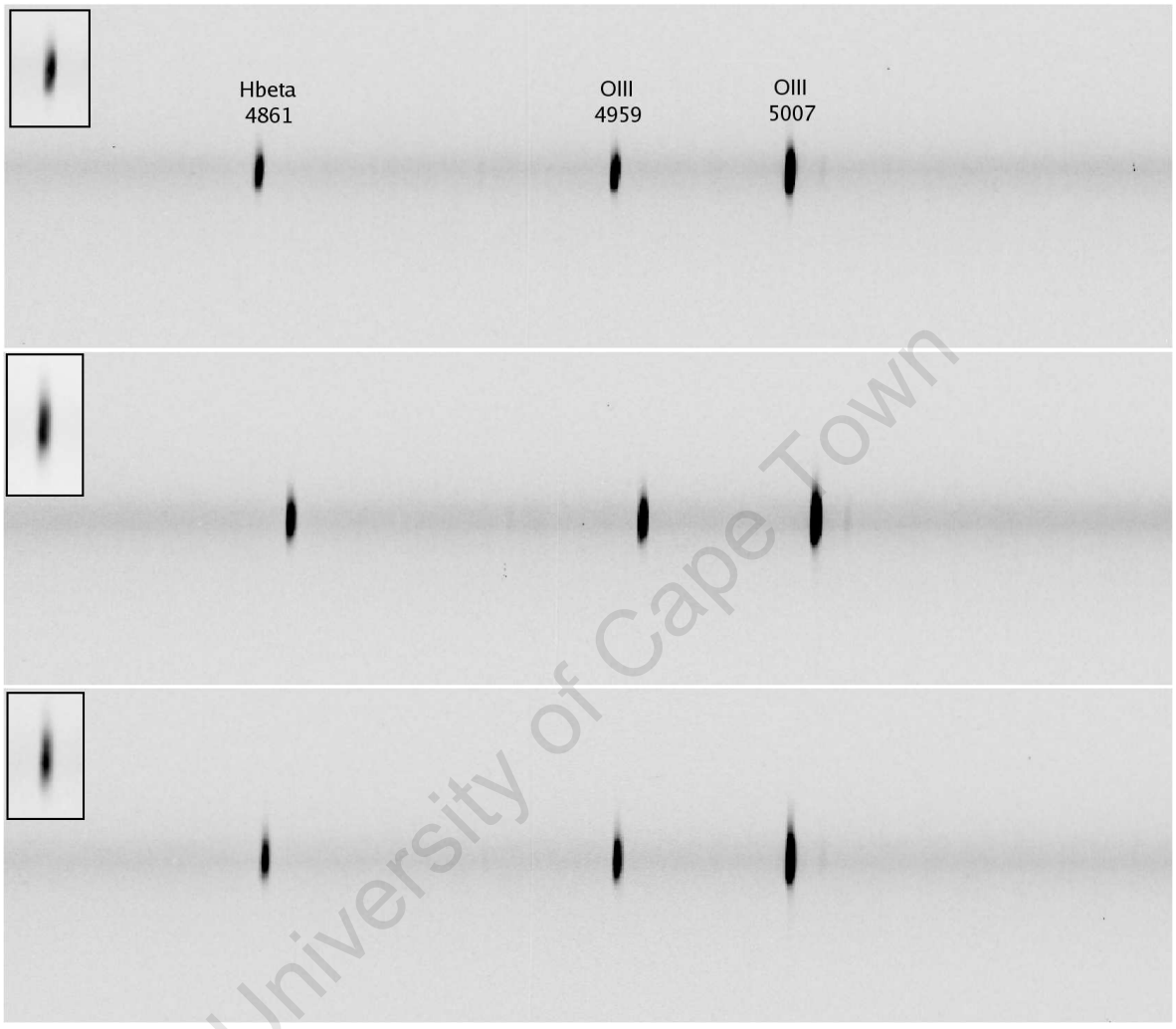

Figure 3.32 Consecutive 2D spectra of NGC 59 obtained with the red (GR2300) grating. The exposure time of the individual spectra is 15-minutes. The wavelength range of the first CCD (4750–5150Å) is shown. The inset on the left of each galaxy spectrum magnifies a region around the Hβ(λ4861) emission line.

3.5.4 Discussion of the Velocity Profile Shapes

The kinematics of the galaxy NGC 59 were extracted from the SALT longslit spectra in sections 3.5.2–3.5.3. The velocity profile of the galaxy was derived from the individual spectra acquired in the blue and red wavelength range. A variation in the velocity profile shape was detected for the different galaxy exposures. This variation in the profile shape is seen in the galaxy exposures which immediately follow one another and suggests that a change in the observational configuration has taken place. In particular, a possible shift or rotation in the slit position on the galaxy can give rise to the different profile shapes. A comparison of the galaxy spatial profiles, i.e. the light distribution along the slit, from the various spectra provides a simple means of testing whether the slit position has changed from one exposure to the next. We expect the spatial profile of the galaxy spectra to be similar since the same region of the galaxy is being sampled. Differences in overall shape of the spatial profile are therefore an indication of a change in the slit position along the galaxy.

The spatial profile of each galaxy exposure was obtained by summing all the columns (along the dispersion axis) in the 2D spectra (see Figs. 3.13–3.18). The light profile is thus a combination of emission from the galaxy continuum and the ionized gas component. The spatial profiles for the individual galaxy exposures are displayed in Figs. 3.33–3.35. For comparison, the light profiles from galaxy spectra obtained on the same night are grouped together in these figures. The spatial profiles for the nights May 30 and June 5 can be seen in Fig. 3.33. For these nights, up to 40% lower flux is measured in the profiles obtained from the second galaxy exposures. In addition, the spatial profile for the second galaxy exposures is flatter with a less defined peak in intensity compared to the first exposures. The spatial profile of the galaxy has a certain degree of asymmetry about the strongest peak in intensity. This is evident for the second galaxy exposure of the night May 30 which shows a weaker intensity peak at ~ 10 pixels (or $4\farcs5$) to the right of the galaxy center. On the other hand, the second galaxy exposure of June 5 does not exhibit a well-defined peak in the intensity. The spatial profile of this galaxy exposure is flat-topped with a slight dip in the intensity close to the galaxy center. A clear difference in the galaxy spatial profiles of consecutive spectra is revealed for these two nights. The significant decrease in the galaxy flux and overall change in the profile shapes indicate that these spectra are sampling different regions of the galaxy. The spatial profiles of the galaxy spectra acquired on the night May 31 are shown in Fig. 3.34. A similar light profile is seen for the spectra obtained on this night. This correlates with the derived velocity profiles from these spectra which were found to have similar rotation-like structure. The light profile shapes for this night suggest that the slit has maintained the same position throughout the observations. A comparison of the spatial profiles obtained from the blue spectra for all nights is also shown in Fig. 3.34. This figure illustrates how the spatial profiles vary from one night to the next which should be accounted for when combining the galaxy spectra to increase the S/N levels.

The light profiles for the red galaxy spectra are shown in Fig. 3.35. Again, the flux and shape of the spatial profiles vary for the three galaxy exposures. The largest flux is measured for the second galaxy exposure. The shape of the spatial profiles are slightly different for the three exposures with the first galaxy exposure being the most symmetrical about the peak

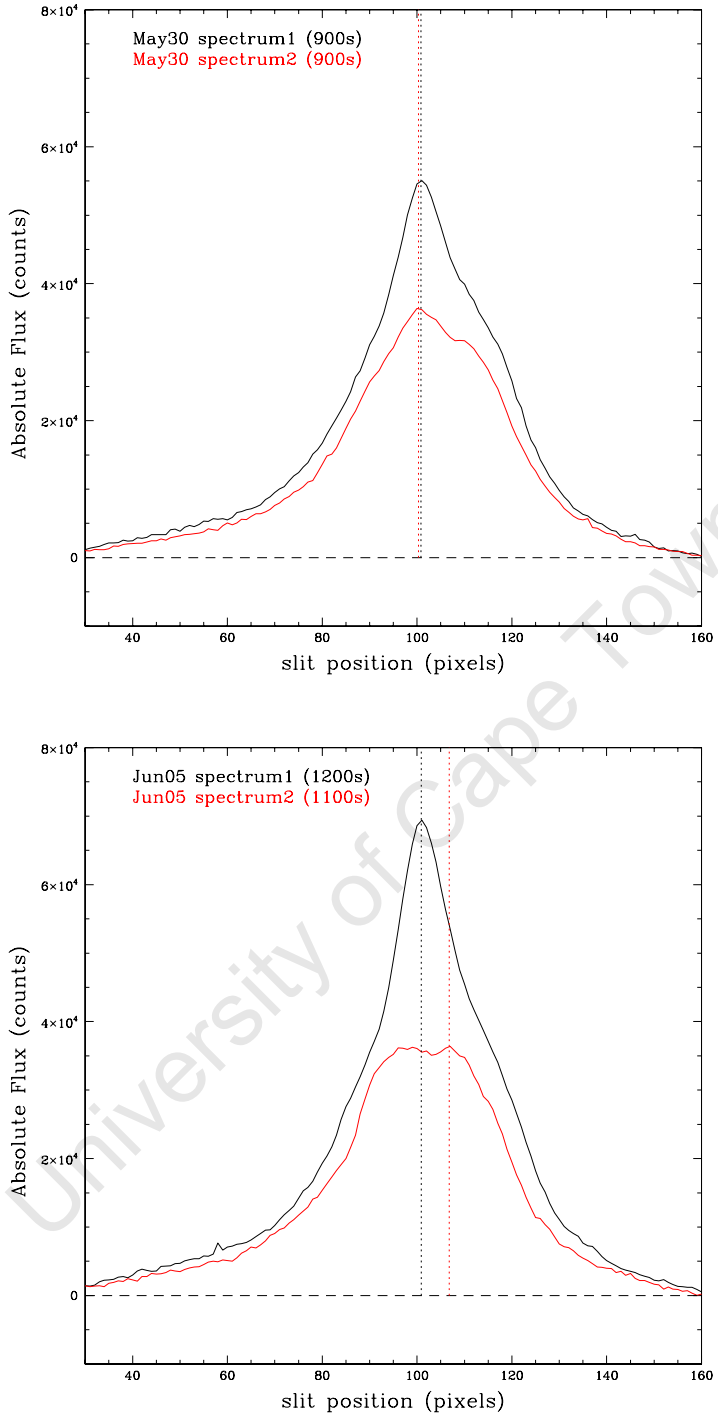

Figure 3.33 Spatial profiles for blue spectra of NGC 59 for the nights May 30 (*top*) and June 5 (*bottom*). The horizontal axis gives the CCD row number along the slit. The first and second galaxy exposures are shown in black and red, respectively. The vertical line indicates the position of the peak in the spatial profile of each spectrum.

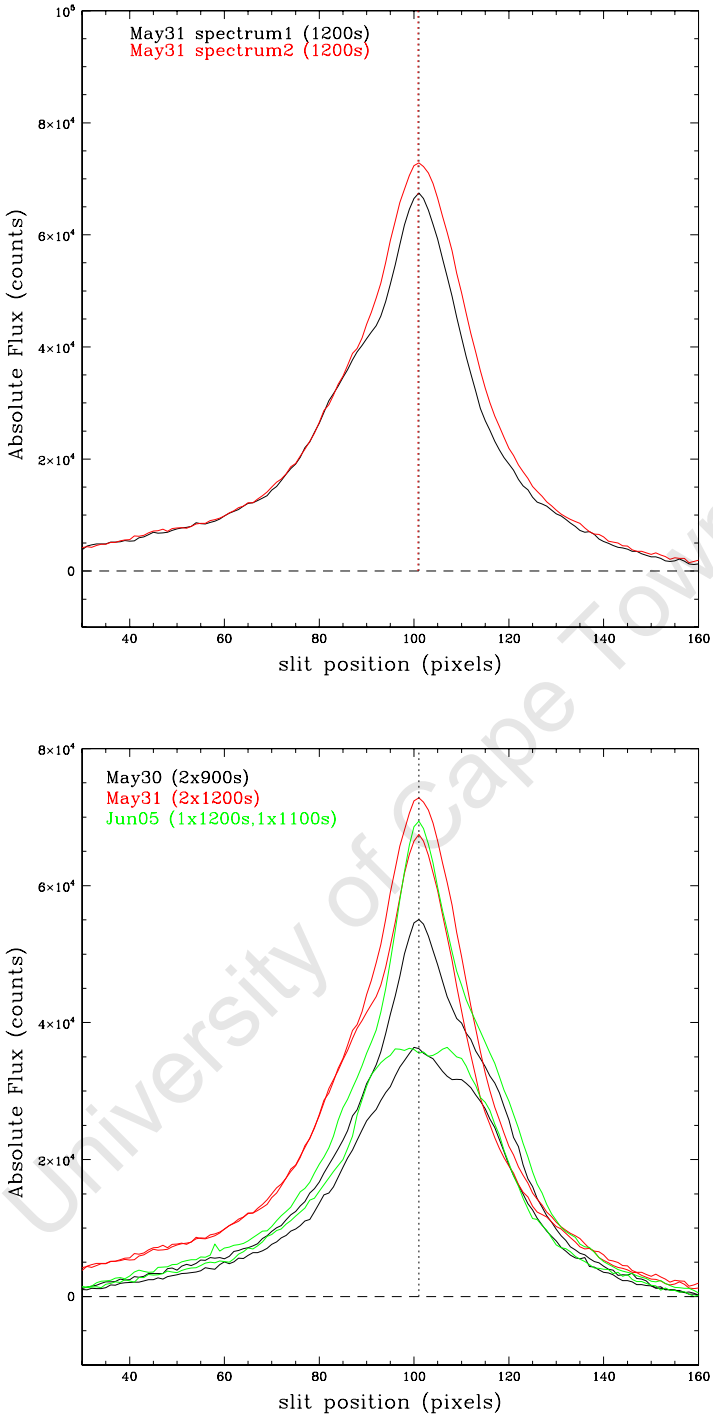

Figure 3.34 *Top*: Spatial profiles of NGC 59 for blue spectra acquired on the night May 31. *Bottom*: The galaxy spatial profiles obtained for the blue spectra of the three nights of observation. The various nights are represented by the different colors: May 30 – black, May 31 – red and June 5 – green. The horizontal axis gives the CCD row number along the slit. The vertical line indicates the location of the peak in the spatial profile of each spectrum.

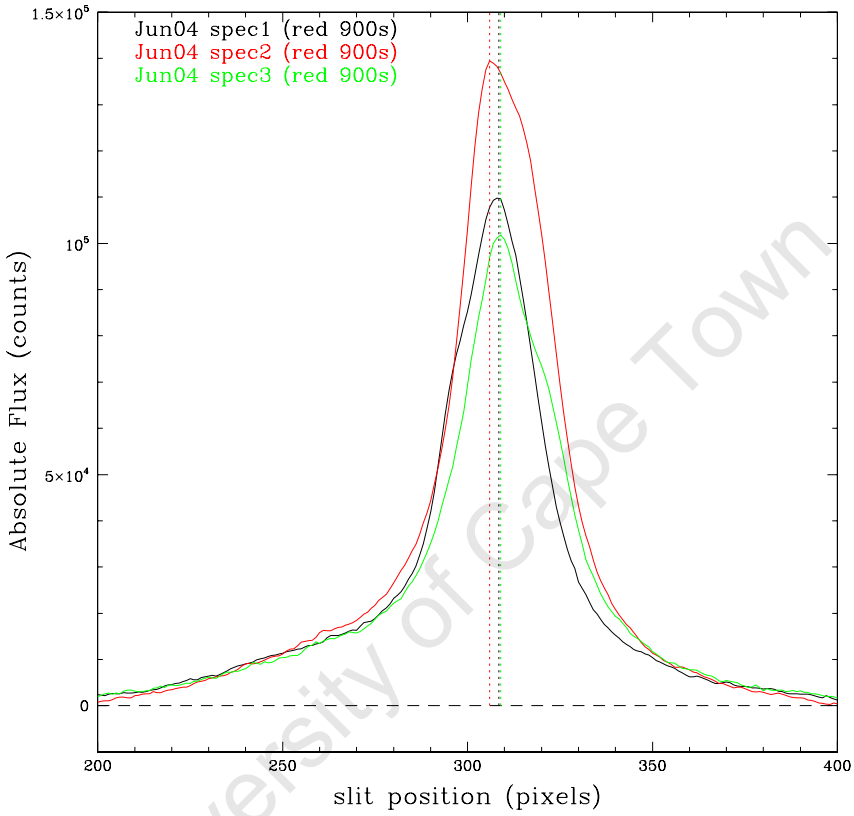

Figure 3.35 Spatial profiles for red spectra of NGC 59. The horizontal axis gives the CCD row number along the slit. The first (*black*), second (*red*) and third (*green*) galaxy exposures are shown. The vertical line indicates the location of the peak in the spatial profile of each spectrum.

in intensity. This symmetry is reflected in the velocity profile derived from the first galaxy exposure (see Fig. 3.31). A slight change in the slit orientation along the galaxy can cause the degradation of the velocity profile seen in the second and third exposures.

Further clarification of the variations in the velocity and light profile shapes can be gained by modeling possible changes in the slit position. We have used the deep H-band image of NGC 59 from Chapter 2 to re-construct the slit position and orientation along the galaxy. Figure 3.36 shows the slit orientation along the galaxy. The dimensions of the slit have been proportionately scaled to represent the $1\farcs5$ slit width of the SALT/RSS. This figure illustrates the "ideal" observational configuration of NGC 59 needed to accurately measure the kinematics along the major axis of the galaxy. The galaxy central coordinates and the position angle (as measured in the optical) are given by NED (Table 3.2) and Lauberts & Valentijn (1989), respectively. Skillman et al. (2003) have detected ionized gas in the central $15''$ of NGC 59 which was then decomposed into four H II regions each showing a peak in the Hα emission. The location of these peaks are shown by the blue points in Fig 3.36. The uncertainty in the coordinates of the peaks in Hα emission is $\lesssim 2''$.

Figure 3.36 shows that the optical center of NGC 59 is situated between the two nuclear components identified in the NIR. The maximum of both nuclear components lie within the $1\farcs5$ slit since the optical center of the galaxy was specified. Two of the Hα emission peaks are also located in the slit. These peaks are seen on the opposite sides of the optical center and are separated by $\Delta r \sim 4\farcs2$. The main contribution to the Hα emission comes from the peak to the left of the galaxy center. This peak corresponds to the dominant H II region in the center for which at least five times greater flux in the Hα was measured compared to the neighbouring regions. This ionized region is situated well within the slit and is the origin of the prominent emission lines in the galaxy spectra. The dominant peak lies $\Delta r \sim 2\farcs2$ from the northern nuclear component. Given the astrometric uncertainty of $\lesssim 2''$ in the coordinates of the Hα emission peaks, it is thus possible for the dominant peak to overlap with the northern nuclear component. This correlates with the result of Chapter 2 (section 2.7.3) where the northern component shows the most recent burst of star formation activity.

The symmetric velocity profile derived from the first galaxy exposure in the red (Fig. 3.31) was most likely obtained if the slit is centered on the dominant Hα peak. This orientation will additionally result in the northern nuclear component being centered in the slit which gives the symmetric light profile. In Fig. 3.36, the positive radii r of the velocity profiles are seen to the left of the galaxy center while negative radii are measured to the right. The asymmetry in the light profiles (seen at positive radii) is thus caused by a gradual, counter-clockwise rotation of the slit orientation which leads to the sampling of the southern nuclear component. The asymmetry in the spatial profiles is introduced when this component is sampled in the slit. The larger flux detection for the second galaxy exposure in the red is therefore a combination of both nuclear components. The slit rotation, however, distorts the velocity profile derived from this spectrum so that the kinematics is no longer measured about the galaxy major axis. Note that the velocity profiles derived from the second and third galaxy exposures provide evidence for a slit rotation rather than a shift in its position on the galaxy. A rotation in the slit can result in the preservation of the rotational structure

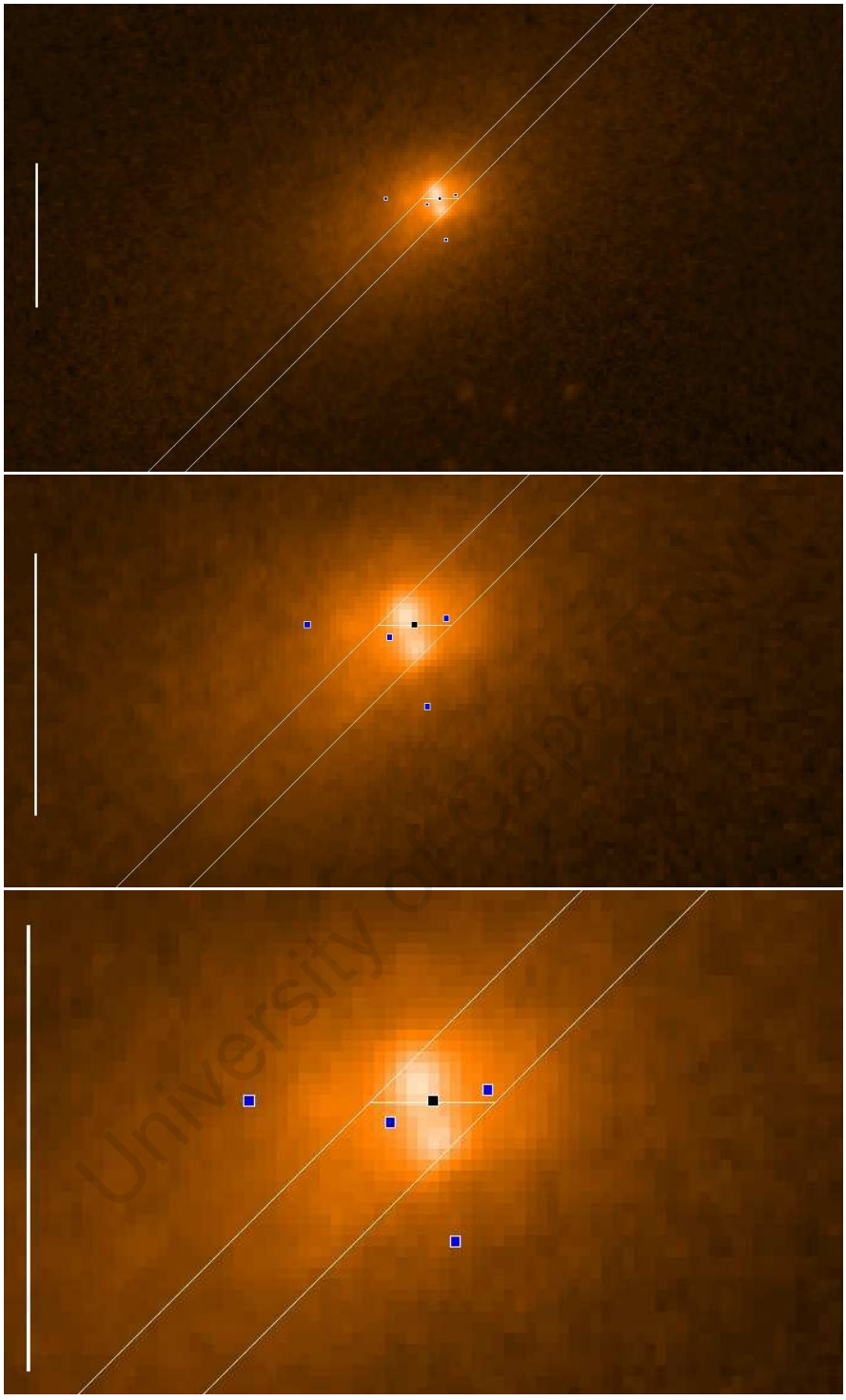

Figure 3.36 Slit orientation along the H-band image of NGC 59. The consecutive images (from top to bottom) zoom into the galaxy center with a relative scale of $20''$ shown by the vertical bar on the right of the image. The white lines represent the $1\farcs5$ slit which is centered on the optical center of NGC 59 (black point). The location of the four peaks in the Hα emission is shown by the blue points. The dominant peak in the Hα emission lies within the slit and is seen to the left of the galaxy center.

observed at negative radii in Fig. 3.31. A similar argument can be given for the blue spectra of the nights May 30 and June 5 in which the first galaxy exposures have been obtained with the slit centered on the northern nucleus. The rotation in the slit leads to the different profile shapes observed in the second galaxy exposures. The slit orientation was however maintained on the night May 30 giving similar velocity profiles of the galaxy. The changes in the slit orientation are an effect of the guiding system of the SALT/RSS. These observations were performed using a single guide star in the FoV which can lead to the changes in the slit orientation. These effects are most significantly seen for long exposure observations. Clearly, the stability of the SALT/RSS guiding system needs to be addressed before carrying out long exposure spectroscopic observations with this instrument.

Overall, the kinematic results suggest that the northern component is the "true" nucleus of NGC 59. A rotational velocity of $v_{\rm rot} \sim 20$km s^{-1} was measured from the ionized gas kinematics. For the kinematical analysis presented in section 3.5.5, we have assumed that the slit position has been centered on the nucleus in the first galaxy exposures of NGC 59. It has also been assumed that similar changes in the slit orientation have taken place in the galaxy spectra obtained for the nights May 30 and June 5. These assumptions allow for the stacking of the blue spectra that sample more or less the same regions of the galaxy.

3.5.5 Velocity Profile Modeling of NGC 59

Method

The galaxy spectrum is a superposition of spectra from individual stars along the line-of-sight. The spectra of the individual stars are however shifted in wavelength as each star has a different motion with respect to the galaxy. The net effect of these shifts in wavelength is seen as a broadening of the absorption lines in the galaxy spectrum. To quantify these effects of broadening the line-of-sight velocity distribution (LOSVD) is defined as the fraction of stars in the galaxy spectrum with a line-of-sight velocity between $v_{\rm los}$ and $v_{\rm los} + {\rm d}v_{\rm los}$. The basic assumption is that the galaxy spectrum $G(v)$ is the convolution of a suitable template spectrum $S(v)$ and a certain LOSVD $L(v_{\rm los})$:

$$G(v) \approx \int L(v_{\rm los}) S(v - v_{\rm los}) {\rm d}v_{\rm los} \ , \tag{3.1}$$

where v is the stellar velocity. To the lowest order, the LOSVD is well approximated by a Gaussian as seen for the Fourier cross-correlation analysis in section 3.5.2. However, the higher spectral resolution brought about by improvements in the detectors allows for the measurement of deviations from the Gaussian shape.

In this section, the galaxy kinematics are derived from the stellar component by modeling the LOSVD as a Gauss-Hermite series of the form:

$$L(v_{\rm los}) = \frac{1}{\sigma}\alpha(w)\left[1 + \sum_{j=3}^{N} h_j H_j(w)\right], \qquad w \equiv (v_{\rm los} - v)/\sigma, \qquad \alpha(w) = \frac{1}{\sqrt{2\pi}} {\rm e}^{-\frac{1}{2}w^2}. \tag{3.2}$$

The lowest order term of the series $\alpha(w)$ is a standard Gaussian. The parameters v and σ are the mean velocity and velocity dispersion of the best-fitting Gaussian. The higher order terms

in the series are orthogonal to this Gaussian. The functions H_j are the Hermite polynomials. The Gauss-Hermite moments h_j measure deviations from the Gaussian shape. The lowest order anti-symmetric deviations from a Gaussian are quantified by the moments h_3 and h_5, while the lowest order symmetric deviations are given by h_4 and h_6.

The kinematics of the stellar component of NGC 59 were determined using Gauss-Hermite Pixel Fitting software of van der Marel (1994). For this pilot study, we only present the mean velocity v and velocity dispersion σ profiles of the galaxy. The velocity dispersion profile will be used to explore the stellar kinematics in the galaxy center which can give the first clues of a possible IMBH at the center of NGC 59.

Data Preparation

The kinematical analysis was carried out for the blue spectra of NGC 59. A minimum S/N ratio of ~ 10 is required to successfully extract the galaxy kinematics using the Gauss-Hermite Pixel Fitting software. The blue spectra were carefully stacked to reach this S/N level beyond the central regions of the galaxy.

The systemic velocity of the individual galaxy spectra was measured in section 3.5.2. The velocities from the individual spectra were found to agree within $\Delta v_{\rm sys} \sim 30$km s^{-1}. This velocity difference between the galaxy spectra corresponds to a maximum offset of ~ 2 pixels in the dispersion scale. A direct stacking of these spectra can therefore degrade the absorption (and emission) line features which is seen as a broadening effect in the combined galaxy spectrum. To preserve the line widths of the absorption features, each of the galaxy spectra was shifted in wavelength to a zero velocity scale. The systemic velocities listed in Table 3.6 were used to shift the individual spectra to zero velocity. The resulting spectra were then used to create the combined galaxy spectrum.

In section 3.5.4, we found that the differences in the velocity profile shape for each galaxy exposure was due to the rotation of the slit. The galaxy spectra were thus combined in three stages in order to preserve the stellar kinematics about the major axis:

1. The first galaxy exposures of the nights May 30 and June 5 were combined. A clear rotation is seen in the emission lines of these spectra. Assuming that the slit has rotated in the same manner, the second galaxy exposures of these nights were combined separately.

2. The first galaxy exposures for the three nights May 30, May 31 and June 5 were combined. In addition, the second galaxy exposures for the three nights were independently combined.

3. The six galaxy exposures obtained for the three nights were combined.

Steps 1 and 2 assume that similar changes in the observing configuration have taken place for each of the three nights. This allows for the separate stacking of the first and second galaxy exposures of the various nights. The galaxy kinematics were then extracted from each of the combined 2D galaxy spectra.

Velocity Profiles using Gauss-Hermite Pixel Fitting Software

A 1D template spectrum and 2D galaxy spectrum are needed as inputs by the Gauss-Hermite Pixel Fitting software. The K0 III template star was chosen to best describe the stellar population of the galaxy NGC 59. A single K0 III template spectrum was selected for the kinematical analysis. The template and galaxy spectra were rebinned logarithmically in

wavelength before running the Pixel Fitting software.

The kinematic profiles of the galaxy were determined using three different programs of the Pixel Fitting software. The first program prepares the template spectrum for the cross-correlation with the galaxy spectrum by convolving it with Gaussian distributions having various dispersions. A range of velocity dispersions for the galaxy was selected. An estimate of the velocity difference between the galaxy and template spectrum was also specified. The second program prepares the 2D galaxy spectrum for the cross-correlation analysis. This program allows for various regions in the galaxy spectrum to be masked. The emission lines in the galaxy spectrum were effectively masked by specifying the wavelength ranges of these features. The rows in the galaxy spectrum were rebinned to achieve a minimum S/N of ~ 15. The center of the galaxy corresponds to the bin with the largest S/N ratio. The third program determines the best-fitting LOSVD to each row of the rebinned galaxy spectrum using the different convolutions of the template spectrum. The Pixel Fitting method uses a χ^2 minimization technique defined by:

$$\chi^2 = \sum_{pixels} \left[G(v) - S(v) \cdot L(v_{\rm los})\right]^2 \ . \tag{3.3}$$

The convolution $S(v) \cdot L(v_{\rm los})$ is evaluated by the first program and is directly compared to the galaxy spectrum in a χ^2 sense. The χ^2 minimization is carried out in pixel space, neglecting all masked pixels in the galaxy spectrum. A fifth-order polynomial was specified as the maximum order to be used in the continuum fitting. It should be noted that the K0 III template is not representative of the younger stellar population detected in the center of NGC 59. This can result in a significant template mismatch with the galaxy spectrum. A larger variety of template star spectra are however needed to find the best matching stellar template or combination of templates for the spectrum of NGC 59. The mean velocity and velocity dispersion profiles for the different combinations of the galaxy spectra are displayed in Figs. 3.37–3.39. The measured velocity dispersion in these figures represents the intrinsic dispersion of the galaxy itself. The effects due to instrumental broadening of the absorption lines have been eliminated since the galaxy and template star were acquired using the same observational configuration.

The kinematical results derived from the first and second galaxy exposures are shown by the black and red points, respectively, in Figs. 3.37 and 3.38. The rotation of the stellar component of the galaxy is clearly seen in the velocity profile derived from the first exposures of the nights May 30 and June 5 (Fig. 3.37). The rotation is measured in the central $\sim 15''$ region of the galaxy with receding velocities detected at negative radii. The rotation of the stellar component is opposite to that measured for the ionized gas component (see Fig. 3.31). This provides evidence for a counter-rotating disk in the galaxy NGC 59. A maximum rotational velocity of $v_{\rm rot} \sim 20$km s^{-1} is however observed for both components. The velocity dispersion as a function of radius for the combined galaxy spectrum of the nights May 30 and June 5 is also shown in Fig. 3.37. The dispersion at each radius was determined with an accuracy of $\Delta\sigma \lesssim 30$km s^{-1}. A central velocity dispersion of $\sigma_0 \sim 70$km s^{-1} was measured from the first galaxy exposures. An increase in the dispersion profile is observed for positive radii which on average give a dispersion of $\sigma \sim 100$km s^{-1} for the galaxy. The low S/N ratio of the

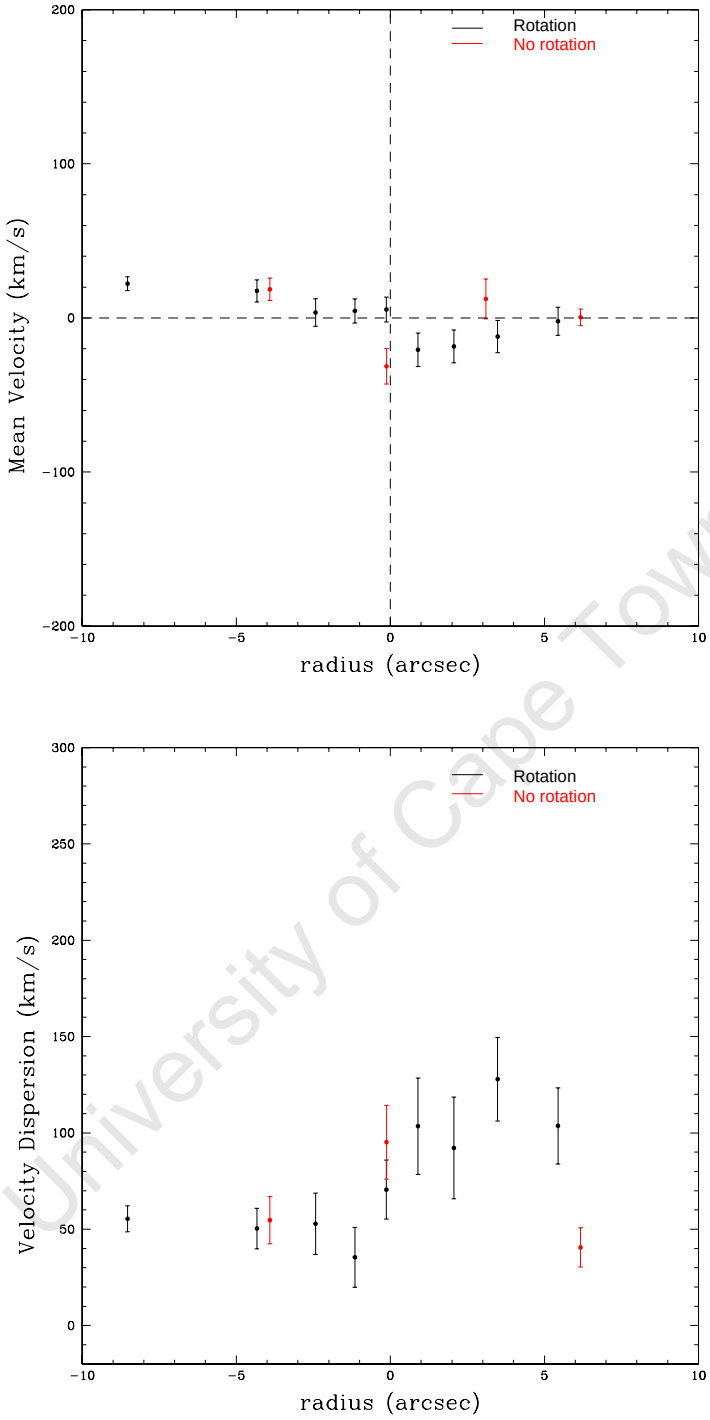

Figure 3.37 Mean velocity (*top*) and velocity dispersion (*bottom*) profiles of the combined galaxy spectra from the nights May 30 and June 5. Each of the combined spectra correspond to an ∼35 minute galaxy exposure. The black points are the results obtained from first galaxy exposures which show a rotation in the emission lines. Red points are the results obtained from second galaxy exposures.

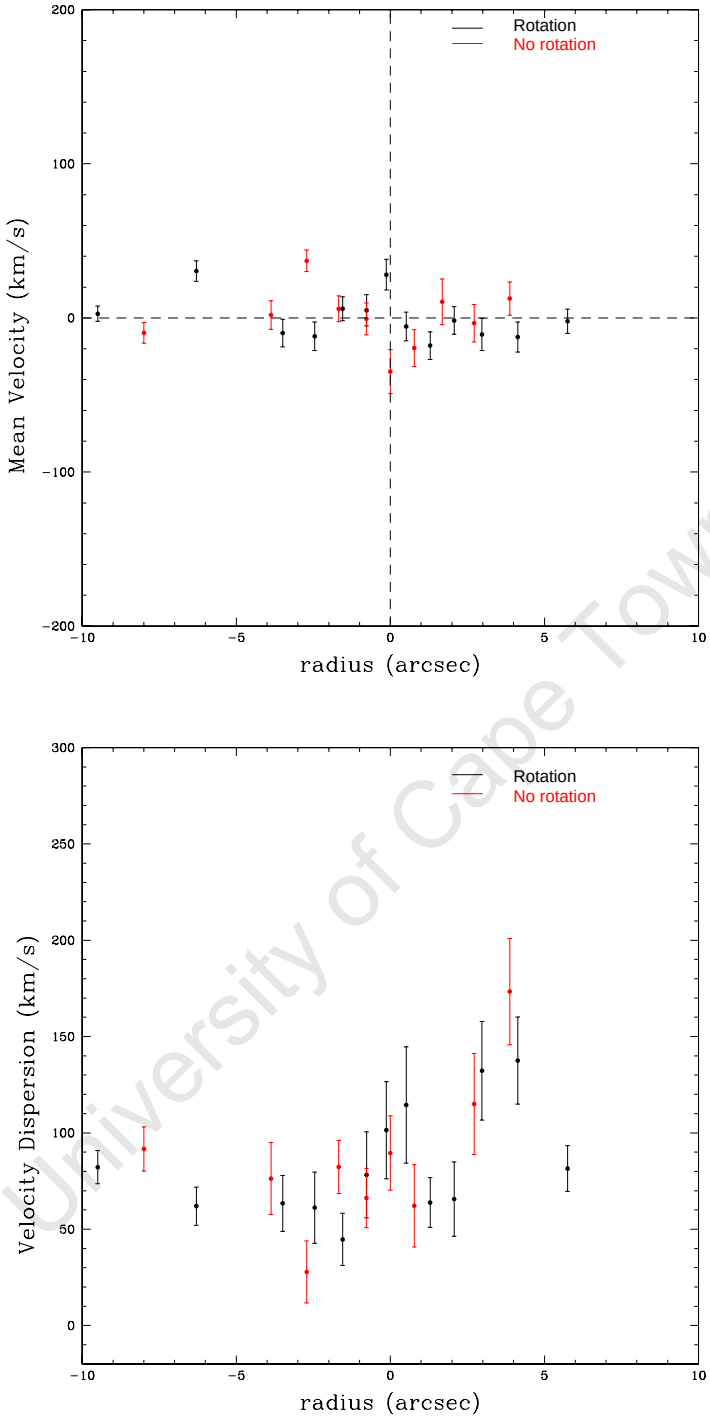

Figure 3.38 Mean velocity (*top*) and velocity dispersion (*bottom*) profiles of the combined galaxy spectra from the three nights (May 30, May 31 and June 5). Each of the combined spectra correspond to an ∼55 minute galaxy exposure. The black and red points are the results obtained from first and second galaxy exposures, respectively.

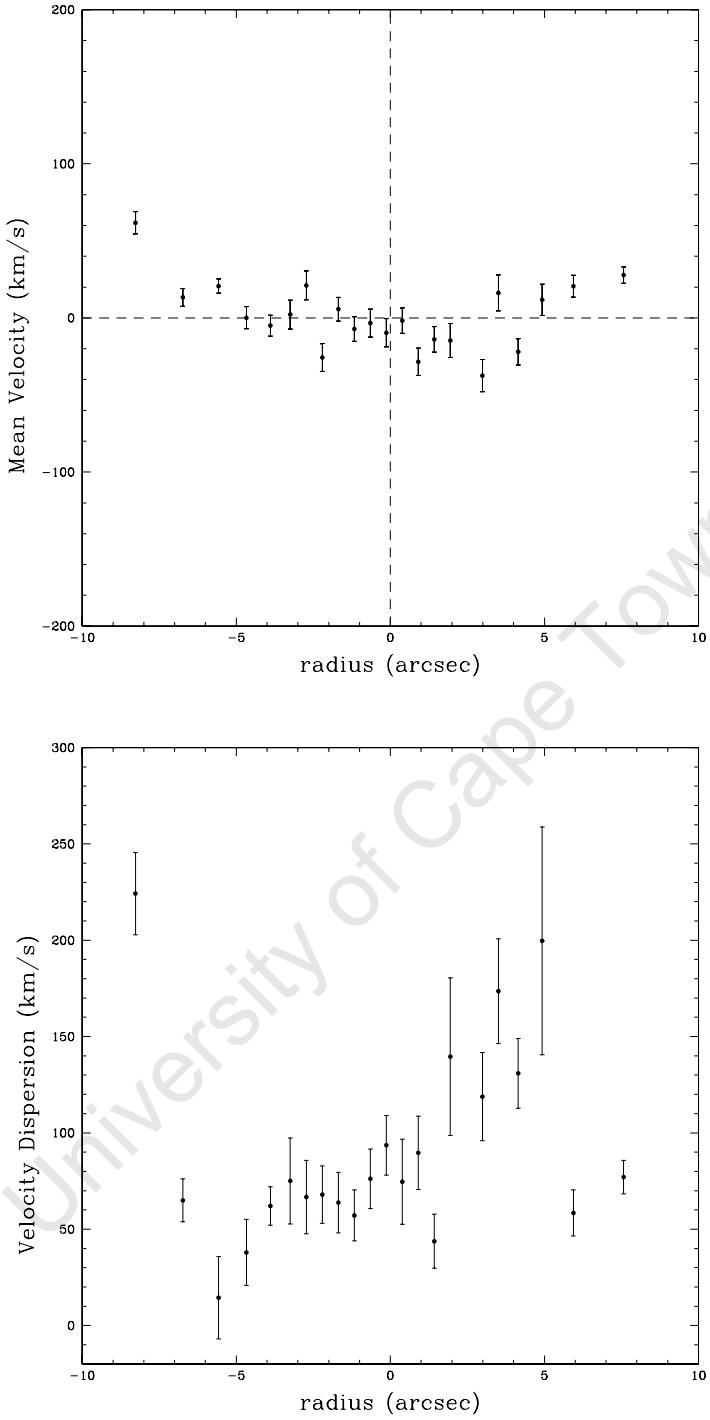

Figure 3.39 Mean velocity (*top*) and velocity dispersion (*bottom*) profile of the combined spectrum obtained by stacking the six galaxy spectra. The combined spectrum corresponds to a 105-minute galaxy exposure.

second galaxy exposures results in much fewer points in the mean velocity and dispersion profiles derived from these spectra. These points do however show similar velocity trends to that obtained from the first galaxy exposures. It is expected that the mean velocity and velocity dispersion profiles are minimally affected by the inclination of galaxy. This effect is not significant in those galaxies showing little rotation such as that seen for NGC 59.

The mean velocity and velocity dispersion profiles derived from the respective first and second galaxy exposures for the three nights are shown in Fig. 3.38. The higher S/N level of the combined galaxy spectra leads to a larger sampling of data points in the central 15″ of the galaxy. These velocity profiles illustrate that the rotational structure seen in Fig. 3.37 is lost when adding the galaxy spectra of May 31 to those obtained for the other two nights. This result suggests that the spectra of May 31 were not carried out with the correct slit orientation, i.e. with the slit aligned with the major axis of the galaxy. We expect that the rotational signature in the first galaxy exposures would be preserved if these spectra sample the same regions of the galaxy. The dispersion profiles of the first and second galaxy exposures show a slight peak in velocity dispersion at the galaxy center. These profiles give a central velocity dispersion of $\sigma_0 \sim 100$km s^{-1} for the galaxy.

Figure 3.39 displays the mean velocity and velocity dispersion profiles of the combined spectrum for the three nights. The rotation of the stellar component cannot be easily distinguished in the velocity profile. This is purely a result of the misalignment of the slit with the major axis so that the radial motions of the stars are not always sampled in the galaxy spectra. Again, the velocity dispersion profile shows a slight increase at the center of the galaxy with a central dispersion of $\sigma_0 \sim 90$km s^{-1}. An additional increase in the dispersion is observed in the radial range of $2'' \lesssim r \lesssim 6''$. The large errors of up to $\Delta\sigma \sim 60$km s^{-1} associated with the data points in this range indicate a poor match between the galaxy and convolved template spectrum. This increase in the velocity dispersion cannot be treated as a physical effect of the galaxy.

The kinematic results of NGC 59 from the total combined spectrum were extracted within the central $\sim 20''$ of the galaxy. This spectrum corresponds to an 105-minute galaxy exposure. These results show that the stellar kinematics could not be extracted beyond the central $r \sim 10''$ radius of the galaxy even with the long exposure time. A steep decline in the throughput in the blue wavelength range was observed during the PV phase of the RSS spectrograph: the system efficiency decreased by ∼40% below the nominal sensitivity at 4000Å. This loss of throughput has seriously affected the S/N levels in the blue spectra of NGC 59. We expect that the galaxy kinematics, for the same exposure time, will be measured out to larger radii once the RSS instrument performs according to specifications.

3.5.6 Discussion of Kinematical Results

The Rotation of NGC 59

The kinematic profiles of NGC 59 were derived from the stellar and ionized gas components of the galaxy. Both components display a net rotation about the minor axis of the galaxy. The rotational axis picks out a preferred direction in the galaxy. It is thus expected that the galaxy will be flattened parallel to this axis. The degree to which the galaxy is flattened due

to rotation depends on the balance between ordered ($v_{\rm rot}$) and random motions (σ) of the stars. The quantity $v_{\rm rot}/\bar{\sigma}$ is used to measure the flattening of the galaxy due to rotation, where $v_{\rm rot}$ is the maximum rotational velocity and $\bar{\sigma}$ is the average velocity dispersion.

To quantify the rotational support of NGC 59, a conservative estimate of the ratio $v_{\rm rot}/\bar{\sigma}$ was computed using the stellar kinematic profiles derived from the first galaxy exposures of the nights May 30 and June 5 (see Fig. 3.37). The maximum rotational velocity $v_{\rm rot}$ was computed as the average of the two data points showing the largest rotation on either side of the mean velocity profile. This gives a maximum rotational velocity of $v_{\rm rot} = 21.4\pm5.8$km s^{-1}. The error in $v_{\rm rot}$ was determined by adding in quadrature the error of the mean velocity of the two data points. For negative radii in Fig. 3.37, the mean velocity was found to increase to the outermost point so that the derived rotational velocity should be considered as the lower limit. The average velocity dispersion $\bar{\sigma}$ was determined from the dispersion profile from the total combined galaxy spectrum (Fig. 3.39). Those data points deviating by more than 2σ from the mean velocity dispersion measured from all points in the profile were not included in the analysis. Additionally, data points with velocity dispersion below the instrumental resolution of $\sigma_{\rm instr} \sim 43$km s^{-1} were neglected. An average velocity dispersion of $\bar{\sigma} = 64.3 \pm 18.9$km s^{-1} was determined for the galaxy where the error was calculated as the standard deviation of the mean. The derived values of the maximum rotational velocity and the average velocity dispersion give $v_{\rm rot}/\bar{\sigma} = 0.33$ for NGC 59.

The ratio $v_{\rm rot}/\bar{\sigma}$ versus the mean ellipticity of NGC 59 is plotted in Fig. 3.40. The mean ellipticity of $\epsilon = 0.41$ for NGC 59 was determined from the NIR observations presented in Chapter 2. For comparison, we have added the $v_{\rm rot}/\bar{\sigma}$ ratios for early-type dwarf galaxies from the literature. The previous measurements of $v_{\rm rot}/\bar{\sigma}$ shown in Fig. 3.40 were mainly carried out for dwarfs in the Virgo Cluster. These samples include the seventeen dEs from Geha et al. (2003), four dE and two dS0 galaxies from Pedraz et al. (2002). The measurement obtained for the dE galaxy FS 76 (De Rijcke et al. 2001), a member of the NGC 5044 group ($v_\odot = 2704\pm33$ km s^{-1}), is also shown in Fig. 3.40. The dE galaxy NGC 205 is a companion of M 31 and represents the only LG dwarf for which a detailed kinematic analysis was conducted (Geha et al. 2006). The $v_{\rm rot}/\bar{\sigma}$ ratio expected from an oblate isotropic, rotationally flattened system seen edge-on (Binney 1978) is shown by the curve in Fig. 3.40.

The Virgo dwarfs, shown by the black points in Fig. 3.40, can be distinguished into two distinct classes: dwarf galaxies with no measurable major axis rotation ($v_{\rm rot}/\bar{\sigma} < 0.1$), and dwarfs with rotation velocities approaching that expected from rotationally supported systems. The rotating and non-rotating dwarfs span a similar range in ellipticity. Dwarf galaxies having $v_{\rm rot}/\bar{\sigma} < 0.1$ are found to rotate too slowly to be consistent with the isotropic model. These dEs are therefore primarily flattened by anisotropic velocity dispersions rather than rotation. A significant rotation in the range of $15 \lesssim v_{\rm rot} \lesssim 30$km s^{-1} was detected in the five early-type galaxies of Pedraz et al. (2002). These dwarfs consisting of three dE and two dS0 galaxies were found to be rotationally supported compatible with the isotropic model. The results obtained for the Virgo dwarf galaxies have shown that dwarfs in general can be supported by rotation contrary to earlier claims (e.g., Bender & Nieto 1990). The galaxy NGC 59 shows similar flattening to that observed for the nearby galaxy NGC 205. These two

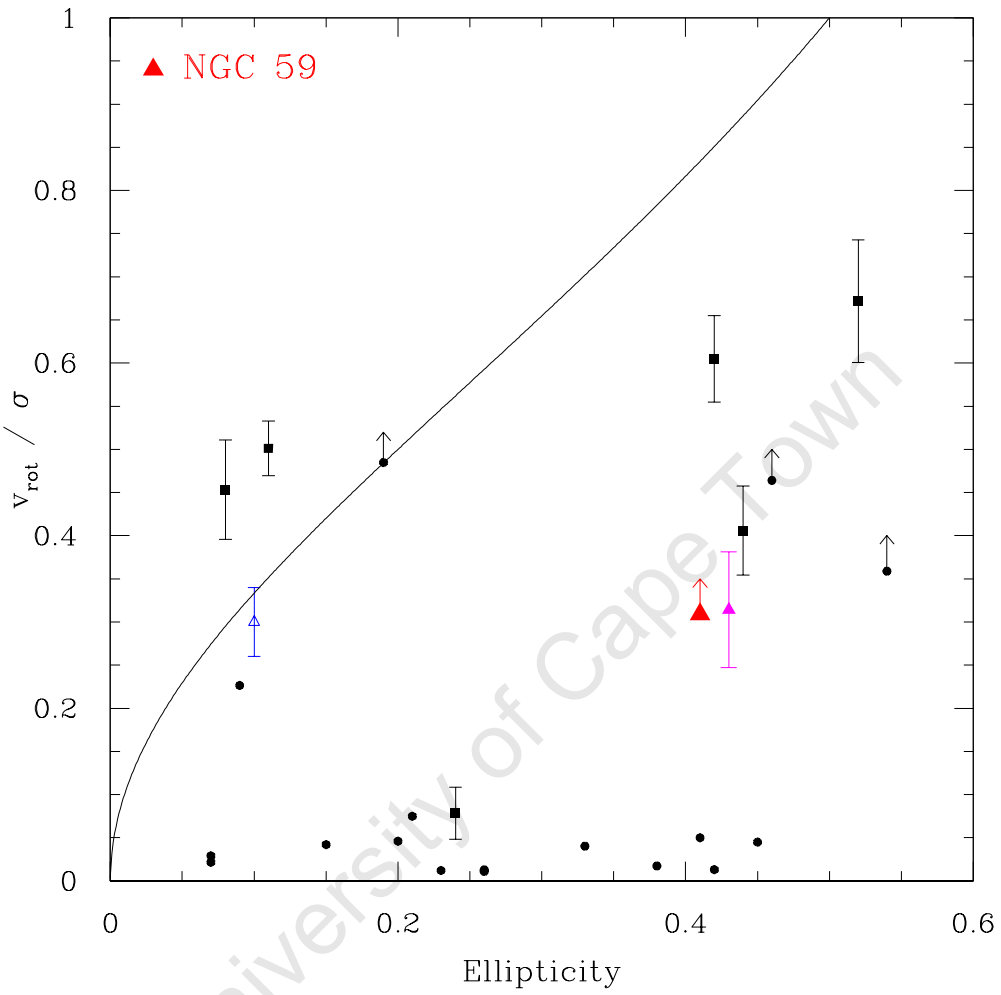

Figure 3.40 Ratio of maximum rotational velocity $v_{\rm rot}$ to average velocity dispersion $\bar{\sigma}$ versus galaxy ellipticity. Black points are early-type dwarf galaxies from the Virgo Cluster taken from Geha et al. (2003) (circles) and Pedraz et al. (2002) (squares). The nearby dE galaxy NGC 205 is shown in magenta. The Sculptor dwarf NGC 59 as determined in this work is indicated by the filled red triangle. The blue triangle represents the dE galaxy FS 76 (NGC 5044 group) from De Rijcke et al. (2001). The solid curve shows the expected relation for an oblate, isotropic galaxy flattened by rotation (Binney 1978).

galaxies are seen to lie midway between a rotationally supported and an anisotropic system. This result suggests that NGC 59 is supported by a combination of rotation and anisotropic pressure as found for NGC 205 (Geha et al. 2006).

The rotation of the galaxy NGC 59 was further investigated by plotting the anisotropy parameter:

$$(v_{\rm rot}/\sigma)^* \approx \frac{(v_{\rm rot}/\bar{\sigma})_{\rm observed}}{(v_{\rm rot}/\bar{\sigma})_{\rm model}} \ , \tag{3.4}$$

where the denominator is the ratio of $v_{\rm rot}/\bar{\sigma}$ predicted by the isotropic model. The ratio of $(v_{\rm rot}/\sigma)^* \simeq 1$ would therefore correspond to a rotationally flattened galaxy. The anisotropy parameter for the dwarf galaxies shown in Fig. 3.40 is plotted against their absolute B-band magnitudes in Fig. 3.41. To compare the properties of the early-type dwarfs with elliptical systems, the sample of giant and intermediate elliptical galaxies corrected to $H_0 =$ 75km s^{-1} Mpc^{-1} from Bender et al. (1992) have been added to this plot. Figure 3.41 shows that the brightest dwarfs tend to be rotationally supported. These dwarfs form an extension of the low-luminosity ellipticals to the dwarf galaxy regime. A range of rotational properties is observed for the dwarf galaxies. Again, the nearby galaxies NGC 59 and NGC 205 are closely grouped in the range showing intermediate rotational support. The current sample of dwarf galaxies is however too small to highlight any trends between the rotational support and luminosity.

We have found the ionized gas component in the central $\sim 20''$ of NGC 59 to be rotating counter-clockwise to the stellar component of the galaxy. This feature is commonly seen in disk (S0) galaxies (Bureau & Chung 2006) and can provide clues to the evolution of these systems. The few systems which have been studied show direct evidence for ongoing accretion (Sadler et al. 2002), signatures of past mergers or tidal interactions (e.g., Chung et al. 2006). The dwarf galaxy NGC 59 shows no tidal interaction and is rather isolated in the Sculptor group. It is thus possible that the counter-rotating gas in the center of this galaxy can be attributed to a merger event. This scenario would provide further support for a double nucleus, rather than a nucleus and star-forming region, in the center of NGC 59. The origin of the counter-rotating gas in NGC 59 however remains speculative with the current data set. A detailed mapping of the stellar and (neutral and ionized) gas components is needed to investigate the origin of the counter-rotating hot gas in this relatively isolated galaxy.

First Clues to a Central IMBH in NGC 59

Ferrarese & Merritt (2000) showed that a correlation between the central BH mass $M_{\rm BH}$ and velocity dispersion of the bulge σ_0 exists for early-type galaxies (see Chapter 1, section 1.2.1). This relationship was established for early-type galaxies having a central BH mass in the range of $10^6 \lesssim M_{\rm BH}\ (M_\odot) \lesssim 10^{10}$. In the following analysis, we assume that the $M_{\rm BH} - \sigma_0$ relationship can be extended to the low BH mass regime ($M_{\rm BH} \lesssim 10^6 M_\odot$). This assumption allows us to infer the mass of a possible BH in the center of NGC 59 given its central velocity dispersion from the SALT/RSS spectra.

An estimate of the central velocity dispersion σ_0 of NGC 59 was obtained using the dispersion profile from the final combined galaxy spectrum shown in Fig. 3.39. The observations are seeing-limited so that the average dispersion was computed from data points within the central $\sim 2''$ (corresponding to $\sim$ 52pc using the Galactocentric scale) of the galaxy. The

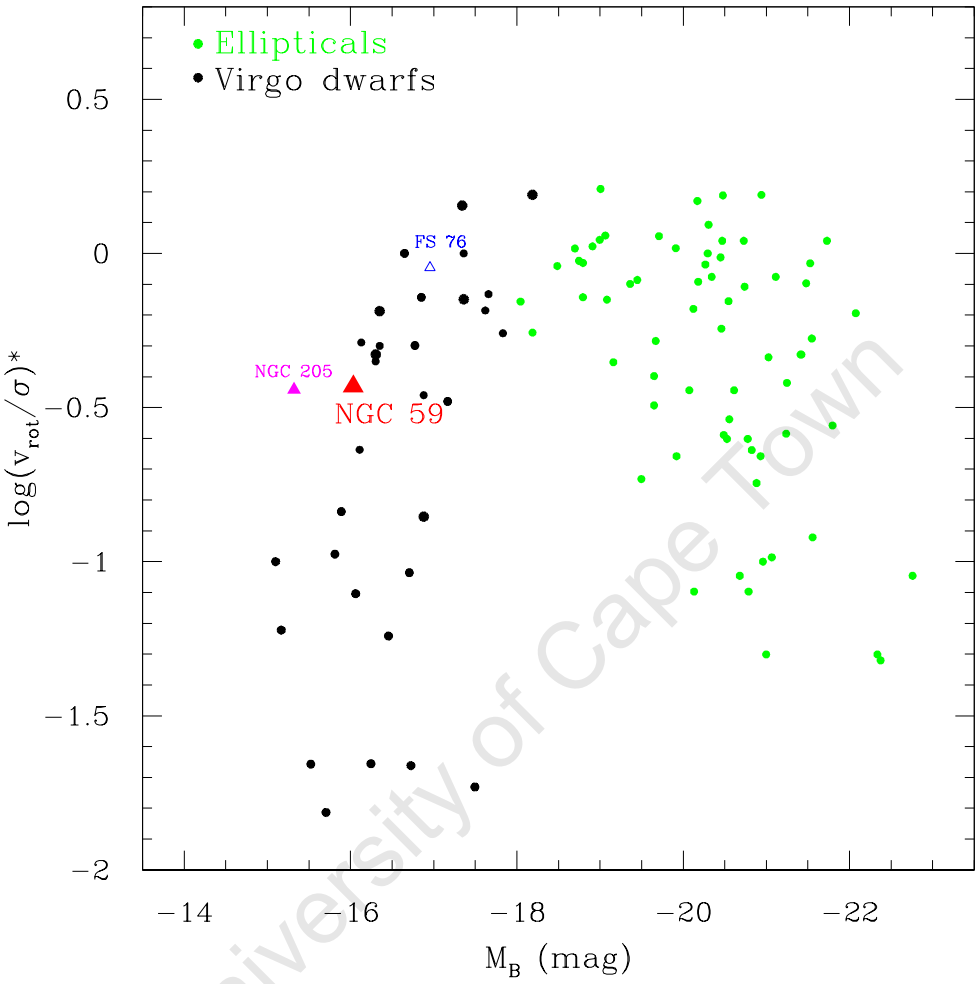

Figure 3.41 Logarithm of anisotropy parameter (ratio of observed $v_{\rm rot}/\bar{\sigma}$ to that predicted by the isotropic model) against absolute B-band magnitude. The sample of giant and intermediate elliptical galaxies from Bender et al. (1992) are shown by the green points. Black points are early-type dwarf galaxies from the Virgo Cluster taken from Geha et al. (2003) and Pedraz et al. (2002). The nearby dwarfs NGC 59 and NGC 205 are shown in red and magenta, respectively. The blue triangle represents the dE galaxy FS 76 (NGC 5044 group) from De Rijcke et al. (2001).

central velocity dispersion of NGC 59 is $\sigma_0 = 83.5 \pm 8.2$km s^{-1}. Given the central velocity dispersion of the galaxy, the linear $M_{\rm BH} - \sigma_0$ relation of Tremaine et al. (2002) was then used to infer the mass of a central BH. The linear relation of Tremaine et al. (2002) gives a central BH mass of $4 \times 10^6\,{\rm M}_\odot$ for NGC 59. The location of the galaxy NGC 59 in the $M_{\rm BH} - \sigma_0$ diagram is indicated in Fig. 3.42. The figure shows that the central velocity dispersion of NGC 59 is considerably higher ($\Delta\sigma_0 \gtrsim 30$km s^{-1}) than that measured for the six Virgo dwarf ellipticals (Geha et al. 2002) and the LG dwarf elliptical NGC 205 (Valluri et al. 2005). It should be noted that the central dispersion for most of these galaxies is lower than the instrumental resolution ($\sigma_{\rm instr} \sim 43$km s^{-1}) of the SALT data. The inferred BH mass of NGC 59 however lies well within the range of the upper BH mass estimates obtained for the Virgo dE galaxies.

For comparison, the mass of a possible central BH in NGC 59 was calculated using the virial mass equation:

$$M_{\rm virial} = \frac{5R\sigma_0^2}{G} \simeq 2.1 \times 10^8\,{\rm M}_\odot\ , \tag{3.5}$$

where the radius R corresponds to $1''$ (or 26pc). The virial mass from equation 3.5 is much larger than that obtained from the $M_{\rm BH}$ versus σ_0 relation. Given the low spatial resolution and poor seeing of the SALT/RSS longslit observations, the dispersion profile of NGC 59 cannot be sampled on sub-arcsecond scales which is needed to penetrate the sphere of influence of a BH. The derived BH masses of $M_{\rm BH} \gtrsim 10^6\,{\rm M}_\odot$ for NGC 59 are therefore not a true representation of the mass contained in the galaxy nucleus. Additionally, the central velocity dispersion is influenced by both nuclear components in NGC 59. It can thus be concluded that these measurements do not strictly represent the central BH mass estimate for the northern source thought to be the "true" nucleus of the galaxy. The NIR imaging of NGC 59 have shown that the two nuclear components are separated by $\sim 2\farcs3$. A narrower slit width ($\lesssim 1''$) is required to spatially resolve the individual nuclear components in the optical spectral range. The gravitational effect of these sources on the surrounding stars can only be further investigated by obtaining longslit spectra of the individual nuclear components.

Figure 3.42 shows that dwarf galaxies exhibit central velocity dispersions below $\sigma_0 \sim 50$km s^{-1}. The galaxy NGC 59 is found to have an unusually high central velocity dispersion of $\sigma_0 = 83.5 \pm 8.2$km s^{-1}, compared to those values typically observed for dwarf galaxies. This high central velocity dispersion can be explained by invoking the presence of a BH in the center of NGC 59. However, insight into the mass distribution of NGC 59, and the possibility of it hosting a BH, can only be achieved through dynamical modeling of the galaxy which represents the next stage in the IMBH search. In the previous subsection, we found that the double nuclear component and counter-rotating ionized gas in the center of NGC 59 suggest that this galaxy may have experienced a merging event. A merging scenario can additionally give rise to the high velocity dispersion in the center of this galaxy. On the other hand, it is also possible that NGC 59 is the remnant of a larger progenitor galaxy. In this case, it is expected that the progenitor galaxy must have had a bulge velocity dispersion of at least $\sigma_0 \sim 84$km s^{-1} as determined for NGC 59. These are just two possible formation theories for the galaxy. The dynamical models of NGC 59 will help to further constrain the formation mechanisms of this galaxy.

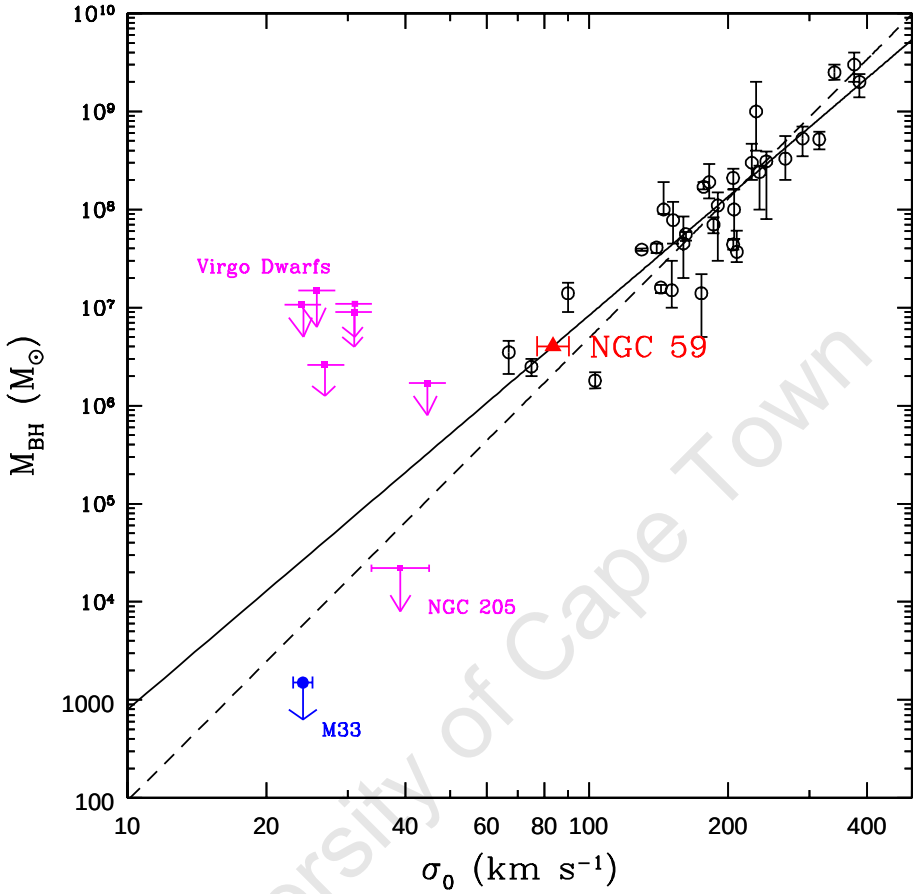

Figure 3.42 BH mass $M_{\rm BH}$ versus central velocity dispersion σ_0 relation. Early-type galaxies taken form Ferrarese & Merritt (2000), Gebhardt et al. (2000a) and Tremaine et al. (2002) are shown in black. BH mass estimates for 6 Virgo dwarfs (Geha et al. 2002) and NGC 205 (Valluri et al. 2005) are shown in magenta. The upper BH mass limit of the LG galaxy M 33 is also indicated (Merritt et al. 2001). The solid and dashed lines indicate $\rm M_{BH} - \sigma_0$ relations derived by Tremaine et al. (2002) and Merritt et al. (2001), respectively. The BH mass estimate for NGC 59 as inferred from the $\rm M_{BH} - \sigma_0$ relation of Tremaine et al. (2002) is shown in red.

3.6 Chemical Abundance Analysis from SALT spectra

The kinematics of the stellar and ionized gas component of the galaxy NGC 59 were determined in section 3.5. To contribute to our current knowledge of this galaxy, the ionized gas component was also used to trace the chemical evolution of the galaxy. In this section, the chemical content of NGC 59 is derived from the SALT/RSS spectra. This study can provide more clues to the evolutionary history of the galaxy.

3.6.1 Overview

The ionized regions in gas-rich dwarfs are frequently used to derive their chemical content. The regions of ionized gas allow for the measurement of H II or nebular abundances from the optical emission lines in the galaxy spectra. The abundance measurements for dwarf irregular (dIrr) galaxies indicate low metallicities in these systems (see e.g., Skillman et al. 1989a,b). These metal-deficient galaxies are ideal probes for studying the early stages of nucleosynthesis and for constraining the primordial helium abundance in the early universe (e.g., Pagel et al. 1992). A correlation between the metallicity of the interstellar-medium (ISM) and the B-band luminosity is observed for dIrr galaxies (Lequeux et al. 1979; Talent 1980; Kinman & Davidson 1981; Skillman et al. 1989a; Richer & McCall 1995; van Zee et al. 1997). A luminosity-metallicity ($L-Z$) relation essentially implies that the lower mass galaxies have their metals removed before it can be used to create stars. This process can be established through galactic winds. A well-defined $L-Z$ relation is observed for dwarf spheroidal (dSph) galaxies in the field (e.g., Caldwell et al. 1992). Unlike dIrr galaxies, these stellar systems are dominated by old stellar populations in which the chemical evolution has stopped. The nature of the $L-Z$ relationship for dIrr galaxies however remains poorly understood as these systems exhibit a variety of star formation rates and gas fractions.

Extensive studies of the chemical content of dIrr galaxies have been carried out in the Sculptor (Scl) and Centaurus A Groups (see Lee et al. 2003; Skillman et al. 2003; Lee et al. 2007). The oxygen abundances obtained from the temperature-sensitive [O III] λ4363 emission line were found to be in agreement with the $L-Z$ relation established for dIrr galaxies in the field and Local Group (Lee et al. 2007). Whether the $L-Z$ relation holds for dwarf lenticular (dS0) galaxies such as NGC 59 remains to be explored. An extension of the $L-Z$ relation to include different morphological types of dwarf galaxies can provide more clarity as to how they evolve. Additionally, a comparison of the derived galaxy abundances in different environments can give more insight to the effects of environment on the $L-Z$ relation.

The Hα-imaging of Skillman et al. (2003) gave the first indication of star-forming activity in the center of NGC 59. Subsequent spectra of this dwarf galaxy were obtained as part of the 6dF Galaxy Redshift Survey[10]. However, these spectra failed to detect the temperature-sensitive [O III] λ4363 emission line in the optical spectrum of the galaxy. More recently, Saviane et al. (2008) have obtained optical spectra for the two brightest central H II regions of NGC 59 using the EFOSC2 instrument (ESO Faint Object Spectrograph and Camera 2, Buzzoni et al. 1984) at La Silla. The [O III] λ4363 emission line was detected in these spectra

[10]The website of the 6dF Galaxy Survey can be found at http://www.aao.gov.au/local/www/6df/ .

allowing for a direct measure of the oxygen abundance. The oxygen abundance measurements for NGC 59 forms part of a sample of nine dIrr galaxies used by Saviane et al. (2008) to explore the $L - Z$ relation in the near-infrared. In star-forming galaxies such as dIrr's, the H-band gives a better indication of the total mass of the galaxy. For this reason, Saviane et al. (2008) have obtained additional H-band observations for each galaxy in their sample. Their initial study suggests that dIrr's in group environments follow a $L - Z$ relation in the NIR.

A clear detection of the [O III] λ4363 emission line was made in the blue spectra of NGC 59 obtained from the SALT/RSS spectrograph. The medium-resolution blue spectra of NGC 59 reveal a well-resolved [O III] λ4363 emission line. In this section, the blue and full-optical range SALT/RSS spectra are used to accurately measure the oxygen abundance of NGC 59. Together with the deep H-band observations of Chapter 2, we are able to re-define NGC 59 in the NIR $L - Z$ diagram with better precision compared to Saviane et al. (2008). This will give an indication of whether dS0 galaxies such as NGC 59 follow the $L - Z$ relation defined by the dIrr's. A similar evolutionary scenario for the two classes of dwarf galaxies would be suggested by such a finding. The results presented for NGC 59 are seen as a pilot study of the nature of dS0 galaxies in a group environment.

3.6.2 Measurement and Analysis

The direct method (see e.g., Osterbrock 1989) was used to derive the oxygen abundance of NGC 59. This technique involves the "direct" conversion of emission-line intensities into ionic abundances. It requires a reliable estimate of the electron temperature T_e(O III) of the ionized gas. The element abundances were measured from the emission lines in the low-resolution spectrum shown in Fig. 3.10.

A dominant presence of the doubly-ionized oxygen ion (O^{++}) in the central H II region of NGC 59 is revealed by the strong [O III] λ4363 emission line in the spectrum. The strong [O III] features allow for the measurement of the electron temperature T_e(O III) from the [O III] (λ4959+λ5007)/λ4363 line ratio. The strength of the [O III] (λ4959+λ5007)/λ4363 line ratio is proportional to the temperature of the ionized gas, i.e. a stronger [O III] ratio indicates a higher electron gas temperature. This estimate of the electron temperature T_e(O III) was used to derive the physical conditions and element abundances in the center of NGC 59.

The precision of the element abundances critically depends on the uncertainties in the [O III] λ4363 line flux measurement. So a careful extraction of the [O III] λ4363 line flux is crucial when dealing with high-excitation H II regions. The higher resolution blue spectrum (3882–4619Å) of NGC 59 was used to improve the accuracy of the [O III] λ4363 line flux measurement. The emission line flux was measured relative to the Balmer Hγ (λ4340) line. We found a 50% increase in the precision of the [O III] λ4363 line flux measurement from the blue spectrum. The improved precision in the flux measurement of the [O III] λ4363 line results in a 30% increase in the accuracy of the derived oxygen abundance.

3.6.3 Emission Line Flux Measurement

The relative intensities of the emission lines in the reduced spectrum of NGC 59 were measured using the software described in Kniazev et al. (2004). This software was initially created for the Hamburg/SAO Survey of emission line galaxies (HSS-ELG) and low-metallicity blue compact/H II galaxy (HSS-LM) projects (see Ugryumov et al. 2001, 2003, for details). The software was later adapted by Kniazev et al. (2004) to measure emission line fluxes of H II galaxies in the Sloan Digital Sky Survey (SDSS).

The software used to measure the emission line intensities is based on the MIDAS command language. In particular, the fitting of the emission/absorption line parameters is a combination of the SET/FIT, FIT/IMAGE, COMPUTE/FIT and SAVE/FIT programmes in the FIT package (MIDAS Users Guide 1998). Each of the emission lines was fit with a single Gaussian in the continuum-subtracted spectrum. The Corrected Gauss-Newton method was used to fit the lines. The [O II] $\lambda\lambda$3727,3729 lines, Hα λ6563 and [N II] $\lambda\lambda$6548,6584 lines, and [S II] $\lambda\lambda$6716,6731 lines were fitted as a blend of two or more Gaussian features.

The continuum-level in the spectrum was determined with the algorithm of Shergin et al. (1996). In this algorithm, a noise estimate for the continuum was produced using an absolute median deviation (AMD) estimator, med($|x-\overline{x}|$), where $\overline{x}$ is the mean value in the distribution (Korn & Korn 1968). The standard deviation of the AMD estimator was calculated as $\sigma_{\rm AMD} \approx 0.674\sigma_n$, where σ_n is the standard deviation for a normal distribution. The final noise estimate was corrected as $\sigma = \sigma_{\rm AMD}/0.674$. Kniazev et al. (2004) demonstrated the stability of this algorithm given various noise distributions. It was found that the calculated noise estimate does not depend on the intensity of noise spikes in the continuum. This feature of the noise estimate algorithm makes it ideal for the use in strong emission line spectra.

The final error in the measured line intensities was calculated as

$$\sigma_{\rm tot} = \sqrt{\sigma_{\rm f}^2 + \sigma_{\rm c}^2}, \tag{3.6}$$

where $\sigma_{\rm f}$ is the fitting error of the emission line from the FIT/IMAGE program in MIDAS. The fitting error $\sigma_{\rm f}$ is related to the Poisson statistics of the line photon flux. The second component, $\sigma_{\rm c}$, is the error resulting from the continuum fit using the noise estimate algorithm described above. For faint lines, $\sigma_{\rm c}$ is the largest contributor to the final error. The final errors in the emission line intensities were propagated in the calculation of the element abundances.

The measured emission line intensities, $F(\lambda)$, were corrected for both reddening and the underlying stellar absorption following Izotov et al. (1994). This procedure involves the simultaneous derivation of the extinction coefficient, C(Hβ), and the absorption equivalent width of the hydrogen lines, EW$_a(\lambda)$, using the equation

$$\frac{\rm I(\lambda)}{\rm I(H\beta)} = \frac{\rm EW_e(\lambda) + EW_a(\lambda)}{\rm EW_e(\lambda)} \frac{\rm EW_e(H\beta)}{\rm EW_e(H\beta) + EW_a(H\beta)} \times \frac{\rm F(\lambda)}{\rm F(H\beta)} 10^{[C({\rm H}\beta) f(\lambda)]} \ . \tag{3.7}$$

I(λ) is the intrinsic line flux of the emission lines whereas F(λ) represents the observed line flux corrected for atmospheric extinction. The equivalent widths of the Balmer emission line and underlying absorption are given by the quantities EW$_e(\lambda)$ and EW$_a(\lambda)$, respectively. The reddening function $f(\lambda)$ was taken from Whitford (1958) and is normalized at $H\beta$.

Izotov et al. (1994) found that the reddening function over the entire spectral range can be approximated by

$$f(\lambda) = 3.15854 \cdot 10^{-1.02109\lambda} - 1, \tag{3.8}$$

where λ is in units of μm. This form of the reddening function was used to derive the intrinsic flux measurements of the emission lines.

The Balmer theoretical ratios of Brocklehurst (1971) for the intrinsic hydrogen line intensity were applied in solving for C(Hβ) and EW$_a(\lambda)$ in equation (3.7). The derived values of the extinction coefficient and absorption equivalent width are listed in Table 3.7.

The absorption equivalent width was taken as EW$_a(\lambda)$=0 for lines other than hydrogen. This reduces equation (3.7) to the form of

$$\frac{I(\lambda)}{I(\mathrm{H}\beta)} = \frac{F(\lambda)}{F(\mathrm{H}\beta)} 10^{[C(\mathrm{H}\beta)f(\lambda)]} \ , \tag{3.9}$$

from which the intrinsic line fluxes were calculated. The intrinsic line flux of the observed emission lines in the spectrum of NGC 59 are also listed in Table 3.7.

Saviane et al. (2008) have obtained longslit spectra for the two brightest H II regions in the center of NGC 59. These spectra were acquired with the 1″ slit which gives a resolution of ∼13Å $FWHM$ near 5000Å. The reddening-corrected fluxes were measured relative to the Hβ (λ4861) line in the spectra. The relative intensities of the emission lines for the brightest H II region were measured with approximately twice the accuracy as that obtained from the second region. The low-resolution SALT/RSS spectrum yields a spectral resolution of 5–6Å $FWHM$. By placing the slit along the major axis of NGC 59, the emission lines in the SALT/RSS spectrum results from a combination of the central H II regions (see Fig. 3.5). The emission line fluxes from the SALT/RSS spectrum cannot therefore be directly compared to that of Saviane et al. (2008). However, it is worth noting that the relative intensity of emission lines in the SALT/RSS spectrum more closely matches that seen in the second brightest H II region. The relative intensity of the [O III] λ4363 line from the SALT/RSS spectrum is measured with 20%-better precision compared to the measurements for this H II region. Saviane et al. (2008) measured a two times lower [O III] λ4363 intensity ratio for the brightest H II region in the center of NGC 59. The accuracy in the [O III] λ4363 intensity ratio from the blue SALT/RSS spectrum therefore exceeds the measurements obtained by Saviane et al. (2008).

3.6.4 Determination of Element Abundances

The physical conditions and element abundances were measured from the reddening-corrected emission line fluxes listed in Table 3.7. The abundances of the elements O, N, S and Ne were derived using the electron temperature from the [O III] (λ4959+λ5007)/λ4363 line ratio. This electron temperature T_e(O III) diagnostic forms the basis of the abundance determination using the "standard" method. The element abundances were measured indirectly from the electron temperature T_e(O III) using a series of relations established from photoionization models of H II galaxies (Stasińska & Izotov 2003).

Table 3.7 Emission line intensities from central H II region in NGC 59

λ_0(Å) Ion	F(λ)/F(Hβ)	I(λ)/I(Hβ)
3727 [O II]	2.676±0.202	2.746±0.235
3868 [Ne III]	0.471±0.039	0.479±0.044
3889 He I + H8	0.096±0.015	0.174±0.049
3967 [Ne III] + H7	0.175±0.060	0.237±0.093
4101 Hδ	0.201±0.031	0.263±0.054
4340 Hγ	0.417±0.032	0.466±0.047
4363 [O III]	0.062±0.010	0.061±0.010
4471 He I	0.038±0.015	0.037±0.016
4861 Hβ	1.000±0.078	1.000±0.085
4959 [O III]	1.605±0.123	1.520±0.123
5007 [O III]	4.749±0.358	4.486±0.356
5869 He II	0.125±0.022	0.113±0.021
6300 [O I]	0.033±0.005	0.029±0.004
6312 [S III]	0.025±0.004	0.022±0.004
6364 [O I]	0.015±0.014	0.014±0.013
6548 [N II]	0.047±0.005	0.041±0.005
6563 Hα	3.184±0.238	2.828±0.242
6584 [N II]	0.142±0.019	0.125±0.018
6678 He I	0.026±0.008	0.023±0.008
6717 [S II]	0.236±0.018	0.206±0.018
6731 [S II]	0.215±0.016	0.188±0.016
C(Hβ) dex	0.10±0.10	
EW(abs) Å	1.10±0.52	
EW(Hβ) Å	22± 1	

The standard two-zone model for H II regions (Aller 1984) was adopted in deriving the oxygen abundance. This model distinguishes between a low- and high-ionization region characterized by the electron temperatures T_e(O II) and T_e(O III), respectively. The electron temperature in the high-ionization region T_e(O III) was measured from the [O III] (λ4959+λ5007)/λ4363 emission line ratio. The electron temperature T_e(O III) was derived through an iterative procedure using the equation from Aller (1984):

$$\frac{I(4959+5007)}{I(4363)} = C_T\Big[\frac{1+a_1x}{1+a_2x}\Big]10^{1.432/t}, \tag{3.10}$$

where $t = 10^{-4}T_e$(O III) and $x = 10^{-4}\mathrm{N_e t^{-0.5}}$. The parameters C_T, a_1 and a_2 were calculated from the interpolations:

$$C_T = 8.44 - 1.09t + 0.5t^2 - 0.08t^3, \tag{3.11}$$

$$a_1 = 2\cdot10^{-4} + 3.13\cdot10^{-4}t - 1.6\cdot10^{-4}t^2 + 2.67\cdot10^{-5}t^3, \tag{3.12}$$

$$a_2 = 0.0291 + 0.0253t - 0.0128t^2 + 0.00213t^3. \tag{3.13}$$

The electron density $\mathrm{N_e}$ was derived iteratively using the [S II] λ6717/λ6731 line ratio. The [O III] λ4363 auroral line was corrected for recombination excitation following the equation from Liu et al. (2000b).

The electron temperatures for the remaining ions were calculated either from the relations in Garnett (1992) or following the equations from the H II photoionization models of Stasińska (1990):

$$t_e(\mathrm{O\ II}) = 0.243 + t_e(\mathrm{O\ III})\,[1.031 - 0.184\,t_e(\mathrm{O\ III})]\,, \tag{3.14}$$

$$\mathrm{t_e(NeIII) = t_e(OIII)}, \tag{3.15}$$

$$\mathrm{t_e(NII) = t_e(OII)}, \tag{3.16}$$

$$\mathrm{t_e(SII) = t_e(OII)}, \tag{3.17}$$

$$\mathrm{t_e(ArIII) = 0.83t_e(OIII) + 0.17}, \tag{3.18}$$

$$\mathrm{t_e(SIII) = t_e(ArIII)}, \tag{3.19}$$

where $t_e = T_e/10^4$K. We do not expect the electron temperatures given by equations (3.14)–(3.19) to be the same since different ions reside in different parts of the H II region.

The electron temperatures derived from equations (3.14)–(3.19) were used to determine the ionic abundances given in Table 3.8. A lack of the O^{3+} ion is immediately implied by the absence of the He II λ4686 emission line in the galaxy spectrum. Thus, the total oxygen abundance was determined using the relation:

$$\frac{\mathrm{O}}{\mathrm{H}} = \frac{\mathrm{O^+}}{\mathrm{H^+}} + \frac{\mathrm{O^{2+}}}{\mathrm{H^+}}. \tag{3.20}$$

For the remaining elements, an ionization correction factor (ICF) accounts for the missing ions whose emissions cannot be directly measured from the galaxy spectrum. The ICF's

for nitrogen, neon and sulfur were calculated using the equations from Torres-Peimbert & Peimbert (1977), Garnett (1990), Izotov et al. (1994) and Thuan et al. (1995):

$$\mathrm{ICF(N)} = \frac{\mathrm{O}}{\mathrm{O}^{+}}, \tag{3.21}$$

$$\mathrm{ICF(Ne)} = \frac{\mathrm{O}}{\mathrm{O}^{2+}}, \tag{3.22}$$

$$\mathrm{ICF(S)} = \frac{\mathrm{S}}{\mathrm{S}^{+} + \mathrm{S}^{2+}} = \{0.013 + x[5.10 + x(-12.78 + x(14.77 - 6.11x))]\}^{-1},$$

where $x = \mathrm{O}^{+}/\mathrm{O}$. The ionic and total abundances of the different elements are listed in Table 3.8. The derived oxygen abundance for NGC 59 deviates by up to ~ 0.3 dex from the values obtained by Saviane et al. (2008) for the two brightest H II regions. The electron number density (N_e) is ten times smaller than that seen for the second brightest H II region. This result is suspicious since this region has comparable line strength to that measured from the SALT/RSS spectrum. The difference in the electron number density arises from the poor resolution of the S II ($\lambda\lambda$6717,6731) lines in the spectra of Saviane et al. (2008). The failure to resolve the S II features can lead to erroneous results for the electron number density and temperatures. This factor gives up to six times larger uncertainty in the electron temperatures. The oxygen abundance from the SALT/RSS spectra is derived with $\sim 58\%$ better precision than that of Saviane et al. (2008). These results illustrate the high quality of the SALT/RSS spectrum for deriving accurate abundances.

Neon and sulfur are a product of α-processes predominantly produced in short-lived massive stars. The log(Ne/O) and log(S/O) ratios are expected to show no dependence on the oxygen abundance O/H since these elements share a common origin, i.e. neon and sulfur are produced by the same massive stars that make oxygen. An accurate measurement of the α-element-to-oxygen abundance ratios was made by Izotov & Thuan (1999) for a large sample of H II regions in blue compact galaxies. They found $\log(\mathrm{Ne/O}) = -0.72 \pm 0.06$ and $\log(\mathrm{S/O}) = -1.55 \pm 0.06$. The abundance ratios obtained for NGC 59 are in good agreement with these values. This supports the idea that the abundance ratios of Ne/O and S/O show no dependence on metallicity.

The dominant processes leading to the enrichment of nitrogen in galaxies is a largely debated topic (see review by Henry et al. 2000). In massive spiral galaxies, the N/O ratio is observed to increase almost linearly with O/H indicating that the nitrogen is produced through a secondary process (Vila Costas & Edmunds 1993). The secondary production of nitrogen results from the CNO cycle in intermediate-mass stars which is released into the galaxy ISM by red giant winds and planetary nebula. On the other hand, dIrr galaxies show a relatively constant N/O ratio at low metallicities (Garnett 1990; Thuan et al. 1995; Kobulnicky & Skillman 1996). A constant N/O ratio over a large range of metallicities implies that nitrogen is produced through some primary process (Pagel 1985). Various processes have been suggested to account for this primary production of nitrogen. These include the possibility that the spread in the N/O values at a given metallicity can be attributed to a delay in the oxygen and nitrogen delivery to the ISM. Garnett (1990) determined an average N/O abundance ratio of $\log(\mathrm{N/O}) = -1.47$ for dIrr galaxies. This value overlaps with the mean

Table 3.8 The derived element abundances for central H II region in NGC 59

Value	NGC 59
T_e(OIII)(K)	12,944±923
T_e(OII)(K)	12,693±844
T_e(SIII)(K)	12,819±766
N_e(SII)(cm^{-3})	398±258
$O^+/H^+(\times10^5)$	4.244±0.939
$O^{++}/H^+(\times10^5)$	7.200±1.519
O/H($\times10^5$)	11.440±1.785
12+log(O/H)	8.06±0.07
$N^+/H^+(\times10^7)$	13.030±2.237
ICF(N)	2.696
N/H($\times10^5$)	0.35±0.06
12+log(N/H)	6.55±0.07
log(N/O)	-1.51±0.10
$Ne^{++}/H^+(\times10^5)$	1.831±0.428
ICF(Ne)	1.589
Ne/H($\times10^5$)	2.91±0.68
12+log(Ne/H)	7.46±0.10
log(Ne/O)	-0.59±0.12
$S^+/H^+(\times10^7)$	5.525±0.735
$S^{++}/H^+(\times10^7)$	18.730±4.823
ICF(S)	1.276
S/H($\times10^7$)	30.94±6.22
12+log(S/H)	6.49±0.09
log(S/O)	-1.57±0.11

N/O abundance ratio from van Zee & Haynes (2006), who obtained $\log(\mathrm{N/O}) = -1.43 \pm 0.15$ for a sample of 21 dIrr galaxies. We find the N/O abundance ratio for NGC 59 to be in good agreement with the average N/O values obtained for both dIrr and blue compact galaxies ($\log(\mathrm{N/O}) = -1.46 \pm 0.14$, Izotov & Thuan 1999).

3.6.5 The NIR Luminosity-Metallicity Relation

A first study of the $L-Z$ relation using the H-band luminosities of dIrr galaxies was conducted by Saviane et al. (2008). For these star-forming galaxies, the NIR gives a more accurate measure of the total luminosity compared to the optical. Saviane et al. (2008) proposed to investigate the nature of the NIR $L-Z$ relation for dIrr's in group environments. Their pilot study consisted of acquiring both optical spectra and H-band observations for a sample of nine dIrr galaxies. These galaxies were selected from the nearby Scl and M81 groups. For each galaxy, the optical spectra were obtained for the two brightest H II regions located in the galaxy center. If a single H II region resides in the galaxy, optical spectra were acquired for this region only. The [O III] λ4363 emission line was detected in the central H II regions of seven dIrr's in their sample which includes the galaxy NGC 59. A direct measure of the oxygen abundance was determined for these galaxies. The oxygen abundance of the brightest H II region together with the derived H-band luminosity give the location of each dIrr in the $L-Z$ diagram. The $L-Z$ diagram for the dIrr's having a direct measure of the oxygen abundance is shown in Fig. 3.43. The distances for dIrr galaxies in the Scl group were obtained from their recessional velocities as listed in Skillman et al. (2003). The distances of dIrr's in the M81 group were obtained from the RGB technique given by Karachentsev et al. (2002a). The weighted least-squares fit of Saviane et al. (2008) and 0.11 dex dispersion are shown by the dashed and dotted lines in Fig. 3.43, respectively. A clear trend of increasing metallicity with H-band luminosity is observed for the dIrr galaxies.

The new location of NGC 59 in the $L-Z$ diagram is indicated by the red point in Fig. 3.43. The derived values of the oxygen abundance (Table 3.8) and absolute H-band magnitude (Chapter 2, Table 2.13) were used to relocate this galaxy in the $L-Z$ plane. For comparison, the location of NGC 59 as determined by Saviane et al. (2008) is also shown in the $L-Z$ diagram. Given the new measurement of the oxygen abundance from the SALT/RSS spectrum, we find that NGC 59 still obeys the $L-Z$ relation defined by the dIrr galaxies, i.e. NGC 59 shows the expected metallicity for dIrr galaxies having comparable H-band luminosity. NGC 59 is found to lie within 1σ of the linear $L-Z$ relation. However, the lower metallicity for this galaxy from the SALT/RSS spectrum results in NGC 59 now lying below the linear $L-Z$ relation for dIrr's. In section 3.6.4, we found that the oxygen abundance measurements of Saviane et al. (2008) overestimate the metallicity of this galaxy by as much as 0.3 dex compared to the values obtained from the SALT/RSS spectrum.

Our study suggests that dS0 galaxies experiencing star formation, such as NGC 59, closely follow the NIR $L-Z$ relation defined for dIrr's rather than dE/dSph galaxies. These galaxies show similar abundance trends to dIrr galaxies (see section 3.6.4) making them almost indistinguishable from dIrr's based on their chemical content alone. For dE/dSph galaxies, the $L-Z$ relation can be interpreted using the mass-loss scenario through galactic winds (see

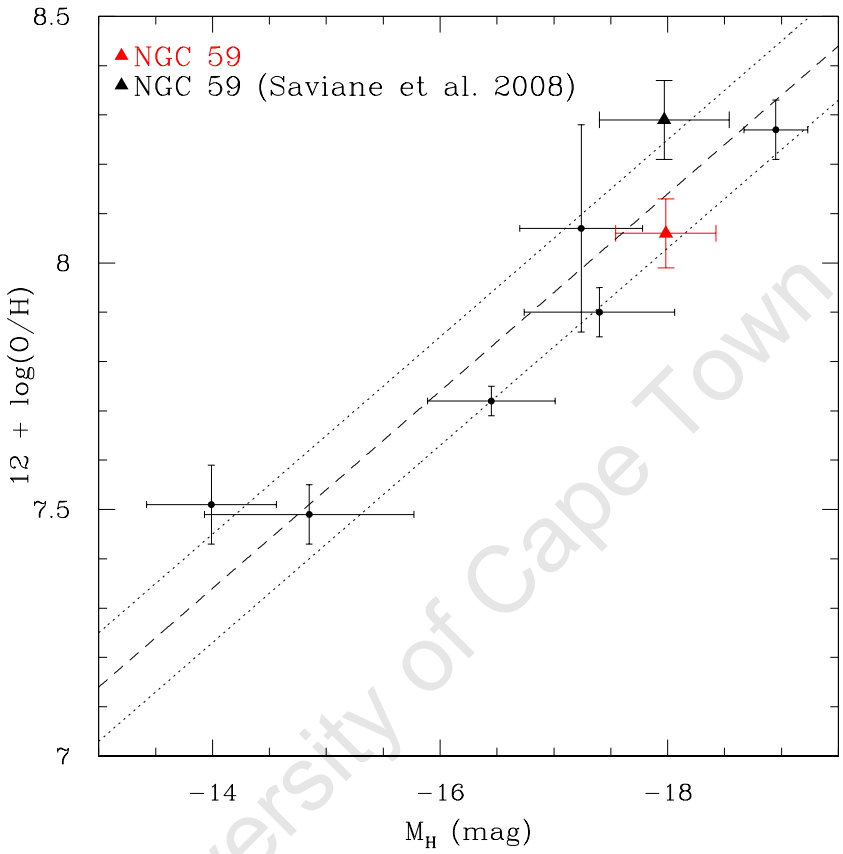

Figure 3.43 *H*-band luminosity-metallicity diagram of central H II region in dIrr galaxies belonging to the Sculptor and M81 groups. The galaxies shown in black are taken from Saviane et al. (2008). The red point indicates the oxygen abundance measurement for the dS0 galaxy, NGC 59, from the SALT/RSS spectrum. The weighted least squares fit to the data points of Saviane et al. (2008) is shown by the dashed line. The dotted lines indicate the $\pm 1\sigma$ dispersion around this fit.

Caldwell et al. 1992). In particular, the ISM of low mass galaxies is more easily lost through galactic winds which results in their chemical evolution being halted before that of the more massive galaxies. The abundances measured for dIrr's are lower than dSph's of comparable luminosity so that the two classes of galaxies do not share the same $L - Z$ relation (e.g., Skillman & Bender 1995). The mass-loss scenario for dSph's can therefore not be directly extended to include dIrr galaxies. To retain the mass-loss scenario for both classes of galaxies, it must then be assumed: (1) as seen for dSph's, this scenario should leave behind an $L - Z$ relation after the galaxy evolution has stopped; (2) the mass-loss scenario results in a possibly different $L - Z$ relation (as seen for the dIrr/dS0's) very early in the history of galaxies and is able to maintain it throughout the evolutionary history of the galaxy. Saviane et al. (2008) point out that the $L - Z$ relation for dIrr's can be explained by assuming a closed-box model for its chemical evolution with low effective oxygen yield. If all dIrr's began their chemical evolution at the same time, then this model predicts that the more massive galaxies are enriched at a faster rate than the lower mass galaxies. The more massive galaxies are therefore more effective in converting their gas into stars.

A larger sample of dIrr and dS0 galaxies is needed to further explore the NIR $L - Z$ relation. The initial results presented for NGC 59 suggests that dS0 galaxies follow a similar chemical evolutionary path as dIrr galaxies. By distinguishing between these two classes of dwarfs, we will be able to investigate the characteristics of dS0 galaxies and how they fit into the evolutionary sequence for dwarf galaxies. A wider spread in the data points of the NIR $L - Z$ diagram is however expected when extending this relation to include other galaxy types (see review by Kunth & Östlin 2000). It should be noted that only two galaxies in Fig. 3.43 are members of the high density M81 group. This small sample of galaxies makes it impossible to assess differences in the $L - Z$ relation for dIrr's in a high density environment such as the M81 group, compared to the more sparsely populated Scl group. Clearly, observations of a large sample of dIrr galaxies in various group environments are required to further study the effects of environment on the $L - Z$ relation.

3.7 Summary and Conclusions

We have derived the kinematics of the dwarf galaxy NGC 59 from optical longslit spectra obtained during the testing phase of the SALT/RSS spectrograph. By positioning the slit along the major axis of the galaxy, the global motions of stars about this axis were measured. The optical spectra of NGC 59 show prominent emission lines within the central $\sim 20''$ of the galaxy. These emission lines were used to derive the heliocentric velocity profile (i.e. the heliocentric velocity as a function of the radius) of the galaxy from the individual exposures. The derived velocity profiles were found to vary from one galaxy exposure to the next. We argue that these differences in the velocity profile shapes are a result of a change in the slit orientation along the galaxy. The variations in the velocity profile shapes can be attributed to a counter-clockwise rotation of the slit while performing the galaxy observations. The spatial profile for the different galaxy exposures is also found to vary from one exposure to the next, providing additional evidence that the slit orientation was not maintained throughout

the galaxy observations. For most nights, the velocity profiles derived from the first galaxy exposures show a rotation-like signature. The change in the slit orientation then leads to the degradation of the rotational structure over the course of the nightly observing run. The most accurate measure of the galaxy rotation about the major axis is therefore obtained from the velocity profiles derived from the first galaxy exposures. The heliocentric velocity profiles from the emission lines give a maximum rotational velocity of $v_{\rm rot} \sim 20$km s^{-1} for NGC 59.

The stellar kinematics of NGC 59 were extracted from the optical spectra using the Gauss-Hermite Pixel Fitting software of van der Marel (1994). The mean velocity and velocity dispersion profiles were determined from various combinations of the galaxy exposures. A rotational velocity of $v_{\rm rot} = 21.4 \pm 5.8$km s^{-1} was measured from the first galaxy exposures showing rotation-like signature. The average velocity dispersion of $\bar{\sigma} = 64.3 \pm 18.9$km s^{-1} was determined from the total combined galaxy spectrum. A measure of the galaxy flattening is given by the ratio of the rotational velocity and the average velocity dispersion. The flattening parameter for NGC 59 is $v_{\rm rot}/\bar{\sigma} = 0.33$. This value of the flattening parameter together with an ellipticity of $\epsilon = 0.41$ places NGC 59 in the range of galaxies supported by a combination of the stellar rotation and anisotropic pressure. The degree of flattening observed for NGC 59 is similar to that detected in one of M31's dwarf elliptical companions NGC 205. These results suggest that nearby ($D \lesssim 10$Mpc) dwarf galaxies may exhibit a variety of rotational properties as seen for dwarf ellipticals in the Virgo Cluster.

The derived velocity profiles for NGC 59 showed that the ionized gas in the center of the galaxy rotates counter-clockwise to the stellar component. This feature together with the double nuclear component detected in the NIR images of NGC 59 suggest this galaxy to have experienced a merger event in its evolutionary history. NGC 59 is situated at the outskirts of the Scl group and shows minimum interaction with neighbouring galaxies. The star formation at the center of the galaxy can therefore not be a consequence of tidal interactions with these neighbouring systems. A merger scenario for the galaxy is preferred in explaining the kinematics of the ionized gas in the center of the NGC 59. This scenario would however favour that the dwarf galaxy NGC 59 hosts a double nucleus rather than a nucleus and star-forming region in its center.

The central velocity dispersion of $\sigma_0 = 83.5 \pm 8.2$km s^{-1} was determined for NGC 59 from the total combined spectrum. The $M_{\rm BH} - \sigma_0$ relation of Tremaine et al. (2002) was used to obtain a mass estimate if a possible BH were to exist at the galaxy center. Here we have assumed that the $M_{\rm BH} - \sigma_0$ relation can be extrapolated to the lower BH mass regime (i.e. $M_{\rm BH} \lesssim 10^7\,{\rm M}_\odot$). Given the derived value of the central velocity dispersion, the linear $M_{\rm BH} - \sigma_0$ relation predicts that NGC 59 can host a BH of mass $M_{\rm BH} \sim 4 \times 10^6\,{\rm M}_\odot$ in its center. This value of the BH mass agrees well with the upper BH mass estimates obtained for dE galaxies in the Virgo cluster. However, a larger central velocity dispersion ($\Delta\sigma_0 \gtrsim 20$km s^{-1}) is measured for NGC 59 compared to the Virgo dwarfs and LG dE galaxy NGC 205. The derived value of the central velocity dispersion of NGC 59 represents the stellar kinematics due to both nuclear components in the galaxy center. The pilot study of NGC 59 has shown that the black hole sphere of influence of the dwarf galaxies in the LV cannot be resolved with the SALT spectra. The SALT/RSS spectrograph can, however, give the first clues of the

Table 3.9. Summary of the derived kinematic properties of NGC 59

Parameter		Value
Rotational velocity	$v_{\rm rot}$ (km s^{-1})	21.4 ± 5.8
Average velocity dispersion	$\bar{\sigma}$ (km s^{-1})	64.3 ± 18.9
Galaxy flattening	$v_{\rm rot}/\bar{\sigma}$	0.33
Central velocity dispersion	σ_0 (km s^{-1})	83.5 ± 8.2
Central BH mass using relation from Tremaine et al. (2002)	$M_{\rm BH}$ ($M_\odot$)	4×10^6

presence of a centrally massive object by detecting a mass over-density in the galaxy center. This can be done with the current resolution of the SALT/RSS as seen for the pilot galaxy NGC 59. The detection of this mass over-density in the center gives further motivation to obtain higher resolution spectra for the galaxy using either space-based telescopes or those using adaptive optics. For NGC 59, spatially resolved spectra of each nuclear component are needed to actually determine the gravitational influence of the individual nuclear sources on the surrounding stars. A summary of the kinematic properties derived from the SALT/RSS spectra of NGC 59 is given in Table 3.9.

The presence of strong emission lines in the spectrum of NGC 59 allowed for the determination of the element abundances in the center of the galaxy. In particular, the well-resolved [O III] λ4363 emission line in the blue spectrum of NGC 59 gives an accurate measurement of the oxygen abundance using the direct method. The derived value of the oxygen abundance from the SALT/RSS spectra is ~ 0.3 dex lower than the most recent measurements for NGC 59 carried out by Saviane et al. (2008). The oxygen abundance obtained from the higher resolution SALT/RSS spectrum is determined with $\sim 58\%$-better precision compared to that of Saviane et al. (2008). The abundance ratios for sulfur, neon and nitrogen were derived from the spectrum of NGC 59. These are found to be in good agreement with the average abundance ratios for blue compact galaxies and dIrr's. In addition, NGC 59 closely follows the NIR luminosity-metallicity relation established for LG dIrr galaxies. These results suggest that NGC 59 has experienced enrichment processes similar to those seen in late-type dwarf galaxies. We find that this star-forming dS0 galaxy cannot be distinguished from dIrr galaxies based on its chemical content alone. This pilot study has shown that the dS0 galaxy NGC 59 exhibits a variety of physical characteristics seen in both early and late-type systems.

Chapter 4

Conclusion

Near-infrared Observations of Nearby Dwarf Galaxies

A detailed near-infrared (NIR) J-, H- and K_s-band photometric study of six nearby ($D \lesssim 10$Mpc) dwarf galaxies was carried out using the 1.4m IRSF telescope. The three most luminous dwarfs in our sample were previously detected by 2MASS. The fainter galaxies are detected for the first time in the NIR. A comparison of the total magnitudes was made for those galaxies observed by 2MASS. It was found that 2MASS underestimates the flux of the detected galaxies by up to $\leq 0^{\rm m}.5$. This is in agreement with Kirby et al. (2008) as well as Andreon (2002). It emphasizes the bias effects of the 2MASS galaxy catalogue against low luminosity galaxies.

The surface brightness profiles of the deep NIR observations could be extracted to low surface brightness of $\mu \sim 25$mag arcsec^{-2} in the J- and H-bands, and $\mu \sim 23.5$mag arcsec^{-2} in the K_s-band. The $J-K_s$, $H-K_s$ and $J-H$ colour profiles show little variation with galaxy radius.

The relation between the $J-K_s$ colour and the absolute K_s-band magnitude was used to explore the metallicities of the galaxies. The IRSF dwarfs show almost constant $J-K_s$ colour with increasing K_s-band luminosity. This is also observed for early-type dwarfs in the Virgo Cluster where a weak correlation is detected between the $J-K_s$ colour and the metallicity of the galaxy.

The IRSF dwarfs closely follow the linear relation between the B- and H-band luminosity established for a range of galaxy types. For the dwarf galaxies, this correlation suggests that similar morphologies are seen in the optical and NIR bands. This correlation is surprising for those galaxies which have experienced recent star-formation and are largely affected by dust attenuation (e.g., spiral galaxies). Intuitively, a direct relation between the dust-dominated B-band and the H-band is not expected for these galaxies.

The stellar masses of the six dwarfs were determined using the H-band photometric results. They are found to have stellar masses in the range of $10^7 - 10^{10}\,{\rm M}_\odot$ using a mass-to-light (M/L) ratio of $\Upsilon_H = 1.4 \pm 0.4$. These results will later be used to derive the dark matter content of the galaxy given their dynamical mass estimate from the follow-up spectroscopic observations.

The Kinematics of Dwarf Galaxy NGC 59

The kinematics of the Sculptor group dwarf NGC 59 were derived from the SALT/RSS longslit spectra. The kinematics were initially derived from the individual galaxy spectra to assess the stability of the SALT/RSS spectrograph in carrying out long exposure observations. The mean velocity and velocity dispersion profile of NGC 59 were derived from the absorption line features in the galaxy spectra. They reveal that NGC 59 rotates with a velocity of

$v_{\rm rot} = 21.4 \pm 5.8$km s^{-1}. The average velocity dispersion of NGC 59 is $\bar{\sigma} = 64.3 \pm 18.9$km s^{-1}. The rotational velocity and average dispersion were used to compute the flattening parameter of $v_{\rm rot}/\bar{\sigma} = 0.33$ for the galaxy. This value of the flattening parameter together with the ellipticity of $\epsilon = 0.41$ for NGC 59 shows that the galaxy is supported by a combination of stellar rotation and anisotropic pressure. The degree of flattening observed for NGC 59 is similar to that detected for the nucleated dwarf elliptical companion of Andromeda, NGC 205.

The velocity profiles derived from the emission lines in the spectra show that the ionized gas in the galaxy center rotates with a maximum velocity of $v_{\rm rot} \sim 20$km s^{-1}. The ionized gas is found to rotate counter-clockwise to that of the stellar component. This feature in the galaxy center gives the first indication that NGC 59 might have experienced a merger event in its evolutionary history. Further evidence for a merger event is provided by the deep NIR imaging of NGC 59 which reveals a double nuclear component at the center of the galaxy. The stellar rotation is measured about the northern nuclear component which is characterized as the "true" nucleus of the galaxy. The NIR colours of the two nuclear components are similar to those measured for star-forming knots in blue compact dwarfs. This suggests that both components have experienced recent star formation. The redder $H-K_s$ colour for the nucleus indicates however that this component has undergone the most recent starburst. Based on the NIR colours alone, it is not clear whether the secondary nuclear component is a star-forming knot or a nucleus. The merger scenario for NGC 59 favours that this dwarf galaxy hosts a double nucleus.

Chemical Content of NGC 59

The presence of the [O III] λ4363 emission line in the galaxy spectrum allowed for the derivation of the chemical content of NGC 59 using the direct method. The oxygen abundance obtained from the SALT/RSS spectrum is determined with $\sim 58\%$-better precision compared to the most recent measurements of Saviane et al. (2008). The abundance ratios for sulfur, neon and nitrogen were shown to be in good agreement with the average abundance ratios for blue compact galaxies and dIrr's. NGC 59 closely follows the NIR luminosity-metallicity relation established for nearby dIrr galaxies. These results suggest that NGC 59 has experienced enrichment processes similar to those seen in late-type dwarf galaxies. Based on the chemical content and relatively large amount of H I in NGC 59, it can be concluded that this galaxy is not a typical early-type dwarf. Instead, it should be classified as a mixed-morphology dwarf galaxy which experiences little interaction with its immediate environment.

First Clues to an IMBH in the Center of NGC 59

A central velocity dispersion of $\sigma_0 = 83.5 \pm 8.2$km s^{-1} was determined for NGC 59. This represents the stellar kinematics due to both nuclear components. The velocity dispersion was determined within the central $2''$ (corresponding to $\sim$52pc) of the galaxy. The mass of a possible BH in the center of the galaxy was inferred by extrapolating the linear $M_{\rm BH} - \sigma_0$ relation to the lower BH mass regime (i.e. $M_{\rm BH} \lesssim 10^7\,{\rm M}_\odot$). Given the derived value of the central velocity dispersion, this relation predicts that NGC 59 could host a BH of mass $M_{\rm BH} \sim 4 \times 10^6\,{\rm M}_\odot$ in its center. Spatially resolved spectra of the individual nuclear components are however required to obtain an accurate measure of the central velocity dispersion about the dynamical center of the galaxy. This value will then be used in modeling the dynamics of the

galaxy to infer the existence of a possible IMBH in the galaxy center. The dynamical models will also provide an upper mass estimate for the central BH.

The resolving capabilities of the SALT/RSS spectrograph limit the search for an IMBH to nearby dwarfs having velocity dispersions greater than the instrumental dispersion of $\sigma_{\rm instr} \sim 43$km s^{-1}. The velocity resolution of the SALT/RSS with the with the narrow $1''$ slit proved insufficient in resolving velocity dispersions of $\sigma \lesssim 20$km s^{-1} observed for Galactic globular clusters. An IMBH search in these stellar systems can be carried out more successfully using multi-object spectroscopy.

4.1 Future Work

The research projects that will follow from the work presented in this thesis include:

• A continuation of the search of an IMBH in the center of nearby dwarf galaxies. This project will be carried out once the SALT telescope is functioning optimally. A list of dwarf galaxy candidates in which the IMBH search will be conducted has already been drawn up. Longslit spectra will be acquired for each galaxy candidate using the SALT/RSS spectrograph. The observational configuration will be similar to that for the pilot study of NGC 59. The stellar kinematics of the dwarf galaxies will be extracted following the same technique described in the second half of this thesis. However, further modeling techniques need to be explored and implemented in determining the overall dynamics of the galaxies.

• Deep NIR imaging will be obtained for the dwarf galaxy candidates in the large sample using the local 1.4m IRSF telescope. Most of the galaxy candidates have not been detected by 2MASS. These observations can therefore be used to establish a NIR photometric database for these low surface brightness galaxies. The study of nearby dwarf galaxies is usually limited due to their low surface brightnesses. The deep NIR imaging will allow for a detailed study of the structure and stellar content of these systems. At the same time, these results will be used in the dynamical modeling of the galaxies to account for the stellar component of the galaxy. The NIR observations together with the optical spectra can be used to investigate the dark matter content of nearby dwarf galaxies.

• The correlation between the B- and H-band luminosities of galaxies needs further investigation. In particular, can this relation be used to recover the B-band magnitudes of galaxies in dust enshrouded regions near the Galactic plane? The B- versus H-band relation can provide an independent means of deriving the B-band luminosities of galaxies suffering from high extinction.

Appendix

A Large Sample of Nearby Dwarf Galaxy Candidates

The list of 44 Local Volume ($D \lesssim 10$Mpc) dwarf galaxy candidates in which the search for an intermediate-mass black hole (IMBH) will be conducted is presented in Table A.1. The columns contain the following data:

Column 1, 2: Galaxy designations

Column 3, 4: Equitorial coordinates (J2000.0)

Column 5: Galaxy morphological type from the NASA/IPAC Extragalactic Database (NED).

Column 6: Galaxy morphological type in numerical code as given by Karachentsev et al. (2004).

Column 7, 8: Distance to the galaxy in Megaparsec from Karachentsev et al. (2004) and Jacobs et al. (2009). The method used for the determination of distances are indicated: (cep) from the luminosity of cepheids; (rgb) from the luminosity of the tip of RGB; (sbf) via fluctuation of surface brightness; (bs) from the luminosity of the brightest stars; (tf) from the Tully-Fisher relation; (mem) from membership in the known groups; (h) from the Hubble relation $V_{\rm LG} = H_0 D$ with the mean local Hubble parameter $H_0 = 72$km s^{-1}Mpc^{-1} (Karachentsev et al. 2003a).

Columns 9, 10: Total apparent and absolute B-band magnitudes of galaxies (Karachentsev et al. 2004, and references therein).

Column 11: $B - R$ color of galaxy.

Column 12: B-band central surface brightness (μ_0) in mag arcsec^{-2}.

Column 13, 14: Effective surface brightness $\mu_{B,\rm eff}$ (in mag arcsec^{-2}) and radius $R_{B,\rm eff}$ (in arcseconds) of galaxies in the B-band.

Column 15: B-band length of the galaxy major axis in arcseconds.

Column 16: B-band position angle (in degrees) measured from north to east.

The photometric parameters in columns 11–14 are taken from Lauberts & Valentijn (1989), Jerjen et al. (2000b) and Parodi et al. (2002). Columns 15 and 16 are the B-band major axis length and position angle of the galaxies as given by NED and Lauberts & Valentijn (1989), respectively.

Table A.1. Large Sample of Local Volume dwarf galaxies.

Name	Other	RA (J2000)	DEC	Classification		Distance	Method	B	M_B	$B-R$	$\mu_{B,0}$	$\mu_{B,\mathrm{eff}}$	$R_{B,\mathrm{eff}}$	Major Axis	PA
1	2	3	4	5	6	7	8	9	10	11	12	13	14	15	16
Sculptor dIrr	ESO349−031	00 08 13.3	-34 34 42.0	IBm	10	3.20	rgb[1]	15.48	-12.63	–	–	–	–	66	–
NGC59	ESO539−004, KK002	00 15 25.1	-21 26 38.0	dSO	-3	4.40	sbf	12.97	-15.74	1.09	19.59	21.27	21.30	156	120
ESO410−005	KK003	00 15 31.1	-32 10 55.4	dE	-1	1.92	rgb[1]	14.90	-11.58	1.02	22.67	23.75	24.20	78	46
Sculptor-dE1	SC22	00 23 51.7	-24 42 18.0	dE	-3	4.21	rgb	17.73	-10.45	–	–	26.30	20.50	54	–
Cetus dSph	KKSG1	00 26 11.0	-11 02 40.0	dSph	-2	0.87	rgb[1]	14.40	-10.18	–	–	–	–	500	–
ESO294−010	PGC001641	00 26 33.4	-41 51 19.0	dSO/Im	-3	1.95	rgb[1]	15.53	-10.91	1.23	23.02	23.83	18.20	66	0
ESO474−018	DDO226, UGCA009	00 43 03.8	-22 14 49.0	IB(s)m	10	4.90	rgb[1]	14.36	-14.17	0.74	23.23	24.91	115.00	126	173
ESO540−030	KK009	00 49 20.9	-18 04 32.0	dE/Im	-1	3.55	rgb[1]	16.37	-11.39	1.12	24.30	25.13	43.20	168	112
ESO540−031	UGCA015, DDO006	00 49 49.2	-21 00 54.0	IB(s)m:	10	3.42	rgb[1]	15.19	-12.50	–	23.41	24.63	79.40	102	34
ESO540−032	KK010	00 50 24.5	-19 54 23.0	dE/Im	-3	3.61	rgb[1]	16.44	-11.32	1.05	24.47	25.21	22.60	102	125
Sculptor dE	ESO351−030	01 00 09.4	-33 42 33.0	E?	-3	0.09	rgb	10.05	-9.77	–	–	–	–	2388	–
PGC009140	KKs3	02 24 42.7	-73 30 46.0	E3	-3	4.10	mem	16.00	-12.28	–	–	–	–	138	–
LEDA166073	KK027	03 21 05.7	-66 19 22.0	dIrr	-3	3.98	rgb	16.50	-11.83	–	–	–	–	72	–
ESO308−022	KK055	06 39 32.9	-40 43 13.0	dIrr	10	7.70	h	16.05	-13.71	–	–	–	–	78	–
Carina dSph	ESO206−020	06 41 36.7	-50 57 58.0	E3	-3	0.10	rgb	11.30	-8.97	–	–	–	–	1404	–
LEDA166099	KK073	09 12 29.2	-24 14 28.0	dE,N	-3	9.80	mem	16.35	-14.46	1.16	23.09	23.95	19.52	54	-60
Antlia Dwarf	PGC029194	10 04 04.0	-27 19 55.0	dE3.5	10	1.35	rgb[1]	16.19	-9.75	–	–	–	–	120	–
UGCA200	KK084, PGC029299	10 05 35.2	-07 44 44.0	dE,N	-3	9.70	mem	16.36	-13.60	1.38:	23.19	24.43:	17.99:	66	-31
NGC3115DW01	PGC029300	10 05 41.6	-07 58 53.5	dE,N	-2	9.70	mem	13.61	-16.55	1.38	22.26	22.76	29.98	102	2
Sextans dSph	LEDA088608	10 13 03.0	-01 36 52.0	dSph	-3	0.09	rgb	12.00	-7.98	–	–	–	–	1800	–
ESO321−014	PGC039032	12 13 49.6	-38 13 53.0	dIrr	10	3.27	rgb[1]	15.22	-12.70	–	–	–	–	84	–
ESO381−020	PGC043048	12 46 00.7	-33 50 13.0	IB(s)m	10	5.40	rgb[1]	14.44	-14.15	0.75	23.09	24.39	104.00	180	2.3
ESO443−009	KK170	12 54 53.6	-28 20 27.0	dIm	10	5.62	rgb[1]	17.06	-12.00	–	–	–	–	72	–
ESO219−010		12 56 09.6	-50 08 38.0	dE,N	-3	4.28	sbf	16.42	-12.70	–	23.65	24.42	15.80	84	–
ESO269−058	PGC045717	13 10 32.9	-46 59 27.0	IO pec	10	3.82	rgb[1]	13.29	-14.95	1.18	21.29	24.04	135.00	180	72.0
ESO269−066	KK190	13 13 09.5	-44 52 56.0	dE,N:	-1	3.66	rgb[1]	14.59	-13.56	–	23.70	24.26	34.30	84	–
NGC5102	ESO382−050	13 21 57.6	-36 37 49.0	dSO	1	3.50	rgb[1]	10.28	-18.08	1.27	17.56	24.67	513.00	522	48.7
PGC046680	KK197	13 22 01.8	-42 32 08.0	dE	-3	3.77	rgb[1]	15.68	-12.76	–	24.90	25.43	35.50	114	–
PGC046885	KK200	13 24 36.2	-30 58 18.5	dIm	9	4.70	rgb[1]	16.67	-11.96	–	–	–	–	51	–
ESO324−024	PGC047171	13 27 37.3	-41 28 50.0	dIrr	10	3.70	rgb[1]	12.90	-15.45	0.78	22.42	24.11	123.00	192	68.7
NGC5206	ESO220−018	13 33 43.9	-48 09 04.0	SB?	-3	2.58	rgb[1]	11.64	-16.66	1.22	20.24	23.88	172.00	222	23.0
ESO444−078	UGCA365	13 36 31.1	-29 14 06.0	Im	10	5.37	rgb[1]	15.53	-13.01	0.67	22.90	24.42	52.50	72	32.3
ESO444−084	PGC048111	13 37 20.0	-28 02.0 42	Cirr	10	4.61	rgb	15.06	-13.56	-0.03	23.45	24.34	58.20	78	125.7
NGC5237	ESO270−022	13 37 38.9	-42 50 51.0	I0?	-3	3.36	rgb[1]	13.23	-15.00	0.91	20.63	22.95	53.70	114	103.0

Table A.1 (cont'd)

Name	Other	RA (J2000)	DEC	Classification		Distance	Method	B	M_B	$B-R$	$\mu_{B,0}$	$\mu_{B,\mathrm{eff}}$	$R_{B,\mathrm{eff}}$	Major Axis	PA
1	2	3	4	5	6	7	8	9	10	11	12	13	14	15	16
IC4316	ESO445−006	13 40 18.1	-28 53 38.0	IBm? Pec	10	4.45	rgb[1]	14.56	-13.90	0.87	22.11	24.26	49.00	102	56.4
NGC5264	ESO445−012	13 41 36.7	-29 54 47.0	dIm	10	4.70	rgb[1]	12.60	-15.90	1.09	21.71	23.61	108.00	150	65.4
PGC048515	KK211	13 42 05.6	-45 12 18.0	dSph	-5	3.61	rgb[1]	16.32	-11.93	–	–	–	–	78	–
ESO325−011	PGC048738	13 45 00.5	-41 51 40.0	dIrr	10	3.50	rgb[1]	13.99	-14.05	–	–	–	–	162	–
ESO384−016	PGC049615	13 57 01.2	-35 19 59.0	dSO/Im	10	4.43	rgb[1]	15.11	-13.06	0.71	21.51	23.22	16.70	78	67.1
UKS1424−460	PGC051659	14 28 03.7	-46 18 06.0	dIrr	10	3.53	rgb[1]	16.50	-11.83	–	–	–	–	144	–
Saggitarius dIrr	ESO594−004	19 29 59.0	-17 40 41.0	IB(s)m:	10	1.04	rgb	14.12	-11.49	–	–	–	–	174	–
Aquarius Dwarf	DDO210	20 46 51.8	-12 50 53.0	IB(s)m	10	0.97	rgb[1]	14.00	-11.09	–	–	–	–	132	–
ESO468−020	KK258	22 40 43.9	-30 47 59.0	E3:pec	-3	3.90	mem	17.36	-10.66	–	–	–	–	126	–
Tucana Dwarf	PGC69519	22 41 49.0	-64 25 12.0	dE4	-2	0.92	rgb[1]	15.70	-9.16	–	–	–	–	174	–

Note. — [1]The most recent distance estimates from the tip of the RGB from HST observations. These distances are listed in the Extragalactic Distance Database of Jacobs et al. (2009).

B Photometric Calibrations of Near-infrared Galaxy Images

B.1 Aperture-corrected Photometry

The NIR imaging of the six dwarf galaxies were calibrated using aperture-corrected photometry as described in section 2.5.3. The growth curve and aperture size in which the flux of the stars was measured are shown in Figs. B.1–B.5 for the individual nights. The aperture corrections listed in Table 2.6 were applied to the stellar flux measurements.

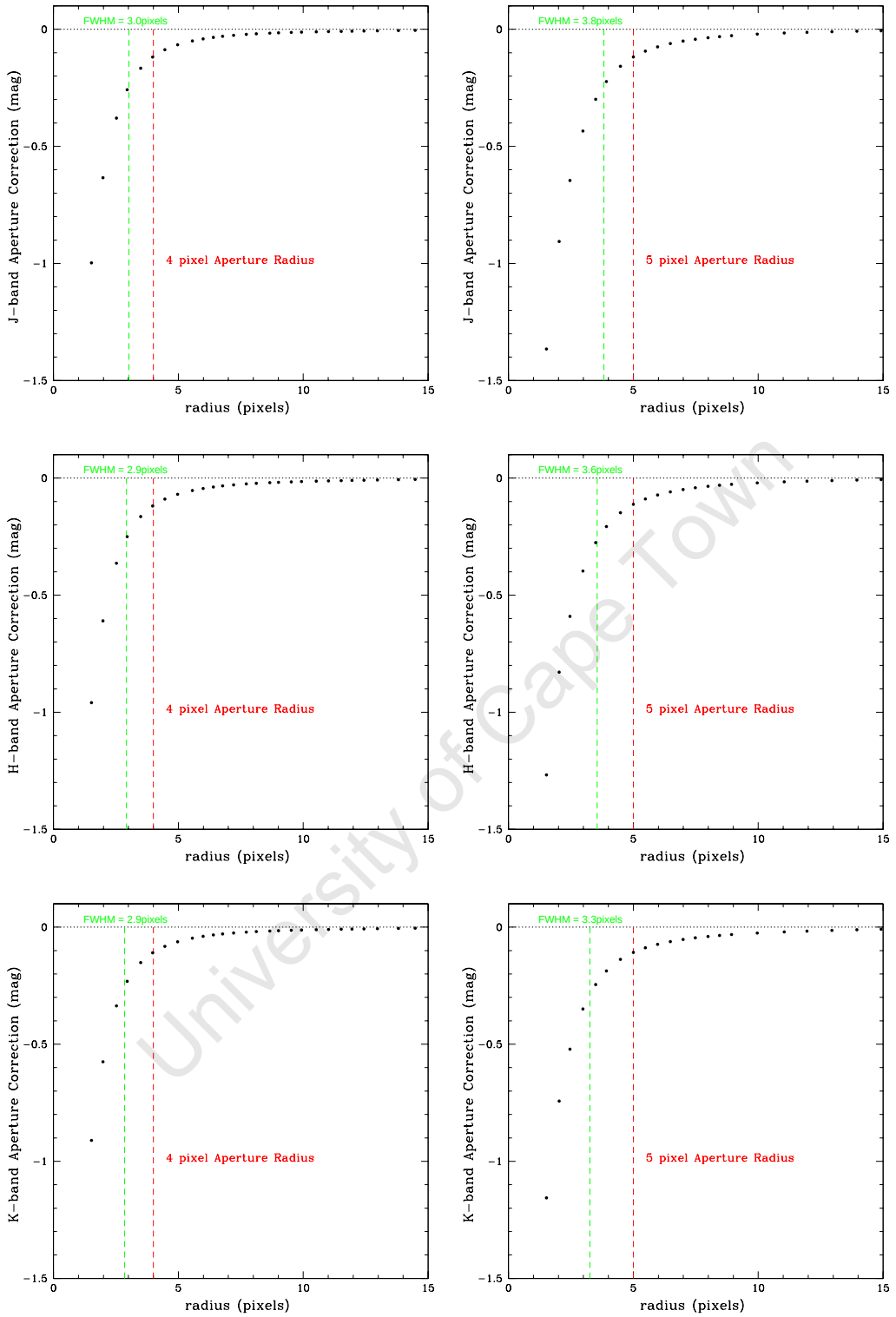

Figure B.1 The magnitude correction as function of the aperture size for galaxy images observed on the nights 17 Feb 2006 (*left*) and 11 June 2006 (*right*). The aperture corrections to be applied to the J- (*top*), H- (*middle*) and K_s-bands (*bottom*) are shown. The Gaussian FWHM of the flux distribution of point sources are indicated by the vertical green line. The chosen aperture radius to which the magnitude correction was applied is shown by the vertical red line.

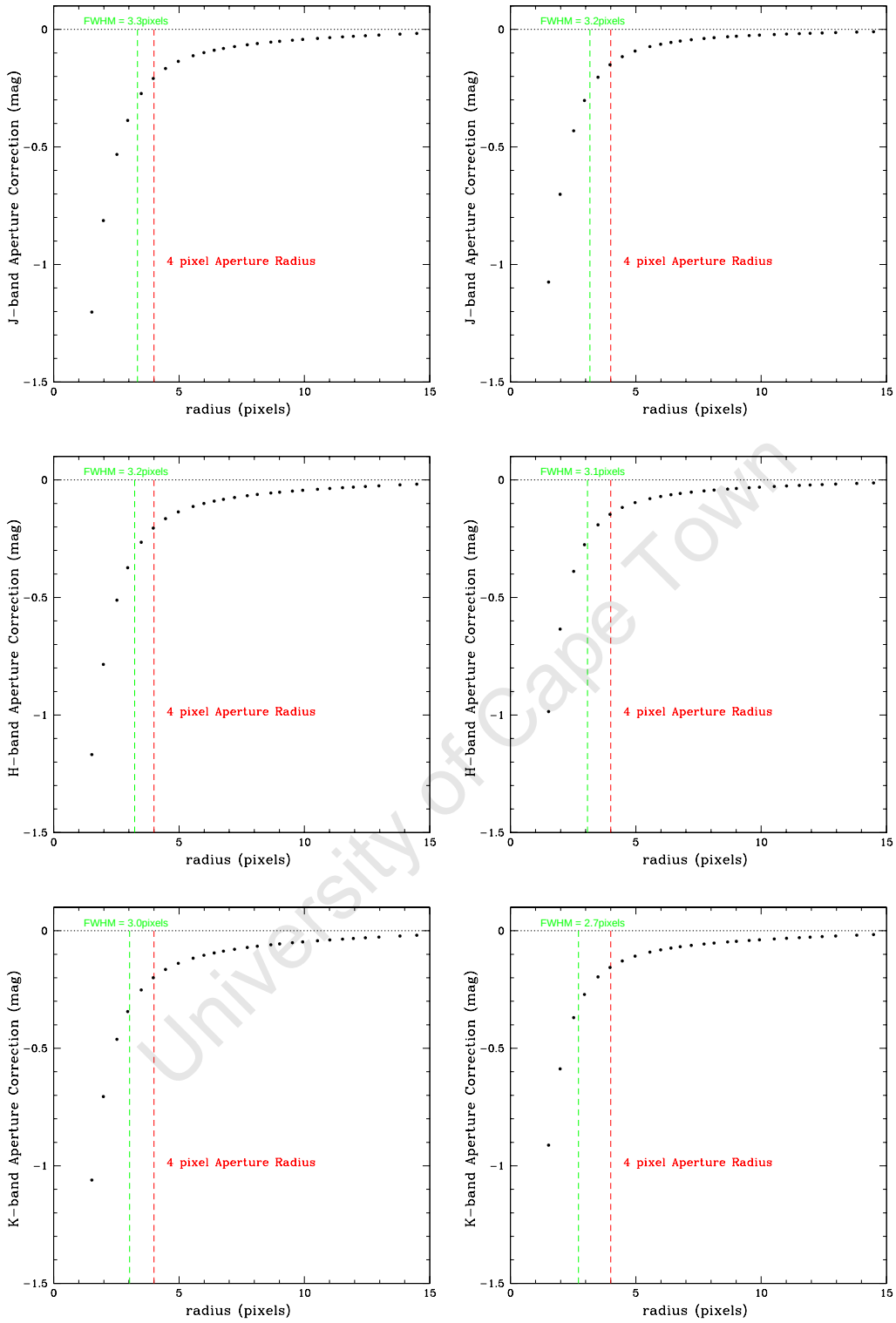

Figure B.2 The magnitude correction as function of the aperture size for galaxy images observed on the night 8 March 2007, see caption for Fig. B.1.

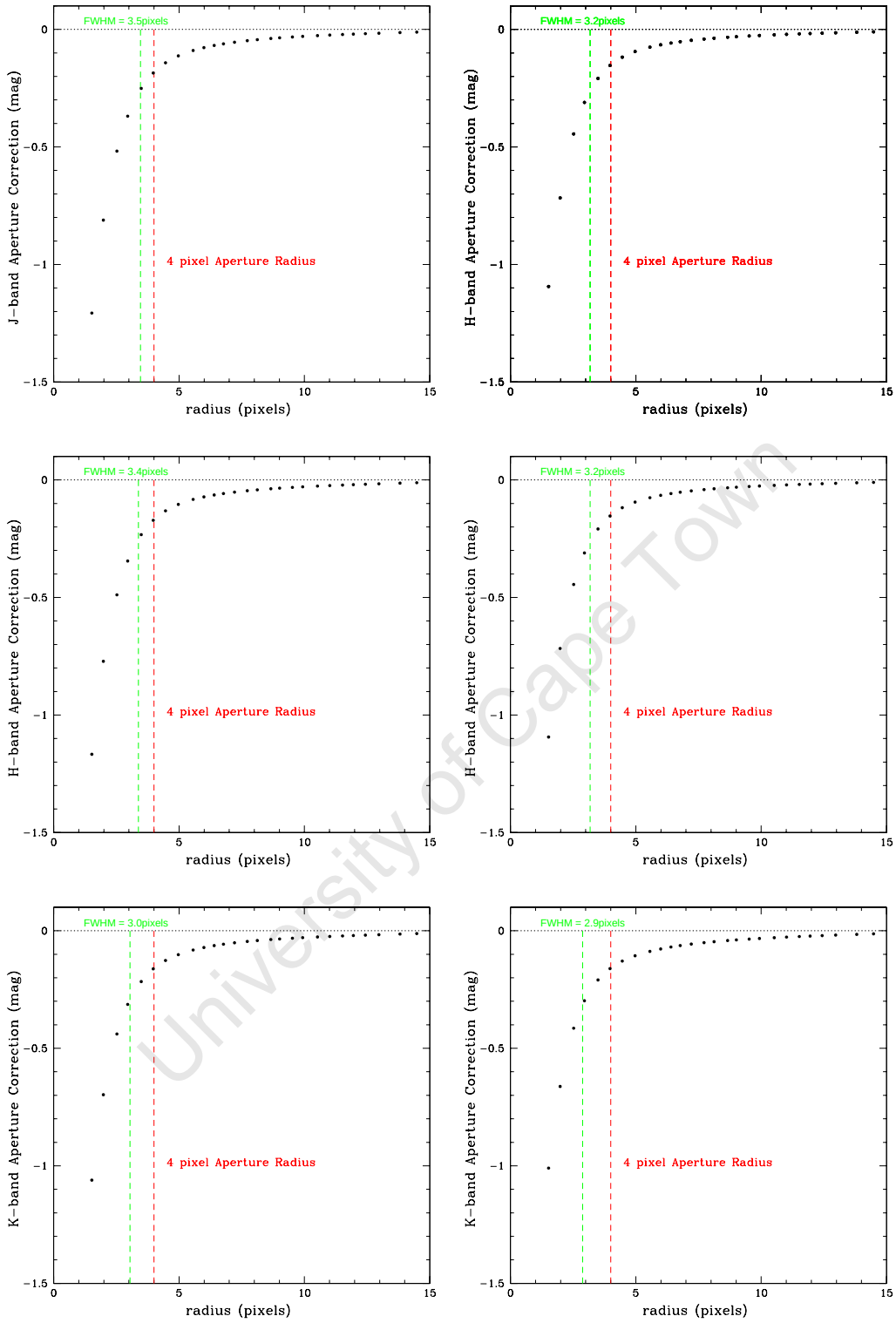

Figure B.3 The magnitude correction as function of the aperture size for galaxy images observed on the nights 9 March 2007 (*left*) and 10 March 2007 (*right*), see caption for Fig. B.1.

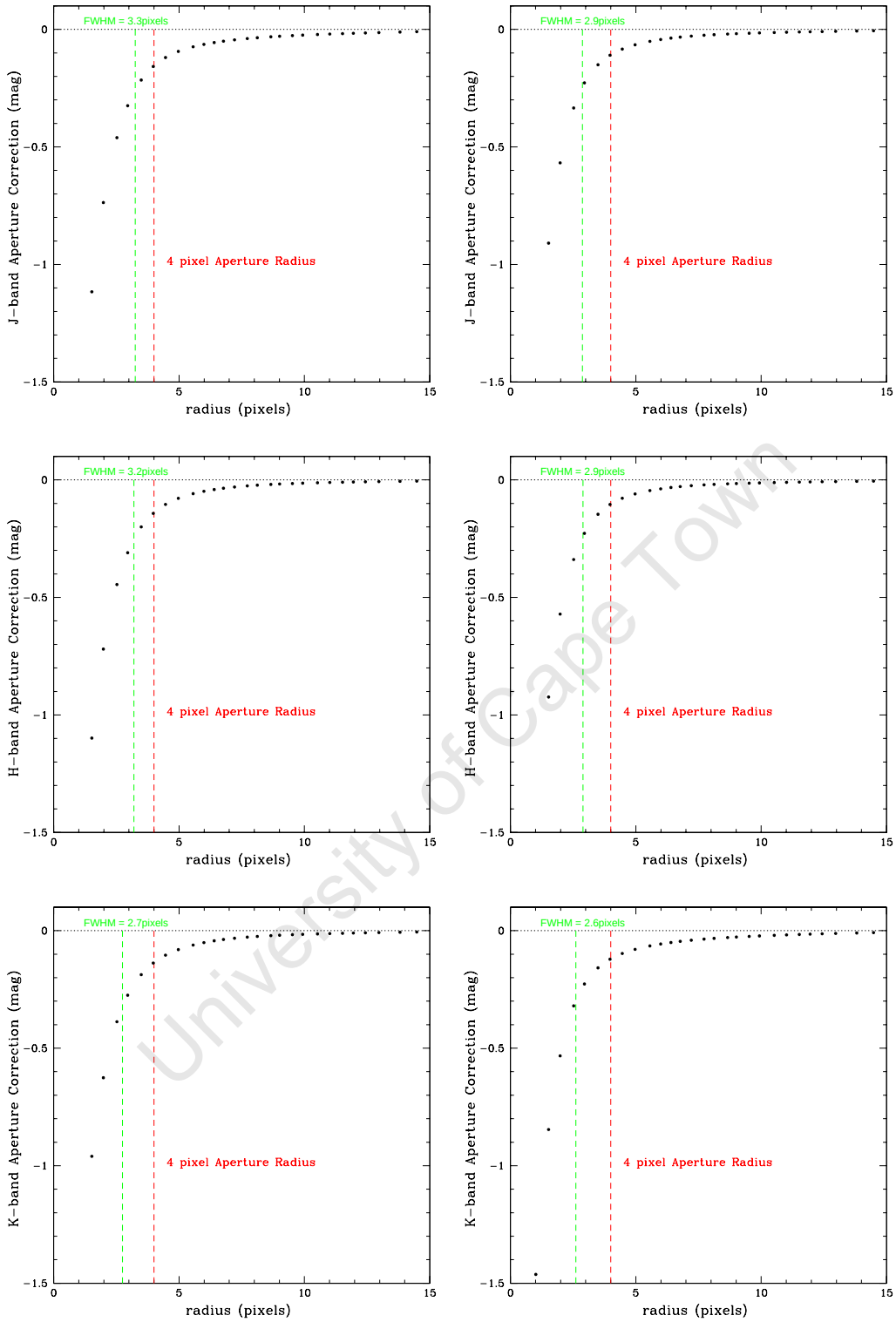

Figure B.4 The magnitude correction as function of the aperture size for galaxy images observed on the nights 10 March 2007 (*left*) and 11 March 2007 (*right*), see caption for Fig. B.1.

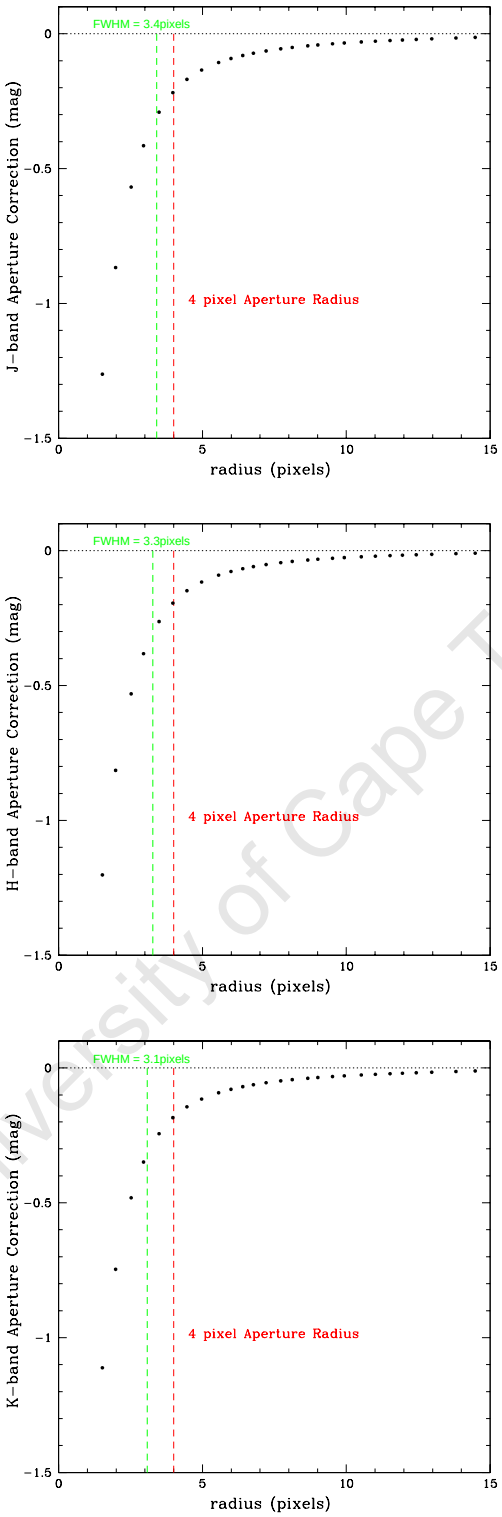

Figure B.5 The magnitude correction as function of the aperture size for galaxy images observed on the night 13 March 2007, see caption for Fig. B.1.

C Wavelength Solutions of Comparison Lamp Spectra

C.1 Wavelength Calibrations for the Full Spectral Range

C.2 Wavelength Calibrations of the First CCD in the Blue

The wavelength solution fitted to the middle row of the two-dimensional spectrum is shown in this section. The first chip of the blue spectral range covers a wavelength range of 3886–4137 Å.

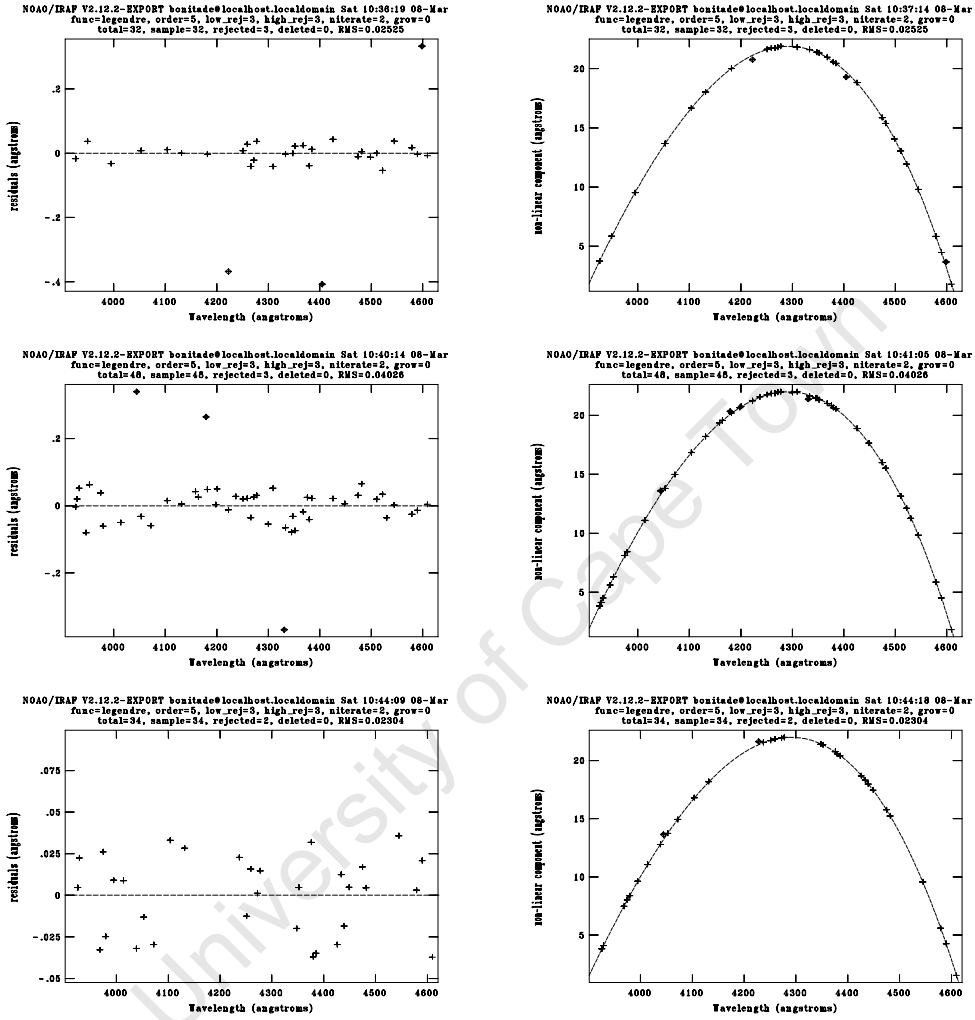

Figure C.1 Wavelength solutions for CuAr comparison lamp spectra taken on 2006 May 29. *left*: residuals in fitting a fifth-order polynomial to measured wavelengths; *right*: quadratic component to the fit.

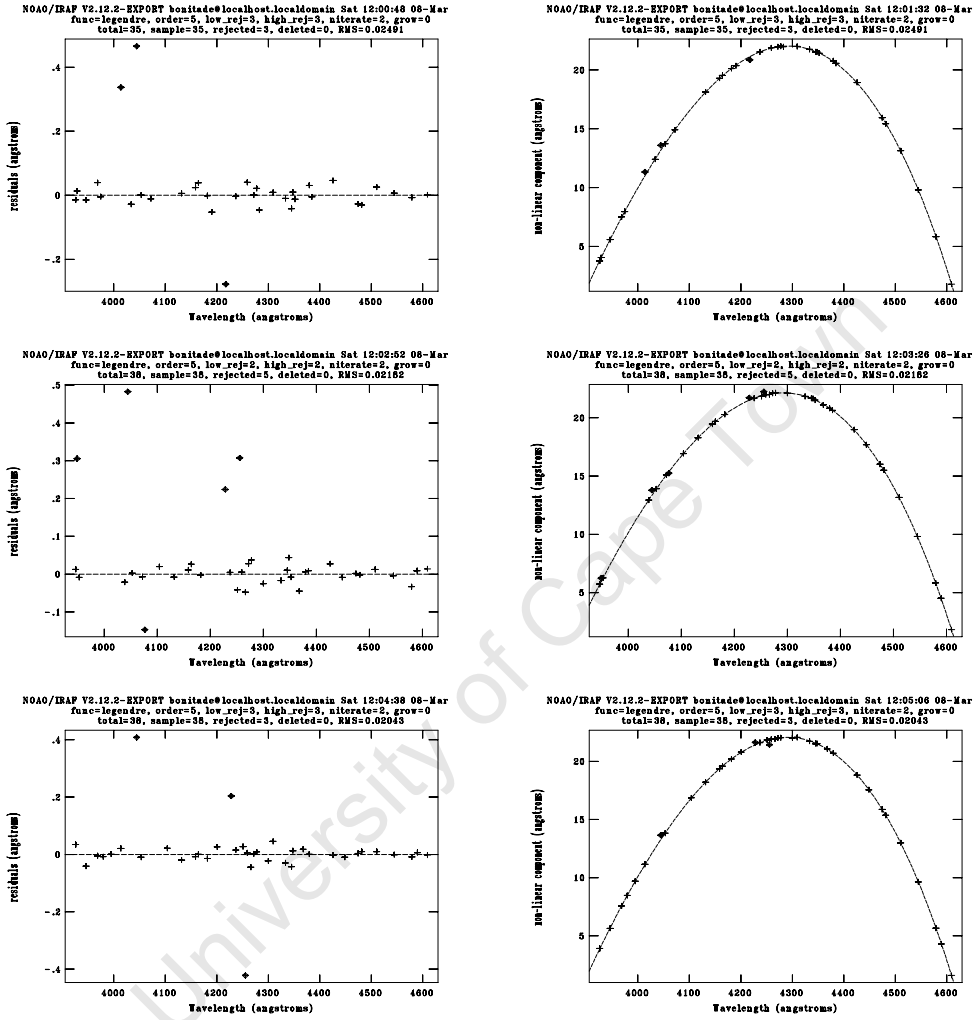

Figure C.2 Wavelength solutions for CuAr comparison lamp spectra taken on 2006 May 30. *left*: residuals in fitting a fifth-order polynomial to measured wavelengths; *right*: quadratic component to the fit.

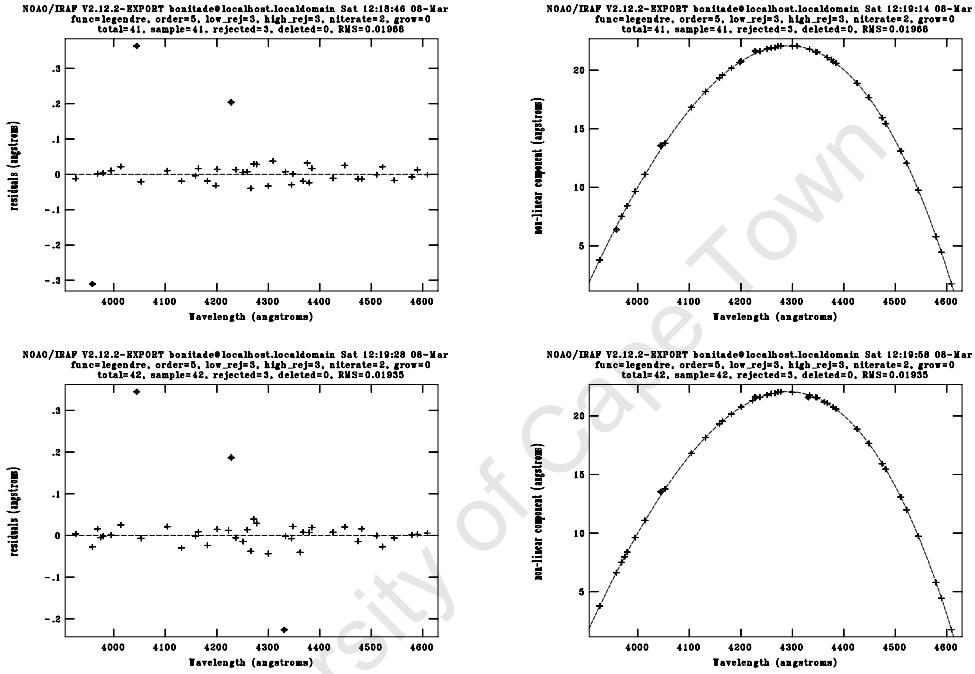

Figure C.3 Wavelength solutions for CuAr comparison lamp spectra taken on 2006 May 31. *left*: residuals in fitting a fifth-order polynomial to measured wavelengths; *right*: quadratic component to the fit.

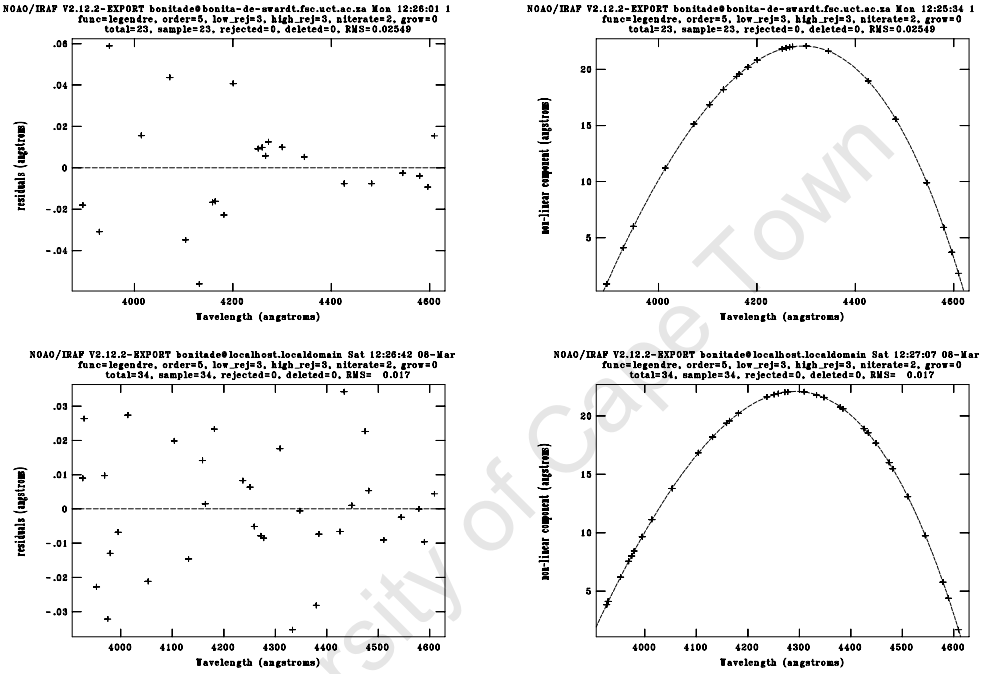

Figure C.4 Wavelength solution of Ar (*top*) and CuAr (*bottom*) comparison lamp spectra taken on 2006 June 5. *left*: residuals in fitting a fifth-order polynomial to measured wavelengths; *right*: quadratic component to the fit.

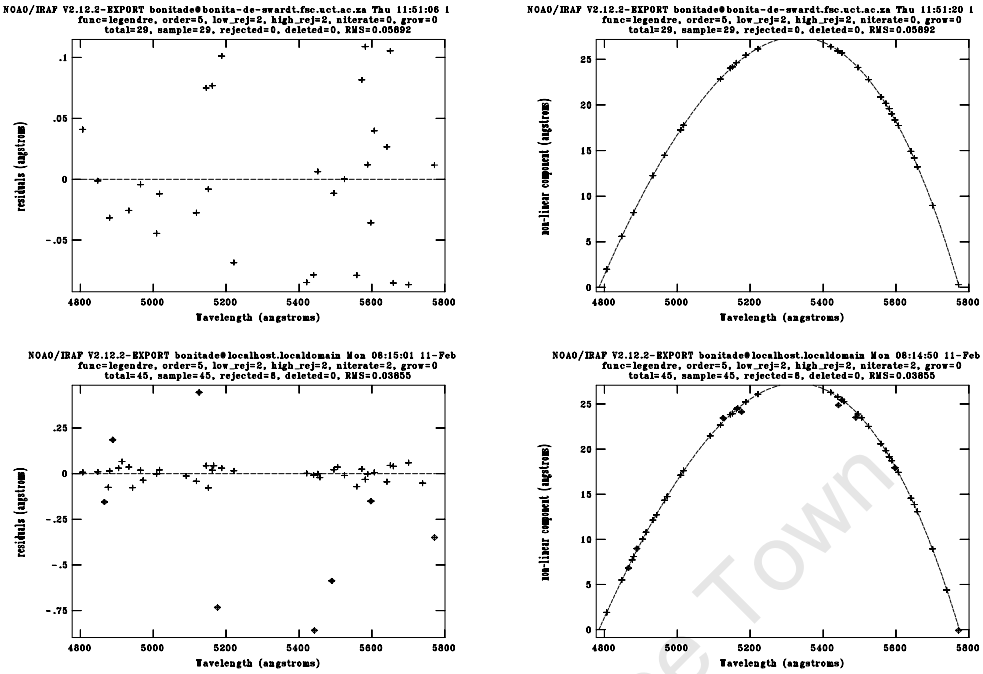

Figure C.5 Wavelength solution of CuAr (*top*) and Ar (*bottom*) comparison lamp spectra taken with the red grating. *left*: residuals in fitting a fifth-order polynomial to measured wavelengths; *right*: quadratic component to the fit.

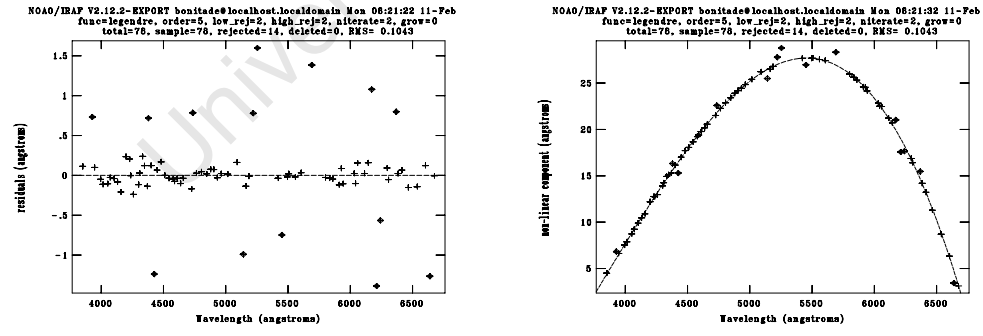

Figure C.6 Wavelength solution of CuAr comparison lamp spectra obtained with the low-resolution grating. *left*: residuals in fitting a fifth-order polynomial to measured wavelengths; *right*: quadratic component to the fit.

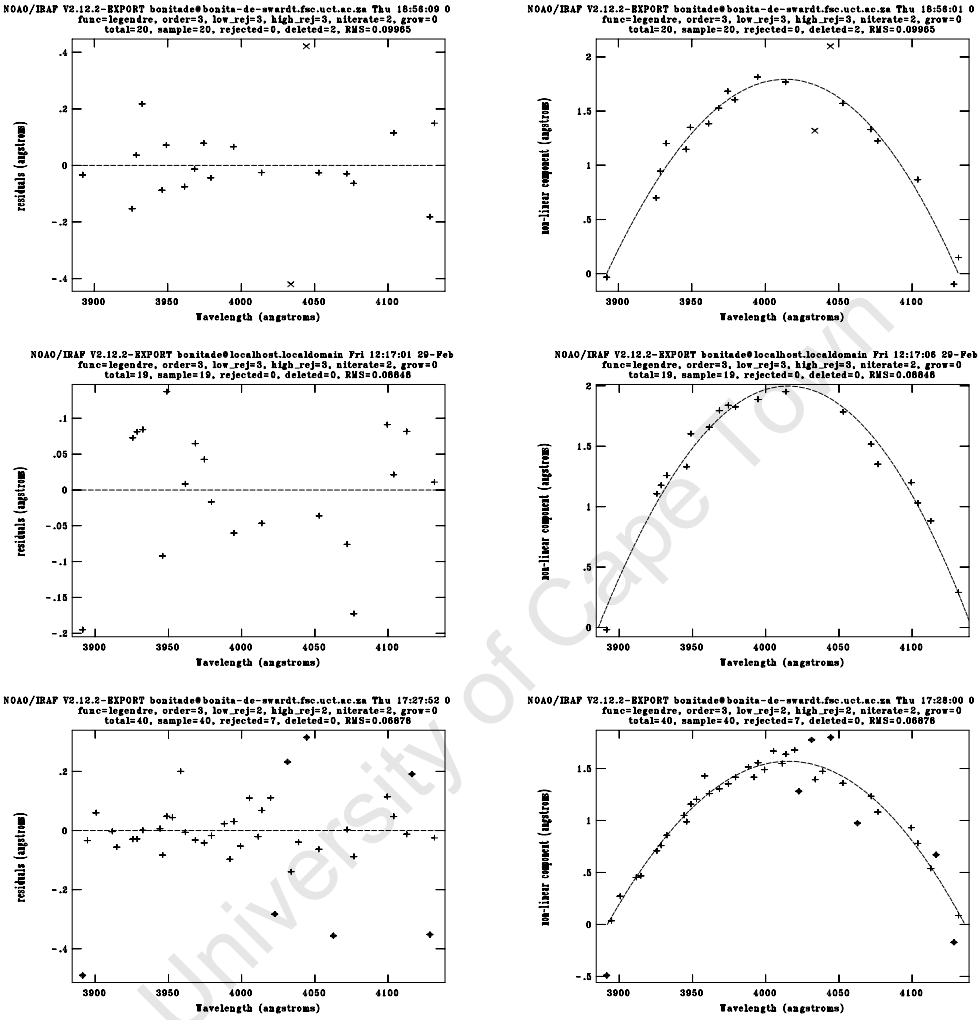

Figure C.7 Wavelength solution of CuAr comparison lamp spectra taken on 2006 May 29. *left*: residuals in fitting a third-order polynomial to measured wavelengths; *right*: quadratic component to the fit.

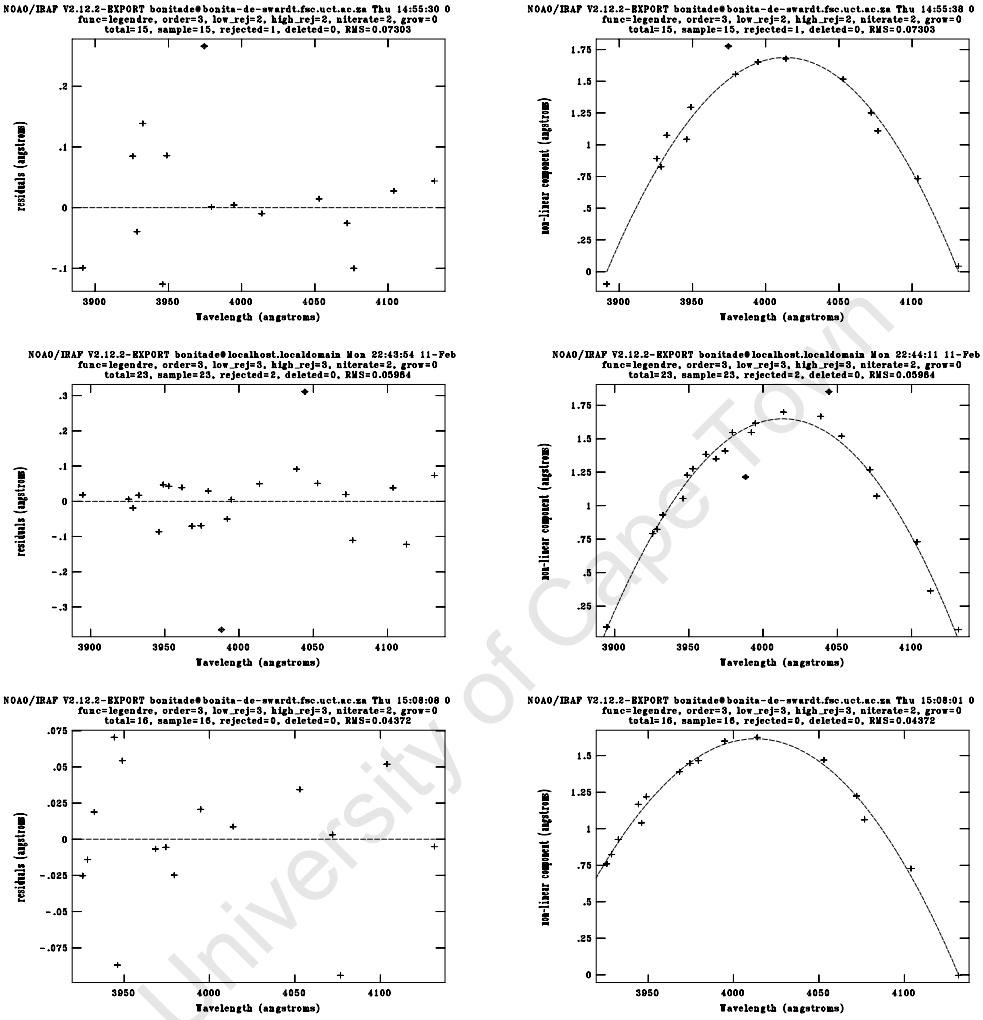

Figure C.8 Wavelength solution of CuAr comparison lamp spectra taken on 2006 May 30. *left*: residuals in fitting a third-order polynomial to measured wavelengths; *right*: quadratic component to the fit.

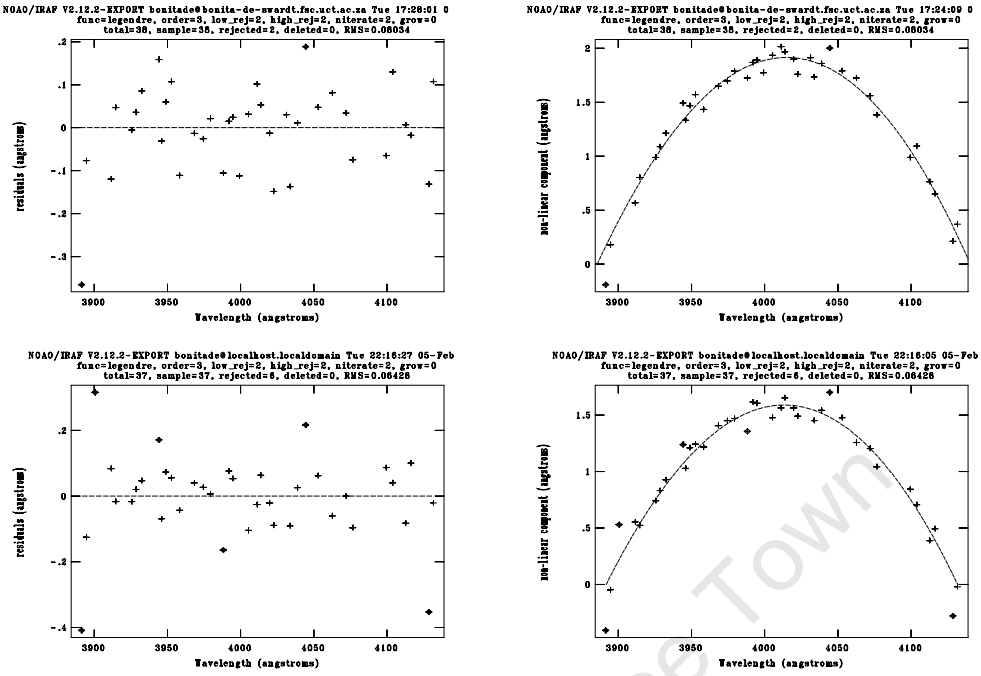

Figure C.9 Wavelength solution of CuAr comparison lamp spectra taken on 2006 May 31. *left*: residuals in fitting a third-order polynomial to measured wavelengths; *right*: quadratic component to the fit.

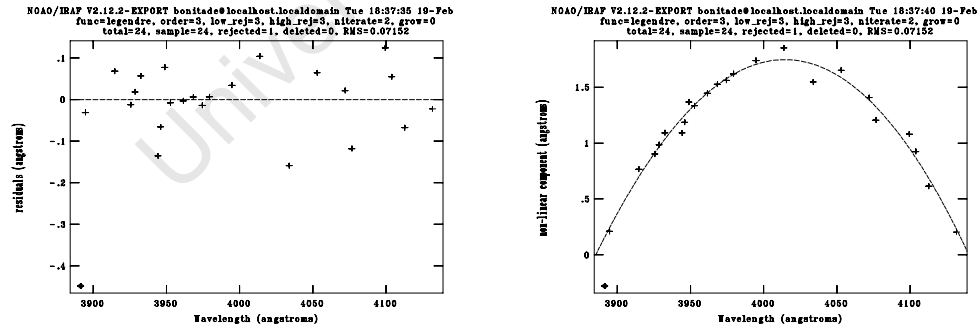

Figure C.10 Wavelength solution of CuAr comparison lamp spectra taken on 2006 June 5. *left*: residuals in fitting a fifth-order polynomial to measured wavelengths; *right*: quadratic component to the fit.

D One-dimensional Spectra of Template Stars

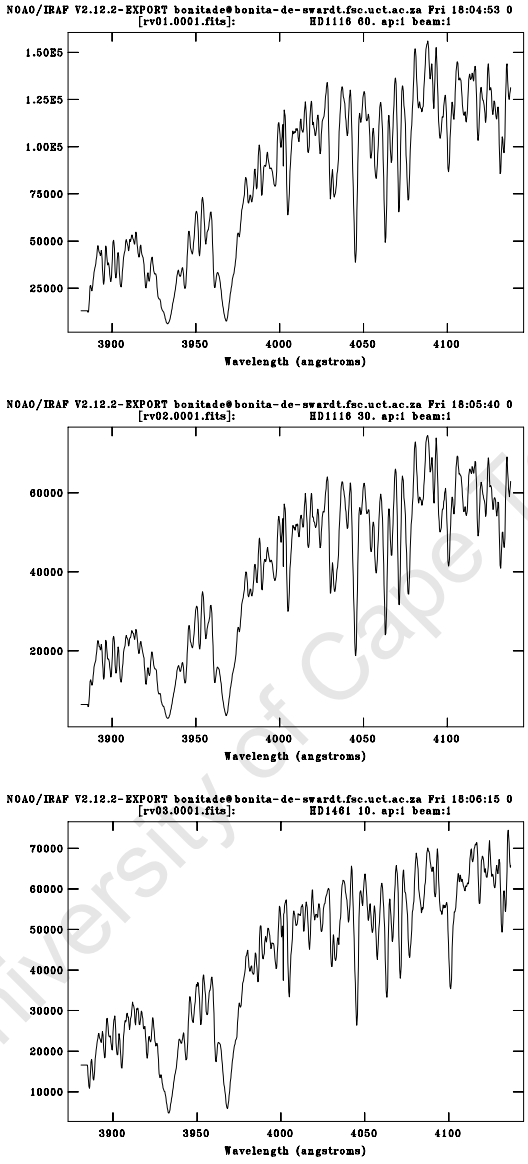

Figure D.1 Wavelength calibrated spectra of template stars acquired on May 30. *top and middle*: HD 1116 (spectral type K0 III); *bottom*: HD 1461 (spectral type G0 V).

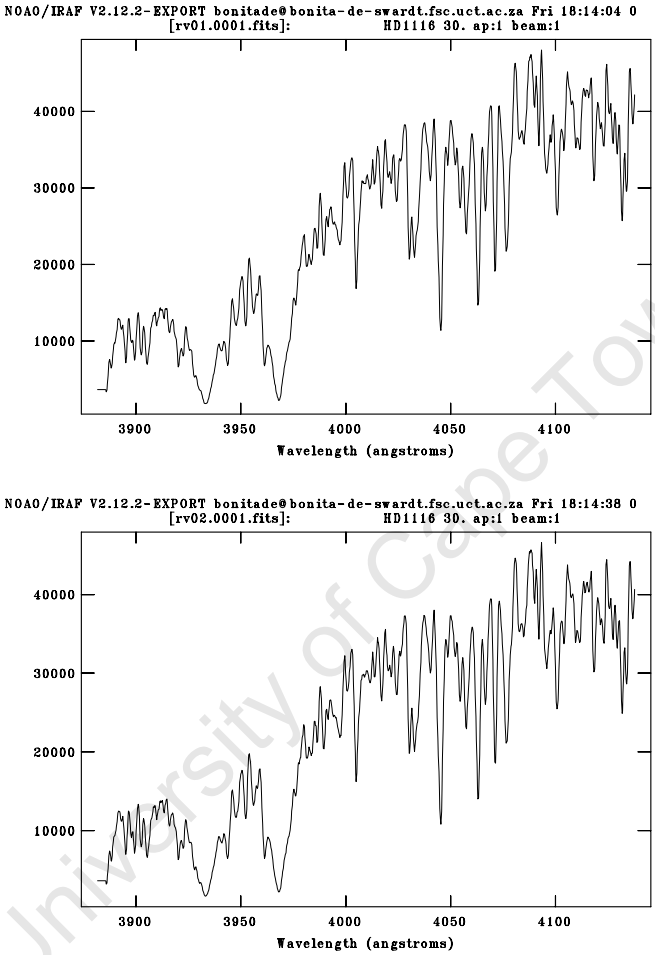

Figure D.2 Wavelength calibrated spectra of template stars acquired on May 31. *top and bottom*: HD 1116 (spectral type K0 III).

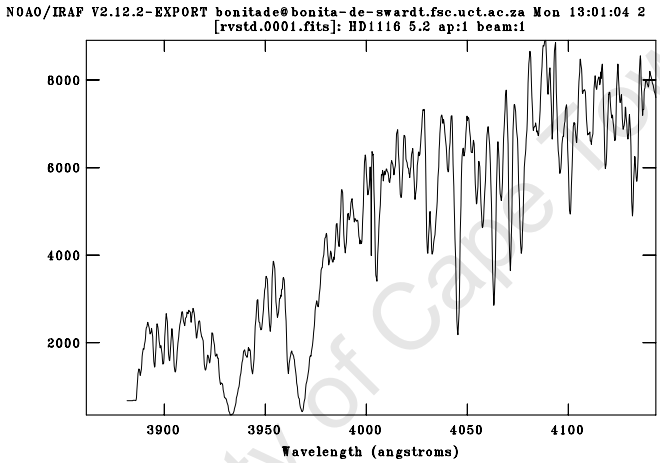

Figure D.3 Wavelength calibrated spectrum of template star HD 1116 (spectral type K0 III) obtained on June 5.

E The Internal Kinematics of Six Galactic Globular Clusters from SALT Longslit Spectra

E.1 Aim

We have obtained optical longslit spectra of six Galactic globular clusters (GCs) using the SALT/RSS spectrograph. Galactic GCs exhibiting a compact and massive core were selected for observation as these are the more likely candidates for hosting an intermediate-mass black hole (IMBH) (see section 1.2.1). The stellar kinematics of the GCs were determined from the longslit spectra. In particular, the mean velocity and velocity dispersion were derived as a function of the GC radius. The first indication of a massive core in these stellar systems will be seen as a distinct rise in the velocity dispersion towards the center of the GC. The proximity of Galactic GCs ensures that high-enough spatial resolution is achieved for detecting this increase in the velocity dispersion towards the center. The observations were carried out during the Performance Verification (PV) phase of the SALT/RSS spectrograph. The observations presented in this appendix are therefore seen as a pilot study for the search of IMBHs in the center of Galactic GCs. Based on our findings for the six GCs, the observing configuration for detecting a central IMBH will later be optimized when conducting follow-up observations with the SALT telescope.

E.2 Sample Selection

A sample of six Galactic GCs were selected from Pryor & Meylan (1993). The following criteria were imposed in selecting suitable targets:

1. Most of the Galactic GCs have central velocity dispersions of $\sigma_0 < 10\text{km s}^{-1}$ (Pryor & Meylan 1993). We have assumed that these stellar systems follow the $M_{\rm BH}$ versus σ_0 relation of Ferrarese & Merritt (2000) so that GCs having $\sigma_0 > 10\text{km s}^{-1}$ are the more likely candidates of hosting an IMBH in their centers. For this reason, the GCs showing the highest central velocity dispersions were selected for observations. The six GC candidates were found to have central dispersions in the range of $10 \leq \sigma_0 \leq 20\,\text{km s}^{-1}$ as shown in Table E.1. By choosing the GCs with the highest central dispersion, we will also ensure that the resolving capabilities of the SALT/RSS spectrograph are met.

2. It is suspected that an IMBH is more likely to form in those GCs having a dense and massive core. These stellar environments are susceptible to gravitational instabilities such as core collapse which can lead to the formation of a central BH (see review by van der Marel 2004). Galactic GCs having a large central mass density ρ_0 were therefore selected. The central mass densities of the six GC candidates are in the range of $4.9 \leq \log(\rho_0) \leq 6$ (see Table E.1).

3. The 2MASS near-infrared (JHK_s) images of the GC candidates were inspected for the presence of a massive core. These images gave further indication of whether the GCs host a compact core.

The V-band DSS images of the six GC candidates are shown in Fig. E.1. It can be seen that the GCs vary in apparent size and luminosity ($-9\overset{\text{m}}{.}5 \lesssim M_V \lesssim -8\overset{\text{m}}{.}2$). The properties

Table E.1. Properties of selected Galactic globular clusters

Name	RA (J2000)	DEC (J2000)	Distance (kpc)	M_V (mag)	$< \mu_V >_{\rm h}$ (mag arcsec^{-2})	$r_{\rm h}$ (pc)	$\mu_{0,V}$ (mag arcsec^{-2})	σ_0 [1] (km s^{-1})	$\log(\rho_0)$ ($M_\odot$/pc^3)
NGC 2808	09 12 02.5	-64 51 46	9.2	-9.32	15.69	1.34	14.43	13.4	4.9
NGC 6266 (M62)	17 01 12.6	-30 06 44	5.5	-8.90	15.60	1.21	13.64	14.3	5.7
NGC 6388	17 36 17.4	-44 44 08	11.0	-9.46	15.24	1.26	13.45	18.9	5.7
NGC 6441	17 50 12.8	-37 03 04	10.7	-9.30	15.39	1.25	13.53	18.0	5.8
NGC 6715 (M54)	18 55 03.3	-30 28 43	21.2	-9.42	16.41	1.57	14.28	14.2	5.0
NGC 6864 (M75)	20 06 04.8	-21 55 20	18.5	-8.24	17.24	1.46	15.03	10.3	4.9

Note. — Parameters are taken from Pryor & Meylan (1993) and Djorgovski (1993). [1] The velocity dispersion σ_0 of globular clusters have been derived from Doppler broadening of integrated light spectra (see Pryor & Meylan 1993, and references therein).

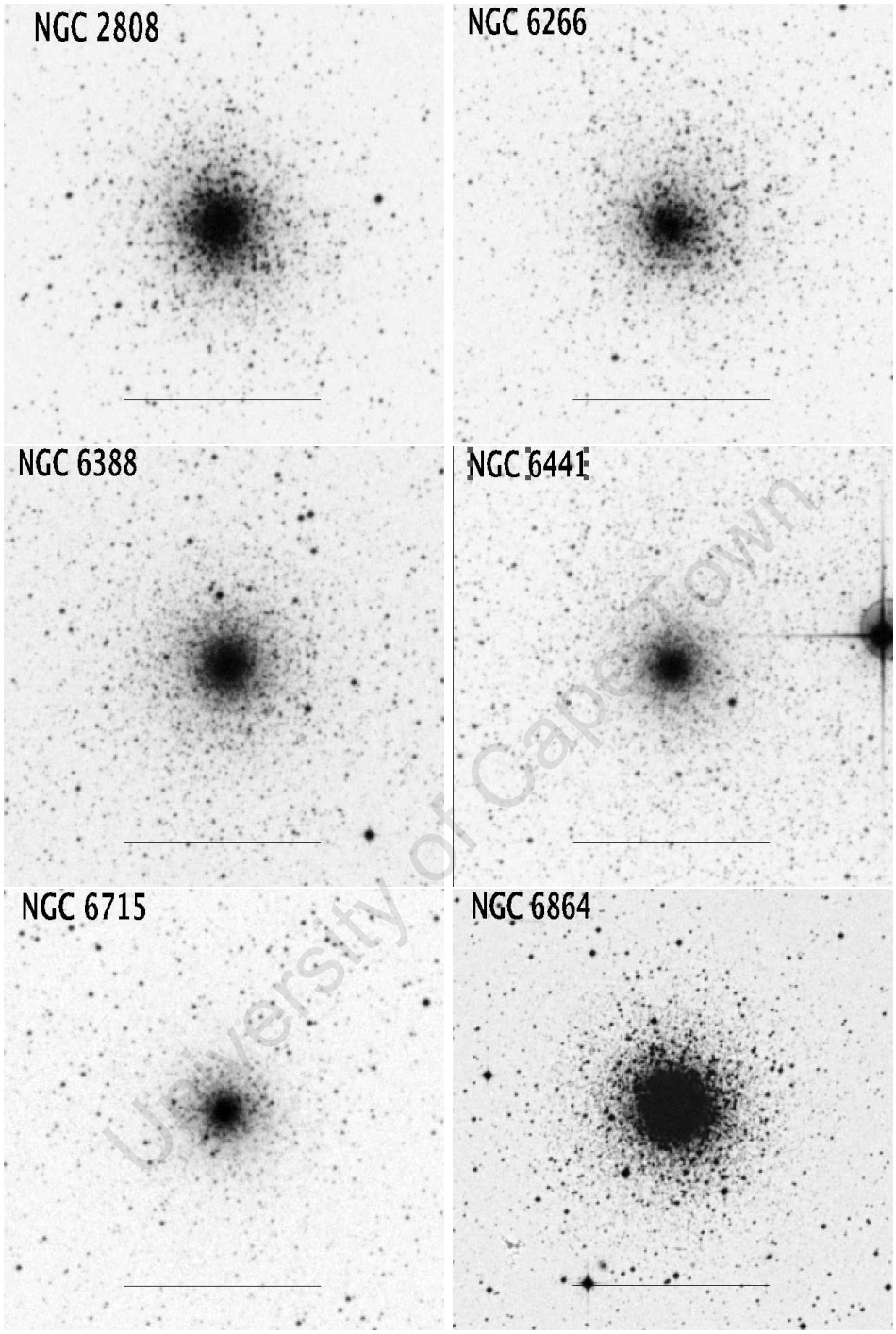

Figure E.1 V-band DSS imaging of the selected Galactic globular clusters: NGC 2808 (*top left*), NGC 6266 (*top right*), NGC 6388 (*middle left*), NGC 6441 (*middle right*), NGC 6715 (*bottom left*), and NGC 6864 (*bottom right*). The horizontal bar at the bottom of each panel indicates a scale of 5-arcminute. North is up and East is to the left.

of the GCs are listed in Table E.1. The GCs vary in distance from 5.5kpc for NGC 6266 to 21.2kpc for NGC 6715. The surface brightness of the GC candidates is given by the parameter $< \mu_V >_h$ (Djorgovski 1993) in Table E.1 which represents the average surface brightness within the half-light radius r_h. The GCs have surface brightness in the range of $15.2 \lesssim < \mu_V >_h$ (mag arcsec^{-2}) $\lesssim 17.2$. The brightest GCs satisfying the criteria 1–3 were selected so that relatively high S/N levels can be achieved with short exposure times.

E.3 Observations

Longslit spectroscopic observations of the Galactic GCs were obtained with the SALT/RSS spectrograph during six nights over the Performance Verification (PV) phase (May to August 2006). Details of the GC observations are listed in Table E.2. The spectra were acquired during grey time with a seeing in the range of $1\farcs3-2\farcs0$.

The GC observations were performed with the $1''$ wide $\times$ $8'$ long slit. The hoyaUV-34 order-blocking filter was used together with the 3000 lines mm^{-1} grating. The spectra cover the wavelength range 3870–4605Å. The spectral range includes the Ca II K(λ3933) and H(λ3968) lines, the Hδ(λ4101) and Hγ(λ4340) Balmer lines, the Ca Ig(λ4226) line, and numerous iron absorption lines. The GC spectra have a spatial scale of $0\farcs256$ per pixel.

Because of the spherical symmetry of GC systems, no constraints were imposed on the position angle of the slit. All observations were carried out with the slit placed in its default position, i.e. North to South, through the GC center in Fig. E.1. The observations were guided both manually and using a V-band auto-guider as described for the galaxy observations in Chapter 3 (section 3.3). The six GCs each have small enough angular size to be fully sampled by the $8\farcm0$ slit length.

The SALT/RSS exposure time calculator was used to determine the required exposure times for the selected GCs. It was found that single 10-15 minute exposures would provide sufficient S/N levels (S/N > 10) for the extraction of the central stellar kinematics. At least two GC exposures were acquired to assist with cosmic ray removal. The complete set of GC observations is listed in Table E.2.

Table E.2 also lists the corresponding radial velocity stars (or template stars) for the GC observations. To assess the stability of the SALT/RSS, a template star exposure was acquired both before and after the GC observations. This observational sequence was carried out for all GCs excluding NGC 6864. For this GC, a template star could only be observed after the cluster observations. The template stars were acquired with the same instrumental setup as the GCs.

A CuAr or Ar comparison lamp spectrum was taken before and after each set of GC observations (see Table E.2) in mapping the wavelength solution.

Table E.2. Longslit spectroscopic observations of the six Galactic globular clusters

Date	Object	RA (J2000)	DEC (J2000)	Type	Grating (lines mm^{-1})	Wavelength Range (Å)	Exp (s)
SALT Data:							
2006 Jun 09	HD 148760	16 31 22.9	-26 32 16	K1 III	3000	3882 – 4619	5
	HD 148760	16 31 22.9	-26 32 16	K1 III	3000	3882 – 4619	5
	Arc	–	–	CuAr	3000	3882 – 4619	45
	Arc	–	–	CuAr	3000	3882 – 4619	45
	NGC 6266	17 01 12.6	-30 06 44	–	3000	3882 – 4619	700
	Arc	–	–	CuAr	3000	3882 – 4619	45
	HD 158630	17 34 05.3	-59 46 33	G2 V	3000	3882 – 4619	5
	HD 158630	17 34 05.3	-59 46 33	G2 V	3000	3882 – 4619	5
	Arc	–	–	CuAr	3000	3882 – 4619	45
2006 Jun 09	HD 182160	19 26 21.6	-54 51 48	K0 III	3000	3882 – 4619	20
	Arc	–	–	CuAr	3000	3882 – 4619	60
	Arc	–	–	CuAr	3000	3882 – 4619	60
	NGC 6715	18 55 03.3	-30 28 43	–	3000	3882 – 4619	550
	NGC 6715	18 55 03.3	-30 28 43	–	3000	3882 – 4619	550
	Arc	–	–	CuAr	3000	3882 – 4619	60
	HD 182160	19 26 21.6	-54 51 48	K0 III	3000	3882 – 4619	40
	Arc	–	–	CuAr	3000	3882 – 4619	60
2006 Jun 10	HD 73678	08 37 40.83	-47 21 43	G0 III	3000	3882 – 4619	60
	Arc	–	–	CuAr	3000	3882 – 4619	60
	Arc	–	–	CuAr	3000	3882 – 4619	60
	NGC 2808	09 12 02.5	-64 51 46	–	3000	3882 – 4619	600
	NGC 2808	09 12 02.5	-64 51 46	–	3000	3882 – 4619	600
	NGC 2808	09 12 02.5	-64 51 46	–	3000	3882 – 4619	600
	Arc	–	–	CuAr	3000	3882 – 4619	60
	HD 85250	09 48 40.0	-56 24 43	K0 III	3000	3882 – 4619	30
	Arc	–	–	CuAr	3000	3882 – 4619	60
2006 Aug 06	Arc	–	–	Ar	3000	3882 – 4619	15
	NGC 6864	20 06 04.8	-21 55 20	–	3000	3882 – 4619	600
	NGC 6864	20 06 04.8	-21 55 20	–	3000	3882 – 4619	600
	NGC 6864	20 06 04.8	-21 55 20	–	3000	3882 – 4619	600
	Arc	–	–	Ar	3000	3882 – 4619	15
	Arc	–	–	Ar	3000	3882 – 4619	15

Observations: 1.9m telescope

Additional longslit spectra were obtained for the GC NGC 6388 using the 1.9m f/2.2 Cassegrain telescope in Sutherland, South Africa. This complementary data set provided an independent means of checking for systematic effects in the SALT/RSS spectra by comparing the kinematic results derived for NGC 6388.

Longslit spectra of NGC 6388 and its companion template stars were obtained with the 1.9m telescope in March 2007.[1] The observations are listed in Table E.2. The detector system of this telescope consists of a SITe CCD of 266×1798 pixels in size. The resulting spatial scale is $0\farcs738$ per pixel. The CCD gain and readnoise are $1e^-$/ADU and $6.5e^-$, respectively. The observations were performed using a $1\farcs5$ slit together with the 300 lines mm^{-1} (blaze of 4600Å at first order) spectral grating. The radial velocity template stars were observed before and after the GC observations. A CuAr comparison lamp spectrum was taken before the GC and template star observations for the wavelength calibrations. The observational sequence is also listed in Table E.2.

The total exposures of the GC observations obtained from the SALT and 1.9m telescopes are listed in Table E.3.

E.4 The Reduced Globular Cluster Spectra

We have followed the data reduction and calibration procedures described for the blue galaxy spectra in Chapter 3, section 3.4. The individual GC and template spectra were wavelength-calibrated using the comparison lamp spectrum closest in time to the actual target observation. For the SALT/RSS spectra, the dispersion solution was fitted across the three CCDs of the comparison lamp spectra. The dispersion solutions for these data were determined with an RMS < 0.05Å. The properties of the wavelength-calibrated GC spectra are listed in Table E.4. The calibrated spectra cover the wavelength range of 3870–4607Å. A spectral dispersion of 0.232Å pixel^{-1} gives a velocity resolution of 17.6km s^{-1} pixel^{-1} at the Ca II K(λ3933) absorption line.

Table E.4 also lists the properties of the NGC 6388 spectra obtained with the 1.9m telescope. These spectra were reduced and wavelength-calibrated in a similar manner to that carried out for the SALT/RSS spectra. A fifth order polynomial was fitted to the wavelengths of emission lines in the CuAr lamp spectra. The polynomial fit gives a dispersion solution with RMS < 0.1Å. The 1.9m data cover the wavelenth range of 3632–4526Å with a spectral dispersion of 0.511Å pixel^{-1} (or 39km s^{-1} pixel^{-1} at the Ca II K absorption line). The 1.9m data has two times lower velocity resolution than the SALT/RSS spectra.

A single reduced (1D and 2D) spectrum for each of the six GCs is displayed in Figs. E.2–E.8. The broad Ca II K(λ3933) and H(λ3963) absorption features are clearly seen on the first CCD of the GC spectra. The spectrum of individual stars is also visible in the 2D GC spectra (e.g., see Fig. E.2). Note that an interpolation of the spectrum across the CCD gaps was not carried out for the GCs shown in Figs. E.2–E.4. The CCD gaps are seen as the vertical lines in the GC spectra. The 1D spectrum of NGC 6388 obtained with the 1.9m telescope is shown in Fig. E.8.

[1]B.D.S would like to acknowledge A.A. Zijlstra for performing these observations.

Table E.2 (cont'd)

Date	Object	RA (J2000)	DEC (J2000)	Type	Grating (lines mm^{-1})	Wavelength Range (Å)	Exp (s)
	HD 196857	20 40 32.5	-16 07 27	K0 III	3000	3882 – 4619	20
2006 Aug 10	HD 158630	17 34 05.3	-59 46 33	G2 V	3000	3882 – 4619	10
	Arc	–	–	Ar	3000	3882 – 4619	15
	NGC 6388	17 36 17.4	-44 44 08	–	3000	3882 – 4619	900
	NGC 6388	17 36 17.4	-44 44 08	–	3000	3882 – 4619	900
	NGC 6388	17 36 17.4	-44 44 08	–	3000	3882 – 4619	900
	NGC 6388	17 36 17.4	-44 44 08	–	3000	3882 – 4619	900
	Arc	–	–	Ar	3000	3882 – 4619	15
	HD 169236	18 25 21.7	-35 59 31	K0 III	3000	3882 – 4619	10
	Arc	–	–	Ar	3000	3882 – 4619	15
2006 Aug 12	HD 158630	17 34 05.3	-59 46 33	G2 V	3000	3882 – 4619	2
	Arc	–	–	Ar	3000	3882 – 4619	15
	Arc	–	–	Ar	3000	3882 – 4619	15
	NGC 6441	17 50 12.8	-37 03 04	–	3000	3882 – 4619	600
	NGC 6441	17 50 12.8	-37 03 04	–	3000	3882 – 4619	600
	NGC 6441	17 50 12.8	-37 03 04	–	3000	3882 – 4619	600
	Arc	–	–	Ar	3000	3882 – 4619	15
	NGC 6441	17 50 12.8	-37 03 04	–	3000	3882 – 4619	600
	NGC 6441	17 50 12.8	-37 03 04	–	3000	3882 – 4619	600
	Arc	–	–	Ar	3000	3882 – 4619	15
	HD 169236	18 25 21.7	-35 59 31	K0 III	3000	3882 – 4619	20
	Arc	–	–	Ar	3000	3882 – 4619	15
1.9m Data:							
2007 Mar 15	Arc	–	–	CuAr	300	3632 – 4526	10
	HD 158630	17 34 05.3	-59 46 33	G2 V	300	3632 – 4526	30
	HD 158630	17 34 05.3	-59 46 33	G2 V	300	3632 – 4526	120
	NGC 6388	17 36 17.4	-44 44 08	–	300	3632 – 4526	1200
	NGC 6388	17 36 17.4	-44 44 08	–	300	3632 – 4526	1200
	NGC 6388	17 36 17.4	-44 44 08	–	300	3632 – 4526	1200
	Arc	–	–	CuAr	300	3632 – 4526	10
	HD 169236	18 25 21.7	-35 59 31	K0 III	300	3632 – 4526	120
	Arc	–	–	CuAr	300	3632 – 4526	10

Table E.3. Total exposures of globular clusters observations

Date	Object	RA (J2000)	DEC (J2000)	Total Exp (min)
SALT Data:				
2006 Jun 09	NGC 6266	17 01 12.6	-30 06 44	11
	NGC 6715	18 55 03.3	-30 28 43	18
2006 Jun 10	NGC 2808	09 12 02.5	-64 51 46	30
2006 Aug 06	NGC 6864	20 06 04.8	-21 55 20	30
2006 Aug 10	NGC 6388	17 36 17.4	-44 44 08	60
2006 Aug 12	NGC 6441	17 50 12.8	-37 03 04	50
1.9m Data:				
2007 Mar 15	NGC 6388	17 36 17.4	-44 44 08	60

E.5 Heliocentric Radial Velocities of the Six Globular Clusters

The internal kinematics of each GC was derived from the total combined spectrum. The heliocentric radial velocity $v_{\odot}$ of the individual GC spectra was needed to create the final combined spectrum as described in Chapter 3 (section 3.5). The radial velocities of the GCs were determined using the Fourier cross-correlation method. The resulting velocities were then used to shift the GC spectra to a zero velocity scale in creating the final combined spectrum.

The radial velocities of the template stars were measured before performing the cross-correlation analysis. The Doppler shift technique was employed to measure the radial velocities (Chapter 3, section 3.5.1). The radial velocities of the template stars were determined from the strong absorption features in the spectra: Ca II K(λ3933) and H(λ3968), Fe I(λ4046), Hδ(λ4101), Ca Ig(λ4226) and Hγ(λ4340). The radial velocity of each template star was computed as the mean velocity given by the six absorption lines. The error in the radial velocity is given as the standard deviation of the mean. The radial velocities of all the template star exposures are listed in Table E.5. The literature values of the radial velocities (Kharchenko et al. 2004) are quoted for comparison. The measured radial velocities can show significant deviation of up to $\Delta v_{\rm rad} \sim 38$km s^{-1} (corresponding to ~ 2 pixels in the SALT/RSS spectra) from the literature values. This scatter in the measured radial velocities is also seen for the template stars acquired with the 1.9m telescope. The best agreement ($\Delta v_{\rm rad} \lesssim 6$km s^{-1}) with the literature values of the radial velocity is observed for the SALT/RSS spectra obtained in August 2006. To ensure consistency in the derived GC radial velocities, the measured velocities of the template stars were used during the cross-correlation analysis.

The 1D spectrum of each GC exposure was created by combining the rows of the CCD out to the background level. The 1D spectrum includes the spectra from individual stars seen just outside of the GC continuum region. The resulting spectrum is therefore a good

Table E.4. Properties of the wavelength-calibrated globular cluster spectra

Date	Object	Exp (sec)	Wavelength Range (Å)	Spectral Dispersion (Å pixel^{-1})	Velocity Resolution[1] (km s^{-1} pixel^{-1})
SALT Data:					
2006 Jun 09	NGC 6266	700	3869−4612	0.235	17.9
	NGC 6715	550	3867−4601	0.232	17.6
	NGC 6715	550	3867−4601	0.232	17.6
2006 Jun 10	NGC 2808	600	3869−4605	0.233	17.8
	NGC 2808	600	3869−4605	0.233	17.8
	NGC 2808	600	3869−4605	0.233	17.8
2006 Aug 06	NGC 6864	600	3870−4606	0.233	17.8
	NGC 6864	600	3870−4607	0.233	17.8
	NGC 6864	600	3870−4607	0.233	17.8
2006 Aug 10	NGC 6388	900	3869−4605	0.233	17.8
	NGC 6388	900	3869−4605	0.233	17.8
	NGC 6388	900	3869−4605	0.233	17.8
	NGC 6388	900	3869−4605	0.233	17.8
2006 Aug 12	NGC 6441	600	3870−4605	0.232	17.6
	NGC 6441	600	3870−4605	0.232	17.6
	NGC 6441	600	3870−4605	0.232	17.6
	NGC 6441	600	3870−4605	0.232	17.6
	NGC 6441	600	3870−4605	0.232	17.6
1.9m Data:					
2007 Mar15	NGC 6388	1200	3632−4526	0.511	39.0
	NGC 6388	1200	3632−4526	0.511	39.0
	NGC 6388	1200	3632−4526	0.511	39.0

Note. — [1] The velocity resolution was calculated at the Ca II K(λ3933) absorption line.

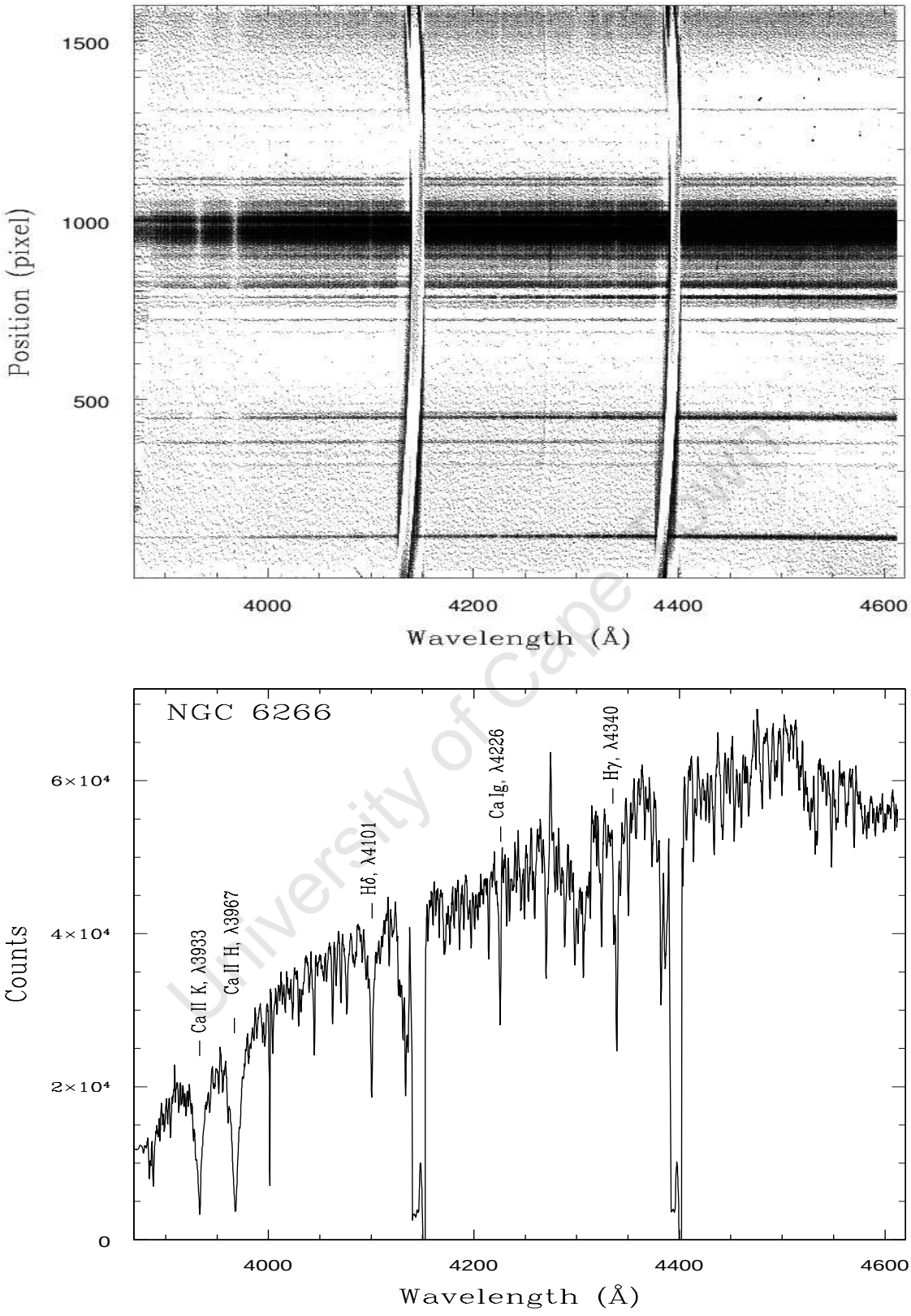

Figure E.2 SALT/RSS spectrum of NGC 6266. The spectrum corresponds to an 11-minute exposure. *Top*: 2D spectrum showing the full spatial range of the CCD. The individual spectra of stars are seen as the horizontal lines on the CCD. *Bottom*: The 1D spectrum of the GC was obtained by summing the rows of the CCD out to a defined background level. The CCD gaps are seen near the wavelengths 4150Å and 4400Å. The prominent absorption features in the spectrum are indicated.

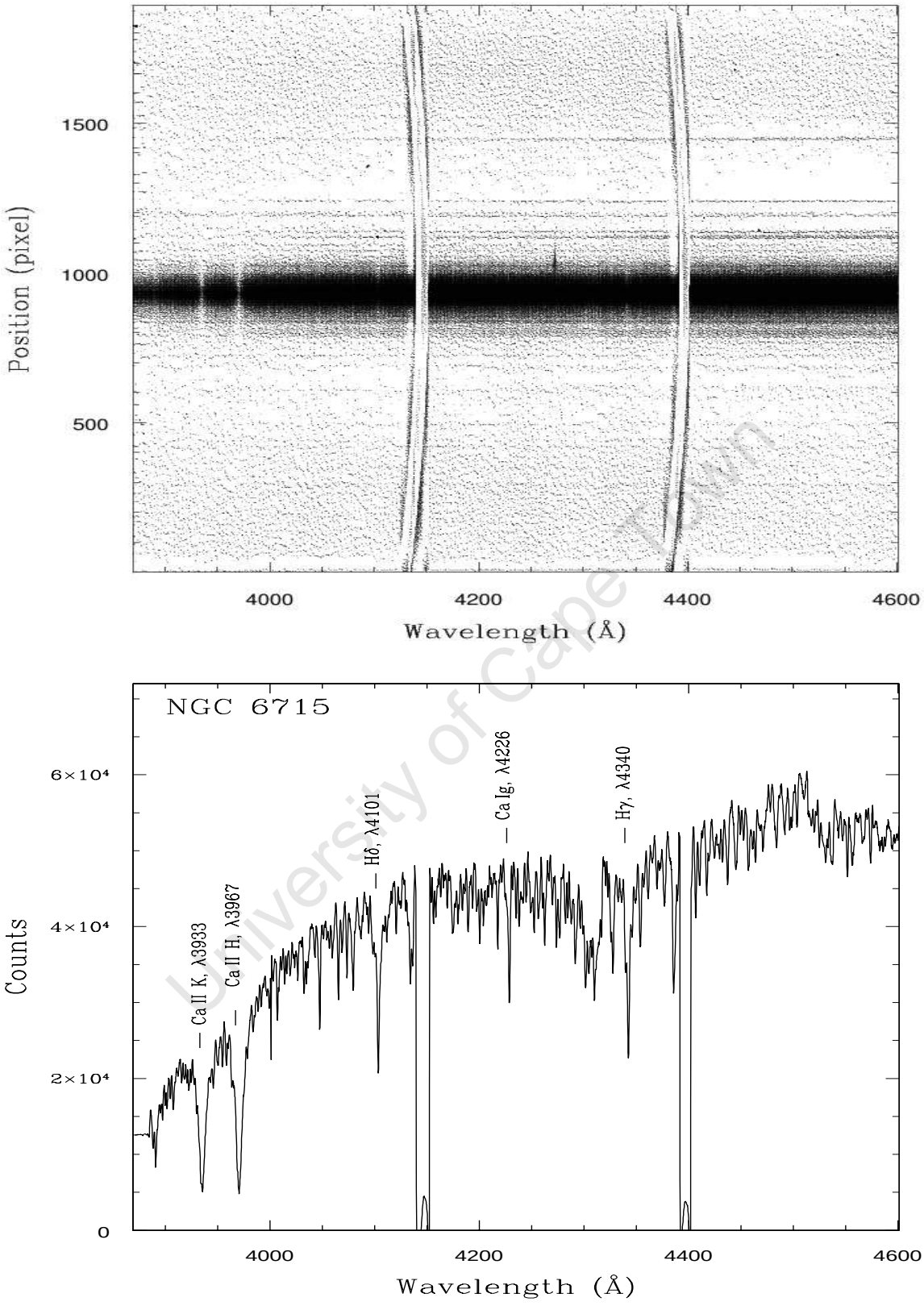

Figure E.3 SALT/RSS spectrum of NGC 6715. The spectrum corresponds to an 9-minute exposure. See caption for Fig. E.2.

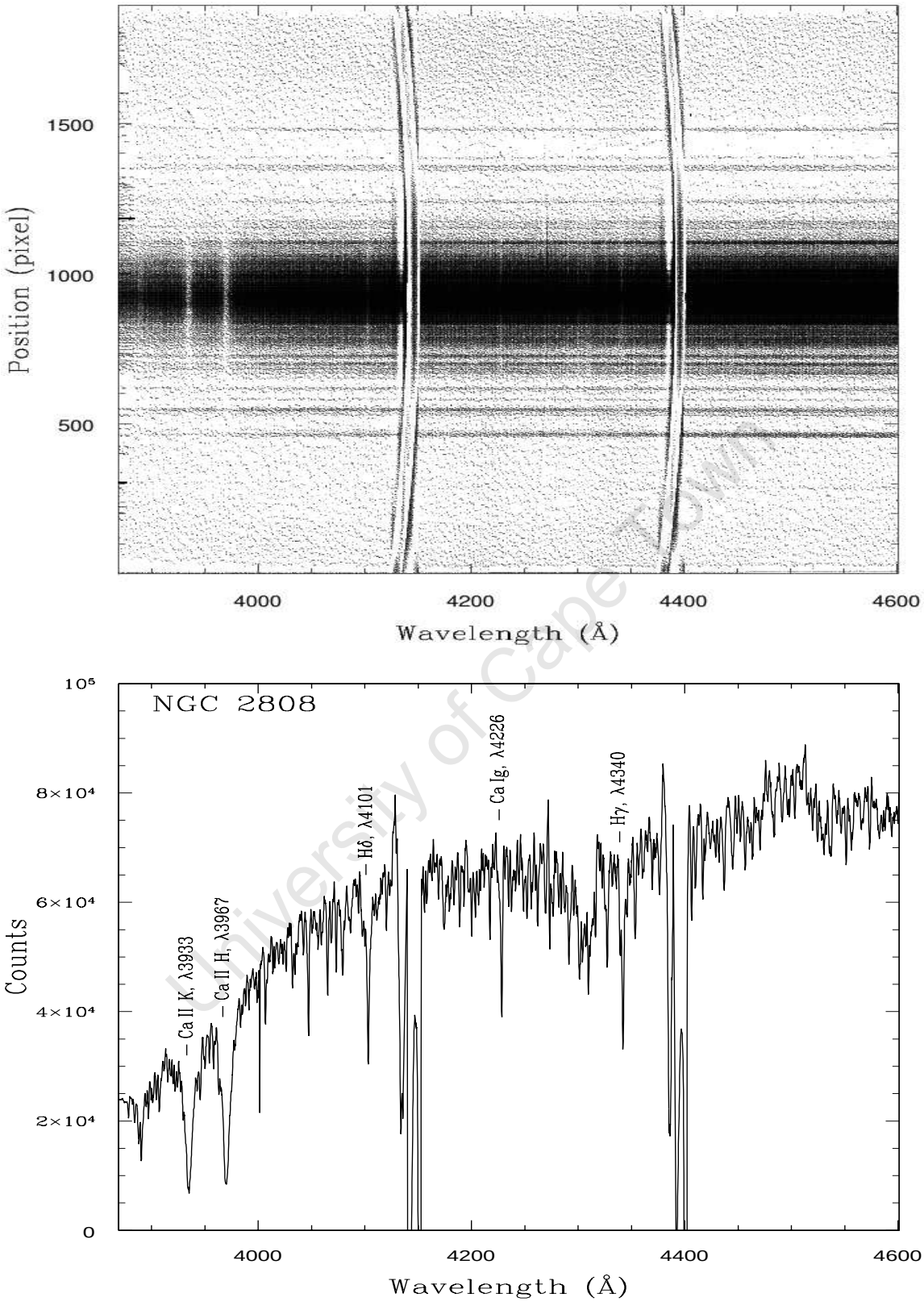

Figure E.4 SALT/RSS spectrum of NGC 2808. The spectrum corresponds to an 10-minute exposure. See caption for Fig. E.2.

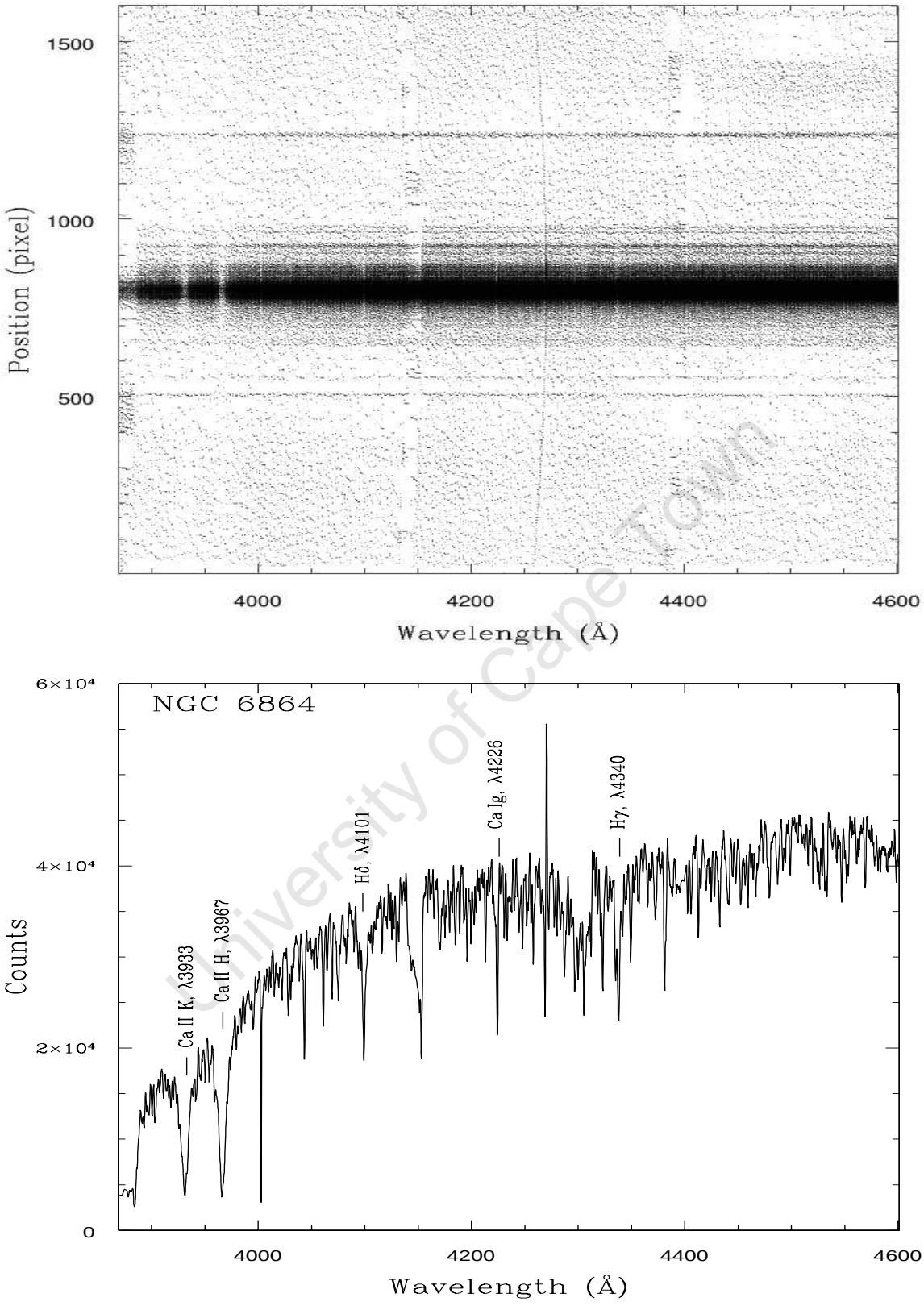

Figure E.5 SALT/RSS spectrum of NGC 6864. The spectrum corresponds to an 10-minute exposure. *Top*: 2D spectrum showing the full spatial range of the CCD. The individual spectra of stars are seen as the horizontal lines on the CCD. *Bottom*: The 1D spectrum of the GC was obtained by summing the rows of the CCD out to a defined background level. An interpolation across the CCD gaps was performed for this spectrum. The prominent absorption features in the spectrum are indicated.

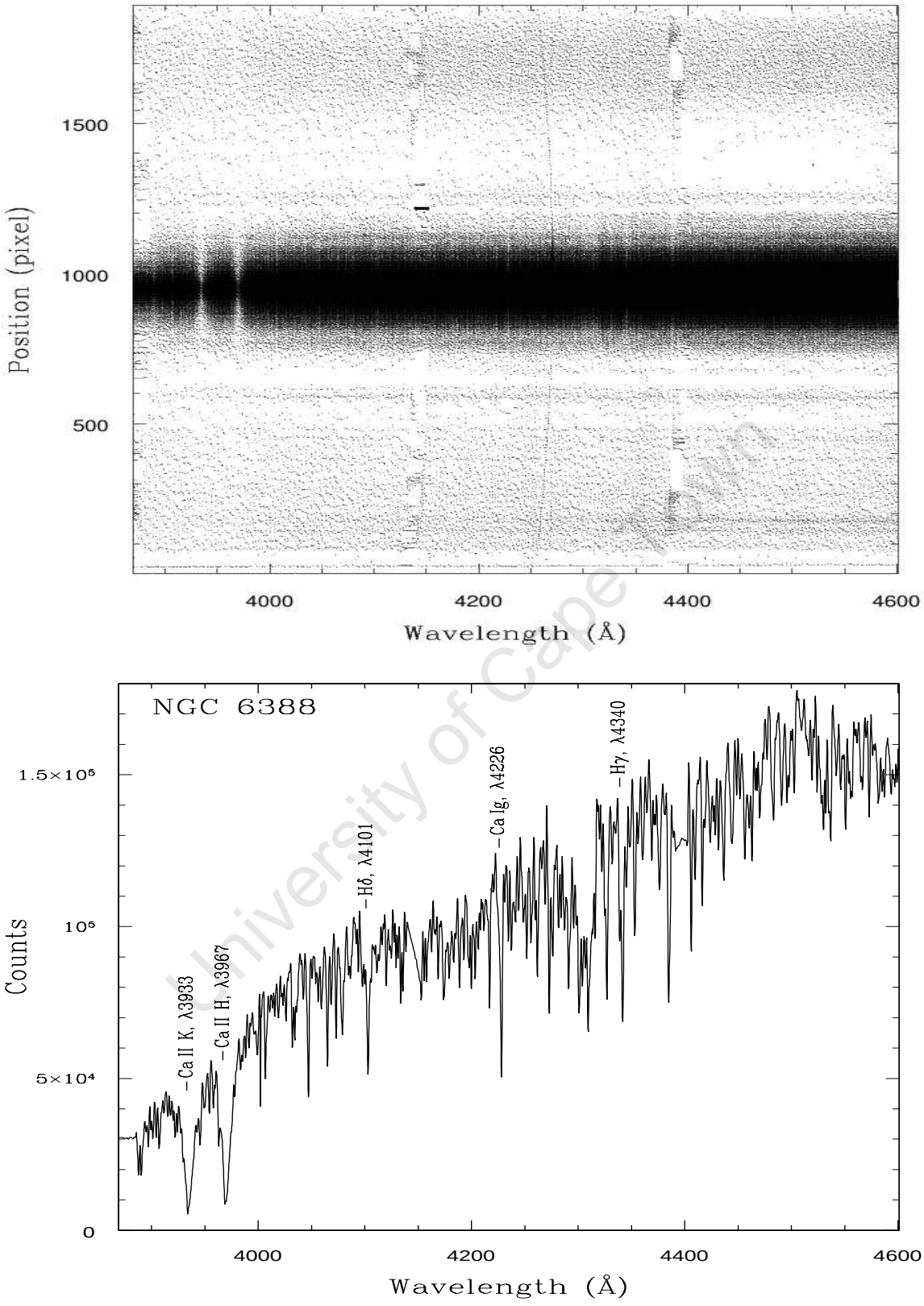

Figure E.6 SALT/RSS spectrum of NGC 6388. The spectrum corresponds to an 15-minute exposure. See caption for Fig. E.5.

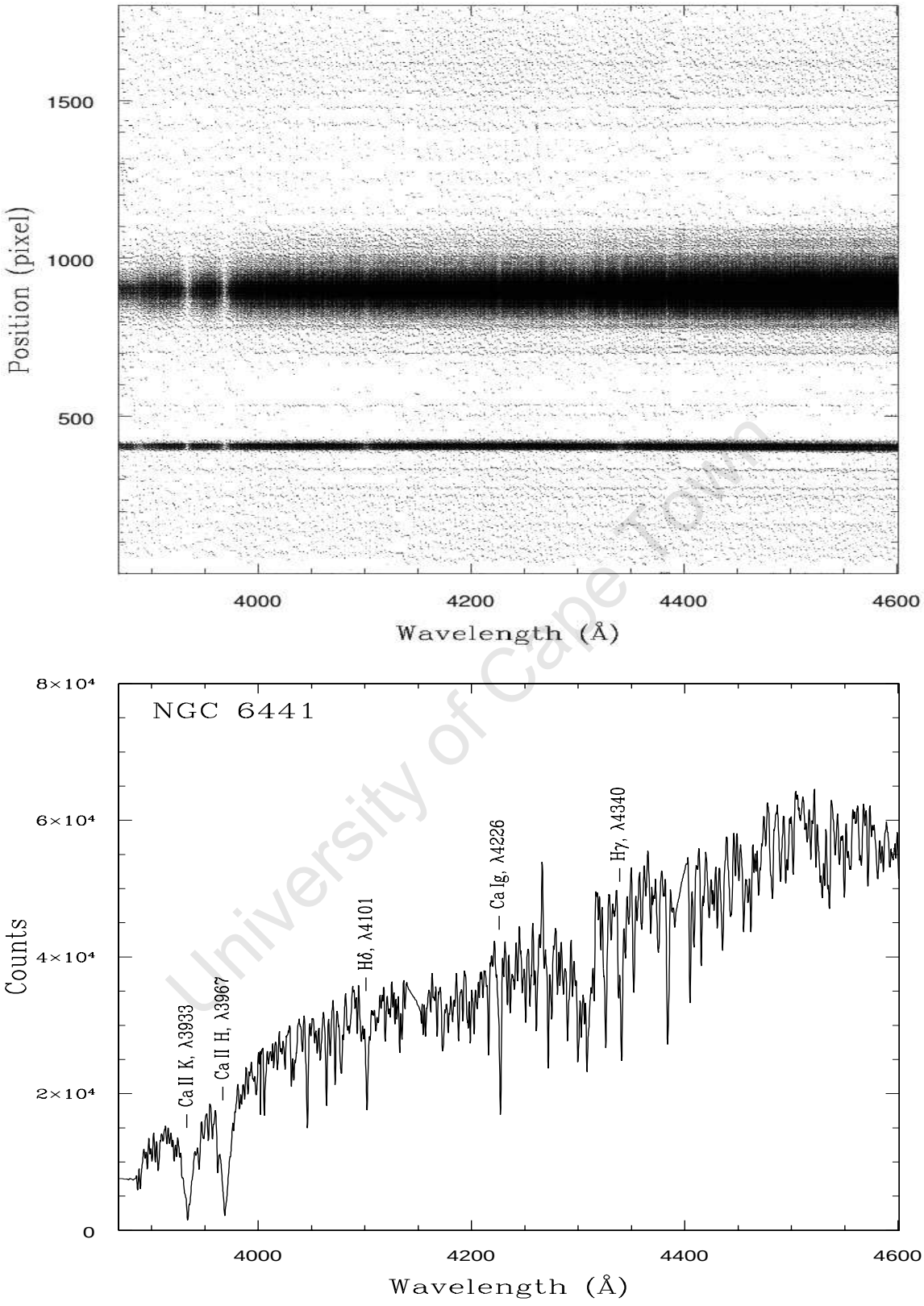

Figure E.7 SALT/RSS spectrum of NGC 6441. The spectrum corresponds to an 10-minute exposure. See caption for Fig. E.5. The spectrum seen at position $\sim$ 400 pixel corresponds to a bright foreground star.

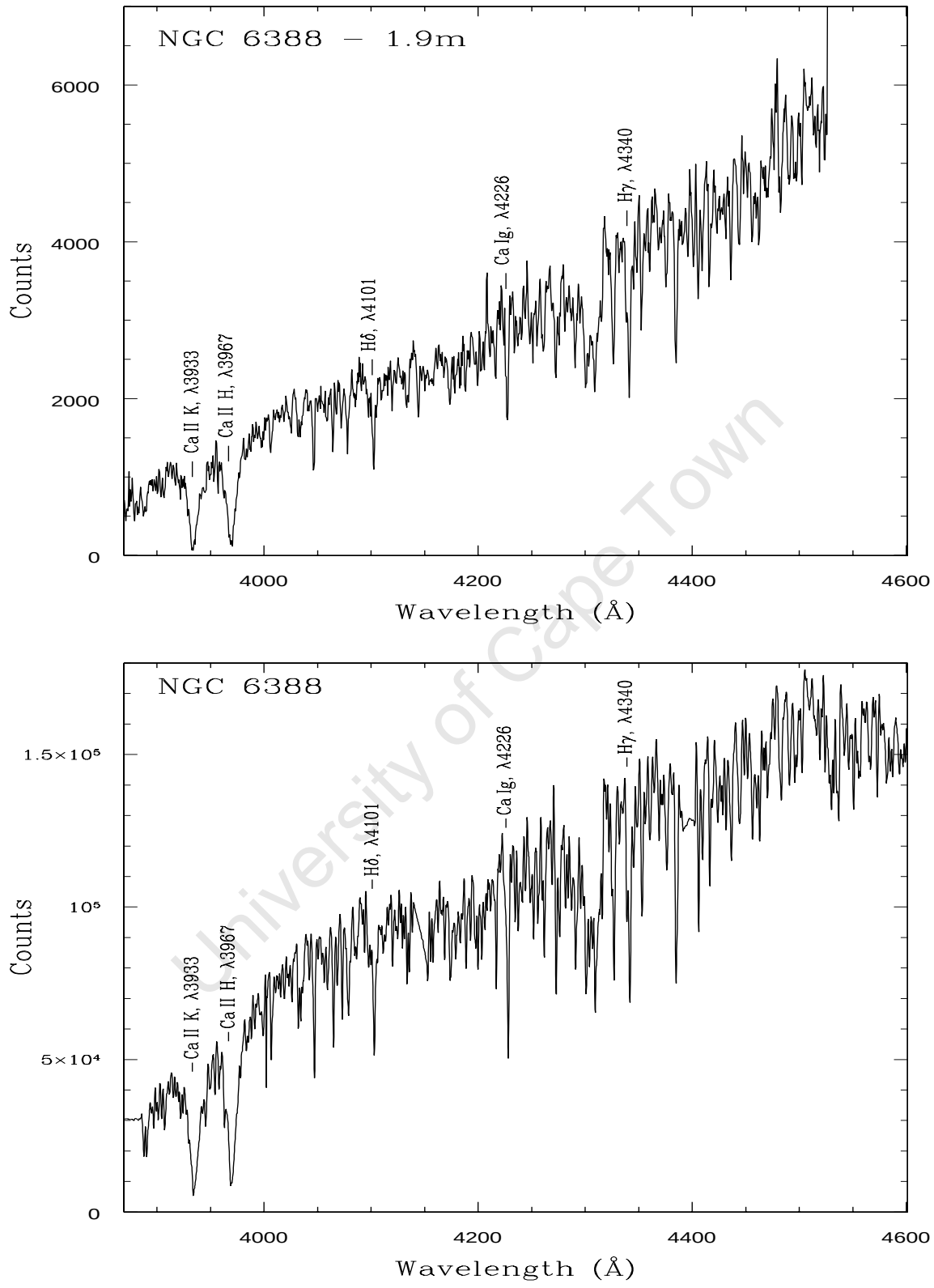

Figure E.8 Comparison of the 1D spectra of NGC 6388 obtained with the 1.9m (*top*) and SALT (*bottom*) telescopes. The 1.9m spectrum corresponds to a 20-minute exposure while the SALT/RSS exposure corresponds to a 15-minute exposure. The SALT/RSS spectrum has two times higher spectral resolution than that obtained with the 1.9m. The prominent absorption lines in the GC spectra are indicated.

Table E.5. Measured radial velocities of template stars

Date	Template	Type	Exp (s)	Radial Velocities $v_{\rm rad}$ Literature[1] (km s^{-1})	Doppler shift[2] (km s^{-1})
SALT Data:					
2006 Jun 09	HD 182160	K0 III	20	-8.1	-24.8±11.4
	HD 182160	K0 III	40	-8.1	-10.9±13.5
	HD 148760	K1 III	5	39.4±0.5	21.6±15.0
	HD 148760	K1 III	5	39.4±0.5	28.2±15.2
	HD 158630	G2 V	5	-26.4±0.7	12.0±3.7
	HD 158630	G2 V	5	-26.4±0.7	0.5±4.6
2006 Jun 10	HD 73678	G0 III	60	8.0	-3.5±8.8
	HD 85250	K0 III	30	6.3±0.1	4.6±7.1
2006 Aug 06	HD 196857	K0 III	20	-3.7	4.0±7.5
2006 Aug 10	HD 169236	K0 III	10	4.1±0.1	2.6±5.1
	HD 158630	G2 V	10	-26.4±0.7	-21.6±8.2
2006 Aug 12	HD 169236	K0 III	20	4.1±0.1	3.2±10.0
	HD 158630	G2 V	2	-26.4±0.7	-24.1±4.8
1.9m Data:					
2007 Mar 15	HD 169236	K0 III	120	4.1±0.1	17.9±13.2
	HD 158630	G2 V	120	-26.4±0.7	-61.4±7.1

Note. — (1) Literature values of the radial velocity are taken from Kharchenko et al. (2004). (2) The mean radial velocity derived from the Ca II K, H($\lambda\lambda$3933,3968), Fe I(λ4046), Hδ(λ4101), Ca Ig(λ4226) and Hγ(λ4340) lines using the Doppler shift technique. The errors in the radial velocities were calculated as the standard deviation of the mean.

representation of the combined light from the stellar population of the GC. The radial velocity of the individual GC exposures was determined using the FXCOR task in IRAF. The GC spectra were cross-correlated with each of the stellar templates obtained during the observational sequence (see Table E.2). The entire wavelength range spanned by the three CCDs (3870–4607Å) was used in performing the cross-correlation analysis. The CCD gaps shown in Figs. E.2–E.4 were however masked before carrying out the cross-correlation of these spectra. The radial velocities of the individual GC exposures are listed in Tables E.6 and E.7 for the 1.9m and SALT/RSS data, respectively. The literature values of the radial velocity for the GCs (Harris 1996) are also listed. Table E.6 shows a good agreement ($\lesssim 1\sigma$) between the measured and literature value of the radial velocity for the NGC 6388 spectra obtained with the 1.9m telescope. Additionally, the stability of the telescope is illustrated by the overlapping velocities derived from the different exposures. The velocities determined using the G2 V template show slightly better agreement with the literature value of the radial velocity.

The radial velocities derived from the SALT/RSS spectra are listed in Table E.7. For these spectra, a good agreement (within $\sim 2\sigma$) between the measured and literature values of the radial velocity is obtained for NGC 6715, NGC 2808 and NGC 6864. The K0 III stars were found to be the best matching templates for these spectra. A large deviation of up to $\Delta v_{\odot} \sim 30$km s^{-1} is seen in the velocities derived for NGC 6266. Neither the K1 III or G2 V template provide a good match to the spectrum of this GC which results in the large scatter in the radial velocities. The spectrum of NGC 6388 is classified as G2 type (Harris 1996). Subsequently, the G2 V star is the best matching template for this GC. The G2 V star is also seen to be the best matching template for the NGC 6388 spectra obtained from the 1.9m telescope (Table E.6). For most nights, considerable scatter is seen in the velocities obtained from consecutive GC exposures. This is evident for NGC 6441 for which the derived radial velocities vary by $\Delta v_{\odot} \sim 18$km s^{-1} over the course of five exposures (corresponding to 50 minutes). The variations in the radial velocities from one exposure to the next persist even though the wavelength calibrations were performed with the comparison lamp exposure closest in time to the GC exposure. These results show that the SALT/RSS instrument has not maintained the stability required for the determination of high-precision kinematics during its testing phase. This remains one of the major issues that will need to be investigated once the SALT telescope comes online again.

The derived radial velocities were used to shift the individual 2D GC spectra to a zero velocity scale. The final GC spectrum was formed by median combining the different exposures. The kinematics of the GCs were determined from the resulting spectra.

Table E.6. Radial velocity of globular cluster NGC 6388: 1.9m telescope

Date (1)	GC (2)	Type (3)	Exp (s) (4)	Template (5)	Type (6)	Exp ID (7)	Radial Velocity Literature (km s^{-1}) (8)	Radial Velocity Measured (km s^{-1}) (9)
2007 Mar 15	NGC 6388	G2	1200	HD 158630	G2 V	1	$+81.2 \pm 1.2$	$+78.6 \pm 4.2$
			1200			2		$+78.1 \pm 4.1$
			1200			3		$+78.5 \pm 8.0$
			1200	HD 169236	K0 III	1	$+81.2 \pm 1.2$	$+75.1 \pm 4.6$
			1200			2		$+74.9 \pm 4.6$
			1200			3		$+75.6 \pm 8.1$

Note. — Explanation of columns: (1) Date of observation; (2) GC observation; (3) Spectral type of globular cluster (Harris 1996); (4) Exposure time of individual GC exposures; (5) Template star used for the Fourier cross-correlation analysis. Radial velocities of template stars are listed in Table E.5; (6) Spectral type of template star (Kharchenko et al. 2004); (7) Galaxy exposure reference number; (8) Literature value of the GC radial velocity (Harris 1996); (9) Measured radial velocity for the GC exposure.

Table E.7. Radial velocities of six Galactic globular clusters: SALT/RSS data

Date (1)	GC (2)	Type (3)	Exp (s) (4)	Template (5)	Type (6)	Exp ID (7)	Radial Velocity Literature (km s^{-1}) (8)	Radial Velocity Measured (km s^{-1}) (9)
2006 Jun 09	NGC 6715	F7/F8	550	HD 182160	K0 III	1	$+141.9 \pm 0.5$	$+145.2 \pm 5.9$
			550			2		$+151.0 \pm 5.7$
			550	HD 182160	K0 III	1	$+141.9 \pm 0.5$	$+142.9 \pm 6.1$
			550			2		$+148.2 \pm 5.7$
	NGC 6266	F9	700	HD 148760	K1 III	1	-68.0 ± 3.2	-95.7 ± 5.7
			700			1		-94.4 ± 6.0
			700	HD 158630	G2 V	1		-99.0 ± 3.9
			700			1		-98.3 ± 3.6
2006 Jun 10	NGC 2808	–	600	HD 73678	G0 III	1	$+99.7 \pm 2.9$	$+113.5 \pm 5.4$
			600			2		$+118.8 \pm 4.6$
			600			3		$+121.4 \pm 4.5$
			600	HD 85250	K0 III	1	$+99.7 \pm 2.9$	$+103.3 \pm 4.9$
			600			2		$+107.9 \pm 4.1$
			600			3		$+109.9 \pm 3.9$
2006 Aug 06	NGC 6864	F9	600	HD 196857	K0 III	1	-189.3 ± 3.6	-184.4 ± 4.3
			600			2		-181.5 ± 4.3
			600			3		-185.4 ± 4.1
2006 Aug 10	NGC 6388	G2	900	HD 158630	G2 V	1	$+81.2 \pm 1.2$	$+78.1 \pm 2.8$
			900			2		$+82.6 \pm 2.9$
			900			3		$+85.3 \pm 2.7$
			900			4		$+89.5 \pm 2.6$
			900	HD 169236	K0 III	1	$+81.2 \pm 1.2$	$+70.7 \pm 2.4$
			900			2		$+75.9 \pm 2.4$
			900			3		$+79.2 \pm 2.2$
			900			4		$+83.9 \pm 2.3$
2006 Aug 12	NGC 6441	G2	600	HD 158630	G2 V	1	$+18.3 \pm 1.7$	$+6.0 \pm 3.2$
			600			2		$+9.9 \pm 3.2$
			600			3		$+12.4 \pm 3.2$
			600			4		$+18.3 \pm 2.9$
			600			5		$+22.2 \pm 2.7$
			600	HD 169236	K0 III	1	$+18.3 \pm 1.7$	$+2.1 \pm 2.2$
			600			2		$+6.2 \pm 2.4$

Table E.7 (cont'd)

Date (1)	GC (2)	Type (3)	Exp (s) (4)	Template (5)	Type (6)	Exp ID (7)	Radial Velocity Literature (km s^{-1}) (8)	Radial Velocity Measured (km s^{-1}) (9)
			600			3		$+9.4 \pm 2.3$
			600			4		$+15.9 \pm 2.1$
			600			5		$+20.6 \pm 2.2$

Note. — Explanation of columns: (1) Date of observation; (2) GC observation; (3) Spectral type of globular cluster (Harris 1996); (4) Exposure time of individual GC exposures; (5) Template star used for the Fourier cross-correlation analysis. Radial velocities of template stars are listed in Table E.5; (6) Spectral type of template star (Kharchenko et al. 2004); (7) Galaxy exposure reference number; (8) Literature value of the GC radial velocity (Harris 1996); (9) Measured radial velocity for the GC exposure.

E.6 Velocity Profile Modeling

The mean velocity v and velocity dispersion σ profiles of the GCs were determined using the Gauss-Hermite pixel fitting software of van der Marel (1994). The method used for deriving the kinematic profiles is similar to that carried out for the galaxy NGC 59 which is described in detail in Chapter 3 (section 3.5.5). The kinematics of the GCs were determined using the wavelength range covered by the first (3882–4136Å) and second CCDs (4160–4387Å). The spectra were binned so that each aperture has a minimum S/N ratio of ~ 30. The mean velocity and velocity dispersion were determined from the different apertures which gives the kinematical profile of the GC. The GC spectra were cross-correlated with each of the template star spectra acquired within the observational sequence (Table E.2). The mean velocity and velocity dispersion profiles of the individual GCs are shown in Figs. E.9–E.14. The velocity profiles obtained from the different stellar templates are displayed in these figures. The center of the GC was determined by fitting a Gaussian distribution to the spatial profile of the cluster. The center of the Gaussian defines the GC center which is indicated by the vertical line in Figs. E.9–E.14.

The mean velocity profiles of the GCs show that these stellar systems exhibit little or no rotation. The kinematics of individual stars results in the scatter in velocity ($\Delta v \gtrsim$ 5km s^{-1}) of the outermost data points. A series of individual stellar spectra is seen in the 2D spectrum of NGC 6266 (Fig. E.2). The velocity profile of this GC is therefore dominated by the kinematics of individual bright stars in the spectrum. A similar effect is observed in the velocity profile of NGC 2808 which shows deviation from a flat rotation curve. In

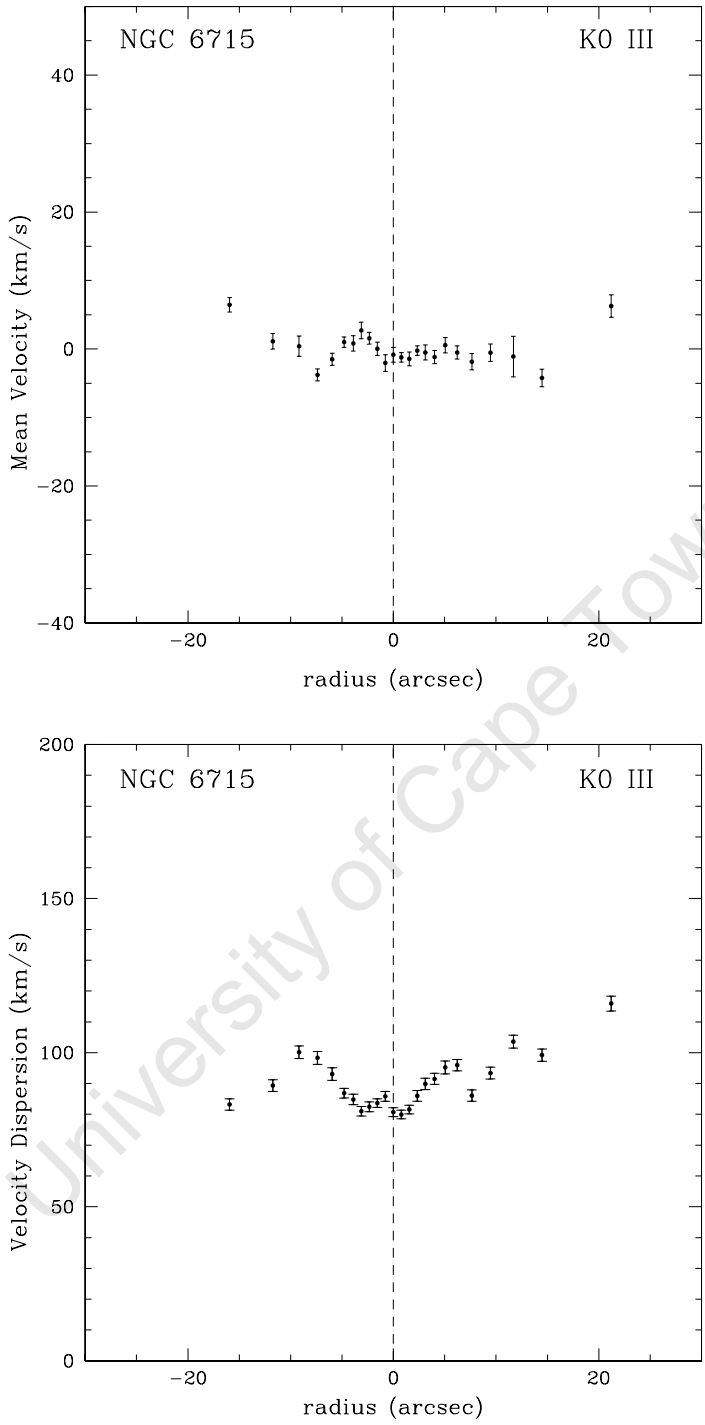

Figure E.9 Mean velocity (*top*) and velocity dispersion (*bottom*) profiles of NGC 6715. The spectral type of the template star used in modeling the line of sight velocity distribution of the GC is indicated in the right corner.

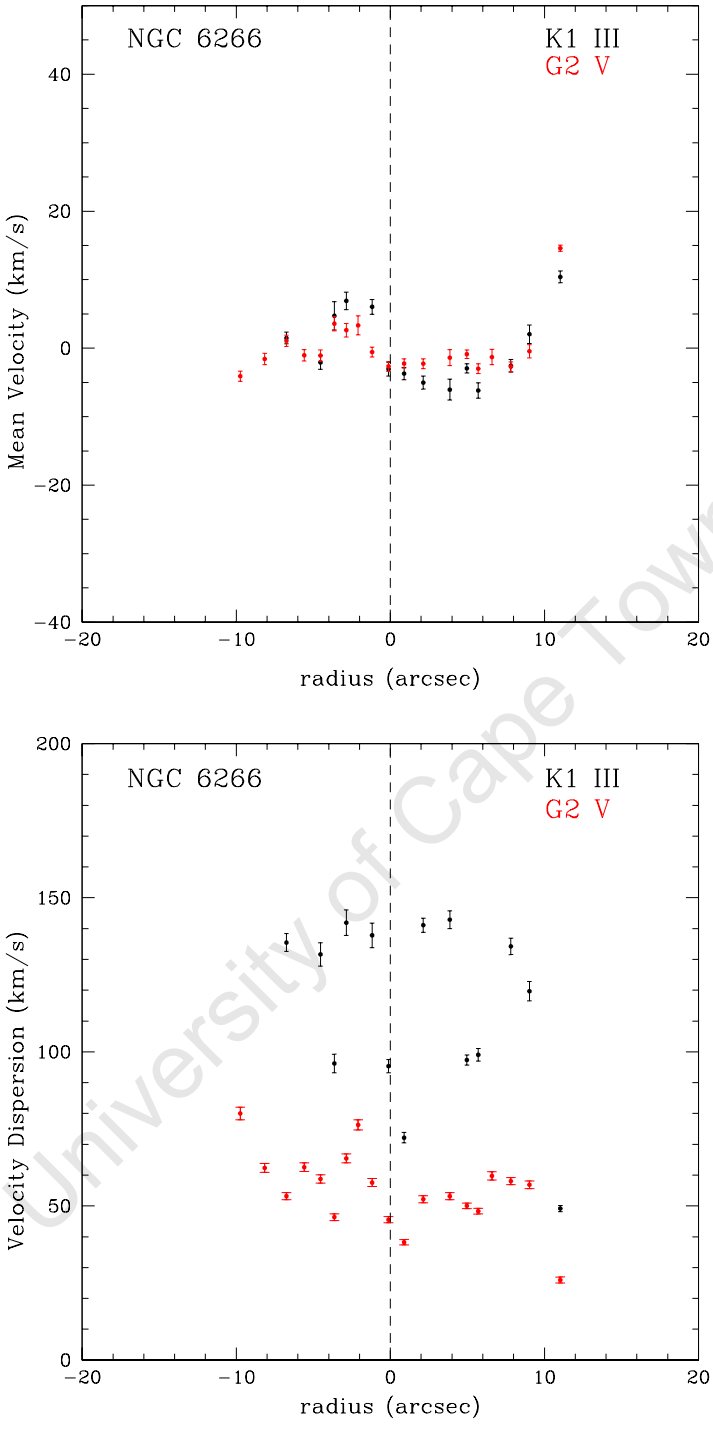

Figure E.10 Mean velocity (*top*) and velocity dispersion (*bottom*) profiles of NGC 6266. The spectral type of the template star used in modeling the line of sight velocity distribution of the GC is indicated in the right corner. Black points correspond to the kinematic profiles derived from the K1 III template whereas the red points correspond to the G2 V template.

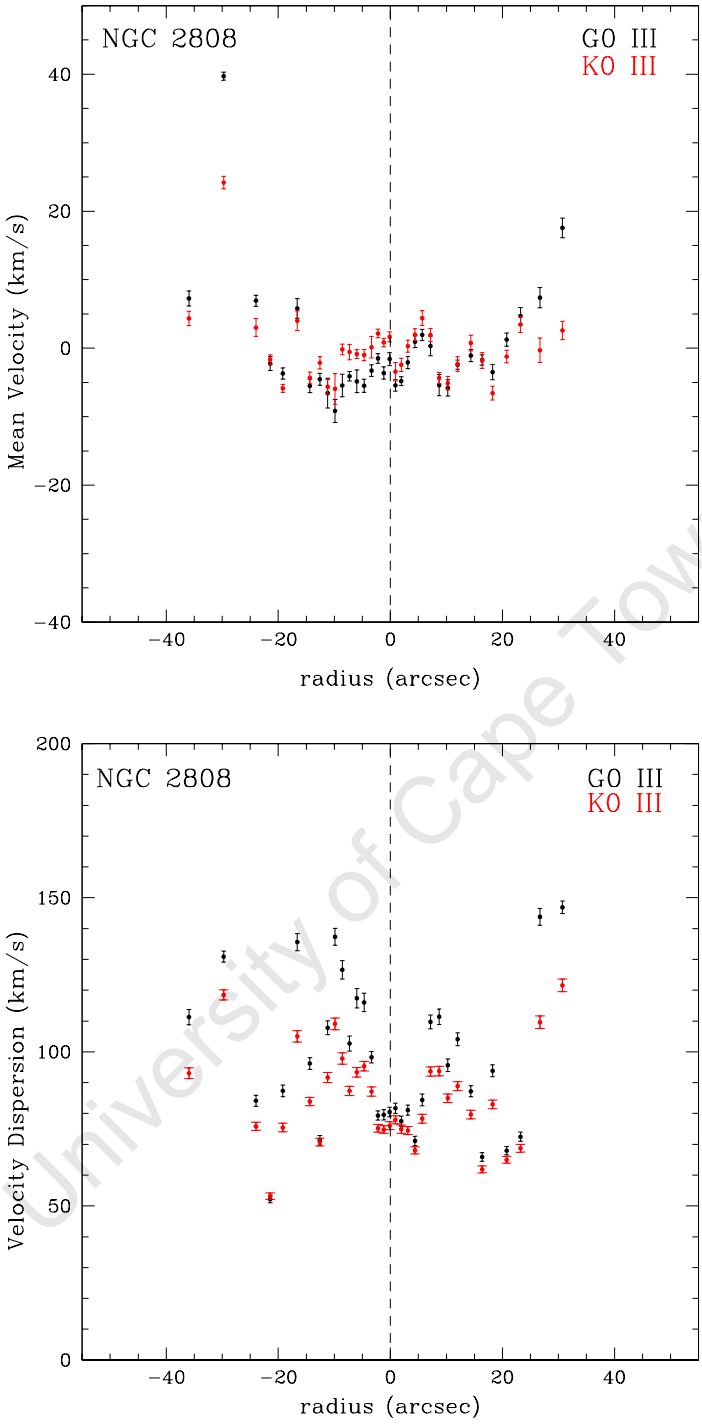

Figure E.11 Mean velocity (*top*) and velocity dispersion (*bottom*) profiles of NGC 2808. The spectral type of the template star used in modeling the line of sight velocity distribution of the GC is indicated in the right corner. Black points correspond to the kinematic profiles derived from the G0 III template whereas the red points correspond to the K0 III template.

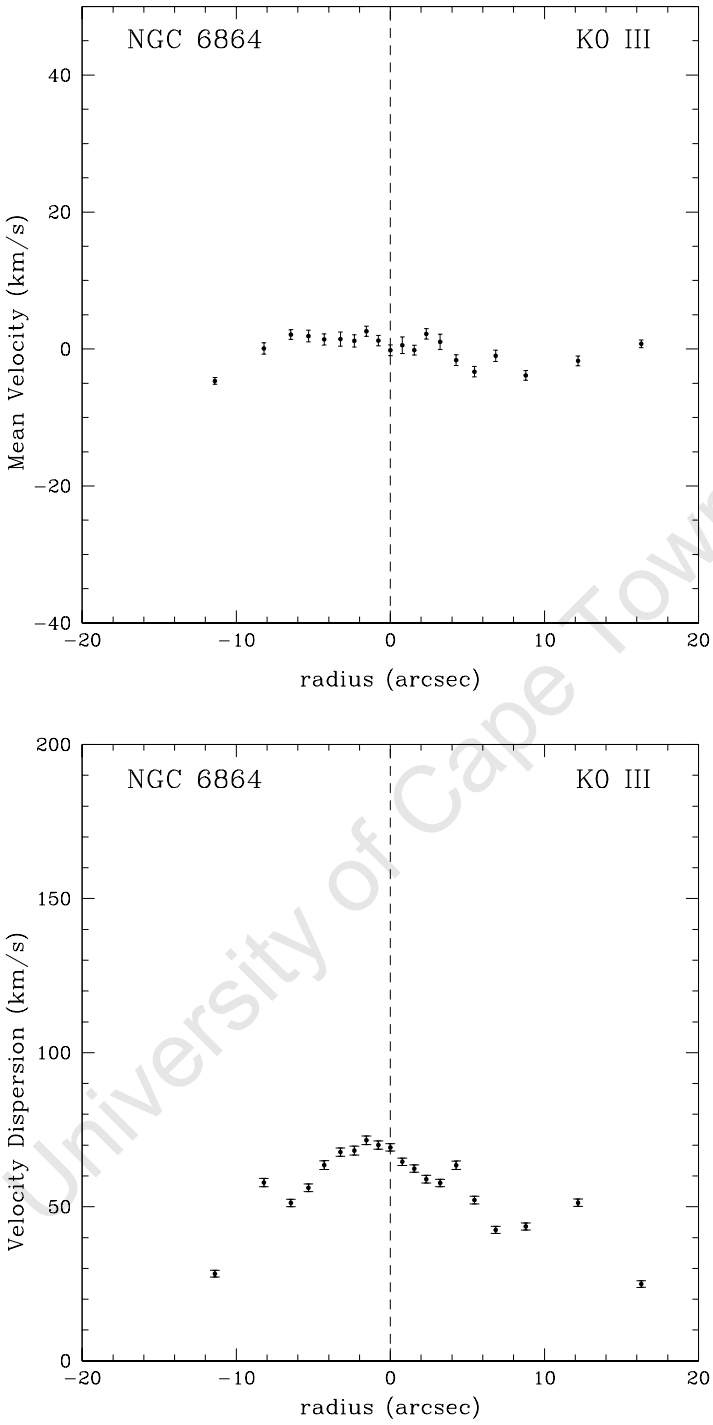

Figure E.12 Mean velocity (*top*) and velocity dispersion (*bottom*) profiles of NGC 6864. The spectral type of the template star used in modeling the line of sight velocity distribution of the GC is indicated in the right corner.

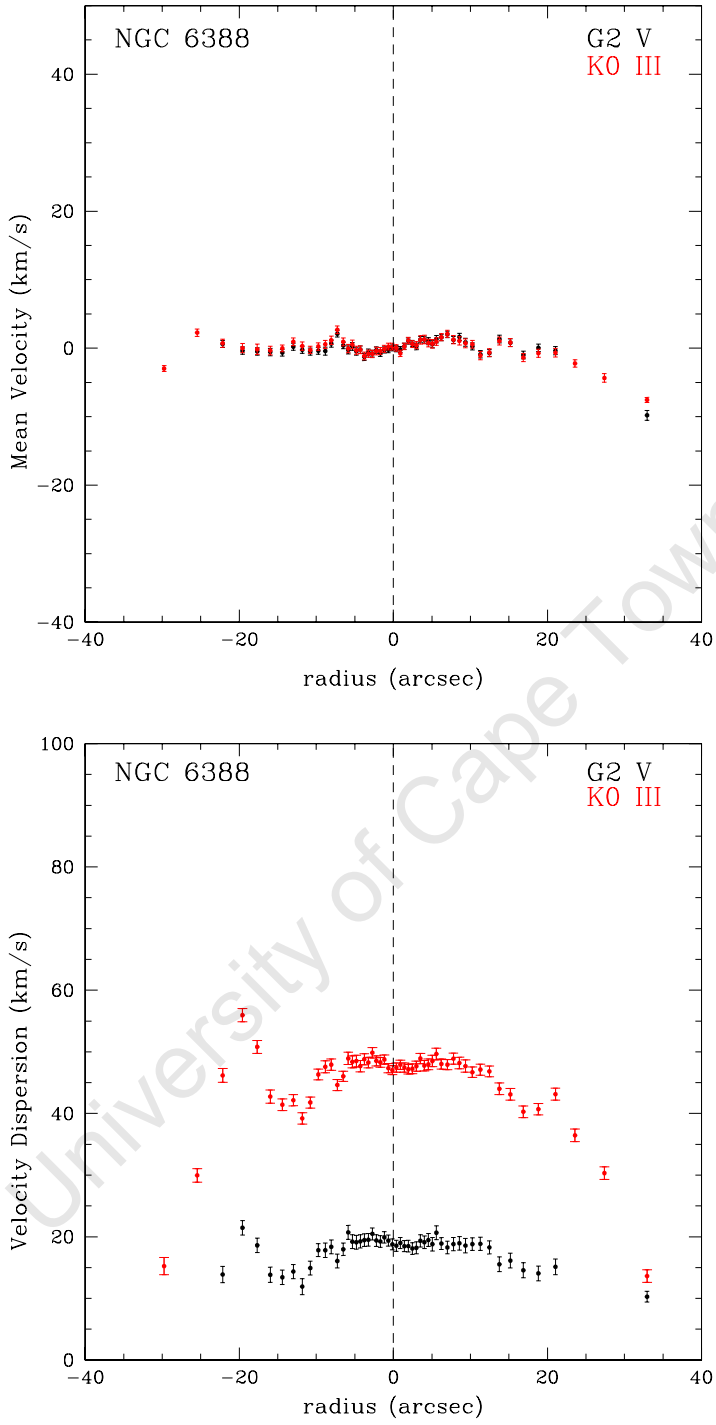

Figure E.13 Mean velocity (*top*) and velocity dispersion (*bottom*) profiles of NGC 6388. The spectral type of the template star used in modeling the line of sight velocity distribution of the GC is indicated in the right corner. Black points correspond to the kinematic profiles derived from the G2 V template whereas the red points correspond to the K0 III template.

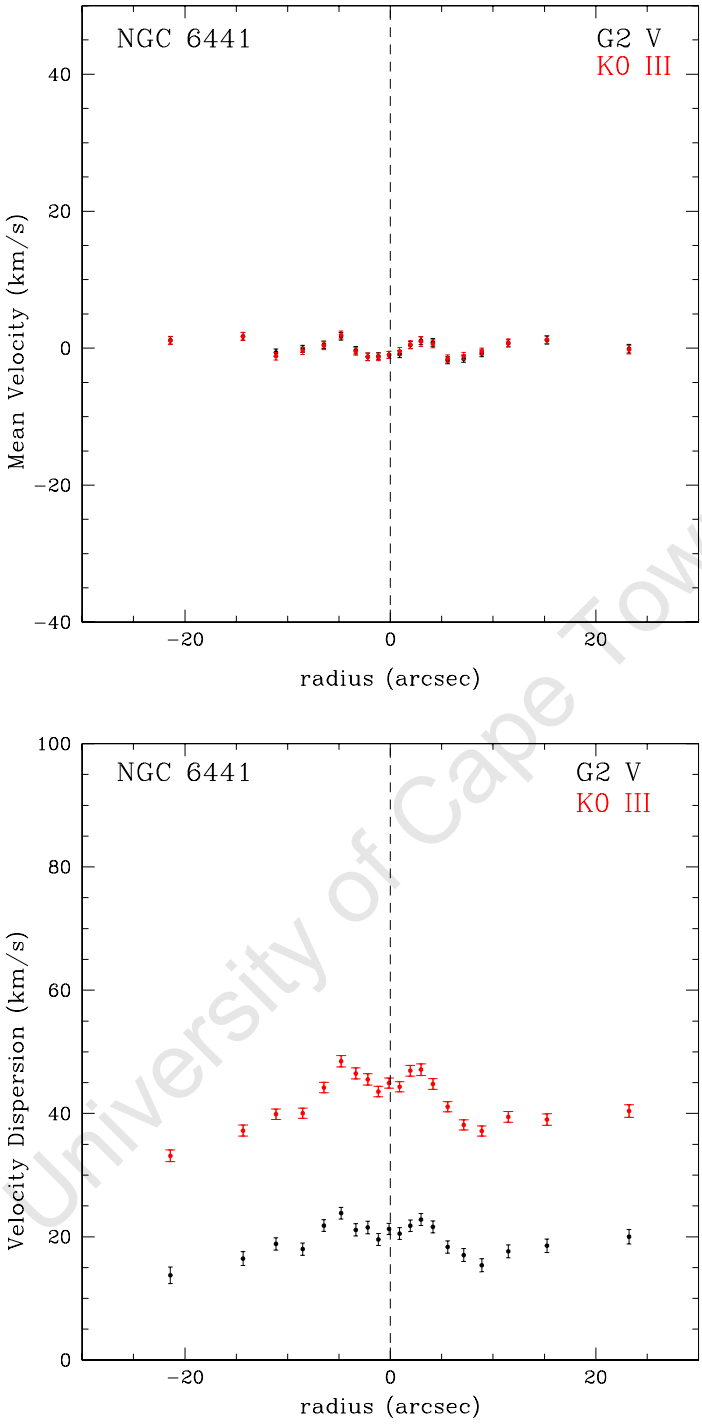

Figure E.14 Mean velocity (*top*) and velocity dispersion (*bottom*) profiles of NGC 6441. The spectral type of the template star used in modeling the line of sight velocity distribution of the GC is indicated in the right corner. Black points correspond to the kinematic profiles derived from the G2 V template whereas the red points correspond to the K0 III template.

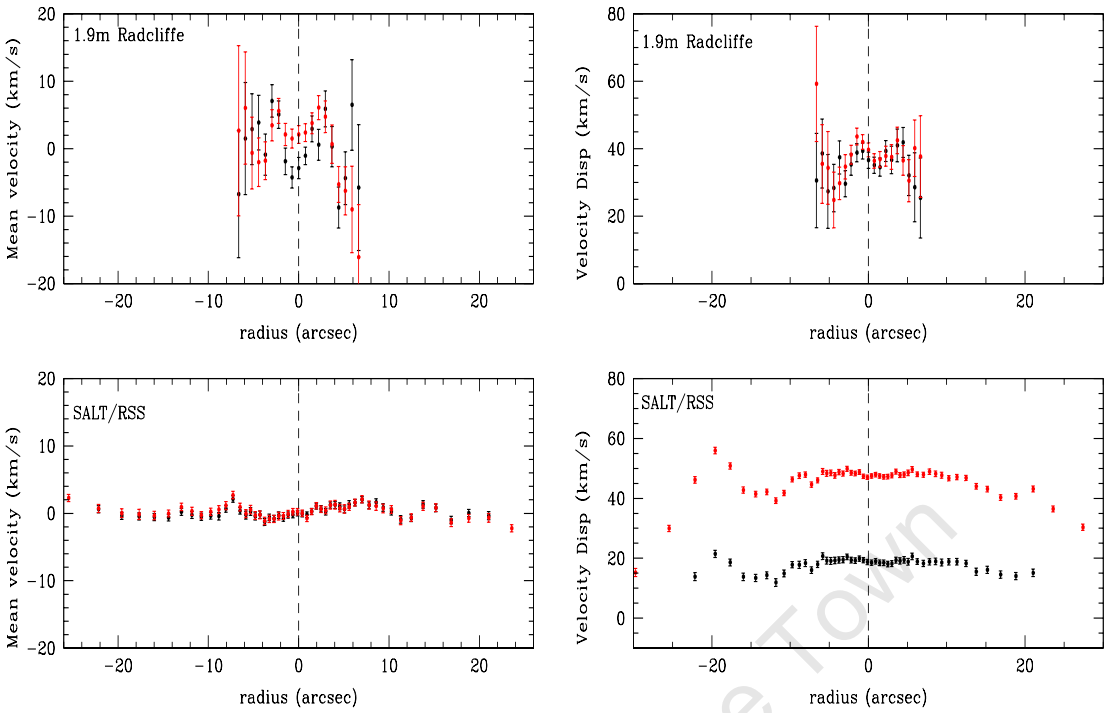

Figure E.15 Mean velocity (*left*) and velocity dispersion (*right*) profiles of NGC 6388. The kinematic profiles derived from the 1.9m and SALT/RSS spectra are shown in the top and bottom panels, respectively. The profiles obtained from the K0 III and G2 V stellar templates are plotted in red and black, respectively.

addition, scattered velocity dispersion profiles are seen for the GCs NGC 6266 and NGC 2808. The scattered dispersion profiles are detected using both stellar templates where the K-giant gives the higher dispersion. For the GCs NGC 6388 and NGC 6441, a systematic offset of $\Delta\sigma \sim 25$km s^{-1} is detected in the dispersion profiles obtained from the G2 V and K0 III templates. The higher velocity dispersions of $\sigma \gtrsim 30$km s^{-1} were determined using the K0 III template. The velocity dispersions from the K0 III template lie just above the instrumental resolution limit of $\sigma_{\rm instr} \sim 35$km s^{-1} for these observations. However, the dispersion profile shapes obtained from both stellar templates are found to be very similar. The source of this systematic offset between the different stellar templates is not currently understood. A slight decrease in the velocity dispersion near the GC center is detected for NGC 6715, NGC 6388 and NGC 6441. NGC 6864 is the only GC in our sample showing an increase in the velocity dispersion towards the center. A maximum velocity dispersion of $\sigma_0 \sim 70$km s^{-1} is measured for this GC.

A comparison of the velocity profiles obtained for NGC 6388 from the 1.9m and SALT telescopes is displayed in Fig. E.15. Large errors of up to $\Delta v \sim 13$km s^{-1} are obtained for the velocity measurements from the 1.9m spectra. The large error in the velocities is a direct result of the lower S/N levels of the 1.9m spectra. The kinematic profiles from the SALT/RSS

spectra are determined out to twice the radius of that seen for the 1.9m spectra. The overall velocity profile shapes are more clearly seen in the extended kinematic profiles from the SALT/RSS spectra. However, the systematic offset in the velocity dispersion profiles from the different stellar templates is not detected in the resulting profiles from the 1.9m spectra. This suggests that the systematic offset in the velocity dispersion of the SALT/RSS spectra is an instrumental effect and not a consequence of the velocity profile modeling. The velocity dispersion profiles from the 1.9m spectra were found to lie above the instrumental resolution limit of $\sigma_{\rm instr} \sim 30$km s^{-1} for the observations. Again, a dip in the dispersion profile is detected near the GC center.

E.7 Conclusion

We have determined the kinematic profiles for six Galactic GCs from longslit spectra acquired with the SALT/RSS. The mean velocity profiles for the GCs show little or no rotation in these stellar systems. The GCs are known to have central velocity dispersions of $\sigma_0 \lesssim 20$km s^{-1} (see Table E.1). The narrower $1''$ slit of the SALT/RSS was found to give a resolving power of $R \sim 3620$ (or $\sigma_{\rm instr} \sim 35$km s^{-1}) in the blue wavelength range of 3882–4136Å. The resolution limit with the narrower $1''$ slit has proved to be insufficient for resolving velocity dispersions of $\sigma \lesssim 20$km s^{-1} typically observed for GC systems. The velocity dispersion profiles presented in section E.6 were found to lie near the resolution limit of the SALT/RSS observations. It is thus unclear whether these dispersion profiles for the GCs can be interpreted physically: in particular, what kind of motions of the stars are required to explain the dip in the velocity dispersion profile near the centers of NGC 6715, NGC 6388 and NGC 6441? These issues can only be further investigated by carrying out the longslit GC observations with a slit width narrower than $1''$, or by performing multi-object spectroscopy for individual stars. Exposures of a variety of template stars are needed to explore the degree of template mismatch in the GC observations.

Bibliography

Aller, H. L., 1984, Physics of Thermal Gaseous Nebulae, Dordrecht, Reidel

Andreon, S., 2002, A&A , 382, 495

Barazza, F. D., Binggeli, B. & Jerjen, H., 2002, A&A , 391, 823

Barth, A. J., Greene, J. E., & Ho, L. C., 2005, ApJL , 619, L151

Barth, A. J., Ho, L. C., Rutledge, R. E., & Sargent, W. L. W., 2004, ApJ , 607, 90

Baumgardt, H., Hut, P., Makino, J., McMillan, S., & Portegies Zwart, S., 2003, ApJL , 582, L21

Baumgardt, H., Makino, J., & Hut, P., 2005, ApJ , 620, 238

Baumgardt, H., Makino, J., Hut, P., McMillan, S., & Portegies Zwart, S., 2003, ApJL , 589, L25

Beaulieu, S. F., Freeman, K. C., Carignan, C., Lockman, F. J., & Jerjen, H., 2006, AJ , 131, 325

Bell, E. F. & de Jong, R. S., 2001, ApJ , 550, 212

Bell, E. F., McIntosh, D. H., Katz, N., & Weinberg, M. D, 2003, ApJS , 149, 289

Bender, R., Burstein, D., & Faber, S. M., 1992, ApJ , 399, 462

Bertola, F., & Capaccioli, M., 1975, ApJ , 200, 439

Bender, R., & Nieto, J.-L., 1990, A&A , 239, 97

Bender, R., Paquet, A., & Nieto, J.-L., 1991, A&A , 246, 349

Binggeli, B., & Cameron, L. M., 1993, A&AS , 98, 297

Binggeli, B., Tarenghi, M., & Sandage, A., 1990, A&A , 228, 42

Binney, J., 1978, MNRAS , 183, 501

Böker, T., Laine, S., van der Marel, R. P., Sarzi, M., Rix, H.-W., Ho, L. C., & Shields, J. C., 2002, AJ , 123, 1389

Bouchard, A, Carignan, C., & Staveley-Smith, L., 2006, AJ , 131, 2913

Bouchard, A., Jerjen, H., Da Costa, G. S., & Ott, J., 2005, AJ , 130, 2058

Bouchard, A., Jerjen, H., Da Costa, G. S., & Ott, J., 2007, AJ , 133, 261

Bouchard, A. and Da Costa, G. S. and Jerjen, H., 2009, AJ , 137, 3038

Brocklehurst, M. 1971, MNRAS , 153, 471

Broeils, A. H., & Rhee, M.-H., 1997, A&A , 324, 877

Bromley, J. M., Somerville, R. S., & Fabian, A. C., 2004, MNRAS , 350, 456

Buckley, D. A. H., Swart, G. P., & Meiring, J. G., 2006, SPIE, 6267,

Bullock, J. S., Kravtsov, A. V., & Weinberg, D. H., 2001, ApJ , 548, 33

Bureau, M., & Chung, A., 2006, MNRAS , 366, 182

Burgh, E. B., Nordsieck, K. H., Kobulnicky, H. A., Williams, T. B., O'Donoghue, D., Smith, M. P., & Percival, J. W., 2003, SPIE, 4841, 1463

Buta, R. J., & McCall, M. L., 1999, ApJS , 124, 33

Buzzoni, B., Delabre, B., Dekker, H., Dodorico, S., Enard, D., Focardi, P., Gustafsson, B., Nees, W., Paureau, J., & Reiss, R., 1984, Msngr, 38, 9

Byun, Y.-I., Grillmair, C. J., Faber, S. M., Ajhar, E. A., Dressler, A., Kormendy, J., Lauer, T. R., Richstone, D., & Tremaine, S., 1996, AJ , 111, 1889

Cairós, L. M., Caon, N., Papaderos, P., Noeske, K., Vílchez, J. M., Lorenzo, B. G., & Muñoz-Tuñón, C., 2003, ApJ , 593, 312

Caldwell, N., Armandroff, T. E., Seitzer, P., & Da Costa, G. S., 1992, AJ , 103, 840

Caldwell, N., & Bothun, G. D., 1987, AJ , 94, 1126

Caon, N., Capaccioli, M., & D'Onofrio, M., 1993, MNRAS , 265, 1013

Cattaneo, A., Haehnelt, M. G., & Rees, M. J., 1999, MNRAS , 308, 77

Chiboucas, K., Karachentsev, I. D., & Tully, R. B., 2009, AJ , 137, 3009

Chilingarian, I., 2008, arXiv e-prints, 0812.3272,

Chung, A., Koribalski, B., Bureau, M., & van Gorkom, J. H., 2006, MNRAS , 370, 1565

Cole, S., Lacey, C. G., Baugh, C. M., & Frenk, C. S., 2000, MNRAS , 319, 168

Colina, L., Bohlin, R. C., & Castelli, F., 1996, AJ , 112, 307

Conselice, C. J., O'Neil, K., Gallagher, J. S., & Wyse, R. F. G., 2003, ApJ , 591, 167

Corsini, E. M., Aguerri, J. A. L., Debattista, V. P., Pizzella, A., Barazza, F. D., & Jerjen, H., 2007, ApJL , 659, L121

Côté, S., Freeman, K. C., Carignan, C., & Quinn, P. J., 1997, AJ , 114, 1313

Côté, P., Piatek, S., Ferrarese, L., Jordán, A., Merritt, D., Peng, E. W., Haşegan, M., Blakeslee, J. P., Mei, S., West, M. J., Milosavljević, M., & Tonry, J. L., 2006, ApJS , 165, 57

Côté, P., Ferrarese, L., Jordán, A., Blakeslee, J. P., Chen, C.-W., Infante, L., Merritt, D., Mei, S., Peng, E. W., Tonry, J. L., West, A. A., & West, M. J., 2007, ApJ , 671, 1456

Couture, J., Harris, W. E., & Allwright, J. W. B., 1990, ApJS , 73, 671

da Costa, L. N., Willmer, C. N. A., Pellegrini, P. S., Chaves, O. L., Rité, C., Maia, M. A. G., Geller, M. J., Latham, D. W., Kurtz, M. J., Huchra, J. P., Ramella, M., Fairall, A. P., Smith, C., & Lípari, S., 1998, AJ , 116, 1

Davidge, T. J., 1998, ApJ , 497, 650

de Jong, R. S., 1996, A&A , 313, 377

Dekel, A., & Silk, J., 1986, ApJ , 303, 39

De Rijcke, S., Dejonghe, H., Zeilinger, W. W., & Hau, G. K. T., 2001, ApJL , 559, L21

De Rijcke, S., Dejonghe, H., Zeilinger, W. W., & Hau, G. K. T., 2003, A&A , 400, 119

De Rijcke, S., Dejonghe, H., Zeilinger, W. W., & Hau, G. K. T., 2004, A&A , 426, 53

de Vaucouleurs, G., 1948, Annales d'Astrophysique, 11, 247

Djorgovski, S., 1993, "Physical Parameters of Galactic Globular Clusters", ed. Djorgovski, S. G. & Meylan, G., Astronomical Society of the Pacific Conference Series, 50, 373

Durrell, P. R., 1997, AJ , 113, 531

Durrell, P. R., McLaughlin, D. E., Harris, W. E., & Hanes, D. A., 1996, ApJ , 463, 543

Erwin, P., Graham, A. W., & Caon, N., 2004, in Coevolution of Black Holes and Galaxies, ed. L. C. Ho (Cambridge: Cambridge Univ. Press), 264

ESO-MIDAS User's Guide, 1998, Volume A

Evans, N. W., Wilkinson, M. I., Kleyna, J. T., Read, J. I., & Gilmore, G., 2005, in IAU Colloq. 198, Near-fields cosmology with dwarf elliptical galaxies, eds. Jerjen, H. and Binggeli, B., 60

Faber, S. M., Tremaine, S., Ajhar, E. A., Byun, Y.-I., Dressler, A., Gebhardt, K., Grillmair, C., Kormendy, J., Lauer, T. R., & Richstone, D., 1997, AJ , 114, 1771

Ferguson, H. C., & Binggeli, B., 1994, A&ARv , 6, 67

Ferrarese, L., 2002, ApJ , 578, 90

Ferrarese, L., Côté, P., Jordán, A., Peng, E. W., Blakeslee, J. P., Piatek, S., Mei, S., Merritt, D., Milosavljević, M., Tonry, J. L., & West, M. J., 2006, ApJS , 164, 334

Ferrarese, L., & Ford, H., 2005, Space Science Reviews, 116, 523

Ferrarese, L., & Merritt, D., 2000, ApJL , 539, L9

Ferrarese, L., Pogge, R. W., Peterson, B. M., Merritt, D., Wandel, A., & Joseph, C. L., 2001, ApJL , 555, L79

Filippenko, A. V., & Ho, L. C., 2003, ApJL , 588, L13

Galaz, G., Dalcanton, J. J., Infante, L., & Treister, E., 2002, AJ , 124, 1360

Garnett, D.R. 1990, ApJ , 363, 142

Garnett, D.R. 1992, AJ , 103, 1330

Gavazzi, G., Boselli, A., Donati, A., Franzetti, P., & Scodeggio, M., 2003, A&A , 400, 451

Gebhardt, K., Bender, R., Bower, G., Dressler, A., Faber, S. M., Filippenko, A. V., Green, R., Grillmair, C., Ho, L. C., Kormendy, J., Lauer, T. R., Magorrian, J., Pinkney, J., Richstone, D., Tremaine, S., 2000, ApJL , 539, L13

Gebhardt, K., Lauer, T. R., Kormendy, J., Pinkney, J., Bower, G. A., Green, R., Gull, T., Hutchings, J. B., Kaiser, M. E., Nelson, C. H., Richstone, D., & Weistrop, D., 2001, AJ , 122, 2469

Gebhardt, K., Pryor, C., O'Connell, R. D., Williams, T. B., & Hesser, J. E., 2000, AJ , 119, 1268

Gebhardt, K., Rich, R. M., & Ho, L. C., 2002, ApJL , 578, L41

Gebhardt, K., Rich, R. M., & Ho, L. C., 2005, ApJ , 634, 1093

Gebhardt, K., Richstone, D., Tremaine, S., Lauer, T. R., Bender, R., Bower, G., Dressler, A., Faber, S. M., Filippenko, A. V., Green, R., Grillmair, C., Ho, L. C., Kormendy, J., Magorrian, J., & Pinkney, J., 2003, ApJ , 583, 92

Geha, M., Guhathakurta, P., Rich, R. M., & Cooper, M. C., 2006, AJ , 131, 332

Geha, M., Guhathakurta, P., & van der Marel, R. P., 2002, AJ , 124, 3073

Geha, M., Guhathakurta, P., & van der Marel, R. P., 2003, AJ , 126, 1794

Geha, M., Guhathakurta, P., & van der Marel, R. P., 2005, AJ , 129, 2617

Gerssen, J., van der Marel, R. P., Gebhardt, K., Guhathakurta, P., Peterson, R. C., & Pryor, C., 2002, AJ , 124, 3270

Gerssen, J., van der Marel, R. P., Gebhardt, K., Guhathakurta, P., Peterson, R. C., & Pryor, C., 2003, AJ , 125, 376

Glass, I. S. & Nagata, T., 2000, Monthly Notes of the Astronomical Society of South Africa, 59, 110

Goerdt, T., Moore, B., Kazantzidis, S., Kaufmann, T., Macciò, A. V., & Stadel, J., 2008, MNRAS , 385, 2136

Graham, A. W., Erwin, P., Caon, N., & Trujillo, I., 2001, ApJL , 563, L11

Graham, A. W., Erwin, P., Trujillo, I., & Asensio Ramos, A., 2003, AJ , 125, 2951

Graham, A. W., & Guzmán, R., 2003, AJ , 125, 2936

Grebel, E. K., 2001, ApSSS , 277, 231

Grebel, E. K., 2005, in IAU Colloq. 198, Near-fields cosmology with dwarf elliptical galaxies, ed. Jerjen, H. and Binggeli, B., 1

Grebel, E. K., Gallagher, III, J. S., & Harbeck, D., 2003, AJ , 125, 1926

Greene, J. E., & Ho, L. C., 2004, ApJ , 610, 722

Harris, W. E., 1996, AJ , 112, 1487

Henry, R. B. C., Edmunds, M. G., & Köppen, J., 2000, ApJ , 541, 660

Hubble, E. P., 1926, ApJ , 64, 321

Izotov, Y.I., Stasińska, G., Meynet, G., Guseva, N.G., & Thuan, T.X., 2006, A&A , 448, 955

Izotov, Y.I., & Thuan, T.X., 1998, ApJ , 500, 188

Izotov, Y. I. & Thuan, T. X., 1999, ApJ , 511, 639

Izotov, Y.I., Thuan, T.X., & Lipovetsky, V.A., 1994, ApJ , 435, 647

Izotov, Y.I., Thuan, T.X., & Lipovetsky, V.A., 1997, ApJS , 108, 1

Jacobs, B. A., Rizzi, L., Tully, R. B., Shaya, E. J., Makarov, D. I., & Makarova, L., 2009, AJ , 138, 332

Jarrett, T. H., 2000, PASP , 112, 1008

Jarrett, T. H., Chester, T., Cutri, R., Schneider, S. E., & Huchra, J. P., 2003, AJ , 125, 525

Jerjen, H., & Binggeli, B., 1997, in ASP Conf. Ser. 116, The Nature of Elliptical Galaxies, eds. Arnaboldi, M., Da Costa, G. S., & Saha, P. (San Francisco: ASP), 239

Jerjen, H., Binggeli, B., & Barazza, F. D., 2004, AJ , 127, 771

Jerjen, H., Binggeli, B., & Freeman, K. C., 2000, AJ , 119, 593

Jerjen, H., Freeman, K. C., & Binggeli, B., 1998, AJ , 116, 2873

Jerjen, H., Freeman, K. C., & Binggeli, B., 2000, AJ , 119, 166

Jerjen, H., Kalnajs, A. & Binggeli, B., 2000, A&A , 358, 845

Jerjen, H., & Rejkuba, M., 2001, A&A , 371, 487

Jones, J. H. S., 1980, Monthly Notes of the Astronomical Society of South Africa, 39, 89

Jones, L. A. & Worthey, G., 1995, ApJL , 446, L31

Hanes, D. A. & Harris, W. E., 1986, ApJ , 304, 599

Held, E. V., 2005, in IAU Colloq. 198, Near-fields cosmology with dwarf elliptical galaxies, ed. Jerjen, H. and Binggeli, B., 11

Held, E. V., Mould, J. R., & de Zeeuw, P. T., 1990, AJ , 100, 415

Huchtmeier, W. K. Karachentsev, I. D., Karachentseva, V. E., & Ehle, M., 2000, A&AS , 141, 469

Karachentsev, I. D., Dolphin, A. E., Geisler, D., Grebel, E. K., Guhathakurta, P., Hodge, P. W., Karachentseva, V. E., Sarajedini, A., Seitzer, P., & Sharina, M. E., 2002, A&A , 383, 125

Karachentsev, I. D., Grebel, E. K., Sharina, M. E., Dolphin, A. E., Geisler, D., Guhathakurta, P., Hodge, P. W., Karachentseva, V. E., Sarajedini, A., & Seitzer, P., 2003, A&A , 404, 93

Karachentsev, I. D., Karachentseva, V. E., & Huchtmeier, W. K., 2001, A&A , 366, 428

Karachentsev, I. D., Karachentseva, V. E., Huchtmeier, W. K. & Makarov, D. I., 2004, AJ , 127, 2031

Karachentsev, I. D., Karachentseva, V. E., Suchkov, A. A., & Grebel, E. K., 2000, A&AS , 145, 415

Karachentsev, I. D., & Makarov, D. A., 1996, AJ , 111, 794

Karachentsev, I. D., Makarov, D. I., & Huchtmeier, W. K., 1999, A&AS , 139, 97

Karachentsev, I. D., Sharina, M. E., Dolphin, A. E., Grebel, E. K., Geisler, D., Guhathakurta, P., Hodge, P. W., Karachentseva, V. E., Sarajedini, A., & Seitzer, P., 2003, A&A , 398, 467

Karachentsev, I. D., Sharina, M. E., Grebel, E. K., Dolphin, A. E., Geisler, D., Guhathakurta, P., Hodge, P. W., Karachentseva, V. E., Sarajedini, A., & Seitzer, P., 2000, ApJ , 542, 128

Karachentsev, I. D., Sharina, M. E., Makarov, D. I., Dolphin, A. E., Grebel, E. K., Geisler, D., Guhathakurta, P., Hodge, P. W., Karachentseva, V. E., Sarajedini, A., & Seitzer, P., 2002, A&A , 389, 812

Karachentsev, I. D., Tully, R. B., Dolphin, A., Sharina, M., Makarova, L., Makarov, D., Sakai, S., Shaya, E. J., Kashibadze, O. G., Karachentseva, V., Rizzi, L., 2007, AJ , 133, 504

Karachentseva, V. E., & Karachentsev, I. D., 1998, A&AS , 127, 409

Karachentseva, V. E., & Karachentsev, I. D., 2000, A&AS , 146, 359

Karachentseva, V. E., Karachentsev, I. D., & Richter, G. M., 1999, A&AS , 135, 221

Karick, A. M., Drinkwater, M. J., & Gregg, M. D., 2003, MNRAS , 344, 188

Kassin, S. A., de Jong, R. S., & Pogge, R. W., 2006, ApJS , 162, 80

Kauffmann, G., White, S. D. M., & Guiderdoni, B., 1993, MNRAS , 264, 201

Kennicutt, Jr., R. C., Tamblyn, P., & Congdon, C. E., 1994, ApJ , 435, 22

Kharchenko, N.V., Piskunov, A.E., & Scholz, R.D., 2004, Astron. Nachr., 325, 439

King, I. R., 1966, AJ , 71, 64

Kinman, T. D., & Davidson, K., 1981, ApJ , 243, 127

Kirby, E., Jerjen, H., Ryder, S., & Driver, S., 2008, AJ , 136, 1866

Kleyna, J., Wilkinson, M. I., Evans, N. W., Gilmore, G., & Frayn, C., 2002, MNRAS , 330, 792

Kniazev, A.Y., Grebel, E.K., Pustilnik, S.A., Pramskij, A.G., Kniazeva, T.F., Prada, F., & Harbeck, D., 2004, AJ , 127, 704

Kniazev, A.Y., Grebel, E.K., Pustilnik, S.A., Pramskij, A.G., & Zucker, D., 2005, AJ , 130, 1558

Kniazev, A. Y., Pustilnik, S. A., Grebel, E. K., Lee, H., & Pramskij, A. G., 2004, ApJS , 153, 429

Kniazev, A.Y., Pustilnik, S.A., Ugryumov, A.V., & Kniazeva, T.F., 2000, Astronomy Letters, 26, 129

Kobulnicky, H. A., & Skillman, E. D., 1996, ApJ , 471, 211

Kobulnicky, H. A., Nordsieck, K. H., Burgh, E. B., Smith, M. P., Percival, J. W., Williams, T. B., & O'Donoghue, D., 2003, SPIE, 4841, 1634

Korn, G.A., & Korn, T.M., Mathematical Handbook for Scientists and Engineers, 2nd enlarged and revised edition, 1968, McGraw-Hill Book Company

Kormendy, J., 1985, ApJ , 295, 73

Kormendy, J., & Richstone, D., 1995, ARA&A , 33, 581

Kotze, J. P., A Deep Photometric Survey of the Abell Cluster S0423. A Pilot Study for the UCT SALT Supercluster Survey, MSc. Thesis, 2007, University of Cape Town

Kraan-Korteweg, R. C., & Tammann, G. A., 1979, Astronomische Nachrichten, 300, 181

Kraemer, S. B., Ho, L. C., Crenshaw, D. M., Shields, J. C., & Filippenko, A. V., 1999, ApJ , 520, 564

Kunth, D., & Östlin, G., 2000, A&ARv , 10, 1

Lacey, C. G., & Ostriker, J. P., 1985, ApJ , 299, 633

Lauberts, A. & Valentijn, E.A. 1989, The Surface Photometry Catalogue of the ESO-Uppsala Galaxies

Lauer, T. R., Faber, S. M., Gebhardt, K., Richstone, D., Tremaine, S., Ajhar, E. A., Aller, M. C., Bender, R., Dressler, A., Filippenko, A. V., Green, R., Grillmair, C. J., Ho, L. C., Kormendy, J., Magorrian, J., Pinkney, J., & Siopis, C., 2005, AJ , 129, 2138

Lee, H., Grebel, E. K. & Hodge, P. W., 2003, Astronomische Nachrichten Supplement, 324, 90

Lee, H., Zucker, D. B. & Grebel, E. K., 2007, MNRAS , 376, 820

Lequeux, J., Peimbert, M., Rayo, J. F., Serrano, A., & Torres-Peimbert, S., 1979, A&A , 80, 155

Lisker, T., Grebel, E. K. & Binggeli, B., 2006, AJ , 132, 497

Liu, M. C., Charlot, S., & Graham, J. R., 2000, ApJ , 543, 644

Liu, X.-W., Storey, P. J., Barlow, M. J., Danziger, I. J., Cohen, M., & Bryce, M., 2000, MNRAS , 312, 585

Magorrian, J., Tremaine, S., Richstone, D., Bender, R., Bower, G., Dressler, A., Faber, S. M., Gebhardt, K., Green, R., Grillmair, C., Kormendy, J., & Lauer, T., 1998, AJ , 115, 2285

Martin, N. F., Ibata, R. A., Chapman, S. C., Irwin, M., & Lewis, G. F., 2007, MNRAS , 380, 281

Martin, N. F., Ibata, R. A., Irwin, M. J., Chapman, S., Lewis, G. F., Ferguson, A. M. N., Tanvir, N., & McConnachie, A. W., 2006, MNRAS , 371, 1983

Massey, P., Valdes, F., & Barnes, J., A User's Guide to Reducing Slit Spectra with IRAF

Mateo, M. L., 1998, ARA&A , 36, 435

Mayer, L., Governato, F., Colpi, M., Moore, B., Quinn, T., Wadsley, J., Stadel, J., & Lake, G., 2001, ApJL , 547, L123

McNamara, B. J., Harrison, T. E., & Anderson, J., 2003, ApJ , 595, 187

Merritt, D., Ferrarese, L., & Joseph, C. L., 2001, Science, 293, 1116

Moore, B., Lake, G., & Katz, N., 1998, ApJ , 495, 139

Moore, B., Ghigna, S., Governato, F., Lake, G., Quinn, T., Stadel, J., & Tozzi, P., 1999, ApJL , 524, L19

Muñoz, R. R., Carlin, J. L., Frinchaboy, P. M., Nidever, D. L., Majewski, S. R., & Patterson, R. J., 2006, ApJL , 650, L51

Nagashima, C., Nagayama, T., Tamura, M., Sugitani, K. et al., 2002, Science with SIRIUS: Simultaneous-color InfraRed Imager for Unbiased Surveys, eds., Tyson, J. A., Wolff, S., Proceedings of the SPIE, 4836, 29.

Noeske, K. G., Papaderos, P., Cairós, L. M., & Fricke, K. J., 2003, A&A , 410, 481

Noyola, E., Gebhardt, K., & Bergmann, M., 2008, ApJ , 676, 1008

O'Donoghue, D., et al. , 2006, MNRAS , 372, 151

Onken, C. A., Ferrarese, L., Merritt, D., Peterson, B. M., Pogge, R. W., Vestergaard, M., & Wandel, A., 2004, ApJ , 615, 645

Osterbrock, D. E., 1989, Astrophysics of gaseous nebulae and active galactic nuclei (University Science Books)

Pagel, B. E. J., 1985, "Abundances of C, N, O in HII regions", ed. Danziger, I. J., Matteucci, F., & Kjar, K., European Southern Observatory Astrophysics Symposia, 21, 155

Pagel, B. E. J., Simonson, E. A., Terlevich, R. J., & Edmunds, M. G., 1992, MNRAS , 255, 325

Parodi, B. R., Barazza, F. D., & Binggeli, B., 2002, A&A , 388, 29

Pedraz, S., Gorgas, J., Cardiel, N., Sánchez-Blázquez, P., & Guzmán, R., 2002, MNRAS , 332, L59

Persson, S. E., Murphy, D. C., Krzeminski, W., Roth, M., & Rieke, M. J., 1998, AJ 116, 2475.

Peterson, R. C., & Caldwell, N., 1993, AJ , 105, 1411

Peterson, B. M., Ferrarese, L., Gilbert, K. M., Kaspi, S., Malkan, M. A., Maoz, D., Merritt, D., Netzer, H., Onken, C. A., Pogge, R. W., Vestergaard, M., & Wandel, A., 2004, ApJ , 613, 682

Prugniel, P., Bica, E., Klotz, A., & Alloin, D., 1993, A&AS , 98, 229

Prugniel, P., Chilingarian, I., Sil'Chenko, O., & Afanasiev, V., 2005, in IAU Colloq. 198, Near-fields cosmology with dwarf elliptical galaxies, eds. Jerjen, H. and Binggeli, B., 73

Pryor, C., & Meylan, G., 1993, "Velocity Dispersions for Galactic Globular Clusters", ed. Djorgovski, S. G. & Meylan, G., Astronomical Society of the Pacific Conference Series, 50, 357

Putman, M. E., 2000, Publications of the Astronomical Society of Australia, 17, 1

Puzia, T. H., & Sharina, M. E., 2008, ApJ , 674, 909

Puzia, T. H., Kissler-Patig, M., Brodie, J. P., & Schroder, L. L., 2000, AJ , 120, 777

Ravindranath, S., Ho, L. C., Peng, C. Y., Filippenko, A. V., & Sargent, W. L. W., 2001, AJ , 122, 653

Rest, A., van den Bosch, F. C., Jaffe, W., Tran, H., Tsvetanov, Z., Ford, H. C., Davies, J., & Schafer, J., 2001, AJ , 121, 2431

Richer, M. G., & McCall, M. L., 1995, ApJ , 445, 642

Richstone, D., Ajhar, E. A., Bender, R., Bower, G., Dressler, A., Faber, S. M., Filippenko, A. V., Gebhardt, K., Green, R., Ho, L. C., Kormendy, J., Lauer, T. R., Magorrian, J., & Tremaine, S., 1998, Nature , 395, A14

Sadler, E. M., Oosterloo, T., & Morganti, R., 2002, ASP Conf. Ser. , "The Dynamics, Structure & History of Galaxies: A Workshop in Honour of Professor Ken Freeman", eds. Da Costa, G. S. & Jerjen, H., 273, 215

Saviane, I., Ivanov, V. D., Held, E. V., Alloin, D., Rich, R. M., Bresolin, F., & Rizzi, L., 2008, A&A , 487, 901

Schlegel, D. J, Finkbeiner, D. P., & Davis, M., 1998, ApJ , 500, 525

Schmidt, K.-H. & Boller, T., 1992, Astronomische Nachrichten, 313, 329

Seitzer, P., Grebel, E. K., Dolphin, A. E., Geisler, D., Guhathakurta, P., Hodge, P. W., Karachentsev, I. D., Karachentseva, V. E., & Sarajedini, A., 2001, Bulletin of the American Astronomical Society, 33, 800

Sérsic, J. L., 1968, Atlas de Galaxias Australes (Córdoba: Obs. Astron. Univ. Nac. Córdova)

Shergin, V.S., Kniazev, A.Y., & Lipovetsky, V.A., 1996, Astronomische Nachrichten, 2, 95

Simien, F., & Prugniel, P., 2002, A&A , 384, 371

Simon, J. D., & Geha, M., 2007, ApJ , 670, 313

Skillman, E. D., & Bender, R., 1995, *RMxAC* 3, 25

Skillman, E. D., Côté, S., & Miller, B. W., 2003, AJ , 125, 593

Skillman, E. D., Kennicutt, R. C. & Hodge, P. W., 1989, ApJ , 347, 875

Skillman, E. D., Terlevich, R., & Melnick, J., 1989, MNRAS , 240, 563

Skrutskie, M. F., Cutri, R. M., Stiening, R., Weinberg, M. D. et al., 2006, AJ 131, 1163.

Spergel, D. N., Bean, R., Doré, O., Nolta, M. R., Bennett, C. L., Dunkley, J., Hinshaw, G., Jarosik, N., Komatsu, E., Page, L., Peiris, H. V., Verde, L., Halpern, M., Hill, R. S., Kogut, A., Limon, M., Meyer, S. S., Odegard, N., Tucker, G. S., Weiland, J. L., Wollack, E., & Wright, E. L., 2007, ApJS , 170, 377

Stasińska, G., 1990, A&AS , 83, 501

Stasińska, G., & Izotov, Y., 2003, A&A , 397, 71

St-Germain, J., Carignan, C., Côte, S., & Oosterloo, T., 1999, AJ , 118, 1235

Stiavelli, M., Miller, B. W., Ferguson, H. C., Mack, J., Whitmore, B. C., & Lotz, J. M., 2001, AJ , 121, 1385

Strigari, L. E., Bullock, J. S., Kaplinghat, M., Simon, J. D., Geha, M., Willman, B., & Walker, M. G., 2008, Nature , 454, 1096

Talent, D. L., A Spectrophotometric Study of HII Regions in Chemically Young Galaxies, PhD thesis, Rice Univ., 1980, Houston, TX

Taylor, J. E. & Babul, A., 2003, ApSS , 284, 405

Thuan, T.X., Izotov, Y.I., & Lipovetsky, V.A. 1995, ApJ , 445, 108

Tonry, J., & Davis, M., 1979, AJ , 84, 1511

Tonry, J., & Schneider, D. P., 1988, AJ , 96, 807

Toomre, A., & Toomre, J., 1972, ApJ , 178, 623

Torres-Peimbert, S., & Peimbert, M. 1977, Revista Mexicana de Astronomia y Astrofisica, 2, 181

Trentham, N., & Tully, R. B., 2002, MNRAS , 335, 712

Tremaine, S., Gebhardt, K., Bender, R., Bower, G., Dressler, A., Faber, S. M., Filippenko, A. V., Green, R., Grillmair, C., Ho, L. C., Kormendy, J., Lauer, T. R., Magorrian, J., Pinkney, J., & Richstone, D., 2002, ApJ , aug, 574, 740

Trujillo, I., Erwin, P., Asensio Ramos, A., & Graham, A. W., 2004, AJ , 127, 1917

Trujillo, I., Graham, A. W. & Caon, N., 2001, MNRAS , 326, 869

Ugryumov, A. V., Engels, D., Kniazev, A. Y., Green, R. F., Izotov, Y. I., Hopp, U., Pustilnik, S. A., Pramsky, A. G., Kniazeva, T. F., Brosch, N., Hagen, H.-J., Lipovetsky, V. A., Masegosa, J., Márquez, I., & Martin, J.-M., 2001, A&A , 374, 907

Ugryumov, A. V., Engels, D., Pustilnik, S. A., Kniazev, A. Y., Pramskij, A. G., & Hagen, H.-J., 2003, A&A , 397, 463

Vaduvescu, O. & McCall, M.L. 2004, PASP , 116, 640

Vaduvescu, O., McCall, M. L., Richer, M. G., & Fingerhut, R. L., 2005, AJ , 1593

Valluri, M., Ferrarese, L., Merritt, D., & Joseph, C. L., 2005, ApJ , 628, 137

van der Marel 1994, MNRAS , 270, 271

van der Marel, R. P., 2004, Coevolution of Black Holes and Galaxies, from the Carnegie Observatories Centennial Symposia. Published by Cambridge University Press, as part of the Carnegie Observatories Astrophysics Series. Edited by L. C. Ho, 37

van den Bergh, S., & Mackey, A. D., 2004, MNRAS , 354, 713

van Zee, L., Haynes, M. P., & Salzer, J. J., 1997, AJ , 114, 2479

van Zee, L., Skillman, E. D., & Haynes, M. P., 2004, AJ , 128, 121

van Zee, L., & Haynes, M. P., 2006, ApJ , 636, 214

Vanzi, L., Hunt, L. K., & Thuan, T. X., 2002, A&A , 390, 481

Vanzi, L., Hunt, L. K., Thuan, T. X., & Izotov, Y. I., 2000, A&A , 363, 493

Vila Costas, M. B., & Edmunds, M. G., 1993, MNRAS , 265, 199

Whitford, A.E. 1958, AJ , 63, 201

Willman, B., Blanton, M. R., West, A. A., Dalcanton, J. J., Hogg, D. W., Schneider, D. P., Wherry, N., Yanny, B., & Brinkmann, J., 2005, AJ , 129, 2692

Worthey, G., 1994, ApJS , 95, 107

Zucker, D. B. et al. , 2004, ApJL , 612, L117

Zucker, D. B. et al. , 2004, ApJL , 612, L121